Technical University of Denmark

Rock-physics modelling of the North Sea greensand

Zakir Hossain

DTU Environment
Department of Environmental Engineering

PhD Thesis
May 2011

Rock-physics modelling of the North Sea greensand

Zakir Hossain

PhD Thesis
May 2011

DTU Environment
Department of Environmental Engineering
Technical University of Denmark

Zakir Hossain

Rock-physics modeling of the North Sea greensand

PhD Thesis, May 2011

The thesis will be available as a pdf-file for downloading from the homepage of the department: www.env.dtu.dk

Address:	DTU Environment Department of Environmental Engineering Technical University of Denmark Miljoevej, building 113 DK-2800 Kgs. Lyngby Denmark
Phone reception:	+45 4525 1600
Phone library:	+45 4525 1610
Fax:	+45 4593 2850
Homepage:	http://www.env.dtu.dk
E-mail:	reception@env.dtu.dk
Printed by:	Vester Kopi Virum, May 2011
Cover:	Torben Dolin
ISBN:	978-87-92654-35-9

Table of Contents

Preface

This PhD thesis entitled "Rock-physics modelling of the North Sea greensand" is based on three years research carried out at the Department of Environmental Engineering, Technical University of Denmark (DTU) with associate professor Ida Lykke Fabricius as the main supervisor. The project was financed by DTU and Dong A/E. Most of the experimental work for this thesis was carried out at DTU, GEO (Danish Geotechnical Institute) and GEUS (Geological Survey of Denmark and Greenland, co-operation with Niels Springer and Dan Olsen). Additional experimental work was carried out at Copenhagen University, Imperial College, London and University of Stavanger, Norway. During the PhD study I stayed around four months in the Stanford Reservoir Forecasting (SRF) group, Department of Energy Research Engineering, Stanford University, USA where I worked together with Associate Professor Tapan Mukerji.

The thesis consists of a synopsis and six papers. The papers include two published papers, one accepted paper, one submitted revised paper, one submitted paper and a peer reviewed conference paper.

Journal papers

I. **Hossain, Z.**, Fabricius, I.L., Grattoni, A. C. and Solymar, M. (2011): Petrophysical properties of greensand as predicted from NMR measurements. *Petroleum Geoscience,* vol 17, No. 2, pp 111-125.

II. **Hossain, Z.**, Fabricius, I.L., Mukerji, T. and Dvorkin, J. (2011): Rock Physics model of glauconitic greensand from the North Sea. *Geophysics* (submitted revised version).

In: SRB Annual Meeting 23-25 June, 2010. Stanford Rock Physics & Borehole Geophysics Project. Annual Report Vol. 121, p. B1-B21, Stanford University, Stanford, CA.

III. **Hossain, Z.**, Fabricius, I.L. and Mukerji, T. (2011): V_p-V_s relationship and AVO modelling for glauconite bearing sandstone. *Geophysical Prospecting* (in press).

IV. **Hossain, Z.** and Fabricius, I.L. (2011). Effect of CO_2 injection of physical properties of greensand. *Journal of Petroleum science and Engineering* (submitted).

Journal papers (related studies):

V. **Hossain, Z.**, and Mukerji, T (2011). Statistical rock physics and Monte Carlo simulation of seismic attributes for greensand (Accepted for EAGE annual meeting, Vienna, May 23-26, 2011).

VI. **Hossain, Z.**, Fabricius, I.L. and Christensen, H.F. (2009): Elastic and non-elastic deformation of greensand. *The Leading Edge*, Volume 28, Issue 1, pp. 86-88.

Acknowledgements

In 2005 I first came to DTU to pursue a Master of Science degree in Petroleum Engineering. I was supposed to go somewhere in the world after finishing my Master degree. However, I was so lucky that I found Associate Professor Ida Lykke Fabricius as my supervisor for my Master thesis. During my thesis Ida offered me for doing PhD in DTU. That was the greatest opportunity in my life so far. My last three years here at DTU have been a fantastic and rewarding experience. I would like to thank Ida Fabricius for being a fantastic advisor; she has guided me along the path that led to where I am today. Last three years with her help I completed not only a PhD thesis but also a wonderful scientific moment in my life.

I would like to thank Associate professor Tapan Mukerji, Stanford University. I had great time with him during my external research in Stanford. I feel very lucky that I was able to visit Stanford and could collaborate with Tapan during my research. I also would like to thank Gary Mavko and Jack Dvorkin, SRB research group, Stanford University. Special thanks to Jack for his collaboration with one of my papers. I also thank my friend Sadeem, Kaushik and Tanima (Exxonmobil) for their help during my stay in Stanford. I also thank Ida to send me Stanford University for my external research.

Furthermore, I want to thank all the people who were somehow involved with my PhD studies. Special thanks to Monzurul Alam for his help and support during my study. Thanks to Ahmed, Morten, Katherine Hedegaard, Katherine Andreassen, Ernest for all the great time I had together with them. I also like to thank all my co-authors for their great collaboration. Sinh Hy Nguyen is thanked for helping me during the lab work. I thank Hector Ampuero Diaz for making my thin sections. I thank Helle, Frederick, Morten, Igor from GEO for their help during the lab work throughout my studies. I thank Dan Olsen for carried out my CO_2 flooding experiment. Niels Spring and Hans Jørgen Lorentzen from GEUS are thanked for advises and help with laboratory work.

I would like to thank Dong E/A for their data, samples, and financial support for my PhD project.

At last but not all, I like to thank my wife Shila and my lovely young sweet daughter Zineta for their big support and understanding. I appreciate their patience and sacrifice during my PhD studies.

Kgs. Lyngby, Zakir Hossain
March 2011

Summary

Greensands are composed of a mixture of stiff clastic quartz grains and soft glauconite grains. Glauconites are porous and composed of aggregates of iron-bearing clay. Greensands from the two formations in the Nini field of the North Sea were studied in this thesis. Hermod Formation is weakly cemented, whereas Ty Formation is characterized by microcrystalline quartz cement. A series of laboratory experiments including core analysis, capillary pressure measurements, NMR T_2 measurements, acoustic velocity measurements, electrical properties measurements and CO_2 injection experiments were done on greensand samples. Thin sections and BSE images are also available for this study.

The objective of the first part of this study is to predict petrophysical properties from nuclear magnetic resonance (NMR) T_2 distributions. NMR is a useful tool in reservoir evaluation. Estimated petrophysical properties from NMR measurements were correlated with measurements from core analysis. NMR underestimates the total porosity due to the presence of iron bearing clay minerals in greensand. Permeability may be predicted from NMR by using Kozeny's equation when surface relaxivity is known. The surface area measured by the BET method is associated with the micro-porous glauconite grains. The effective specific surface area as calculated from Kozeny's equation is associated with macro-pores. Capillary pressure drainage curves may be predicted from NMR T_2 distribution when pore size distribution within a sample is homogeneous.

The central part of this study is rock-physics modelling of greensand. The first of the models is a grain contact model of the North Sea Paleocene greensand. First a Hertz-Mindlin contact model is developed for a mixture of quartz and glauconite. Next step is to use the moduli predicted from this Hertz-Mindlin contact model of two types of grains as the initial moduli for a soft-sand model and a stiff-sand model. Results of rock-physics modelling and thin section observations indicate that variations in the elastic properties of greensand can be explained by two main diagenetic phases: silica cementation and berthierine cementation. Initially greensand is a mixture of mainly quartz and glauconite; when weakly cemented, it has relatively low elastic modulus and can be modeled by a Hertz-Mindlin contact model of two types of grains. Silica-cemented greensand has a relatively high elastic modulus and can be modeled by an intermediate-stiff-sand or a stiff-

sand model. Berthierine cement has a different growth patterns in different part of the greensand, resulting in a soft-sand model and an intermediate-stiff-sand model.

The second rock-physical model predicts V_p-V_s relations and AVO of a greensand shale interface. The relationship between V_p and V_s may be used to predict V_s where only V_p is known. In published work, focus is primarily on the V_p-V_s relationship of quartzitic sandstone. In order to broaden the picture V_p-V_s relationships of greensand were presented. A V_p-V_s relationship derived from modelling is compared with empirical V_p-V_s regressions from laboratory data. The quality of V_s prediction is quantified by statistical analysis. The V_p-V_s relationship derived from modelling works well for greensand shear-wave velocity prediction. AVO modelling shows that brine saturated glauconitic greensand may have similar seismic response to oil saturated quartzitic sandstone and that strongly cemented greensand with oil saturation can have similar AVO response to brine saturated weakly cemented greensand.

The third rock-physical model predicts pore fluid effects on elastic properties of greensand. NMR studies were included to describe the fluid related dispersion in greensand. NMR studies show that Biot's flow should occur only in large pores in the greensand, while Biot's flow should not occur in micro-pores. Differences of fluid flow in macro-pores and micro-pores are described as high frequency squirt flow in greensand.

The objective of the last part of this study is to investigate CO_2 injection effects on physical properties of greensand. Laboratory results indicate that CO_2 injection has no major effect on porosity, electrical properties and elastic properties of greensand. In contrast Klinkenberg permeability of greensand increased after CO_2 injection. An NMR permeability modelling approach was tested to evaluate the effect on matrix permeability of CO_2 injection. It appears that permeability after CO_2 injection increased not due to fracturing but rather due to the increase of macro-pores in the greensand. The increase of macro-pores size is probably due to migration of fine pore-filling minerals. Rock-physics modelling indicates that the presence of CO_2 in a greensand decreases V_p by 2%-41% relative to V_p of brine saturated greensand. CO_2 flooding would at the same time increase V_s, typically 1%-2%, while decreasing density by 3%-5%.

Dansk sammenfatning

Grønsand består af en blanding af stive kvartskorn og blødere glaukonitkorn. Glaukonitkorn er porøse aggregater af jernholdigt ler. I denne ph.d.-afhandling undersøges grønsand fra to formationer i Nordsøens Nini felt. Hermod Formationen er kun svagt cementeret, mens Ty Formationen indeholder mikrokrystallin kvartscement. På kerneprøver fra de to formationer blev der foretaget laboratoriemålinger af bl.a. kapillartrykskurver, kernemagnetisk resonansspektrometri (NMR), hastighed af elastiske bølger (Vp og Vs), elektriske egenskaber samt effekten af CO_2-injektion. Tyndslibsbeskrivelser og elektronmikroskopbilleder var til rådighed.

I første del af afhandlingen undersøgtes anvendelsen af NMR til at forudsige reservoiregenskaber. Ved at sammenligne fysiske egenskaber målt direkte på kerneprøver med de samme egenskaber modelleret ud fra NMR vistes det, at NMR er et nyttigt redskab til reservoirkarakterisering. Porøsitet bestemt ud fra NMR er dog for lav, sandsynligvis på grund af glaukonits indhold af jern. Permeabilitet kan modelleres ret nøjagtigt ved en ny metode til anvendelsen af Kozenys ligning. Metoden kræver kendskab til mineralernes overfladerelaksering. Det ses, at den specifikke overfalde som målt med kvælstofadsorption (BET) domineres af bidrag fra de porøse glaukonitkorn, mens den effektive specifikke overflade beregnet ved hjælp af Kozenys ligning må associeres til makroporerne. For homogene prøver kan kapillartrykskurven modelleres ud fra NMR.

Afhandlingens centrale afsnit omhandler bjergartsfysisk modellering af grønsand. Først undersøgtes en kornkontaktsmodel af Hertz-Mindlin typen for blandinger af kvartskorn og glaukonitkorn svarende til det palæogene nordsøfelt. Denne kornkontaktmodel dannede basis for videre modellering ved hjælp af ”soft-sand” og ”stiff-sand” modeller. Resultaterne af den bjergartsfysiske modellering kombineret med observationer i tyndslib viste, at variationen i grønsandets elastiske egenskaber kan forklares ud fra to diagenetiske faser: kiselcementering og cementering med berthierin. I udgangspunktet er grønsand en blanding af kvartskorn og glaukonitkorn. Når det kun er svagt cementeret, har det lave elastiske moduli, som kornkontaktmodellen er tilstrækkelig til at modellere. Kiselcementeret grønsand har relativt høje elastiske moduli, som kan modelleres ved hjælp af ”intermediate-stiff-sand” og ”stiff-sand” modeller.

Berthierincementering giver anledning til elastiske moduli, der kan modelleres ved hjælp af ”soft-sand” eller ”intermediate-stiff-sand” modeller.

Dernæst undersøgtes modeller til at forudsige Vp-Vs relationer og til AVO analyse af en kontaktflade mellem lerskifer og grønsand. Vp-Vs relationer bruges til at forudsige Vs, når kun Vp kendes. Der findes allerede publicerede Vp-Vs relationer for kvartssand, mens grønsand er mindre velkendt. De bjergartsfysisk modellerede Vp-Vs relationer svarer inden for måleusikkerheden til direkte målte Vp-Vs relationer. AVO modellering viste, at vandmættet grønsand kan give samme seismiske respons som oliemættet kvartsand; samt at stærkt cementeret grønsand med olie kan give samme seismiske respons som vandmættet svagt cementeret grønsand.

Den tredje bjergartsfysike model af grønsand beskriver porevæskens indvirkning på de elastiske moduli. NMR data blev inddraget til at beskrive grønsand som en blanding af mikroporøse korn, der typisk vil være lavfrekvente i henhold til Biots model, og af korn og store porer, der kan beskrives som et højfrekvent system i henhold til Biot. Trykgradienter i porevæsken på grund af kontraster i porestørrelsen kan beskrives ved hjælp af en Squirt model.

Den sidste del af afhandlingen omhandler effekten af CO_2-injektion i vandmættet grønsand. Laboratoriemålingerne viste ingen tydelig effekt på porøsitet, elektriske egenskaber eller elastiske egenskaber af det vandmættede sand. Derimod iagttoges en forstørret permeabilitet. For at vise at denne effekt ikke bare skyldtes opsprækning, modelleredes permeabiliteten ud fra NMR data, og det vistes, at permabilitetsforøgelsen kan skyldes ændring i porestørrelsesfordelingen på grund af omfordeling af fine partikler. Den forventede seismiske respons på CO_2-injektion modelleredes. Vp forventes at ville mindskes med 2%-41%, Vs at ville øges med 1%-2%, mens massedensiteten vil mindskes med 3%-5%.

1. Introduction

Greensands are glauconite bearing sandstones. Greensand petroleum reservoirs can be found all over the world, e.g. the Mid-Cretaceous Safaniya Sandstone Member in Saudi Arabia (Cagatay et al., 1996), a Lower Cretaceous Glauconitic Sandstone in Alberta, Canada (Tilley and Longstaffe, 1984), the Upper Cretaceous Shannon Sandstone in Wyoming, USA (Ranganathan and Ty, 1986), a Lower Cretaceous Greensand offshore Ireland (Winn, 1994) and Late Paleocene Greensand in central part of the North Sea (Solymar, 2002; Solymar et al., 2003; Schiøler et al., 2007; Stokkendal et al., 2009; Hossain et al., 2009; Hossain et al., 2010a; Hossain et al., 2010b; Hossain et al., 2010c; Hossain et al., 2010d; Hossain et al., 2011a; Hossain et al., 2011b; Hossain et al., 2011c). Greensands are composed of a mixture of stiff clastic quartz grains and soft glauconite grains. Glauconites are also porous and composed of aggregates of iron-bearing clay (Figure 1.1). In fact, evaluation of greensand reservoirs has challenged geologists, engineers as well as petrophysicists. Diaz et al. (2003) found that the amount of glauconite in greensand has effect on porosity, permeability and elastic properties of reservoir rocks. Glauconite is also ductile (Ranganthan and Ty, 1986) therefore glauconites can cause non-elastic deformation (Hossain et al., 2009). Slot-Petersen et al. (1998) and Hamada et al. (2001) found that greensands show low resistivity in the reservoir zone due to the large amount of bound water in the glauconite. Furthermore, Rueslåtten et al. (1998a) described that paramagnetic glauconite or pore filling berthierine in greensand may induce magnetic gradients on the pore level causing the NMR T_2 relaxation time to be shortened dramatically.

The combination of conventional core analysis, such as Helium porosity, Gas permeability, specific surface area by BET and image analysis of thin section micrographs is effective in the evaluation of normal reservoir rocks. However, for glauconite bearing greensand where a high proportion of micro-porosity in glauconite grains creates an uncertainty with respect to fluid distribution and fluid saturation, an accurate determination of petrophysical properties by using conventional core analysis is difficult (Rueslåtten et al., 1998b). Therefore, NMR measurements may be used to quantify petrophysical properties of greensand. The objective of Nuclear Magnetic Resonance (NMR) measurements on reservoir core samples is to obtain an improved interpretation of logging data. NMR is a non-invasive technique that causes net magnetization of a hydrogen atom (^1H) in the presence of an external magnetic field. NMR spectrometry involves a series of manipulations of the hydrogen proton found in pore fluids of a sedimentary rock. A measurement sequence starts with proton alignment to a magnetic field followed by spin tipping and decay. The quantities measured include signal amplitude which is proportional to the number of hydrogen nuclei and decay, also called relaxation time (Kenyon et al., 1995). The relaxation time is normally used to quantify porosity, permeability and the capillary pressure curve of a reservoir rock. The relaxation time may also be used to quantify the fluid flow within macro-pores and micro-pores in greensand.

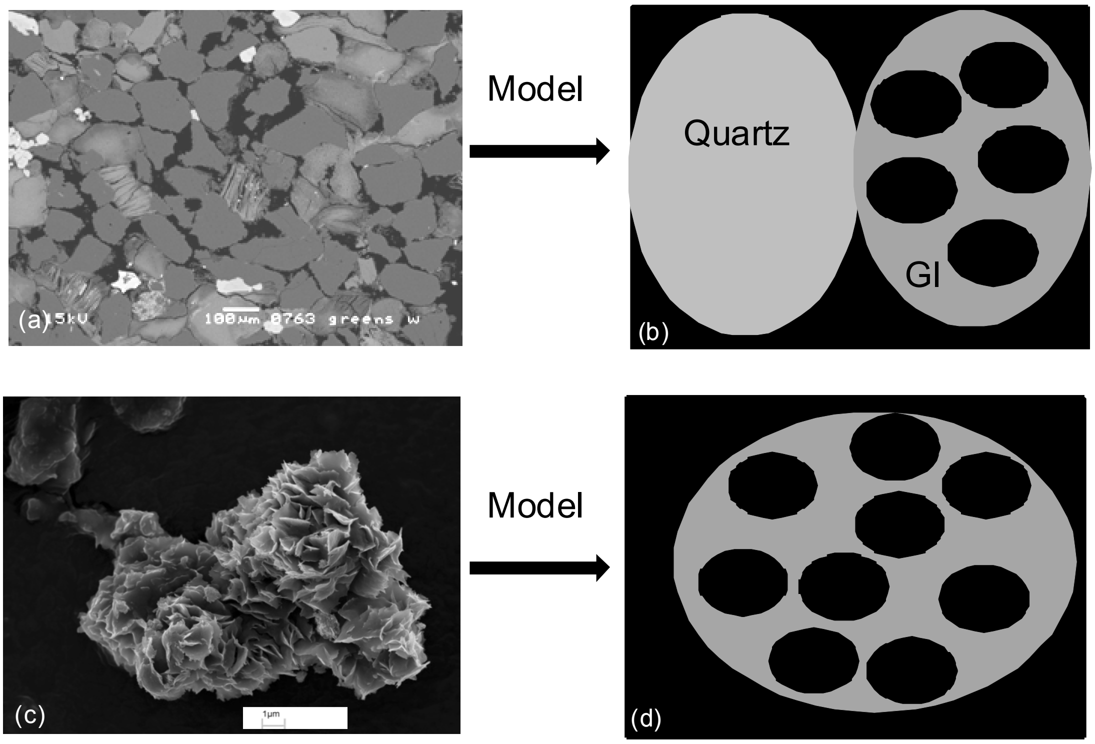

Figure 1.1. *(a) BSE image of the North Sea greensand and (b) its idealized model. (c) Glauconite grain from Arnager greensand (courtesy of Egil Nybakk) and (d) its idealized model. Scale bar for greensand is 100 µm and the image represents macro-porosity, quartz and glauconite grains. Scale bar for glauconite grain is 1 µm. Micro-pores reside within glauconite grain.*

Rock-physics modelling becomes an integral part of geophysics, petrophysics and geology. Rock-physics modelling bridges the elastic properties and geological properties. Rock-physics modelling has been used as a tool to 4D seismic monitoring of a reservoir, to discriminate seismic lithology and to detect hydrocarbon. In published work, laboratory ultrasonic measurements have been performed in quartz sandstone and shaly sandstone, and various theoretical models have been developed (see overview in Mavko et al., 2009). However, rock-physics models for greensand are not well defined yet. Even though lots of rock-physics models are cited in the literature, their limitations and assumptions have always made it difficult to compare models to real rock properties. In order to make a rock-physics model universal, physical behavior of rocks should be honored. Hence an accurate estimation of physical properties can be a useful input for rock-physics modelling of greensand.

Granular media contact models are widely used rock-physics models for calculating the elastic properties of rocks. Contact models determine the elastic properties of granular media by deformability and stiffness of grain to grain contacts. Most of the contact models are developed based on the Hertz-Mindlin theory for the elastic behavior of two spheres in contact. However, for the sand-pack for sandstone, it is assumed that only quartz grains are packed together, and the normal and shear stiffness are calculated based on the contact of two quartz grains. For rocks with mixed mineralogy, a homogeneous mineral modulus is assumed. Then the normal and shear stiffnesses are calculated based on the contact of two average-mineralogy grains. Average-mineralogy is normally derived by using Hill's average. In fact, this is probably only applicable when the moduli of mixed minerals are quite comparable. This is probably not adequate when the elastic contrasts between mixed minerals are quite different. For greensands, the initial sand-pack is a mixture of quartz and glauconite, and because both of them are load bearing, elastic properties in between those of quartz and glauconite are anticipated. A Hertz-Mindlin contact model based on single grain type is not enough to estimate the elastic properties of mixtures of quartz and glauconite.

A part of rock-physics modelling is establishing V_p-V_s relationship and AVO analysis. A V_p-V_s relationship is normally used to predict V_s where only V_p is known. It is also used for AVO analysis and to identify the pore fluids from seismic data. Without V_s it is often difficult to separate the seismic signature according to lithology, pore fluids and pore pressure. In published work, focus is primarily on the V_p-V_s relationship and AVO analysis of quartzitic sandstone. However, the V_p-V_s relationship of greensand has not yet been defined. Furthermore, the elastic moduli of micro-porous glauconite grains and their effect on the V_p-V_s relationship are also unknown. AVO modelling is a step in multidisciplinary integration of petrophysics, rock physics, seismic data, geology as well as petroleum engineering. One of the main objectives for AVO analysis is to predict the lithology and pore fluids from seismic data. However, in some cases AVO has been applied without success and the use of a too simple geological model is one of the reasons for failure. Therefore, the understanding of AVO response based on greensand properties is essential before using it for reservoir characterization.

Gassmann's fluid substitution method is widely used to predict velocities for saturated rock based on the velocities from dry rock. Gassmann's equations generally work at low frequency and do not take into consideration the fluid related dispersion. In some cases Biot's theory is used to describe the fluid related dispersion. In fact, several studies showed that Biot's theory does not fully explain the frequency dispersion for natural saturated rocks. By squirt relations, Mavko and Jizba (1991) show that water saturated rock may have larger velocity dispersion that would be predicted from Gassmann's equations and even prediction from Biot's high frequency case. Nevertheless, frequency related dispersion is not well studied for complex rocks as greensand. In the squirt flow mechanisms, the local flow in small cracks gives rise to local stiffening pressure gradients in the fluid. In greensand, it is possible that the contrast between flow in macro-pores and micro-pores within glauconites gives rise to a local stiffening pressure gradient in the fluid. Then fluid flow in greensand could then be described as squirt flow.

CO_2 capture and storage (CCS) is a technique to reduce CO_2 emission, and CO_2 is also used in EOR (enhanced oil recovery). It may increase oil production by 15%-25% from an oil field. CO_2 may be stored either as gas or dissolved in an aqueous solution in aquifers or in depleted oil or gas reservoirs. The consequence of CO_2 injection into a geological formation needs to be considered including the physical and chemical interaction of CO_2 with rock minerals and pore fluids. At reservoir conditions, CO_2 dissolved in water is in equilibrium with carbonic acid. The acid reacts with the rock thus changing its physical and mechanical properties. Even though CO_2 injection effect studies are common, they do not cover greensand reservoirs. The CO_2 injection processes in greensand could be more complicated than in quartz sand, because, interaction of CO_2 with glauconite is expected rather than with quartz. Furthermore, greensand from the North Sea contains micro-crystalline quartz and pore-filling clay (berthierine) cement (Solymar et al., 2002; Hossain et al., 2011b). Moreover, in the case of Nini field a question is whether injected CO_2 can be detected seismically.

1.1 Scope of study

The title of the present PhD research project is rock-physics modelling of the North Sea greensand. This study was divided into several parts. The first part was related to the use of NMR to predict petrophysical properties of greensand. The central part of this study is concerned with rock-physics modelling of greensand including a contact model, an empirical model, AVO analysis, and fluid related dispersion analysis. The last part of this study addresses CO_2 injection effect on physical properties of greensand.

In the first part of this study related to predicting petrophysical properties from NMR T_2 distributions. Estimates of porosity, permeability, irreducible water saturation derived from NMR measurement were correlated with data from core analysis. The potential use of surface area data is also described and illustrated. Kozeny's equation was used for NMR permeability prediction. Furthermore P_c curves were estimated from NMR measurements and compared with laboratory results.

The central part of this study is concerned with rock-physics modelling of greensand. Effective medium models were applied to model the porous grain of glauconite. In greensands, the initial sand-pack is a mixture of quartz and glauconite, and because both of them are load bearing, elastic properties between those of quartz and glauconite are anticipated; a Hertz-Mindlin contact model for mixtures of quartz and glauconite was presented in this study. Then this Hertz-Mindlin contact model of two types of grains was used as initial modulus for a soft-sand model and a stiff-sand model. Using these rock-physics models, the effect of microstructure on the elastic properties of greensand was explored and finally the rock-physical properties were linked to greensand diagenesis by results from thin section analysis.

The second part of the rock-modelling addresses empirical V_p-V_s relationships and AVO modelling of greensand. The objectives of this study are to predict the velocity of the elastic shear wave (V_s) from velocity of the elastic compressional wave (V_p) and to investigate the AVO response of greensand. The effective medium based Iso-frame model was used to derive a V_p-V_s relationship for greensand. Empirical V_p-V_s relationship for greensand was also derived from laboratory measured data. Widely used V_p-V_s relationships in literature are also used to predict V_s for giving a V_p. Statistical analysis was done to compare the predictions by using different relations. AVO modelling of glauconitic greensands was also done with the goal of better understanding AVO behavior for this kind of rock.

The third part of rock-physics modelling is concerned with pore fluid effects on elastic properties of greensand. The widely used Gassmann fluid substitution model was used to predict saturated moduli of greensand from dry moduli. Biot's critical frequency and NMR T_2 were combined to describe the differences in fluid flow within macro-pores and within micro-pores. Differences in fluid flow from micro-pores to macro-pores were described by a squirt model.

The last part of this study is related to CO_2 injection effects on physical properties of greensand. A CO_2 experiment on greensand samples was carried out to detect the CO_2 injection effect on physical properties. Petrophysical properties, elastic properties and electrical properties were compared before and after CO_2 injection. An NMR permeability modelling approach was used to evaluate the effect on matrix permeability of CO_2 injection. Furthermore, rock physics-based models were used to predict the changes of seismic properties due to the CO_2.

1.2 Geological and data setting for the Nini 1 field

The Nini field is located in Siri Canyon. Siri Canyon is part of a large system of submarine canyons in the Paleocene in the Norwegian-Danish Basin (Stokkendal et al., 2009). The reservoir consists of sand deposited in the Siri Fairway (Schiøler et al., 2007). The glauconite bearing sandstone in the Nini field is formally included in the Hermod Formation and in the older Ty Formation. These Paleocene reservoir sands are characterized by glauconite rich (20-30 vol %) fine grained and well sorted sand. In greensand both quartz grains and glauconite pellets are part of the load-bearing matrix. The greensand beds occur in a shale-sequence. In the Nini wells, the Hermod sand was found to be more massive, more porous and more permeable than Ty sand (Schiøler et al., 2007).

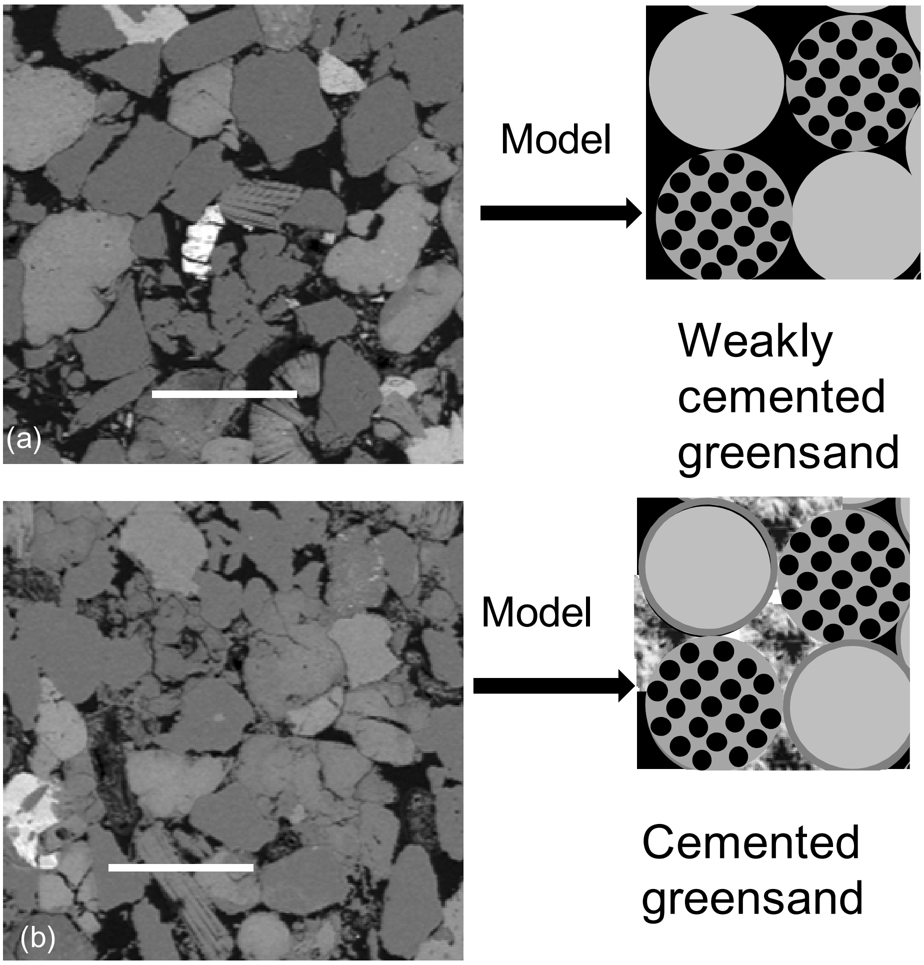

Figure 1.2. *BSE images of two types of greensands. Scale bar is 200µm. (a) Weakly cemented greensand and its idealized model and (b) cemented greensand and its idealized model.*

Solymar (2002) performed the petrographic thin section analysis of the studied greensand samples. Thin section analysis indicates that the studied Paleocene greensand are well to very well sorted, dominated by quartz but also large volume of glauconite (20-25 vol%). A smaller amount of feldspar, mica, as well as pore filling and pore lining minerals are also present in the studied greensand samples. Samples from Hermod Formation contain glauconite grains of size between 100 and 200 µm, some glauconite grains are larger (300 to 400 µm). Samples from Ty Formation contain glauconite grains of size between 100 and 150 µm, although some glauconite grains are larger (200 to 300 µm). The grains are sub-angular to sub-rounded in both Formations. However, the main difference between these two formations is that Hermod Formation is only weakly cemented, whereas samples from Ty Formation contain berthierine or microcrystalline quartz cement (Figure 1.2).

A series of log data including compressional wave velocity, shear wave velocity, density, gamma ray and resistivity from Nini 1 are available for this study. Sixteen one-and-half inch horizontal core plugs from the two greensand formations of the Nini field are included in this study. The samples have already been used for routine core analysis and were chosen to cover the range of variation in porosity (25%-40%) and air permeability (60 mD-1000 mD). All cores were cleaned of brine and hydrocarbons by soxhlet extraction with methanol and toluene prior to analysis. Thin sections were prepared from the end of each plug. Backscattered Electron Micrographs (BSE) from thin sections (courtesy of Mikael Solymar) are also available for this study. A series of laboratory experiments were performed on the greensand samples. Methods of petrophysical properties measurements including porosity, permeability, specific surface area, NMR and capillary pressure curves are described in Paper I. Methods of measuring elastic properties dry and brine saturation condition are described in Paper III. CO_2 injection methods on greensand samples are described in Paper IV. Methods of electrical properties measurement are described in Paper IV.

2. Petrophysical properties of greensand

2.1 NMR studies

NMR studies are widely used for characterization of petrophysical properties (e.g. Kenyon, 1997; Al-Mahrooqi et al., 2003; Al-Mahrooqi et al., 2006). Longitudinal relaxation time (T_1) measures the decay of spin alignment; transverse relaxation time (T_2) measures the decay of precession. Although T_1 measurements are more common in the literature, they are more time consuming than T_2 measurements. Hence, pulsed NMR logging tools preferentially measure T_2 for faster logging speeds (Straley et al., 1997). NMR transverse relaxation (T_2) of fluids confined in a porous rock is affected by pore surface, by the bulk relaxation process in the fluid and additionally by dephasing in case of molecular diffusion. T_2 may be expressed by the fundamental equation governing the NMR relaxation spectrum (Coates et al., 1999):

$$\frac{1}{T_2} = \frac{1}{T_{2Surface}} + \frac{1}{T_{2Bulk}} + \frac{1}{T_{2Diffusion}}. \tag{2.1}$$

In the above equation, $T_{2Surface}$ is the surface relaxation which is the dominating mechanism in porous media, controlled by pore surface area. The relation between NMR relaxation and pore surface area results from strong interaction between the protons and the surface because the surface relaxivity (ρ) causes rapid alignment of hydrogen protons on the pore wall, while protons in the remaining fluid decay through itself (bulk relaxation, T_{2Bulk}), which is much slower (Howard et al., 1993). Bulk relaxation is thus significantly smaller than the surface relaxation and so where relation of diffusion ($T_{2Diffusion}$) is slow, the transverse relaxation (T_2) may be related to surface to volume ratio of pores (*Sp*) and surface relaxivity:

$$\frac{1}{T_2} = \rho_2 S_P. \tag{2.2}$$

The NMR T_2 distributions of sixteen greensand samples are presented in graphical form and the populations are expressed in porosity units (p.u.) (Figure 2.1). All greensands have bimodal distribution. Each T_2 time corresponds to a particular pore size therefore, broader distribution reflect greater variability in pore size. The T_2 cutoff of 5.2 ms for the sample from Hermod Formation and

3.7 ms for the sample from Ty Formation was determined in the laboratory (details in Paper I). Therefore, in greensand samples a peak close to 1 ms should correspond to glauconite water, whereas all samples also present a second peak close to 100 ms that corresponds to movable fluid. Higher permeability greensands from Hermod Formation show larger amplitude in the movable fluid than samples from Ty Formations, whereas lower permeability samples from Ty Formation shows slightly larger amplitude in capillary bound glauconite water (Figure 2.1).

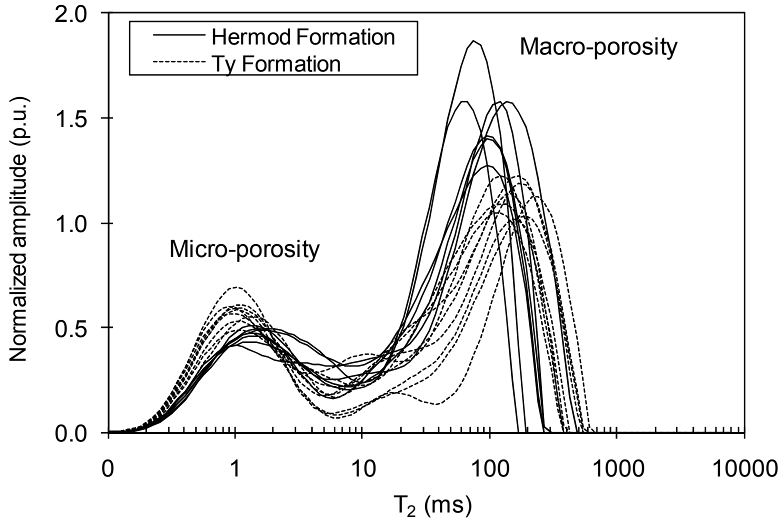

Figure 2.1. *NMR T_2 distribution curves shows two peaks for all greensand samples. The peaks close 1 ms represent micro-porosity and the peaks close to 100 ms represents macro-porosity.*

2.2 Porosity

Porosity is the key and primary parameter to evaluate the amount of hydrocarbon in a reservoir. NMR could be used as an effective tool to measure the formation porosity. However, several factors need to be considered before using an NMR tool in the greensand reservoir. Significant differences between NMR measured porosity and core analysis porosity was reported by several authors. Factors influencing the NMR T_2 measurements include paramagnetic minerals in the reservoir rock which may cause diffusion relaxation and hence reduce the T_2 relaxation time (Xie et al., 2008). They may also affect the surface relaxivity and produce a shift of the relaxation distribution to shorter time (Dodge et al., 1995).

Porosity of greensand ranges from 28 to 42 p.u. with a maximum uncertainty 1.5 p.u. However, laboratory measured Helium porosity, Archimedes porosity and NMR porosity are not equal (Figure 2.2). Helium porosity represents the total porosity of greensand including micro-porosity within glauconite and it shows the highest values among the three types of porosity data. In principle Archimedes porosity and NMR porosity should also represent the total porosity in greensand unless the saturation is below 100%. Although the Archimedes porosity is close to Helium porosity, NMR porosity tends to be the lowest. Both Archimedes and NMR porosity were measured assuming that samples are 100% saturated. Therefore, the discrepancy between Archimedes porosity and NMR porosity could be due to the some factor that has influence on one of the measurement techniques. Paramagnetic iron-bearing minerals in reservoir rock may be an important factor influencing T_2 measurements as shown by Dodge et al. (1995). Paramagnetic iron-bearing minerals have no effect on Archimedes porosity measurements. The presence of paramagnetic ions increases the rate of relaxation of the hydrogen proton. This is expected for greensand because glauconite and berthierine are iron-bearing. These clay minerals have large surface area and high magnetic susceptibilities leading to large internal gradients and short T_2 (Straley et al., 1997). Rueslåtten et al. (1998a) studied NMR of iron-rich sandstone from the North Sea and illustrated the influence of chlorite (berthierine) and glauconite on the difference between Helium porosity and NMR T_2 derived porosity (delta porosity) and found broad positive correlation between delta porosity and chlorite content, whereas they found no correlation with glauconite content. Thus they pointed to the detrimental effect of chlorite or berthierine on NMR estimated porosity.

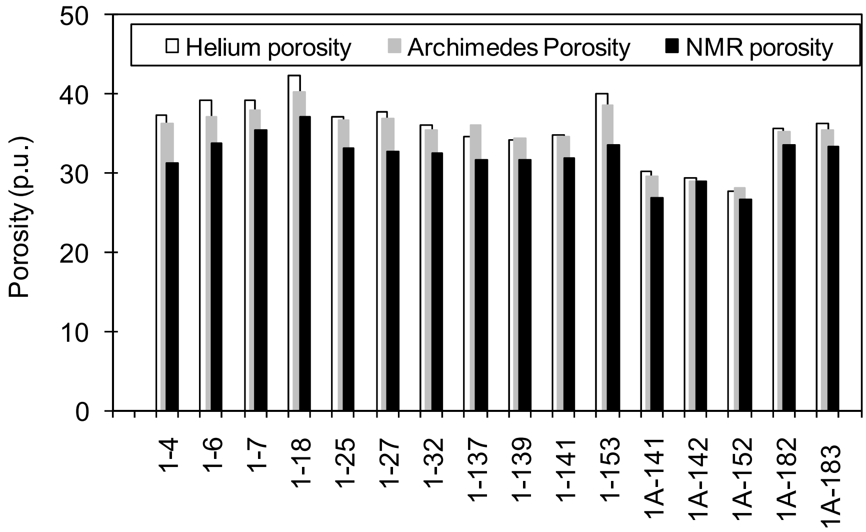

Figure 2.2. *Helium porosity, Archimedes porosity and NMR measured porosity of sixteen greensand samples. Helium porosity tends to be the highest, whereas porosity is underestimated by NMR measurements due to the iron bearing minerals in greensand.*

2.4 Permeability

Permeability is essential for reservoir characterization but can only be measured in the laboratory. Laboratory measured permeability provide the absolute permeability at core scale which could be different from formation permeability. NMR is the only tool that attempts to estimate *in-situ* formation permeability (Hidajat et al., 2002; Glover et al., 2006). Timur-Coates formula (Coates et al., 1999) is one of the most popular NMR derived permeability correlations used to calculate the formation permeability:

$$k_{NMR} = (C\phi)^m \left(\frac{FFI}{BFI}\right)^n , \tag{2.3}$$

where, ϕ is the porosity, *FFI* is the free fluid volume and *BFI* is the bound irreducible fluid, as determined from NMR T_2 distributions. Formation dependent constants *C*, *m* and *n* may be assumed to be 10, 4 and 2 for sandstones respectively, where NMR permeability, k_{NMR} is given in mD. This equation is just an empirical derived relationship that links various NMR-derived parameters to permeability and the complicated pore structure may not be described by the model. Therefore, predicted permeability by using this relationship may be unrealistic unless empirically calibrated parameters are used. In most cases these empirical parameters have no physical meaning and thus are only valid for special facies types and for local investigation. Kozeny's equation (Kozeny, 1927) is probably the most widely used physical permeability model. The Kozeny's equation may be implemented as (Kozeny, 1927; Mortensen et al. 1998):

$$k = c\frac{\phi^3}{S^2}, \tag{2.4}$$

where, *S* is the effective specific surface area, ϕ is the effective porosity and c is Kozeny's factor which can be estimated from the porosity via a simples model of 3D interpenetrating tubes (Mortensen et al., 1998):

$$c = \left[4\cos\left\{\frac{1}{3}\arccos\left(\phi\frac{8^2}{\pi^2}-1\right)+\frac{4}{3}\pi\right\}+4\right]^{-1}. \tag{2.5}$$

Specific surface of pores (Sp) can then be calculated as:

$$Sp = \frac{S}{\phi}. \tag{2.6}$$

Comparing Timur-Coates formula with Kozeny's equation indicates that porosity or pore volume strongly controls the permeability together with effective specific surface area as expressed by *FFI/BFI*. For homogenous sediments like chalk where the effective surface is equivalent to the one measured by nitrogen adsorption (BET), Kozeny's equation works well without introducing empirical factors (Mortensen et al., 1998). For less homogenous sediments like greensand, where effective surface is equivalent to the one measured by image analysis, Kozeny's equation works well to estimate permeability without introducing any empirical factors (Solymar, 2002). Kozeny's equation may be extended to calculate permeability from NMR T_2 distribution. By combining equation (2.2), (2.4), and (2.6) the permeability model for NMR measurements may be written as:

$$k = c\phi(T_2\rho_2)^2. \tag{2.7}$$

Equation (2.7) may be rewritten by summing the total permeability among the T_2 distribution accordingly:

$$k = c\phi\rho_2^2 \sum_{i=1}^{N} f_i (T_{2i})^2, \tag{2.8}$$

where, fi is a fraction of the total amplitude of each T_{2i}. The Kozeny factor, c is calculated by using equation (2.5).

The T_2 distribution of sample 1-18 peaks at longer time than for sample 1-6, thus the larger porosity of sample 1-18 is due to the larger pores which also cause higher permeability (Figure 2.2a). Predicted permeability distribution obtain by using equation (2.8) is shown in Figure 2.2b. Below 5.2 ms, the amplitude of permeability is close to zero which means micro-porosity within glauconite does not contribute significantly to fluid flow. Form 5.2 ms to 100 ms, the amplitude of permeability is small but above 100 ms the contribution permeability increases.

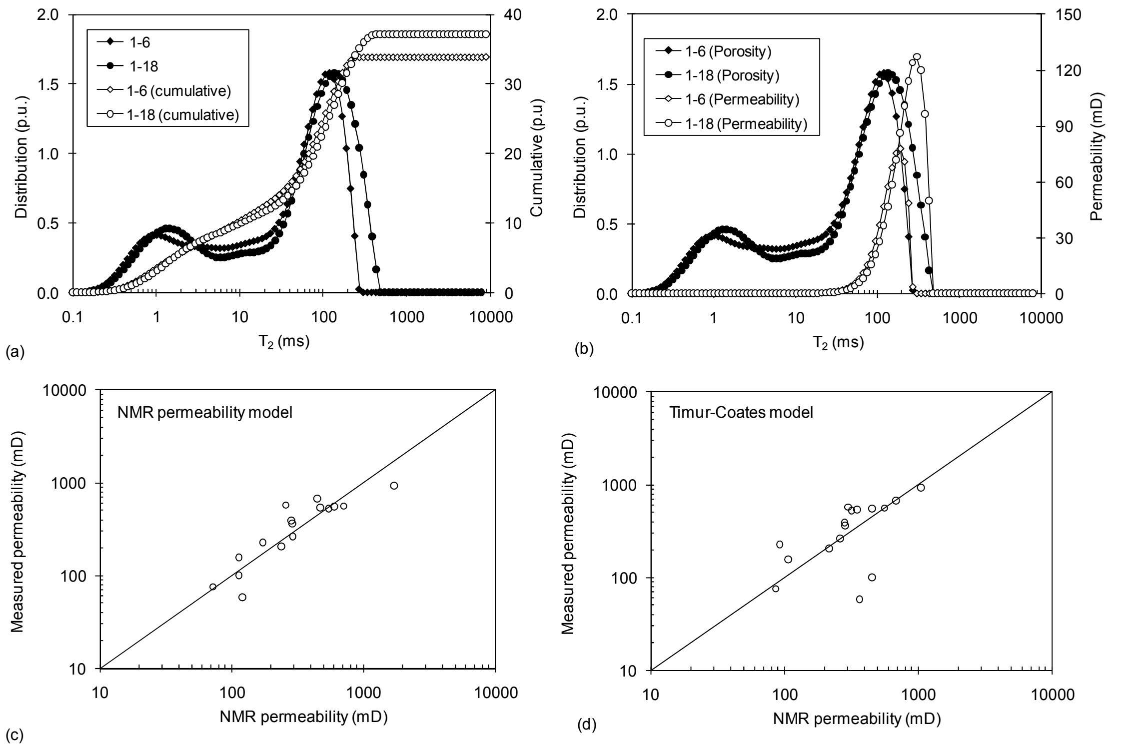

Figure 2.3. *(a) Porosity distribution and cumulative porosity of two greensand samples. (b) Porosity and permeability distribution of two greensand samples. (c) Klinkenberg permeability versus NMR predicted permeability by using Kozeny's (Kozeny 1927) equation. (d) Klinkenberg permeability versus NMR predicted permeability from Timur-Coates model.*

Predicted permeability by using equation 2.8 agrees well with measured permeability (Figure 2.2c). Predicted permeability by using Timur-Coates model works rather well if a formation dependent constant, C=8.3 is used which was optimized in a least-squares sense such that the sum of the squared error between the measured and predicted permeability is minimized.

2.5 Specific surface area

Specific surface area is a significant petrophysical parameter to understand the physics of porous media and to predict permeability. Specific surface area is related with porosity and permeability (Kozeny, 1927; Borre et al., 1997; Mortensen et al., 1998), with the fundamental equation governing the NMR relaxation spectrum (Coates et al., 1999), with capillary entry pressure (Røgen et al., 2002), with irreducible water saturation (Hamada et al., 1999; Hamada et al., 2001), with relative permeability (Morgan and Gordon, 1970), with Biot's critical frequency (Fabricius et al., 2010) and with cementation factor (Olsen et al., 2008). Riepe (1998) described that specific surface area never fully incorporated into special core analysis programs due to lack of petrophysical understanding and concepts for correct evaluation. Nitrogen adsorption methods (BET) yield high specific surface value as nitrogen enters the pores in the sample. By using image analysis to determine the specific surface area, usually a much smaller value is derived, and the value depends upon the resolution (Solymar et al., 2003). Therefore, by using a high resolution BET surface or a highly smoothed surface derived from image analysis, the calculated permeability can be varied several orders of magnitude (Riepe, 1998). Thus specific surface measured by different methods reflects the pore properties at different scales.

The relationship between macro-porosity and permeability are correlated with specific surface area of pores determined from Kozeny's equation (Figure 2.4a). Therefore, specific surface area estimated from Kozeny's equation is associated with effective surface area and related to macro-porosity. Nitrogen adsorption has a very high resolution; therefore this method determines the specific surface of the total porosity, including micro-porosity. The specific surface area of separated glauconite grains are in order of 1300-1600 μm^{-1} (Solymar, 2002), whereas the specific surface area of quartz grains is less than 1 μm^{-1}. So rather than of quartz grains, it is the specific surface of glauconite grains which are measured by BET method. For a few samples relations between micro-porosity and permeability within micro-porosity are correlated with specific surface area of pores determined by the BET method (Figure 2.4b). Correlations were calculated by using Kozeny's equation where permeability within micro-pores was quantified from NMR T_2 distribution. Still most of the samples have higher permeability within micro-pores than that can be predicted from specific surface area by BET method. A higher specific surface area by the BET method is reflected in pore filling/lining clays. Thus, specific surface area by the BET method is reflected not only by the micro-pores of glauconite grains but also by pore filling/lining clays.

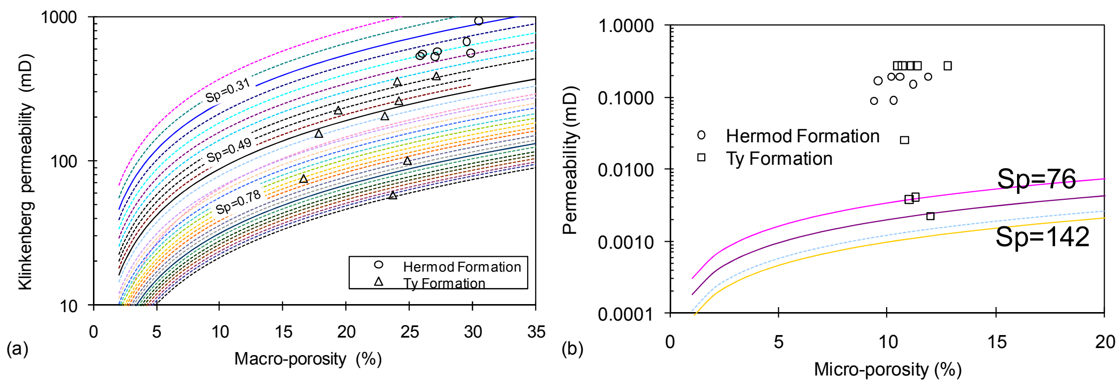

Figure 2.4. *(a) Relationship between macro-porosity and permeability. The reference lines represent the specific surface area of pores determined from Kozeny's equation. (b) Relationship between micro-porosity and permeability within micro-pores determined from NMR T_2 distribution. The reference lines represent the specific surface area of pores determined from BET method. Sample from Hermod Formation have similar porosity and permeability, whereas the samples from Ty Formation are more scattered.*

2.6 Capillary pressure curves

Capillary pressure curve (P_c) can be determined only from laboratory core analysis. However, several authors (e.g. Kleinberg, 1996, Grattoni et al., 2003, Marshal et al., 1995 and Volokitin et al., 1999) have also focused on the relationship between T_2 distribution and P_c curves and their general conclusion is that if the bulk relaxation and diffusion effect are ignored, a simple relation between T_2 and becomes:

$$P_c = \frac{K}{T_2}, \tag{2.9}$$

where, K is an empirical scaling factor introduced to predict capillary pressure curves. NMR derived P_c curves could be a fast, cheap and non-destructive estimation procedures. However the match between laboratory measured P_c curves and NMR derived P_c curves is not universal (e.g. Kleinberg, 1996). Equation (2.9) reflects that both the T_2 distribution and P_c curves are affected by pore structures but overlooks the difference between the physics of the processes. In a pore size and hydraulic radius model, P_c is sensitive to the hydraulic radius, whereas the NMR measures the pore body size (Kewan and Ning, 2008).

Laboratory measured capillary pressure curves show that for the higher permeability Hermod Formation samples, the Pc curves have lower irreducible water saturation, whereas Pc curves for the low permeability Ty Formation samples have higher irreducible water saturation (Figure 2.5). Irreducible water saturation of greensand samples was obtained from capillary pressure at 100 psi, and varied between 25% and 42%.

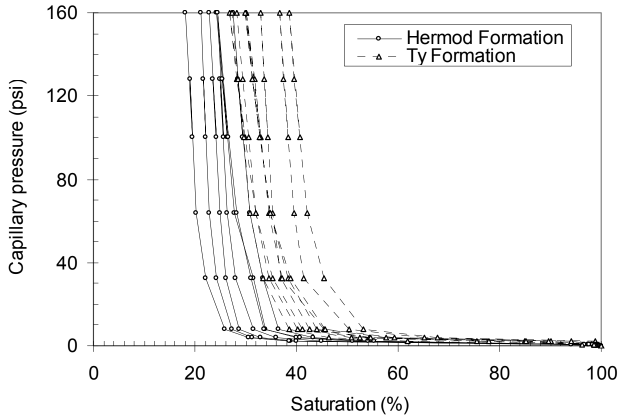

***Figure 2.5**. (a) Capillary pressure curves of greensand samples. Capillary pressure curves of Hermod Formation samples have lower irreducible water saturation, whereas samples from Ty Formation have relatively higher irreducible water saturation. This pattern compares to the relatively lower permeability of Ty sand to the higher permeability of Hermod sand.*

Laboratory measured P_c and NMR derived P_c overlay each other for low permeability samples from the Ty Formation (Figure 2.6). However, the deviation between two types of P_c curves can be observed for the high permeability samples from the Hermod Formation. A deviation is to be expected, because the assumption of this model was that: 1- the pore structure controlling the T_2 distribution and capillary pressure is a bundle of capillary tubes and the drainage is controlled by the hierarchy of pore sizes; 2- the surface relaxivity is constant overall the sample; 3-diffusion relaxation is negligible. A good match between P_c curves from laboratory and NMR measurement is found when average surface relaxivity is equal to surface relaxivity applied to predict P_c curves from NMR. In contrast, a deviation between P_c curves from laboratory and NMR measurements is found when average surface relaxivity is not equal to the surface relaxivity need to match Pc curves. This variation of surface relaxivity within the sample is probably due to the large pores and higher permeability in the greensands of Hermod Formation.

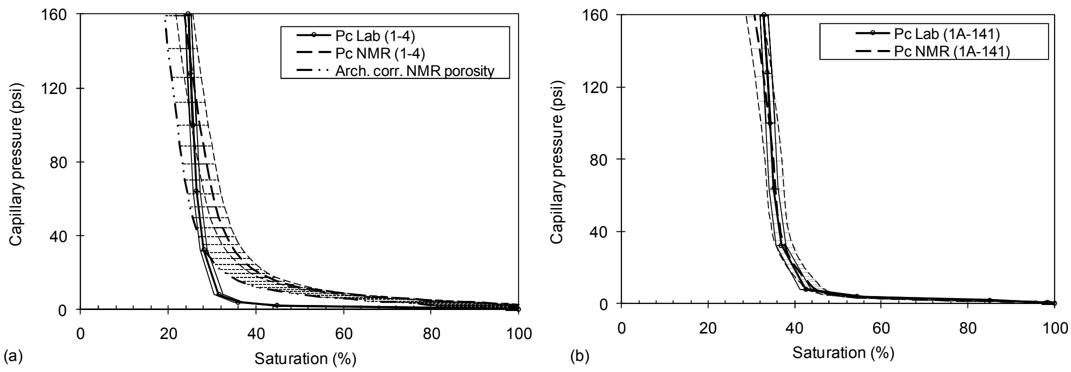

Figure 2.6. *Air brine capillary pressure curves including saturation error compared with NMR derived capillary pressure including saturation error (a) samples from Hermod formation and (b) sample from Ty formation.*

3. Rock-physics modelling of greensand

3.1 Rock-physics models

Rock-physics models in the literature can be divided into effective elastic medium or bound and mixing laws, granular media, fluid effect on wave propagation and empirical models. Effective elastic medium models include Hashin and Shtrikman bounds (Hashin and Shtrikman, 1963), Voigt and Reuss bounds (Voigt, 1910; Reuss, 1929), Hill average (Hill, 1952), Kuster and Toksöz formulation (Kuster and Toksöz, 1974; Berryman, 1980), the self-consistent approximation (Budiansky, 1965; Berryman, 1980), Differential effective medium model (Zimmerman, 1991; Mukerji et al.,1995), pore elastic Backus average (Backus, 1962); BAM model (Marion, 1990) and Iso-frame model (Fabricius, 2003; Fabricius et al., 2007). Granular-medium rock-physics models include the Hertz-Mindlin contact model (Hertz, 1882; Mindlin 1949); the Walton model (Watlon 1987); Digby's model (Digby 1981); The model of Jenkins (Jenkins et al., 2005); the model of Johnson (Norris and Johnson, 1997); the cemented-sand model (Dvorkin and Nur, 1996); the soft-sand model (Dvorkin and Nur, 1996); the stiff-sand and intermediate stiff-sand models (Mavko et al., 2009). Some of the existing granular medium models are summarized by Wang and Nur (1992). Biot's velocity relations (Biot, 1956a; Biot, 1956b), Gassmann's equations, (1951) and the squirt model (Mavko and Jizba, 1991) are mainly used to study the effect of fluid on wave propagations. In fact several models e.g. BISQ model (Dvorkin et al., 1994) and Iso-frame model (Fabricius, 2003) are also used to study the fluid effect on wave propagation. The most used empirical relations in the literature are Wyllie's time-average equation (Wyllie et al., 1956; Wyllie et al., 1958; Wyllie et al., 1962; Wyllie et al., 1963), Raymer-Hunt-Gardner relations (Raymer et al., 1980), Han's empirical relations (Han, 1986a) and Castagna's empirical relations (Castagna, 1985). Furthermore, amplitude variation with offset (AVO) by Zoeppritz's (Aki and Richards, 1984) and by Shuey (Shuey, 1985), elastic impedances (Connolly, 1999; Mukerji et al., 2001) as well as viscoelastic and attenuation are also part of rock-physics modelling.

In this thesis effective medium models were used for modelling of porous glauconite and also to describe the elastic contrast between quartz and glauconite. The Hertz-Mindlin contact model was modified for mixture of quartz and glauconite grains. The soft-sand model, stiff-sand model and intermediate stiff-sand models were used to describe the diagensis of the North Sea greensand. The effective medium based Iso-frame model was used to derive a V_p-V_s relationship for greensand. Empirical V_p-V_s relations of Castagna's and Han's were used to predict V_s from V_p. Zoeppritz's equations and Aki and Richards approximations were used for AVO modelling of greensand. Biot's, Gassmann's and squirt models were used to describe pore fluid effects on greensand. Furthermore, Gassmann's equations were also used to describe the CO_2 injection effect on greensand.

3.2 Modelling of a porous glauconite grain

The simplest effective medium models are Reuss and Voigt bounds. The Reuss bound is the harmonic average of the elastic moduli of individual components of a composite, while the Voigt bound is the arithmetic average. The Hashin-Shtrikman bounds (Hashin and Shtrikman 1963) describe the narrowest possible range for an isotropic, linear elastic composite, when only the volume fractions are known. Tighter bounds exist when spatial correlations are known. The Hashin-Shtrikman bounds give the upper and lower limits of the data distribution for bulk and shear moduli as a function of the volume fractions of mixing materials. These bounds are narrower than those defined by the Reuss lower bound and the Voigt upper bound (Mavko *et al*. 2009).

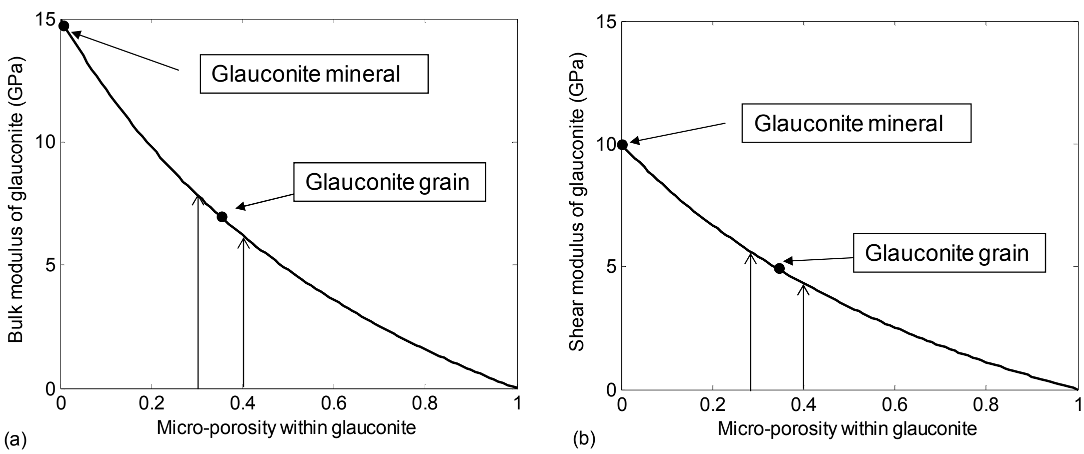

Figure 3.1. *Effective medium modelling of micro-porous glauconite. (a) Bulk modulus and (b) shear modulus of glauconite grain as function of micro-porosity within glauconite by using Hashin-Shtrikman (HS) upper bound. Micro-porosity within glauconite ranges from 30% to 40% for 16 greensand samples and this information was applied to determine the bulk and shear modulus of a micro-porous glauconite grain. Glauconite mineral bulk modulus (15 GPa) and shear (10 GPa) was obtained from Diaz et al. (2002).*

The dominating minerals in greensand are quartz and glauconite. Quartz grains are stiff. Even though glauconite grains are micro-porous, elastic moduli of glauconite mineral are only are reported by Diaz *et al.* (2002). They measured bulk modulus of 15 GPa as bulk and shear modulus of 10 GPa of glauconite mineral from the Cap Mountain Formation, Texas. Because glauconite grains are micro-porous which is physically different from the solid glauconite mineral modulus, it is necessary to calculate the glauconite grain modulus. Hashin-Shtrikman (HS) upper bound (Hashin and Shtrikman, 1963) for mixtures of glauconite mineral and the micro-porosity within glauconite grains was applied for this purpose. Micro-porosity was quantified as the difference between Helium porosity and image macro-porosity as determined from image analysis method (Paper I). Porosity within glauconite was calculated as micro-porosity divided by the amount of glauconite grains as determined by point counting of thin sections (Solymar, 2002; Paper I). Micro-porosity within glauconite varies from 30% to 40% for the 16 greensand samples. By applying these micro-porosities to the HS upper bound, the glauconite grain bulk modulus to be about 7 GPa and shear modulus to be about 5 GPa were determined (Figure 3.1).

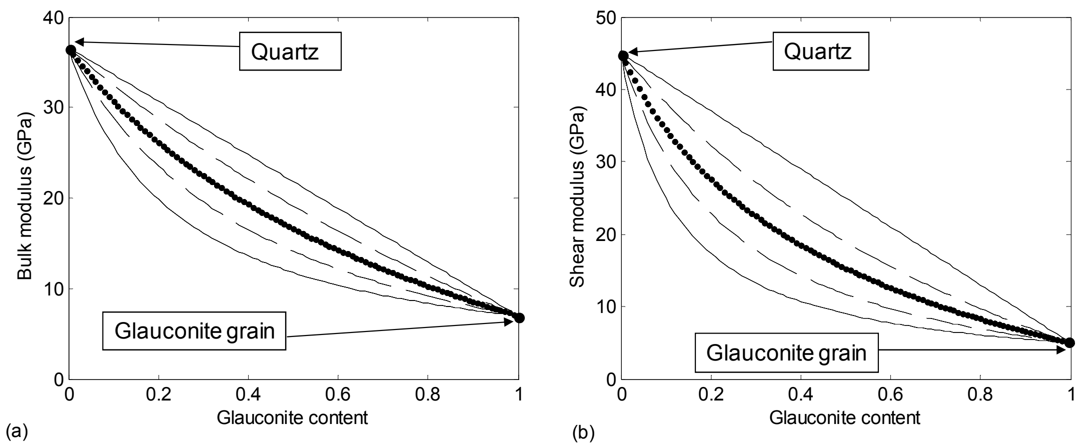

Figure 3.2. *Plots of solid grain elastic moduli of quartz-glauconite mixtures (a) bulk modulus and (b) shear modulus as a function of glauconite fraction. In each figure, the outer two curves represent the Voigt and Reuss Bounds (citation in Mavko et al. 2009). The dashed curves are Hashin-Shtrikman bounds (Hashin and Shtrikman, 1963). The dotted curves in the middle are calculated from Hill's average (Hill, 1952).*

Consider greensand whose grains are mainly quartz and micro-porous glauconite. Bulk and shear moduli of this quartz and glauconite mixture according to Hashin-Shtrikman and Voigt-Reuss elastic bounds are plotted in Figure 3.2. The separation between upper and lower bound depends on how elastically different the constituents are. The elastic bounds are far apart from each other and from Hill's average (Hill 1952) because of the large elastic contrast between quartz and glauconite grains (Figure 3.2). This implies that the effect of micro-porous glauconite may be critical for seismic greensand interpretation.

3.3 Contact model for mixture of quartz and glauconite grains

The Hertz-Mindlin contact model (Hertz, 1881; Mindlin, 1949; Mindlin et al., 1951) calculates the normal and shear contact stiffnesses of two spherical grains in contact. In this model, grain contacts are first exposed to normal loading, with tangential forces applied afterwards. Walton (1987) described that the effective elastic moduli of the granular assembly are then estimated by taking averages of contact forces corresponding to an assumed distribution of strain over all the contacts. Several authors (e.g., Goddard, 1990; Bachrach et al., 2000; Zimmer, 2003; Makse et al., 2004) have explained the discrepancies between measured data and predictions from the Hertz-Mindlin contact model. Makse et al. (2004) reported that the relation between coordination number and porosity from molecular dynamics simulations usually predicts a lower coordination number than Murphy's empirical relation (Murphy, 1982). To mitigate this overprediction, the modeled effective modulus at the critical porosity is often divided by an ad hoc correction factor, and another ad hoc constant is applied in order to use the frictionless versions of the contact models combined with unrealistically high coordination numbers (Dutta, 2009). DeGennes (1996) suggested that the Hertz model is not valid for granular media. However, Coste and Gilles (1990) have experimentally confirmed the validity of the Hertz single contact model.

Still, the Hertz-Mindlin model appears to be the most commonly used contact model for sandstone. Although the Hertz-Mindlin theory is only applicable to perfect elastic contacts of spherical bodies, it works quite well for sands (Avseth et al., 2005). This model is used to calculate the initial sand-pack modulus of the soft-sand, stiff-sand and intermediate-stiff-sand models. For the initial sand-pack for sandstone, it is assumed that only quartz grains are packed together, and the normal and shear stiffness are calculated based on the contact of two quartz grains. For rocks with mixed mineralogy, a homogeneous mineral modulus is assumed, normally derived using Hill's average (Hill, 1952). Then the normal and shear stiffnesses are calculated based on the contact of two average-mineralogy grains. However, this is probably only adequate when the moduli of mixed minerals are quite similar. When the mixed minerals are quite different (such as quartz and glauconite) some of the predictive value may be lost (Avseth et al., 2005)

3.4 Hertz-Mindlin modelling for quartz and glauconite

The effective elastic properties of a granular pack of spheres, for which each pair of grains in contact under normal and tangential load determines the fundamental mechanics were investigated in this study. Typically in granular medium models for unconsolidated sand, all grains are taken to be of the same material. So the Hertz-Mindlin contact model for a single type of grain can be found in Mavko et al. (2009). In this study is considered the contact deformation of two grains made of two different minerals, quartz and glauconite, each with the same radius to calculate the effective bulk and shear modulus for a dry pack.

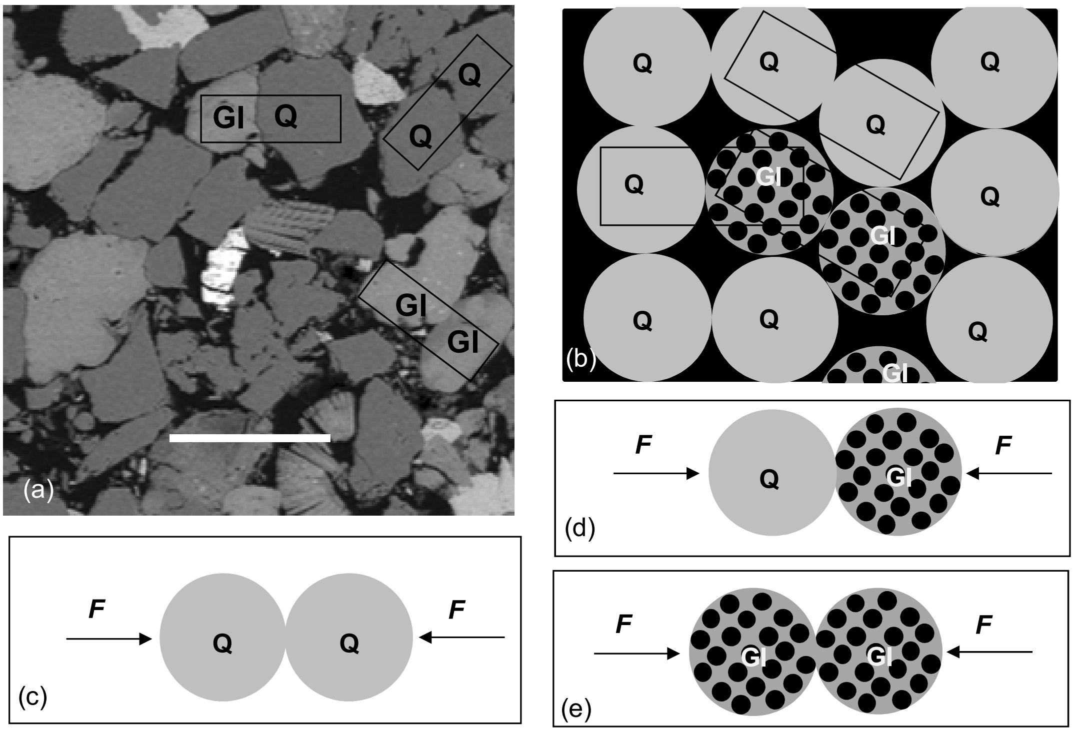

Figure 3.3. *(a) BSE (Backscattered Electron Micrograph) image of the North Sea greensand represents macro-porosity between grains of quartz (Q) and glauconite (Gl). Scale bar for the image is 200 µm. (b) Greensand idealized model. Micro-pores reside within glauconite grains. (c) Schematic representation of Hertz-Mindlin contact model considering quartz and glauconite grains as load bearing (c) quartz-quartz contacts, (d) quartz and glauconite contacts, (e) glauconite-glauconites contacts.*

The derived equations of the Hertz-Mindlin contact model for two types of grains can be found in Paper II. As the amount of quartz grains higher than that of glauconite grains, effective moduli were calculated by balancing among quart-quartz contacts (QQ), quartz-glauconite contacts (QG) and glauconite-glauconite contacts (GG) (Figure 3.1). The elastic moduli a pack of spherical grains are determined from the grains contact area. The grains contact area result from the deformability of grains under pressure.

The P- and S-wave velocities calculated by using the Hertz-Mindlin contact model for two types of grains are presented in Figure 3.4. It is noticed that, in the limit, the Hertz-Mindlin contact model for a single grain type as reported in Mavko et al. (2009) has the same solution as our Hertz-Mindlin model for two types of grains when the fraction of one constituent is 1 and the other is 0 and vice-versa. Calculated velocity for mixtures of quartz and glauconite are higher than velocity calculated from the Hertz-Mindlin contact model for a single grain type by using the effective minerals moduli predicted from Hill's average (Hill, 1952). This demonstrates that the Hertz-Mindlin model with two types of grains may not be approximated by the Hertz-Mindlin single mineral model for a mixture of quartz and glauconite.

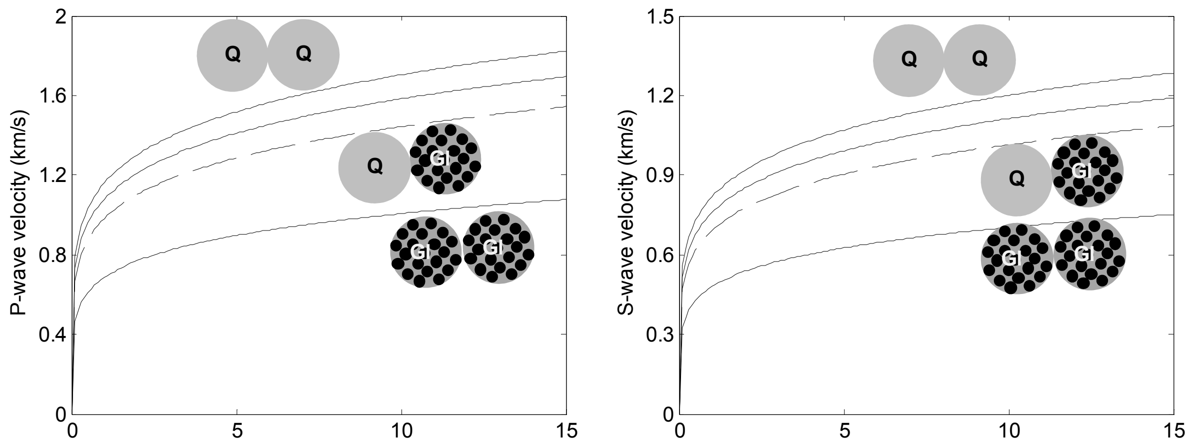

Figure 3.4. *(a) P-wave and (b) S-wave velocity calculated using Hertz-Mindlin contact model with two types of grains. Upper curves are calculated for a quartz fraction of 1 and glauconite fraction of 0. Lower curves are calculated for a quartz fraction of 0 and glauconite fraction of 1. The middle solid curve is calculated for fraction of quartz 0.7 and glauconite is 0.3. The middle dashed curves are from the Hertz-Mindlin contact model for a single grain type by using the effective minerals moduli predicted from Hill's average (Hill, 1952).*

Next, the Hertz-Mindlin model for two types of grains was verified by laboratory experimental results. Figure 3.5 represents the experimental results and results from the Hertz-Mindlin model for two types of grains. From the porosity-coordination number relationship given by Murphy (1982) coordination number 8 was used for this calculation. Thin section analysis shows that this greensand sample is only weakly cemented (Figure 3.3b). For weakly cemented greensand, the Hertz-Mindlin contact model for two types of grains has good agreement with laboratory measured data.

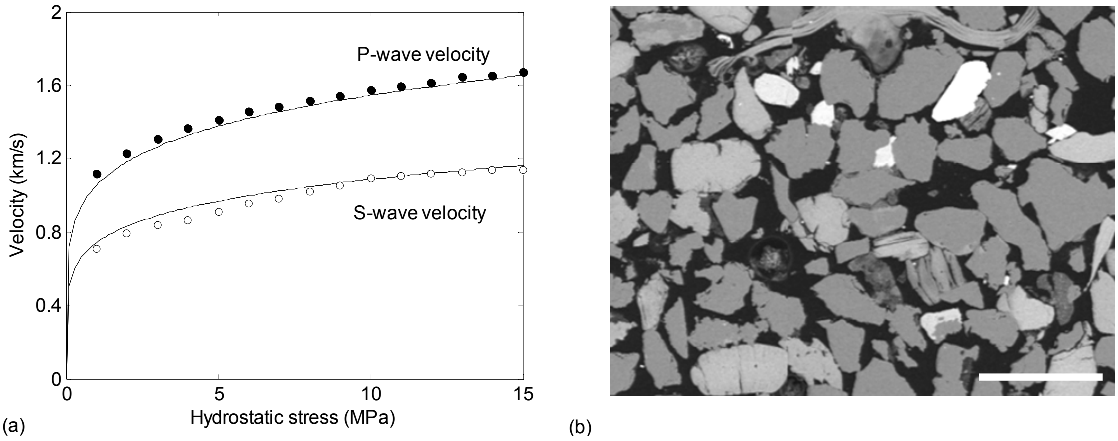

Figure 3.5. *(a) Laboratory measured P-wave velocity (filled circles) and S-wave velocity (open circles) of a weakly cemented greensand and predicted velocity (solid lines) by using Hertz-Mindlin contact model of two types of grains for 70% quartz and 30% glauconite. (b) BSE image of weakly cemented greensand sample.*

3.4 Modelling of the North Sea greensand

Commonly used granular-media models for sandstone are the soft-sand and the stiff-sand models (Dvorkin and Nur, 1996; Mavko et al., 2009). The soft-sand model was introduced by Dvorkin and Nur (1996) for high-porosity sands. The soft-sand model assumes that porosity reduces from the initial sand-pack value due to the deposition of solid matter away from the grain contacts (Figure 3.6). The soft-sand model line is represented by the modified lower Hashin-Shtrikman bound (Hashin and Shtrikman, 1963; Dvorkin and Nur, 1996), and connects the sand-pack porosity end-point and the pure mineral end-point. In the soft-sand model, the effective moduli of the initial sand-pack are computed by the Hertz-Mindlin contact theory (Hertz, 1881; Mindlin, 1949; Mindlin et al., 1951; Mavko et al., 2009), whereas the elastic moduli at the zero-porosity end member are defined by the elastic moduli of the minerals. The porosity reduction between these points will be a gradual stiffening of the rock, as smaller grains fill the pore-space between the larger grains.

A counterpart to the soft-sand model is the stiff-sand model. The stiff-sand model assumes that porosity reduces from the initial sand-pack value due to the deposition of cement at the grain contacts (Figure 3.6). The stiff-sand model line is represented by the modified upper Hashin-Shtrikman bound (Hashin and Shtrikman, 1963; Mavko et al., 2009), and connects the initial sand-pack porosity end-point and the pure mineral end-point. Like in the soft-sand model, the initial sand-pack modulus of the stiff-sand model is determined by the Hertz-Mindlin theory (Hertz, 1881; Mindlin, 1949; Mindlin et al., 1951; Mavko et al., 2009), whereas the mineral end-point is defined by the elastic moduli of the minerals. The porosity reduction from the initial sand-pack will stiffen the rock, as the contacts between the grains grow.

The intermediate-stiff-sand model fills the interval between the stiff-sand and soft-sand model (Mavko et al., 2009). This model uses the function from the soft-sand model, but the high porosity end-point is situated on the stiff-sand model curve (Figure 3.6). The easiest way to generate these curves is by simply increasing the coordination number of the Hertz-Mindlin theory in the soft-sand model (Mavko et al., 2009). The stiff-sand model explains the theoretically stiffest way to add cement with initial sand-pack, while the soft-sand model explains the theoretically softest way to add pore-filling minerals. However, rocks with very little initial contact cement are not well described by either the stiff-sand or the soft-sand model. In this case, the intermediate-stiff-sand model can be used, because it takes into account the initial cementation effect. Equations for soft-sand model, stiff-sand model and intermediate-stiff-sand model are given in Paper II. The Hertz-Mindlin contact model for two types of grains was used to calculate the initial sand-pack modulus for a soft-sand and a stiff-sand model.

Based on laboratory data, log data, and thin section analysis, a schematic rock-physics model of the North Sea greensand was presented. This model is subdivided into several parts (Figure 3.6):

1. Depositional stage: During the deposition of greensand, quartz and glauconite grains are packed together. In clean greensand, where no diagenetic processes have occurred, the elastic properties of greensand can be calculated by using Hertz-Mindlin contact model for two types of grains (Figure 3.4).

2.1. Lack of silica cementation: At first the marginal parts of the reservoir may have received a major flux of silica from the Sele Formation located in the Siri Canyon in the North Sea (Stokkendal et al., 2009). The silica flux did not influence all parts of the greensand reservoir. For this reason, during this stage, some of the greensand remained unchanged compared to the depositional stage. Elastic properties of this kind of greensand can be calculated by using Hertz-Mindlin contact model for two types of grains (Figure 3.5).

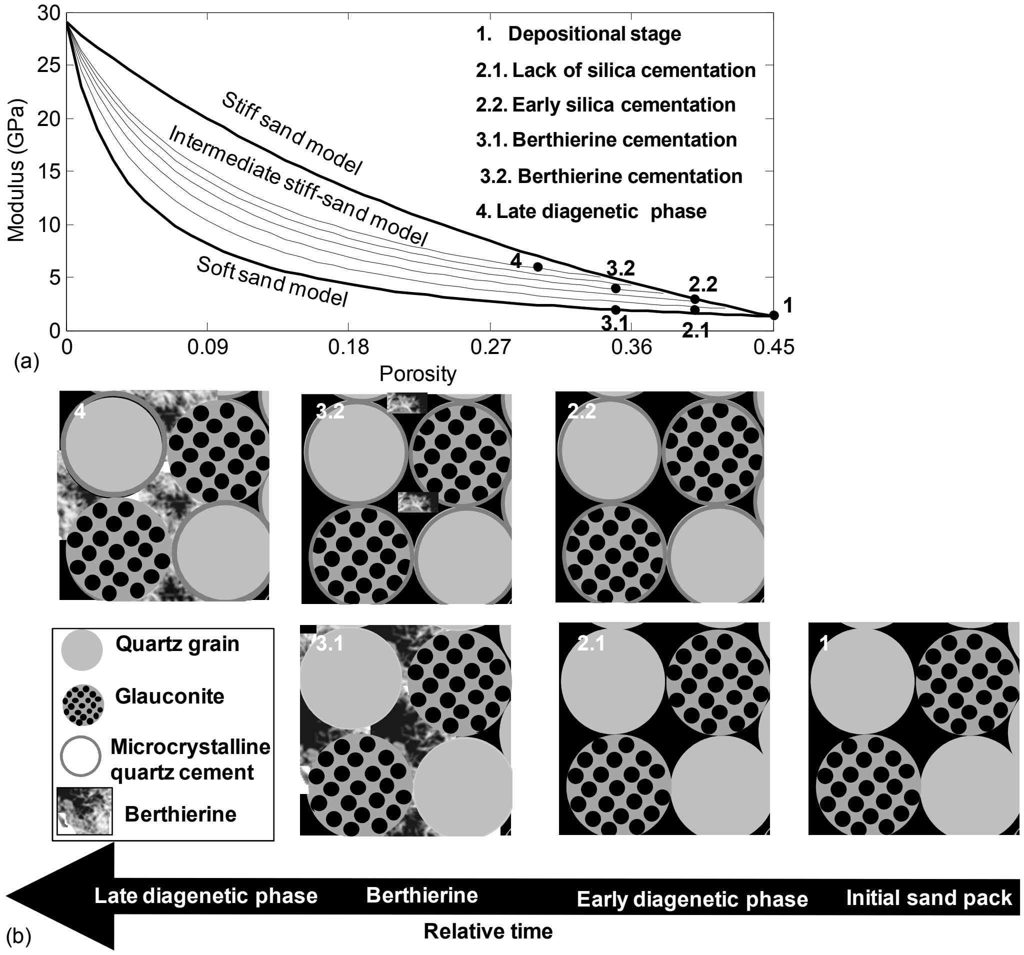

Figure 3.6. *Schematic rock-physics model for the North Sea greensand shows the link between the rock- physics model and greensand diagenesis.*

2.2. Early silica cementation: The first diagenetic mineral to form in the greensand was probably the silica cement. Silica may have formed as an opal rim so that the opal-derived microcrystalline quartz covers all grains. Microcrystalline quartz derived from the opal coating on detrital grains are found in close contact between grains, so this quartz cement has a stiffening effect on the elastic properties of the greensand. Elastic properties of this kind of greensand may be modeled by an intermediate-stiff-sand or a stiff-sand model.

3.1. Pore-filling berthierine cementation: In the greensand reservoir, where microcrystalline quartz cement is absent, berthierine precipitates between the grains, so porosity of this kind of greensand decreases from the initial sand-pack porosity. This kind of greensand can be modeled by a soft-sand model.

3.2. Berthierine in early silica-cemented greensand: Berthierine also precipitates in greensand, where microcrystalline quartz cement is present. Berthierine precipitation between the grains causes major porosity reduction. Elastic properties of this kind of greensand may be modeled by an intermediate-stiff-sand or a stiff-sand model.

4. Late diagenetic phase: If berthierine continues its growth in the pore space, the elastic properties of this kind of greensand may be modeled by an intermediate-stiff-sand or a stiff-sand model.

4. Vp-Vs relationship and AVO modelling

4.1 Vp-Vs relationship of greensand

An important part of rock physics modelling is the V_p-V_s relationship. The V_p-V_s relationship is normally used to predict V_s where only V_p is known. V_p-V_s relationships are also used for AVO analysis and to identify the pore fluids from seismic data. Without V_s it is often difficult to separate the seismic signature of lithology and pore fluids. Furthermore, V_s may also provide information for distinguishing between pore pressure and saturation changes in 4D seismic data and also provide the means for obtaining images in gassy sediments where P-wave is attenuated (Avseth et al., 2005). Therefore, in most cases when V_s is not available or is difficult to obtain, a V_p-V_s relationship is used to calculate V_p from V_s. The V_p-V_s relationship can also be used as a quality control tool even when V_s information is available. Therefore several authors developed physical as well as statistical empirical V_p-V_s relationships to predict V_s from V_p (e.g. Pickett, 1963; Milholland et al., 1980; Castagna et al., 1985; Krief et al. 1990; Greenberg and Castagna, 1992; Han, 1986a; Han et al., 1986b; Xu and White, 1995, 1996; Vernik et al., 2002; Williams, 1990).

Pickett (1963) provided V_p-V_s relations for limestones and dolomite. The relation by Vernik et al. (2002) is nonlinear and works for sandstones. Greenberg and Castagna (1992) have given empirical relations to predict V_s from V_p by taking into account complex lithologies. Xu and White (1995) demonstrated a theoretical model to determine the V_p-V_s relationship of shaly sandstone by mixing two inclusion models with different aspect ratios of pores, which represent respectively sandstone and shale portions. By using dataset from the North Sea, Jørstad et al. (1999) compared the model developed by Xu and White (1995) and concluded that the inclusion models need to be calibrated well by well, whereas the simple regression tuned to the target wells provide good prediction of V_s from the measured V_p. Tsuneyama (2005) presented theoretical assessments of the validity of several known regressions by using effective medium theory and discussed how one should consider modifying the known relationship depending on the character of the target rock.

Castagna et al. (1985) published the most widely used empirical V_p-V_s relationships for rock types including sandstone, mudrock, limestone and dolomite. The empirical V_p-V_s relationship for sandstone offered by Castagna et al. (1985):

$$V_S = 0.80 V_P - 0.86 \textit{ (km/s)}, \qquad (4.1)$$

and the mudrock line of Castagna et al. (1985), which was derived from *in-situ* data:

$$V_S = 0.86 V_P - 1.17 \textit{ (km/s)}. \qquad (4.2)$$

Castagna's regressions provide reasonable results to predict V_s for consolidated rocks with P-wave velocities greater than about 2.6 km/s.

Han et al. (1986a) provided an empirical relationship based on ultrasonic laboratory measurements for clay bearing sandstone:

$$V_S = 0.79 V_P - 0.79 \textit{ (km/s)}. \qquad (4.3)$$

The relations from Castagna et al. (1985) and Han et al. (1986a) for sandstone are essentially the same and give a reasonable average when lithology is not well constrained (Mavko et al., 2009).

Figure 4.1 shows a plot of V_s versus V_p of laboratory measured brine saturated greensand samples. From these data an empirical V_p-V_s regression of laboratory measured brine saturated greensand can be approximated by the least-squares linear fit:

$$V_S = 0.76 V_P - 0.76 \textit{ (km/s)}. \qquad (4.4)$$

The dataset fall along a narrow trend, in spite of variation in porosity, variation in greensand cementation and a confining pressure ranging from 1 to 12 MPa. Even though porosity tends to decrease velocity; clay also tends to lower velocity and confining pressure tends to increase velocity. From the dataset of Han et al. (1986b), Avseth et al. (2005) showed that for clay bearing sandstone, porosity, clay and confining pressure act approximately similarly on V_p and V_s so that the data stay tightly clustered within the same V_p-V_s trend. V_p-V_s relations derived from Iso-frame model (details in Paper III) is:

$$V_S = 0.95V_P - 1.127 \text{ (km/s)} \tag{4.5}$$

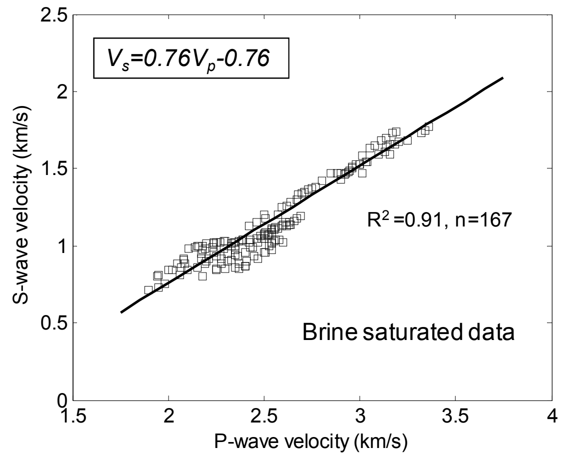

Figure 4.1. *Linear regression between laboratory Vp and Vs data on brine saturated at hydrostatic confining pressure with steps 1 MPa to 12 MPa.*

Predicted V_s and measured V_s agree well by using empirical V_p-V_s regressions of greensand and the V_p-V_s relationship derived from modelling. Figure 4.2 shows the comparison of measured and predicted V_s velocity by using different V_p-V_s regressions. Predictions using the Iso-frame model are quite well although high V_s tend to be overpredicted and low V_s tend to be under predicted (Figure 4.2a). Comparisons between measured and predicted shear wave velocity were quantified by statistical analysis in terms of rms (root mean square) error and r^2 (coefficient of determination). The rms error is 8% and r^2 is 0.9 in the empirical V_p-V_s regression obtained from laboratory data. However, the rms errors are comparatively higher (10%) and the r^2 are comparatively lower (0.82) when using the relation derived from the Iso-frame model.

Although published V_p-V_s relationships for clay bearing sandstone by Han *et al.* (1986a) and for sandstone by Castagna *et al.* (1985) give a reasonable average to predict shear wave velocity when other alternative relationships are unavailable, for greensand they are not consistent. The regression reported by Han et al. (1986a) for clay bearing sandstone underestimates the velocity (Figure 4.2b) while the mudrock line by Castagna et al. (1985) over-estimates the velocity (Figure 4.2c). However, predictions are quite good when using the regression reported by Castagna et al. (1985) for sandstone (Figure 4.2d) and the rms error is 8% and r^2 is 0.88 for this regression. While the rms error is 11% and r^2 is 0.81 by using the regression for clay bearing sandstone reported by Han *et al.* (1986). The rms error is the highest (16%) and r^2 is the lowest (0.63) for the mudrock line (Castagna et al., 1985). Obviously the mudrock line was derived for shales and should not be used for greensands. Nevertheless, the statistical analysis shows that rms error and r^2 for greensand, for clay bearing sandstone by Han et al. (1986a) and for sandstone by Castagna et al. (1985) are close to each other. Therefore, any of these three may be used to predict the shear wave velocity for greensand.

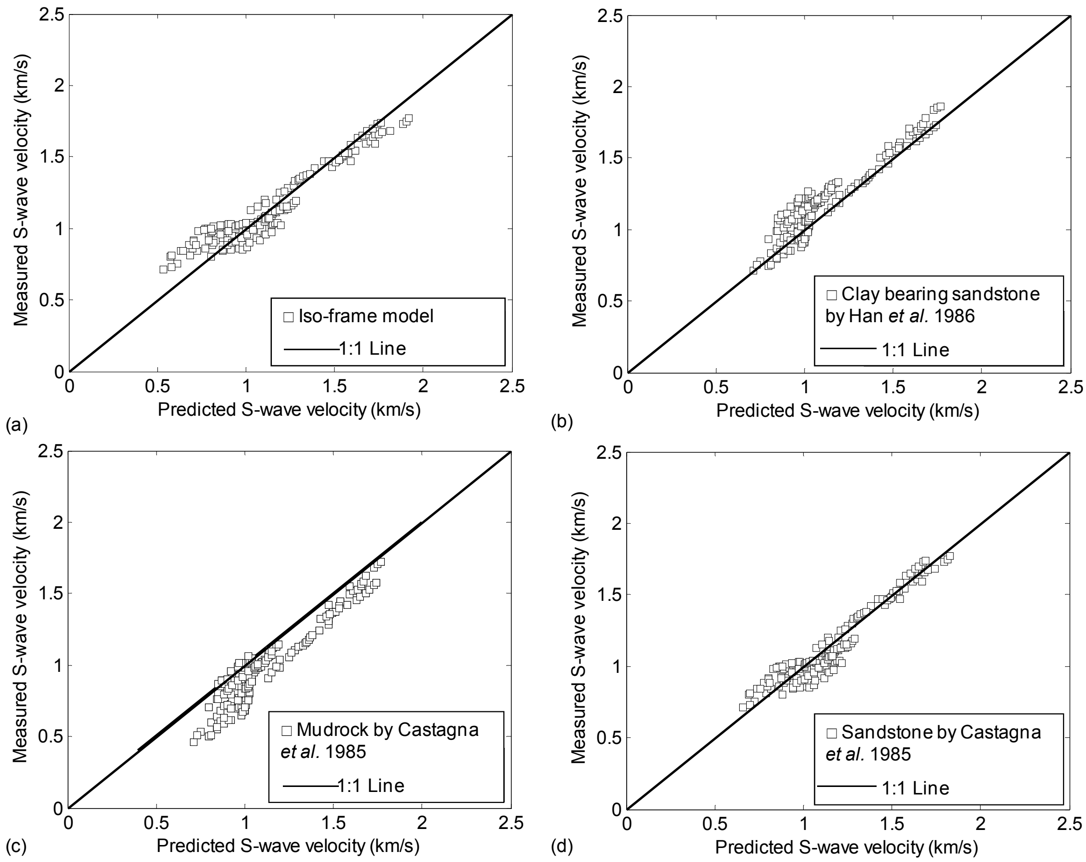

Figure 4.2. *Comparison between predicted and measured shear wave velocities: (a) by using V_p-V_s relationship obtained from the effective medium Iso-frame model, (b) by using regression by Han et al. (1986) for clay bearing sandstone, (c) by using Mudrock line by Castagna et al. (1985), and (d) by using regression by Castagna et al. (1985) for sandstone.*

4.2 AVO modelling of greensand

AVO modelling is a step in multidisciplinary integration of petrophysics, rock physics, seismic data and geology as well as petroleum engineering. AVO modelling is also used to examine the potential use of AVO. To predict the lithology and pore fluid from seismic data are the main objective for AVO analysis (Castagna and Smith, 1994; Castagna et al. 1993; Castagna et al. 1998; Lie et al., 2007). However, Avseth et al. (2005) pointed out that in many cases AVO has been applied without success and that lack of information on shear wave velocity and the use of a too simple geological model are some of the common reasons for failure. Moreover, lithology has significant impact on AVO response which may induce AVO anomalies (Avseth, 2000). Therefore, the understanding of the AVO response based on local geology is important before using it for reservoir characterization.

AVO curves were calculated for glauconitic greensand and quartzitic sandstone each capped by shale. Figure 4.3 represents the PP reflection coefficient (R_{PP}) as a function of incident angle ranging from 0^o to 30^o. Zoeppritz's equations as given in Mavko et al. (2009) were used to calculate the reflection coefficient. Data for sandstone with brine and oil were obtained from Castagna and Swan (1997). Shale data for AVO curves were obtained from the studied Nini 1A well. The shale represents the cap-rock for both greensand and quartzitic sandstone. For greensand, the mean values of V_p, V_s and density of laboratory measured sixteen dry greensand samples were used as input to calculate the reflection coefficient. Data representing the brine and oil saturated state were calculated by using Gassmann's equation (Gassmann 1951). The calculated reflection coefficient is displayed as the thin line on the plot as calculated from mean values of V_p, V_s and density, whereas the gray band represents the range of reflection coefficients as calculated from the maximum and minimum values of V_p, V_s and density. The corresponding AVO response shows a negative zero-offset reflectivity and a positive AVO gradient. AVO responses of brine saturated quartzitic sandstone and brine saturated greensand are distinguishable both at zero and far offset. Oil saturated sandstone and oil saturated greensand are also distinguishable both at zero and at far offset. Although both greensand and quartzitic sandstone are capped by elastically similar shale, greensand produces a stronger negative reflector. However, it is also noticeable that brine saturated greensand may have similar AVO response to oil saturated quartzitic sandstone. The observed difference in seismic response between the greensand and the quartzitic sandstone is due to the difference in grain composition. Thus if the difference between greensand and quartzitic sandstone is ignored, their difference in AVO response could be interpreted as being due to pore fluid.

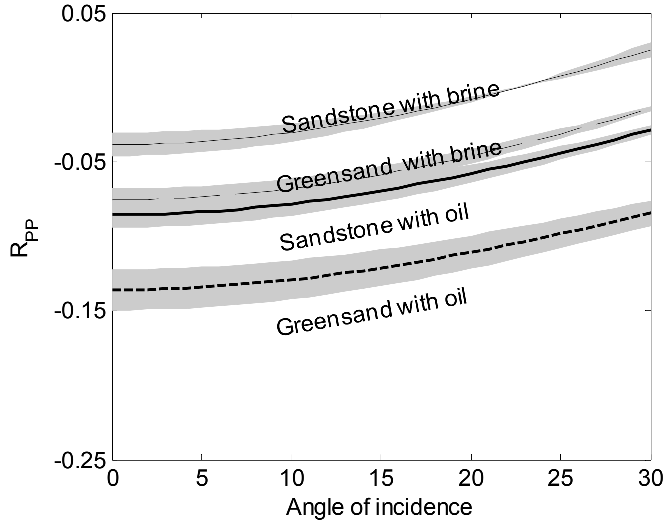

Figure 4.3. *AVO curves for greensand and sandstone capped by shale, in the brine and in the oil saturation condition. PP reflection coefficients were calculated by using Zoeppritz's equations. The brine saturated greensand and oil saturated sandstone have almost similar AVO response. Errors in calculation of reflection coefficient are presented by shaded bands.*

Next, AVO modelling of two types of greensand (the weakly cemented and the cemented) defined by petrographic image analysis and core analysis presents in Figure 4.4. Figure 4.4 represents the PP reflection coefficient as a function of incident angle ranging from 0^o to 30^o calculated from Zoeppritz's equations as given in Mavko et al. (2009). The mean values of V_p, V_s and density of the laboratory measured four greensand samples from Hermod Formation are used as input to calculate the reflection coefficient of weakly cemented greensand, whereas the mean values of V_p, V_s and density of the laboratory measured four samples from Ty Formation are used as input to calculate the reflection coefficient of cemented greensand. Data for the brine and the oil saturated state were calculated using Gassmann's equation (Gassmann, 1951). The calculated reflection coefficient is displayed as the thin line on the plot as calculated from mean values of V_p, V_s and density, whereas the gray band represents the range of of reflection coefficients as calculated from the maximum and minimum values of V_p, V_s and density.

AVO responses of brine saturated weakly cemented greensand and brine saturated cemented greensand are distinguishable both at zero and far offset. Oil saturated weakly cemented greensand and oil saturated cemented greensand are also distinguishable both at zero and far offset. Hydrocarbons cause a stronger negative reflection coefficient, whereas cementation causes a more positive reflection coefficient. It is also noticeable that oil saturated cemented greensand may have similar AVO response to brine saturated weakly cemented greensand. The observed difference in the seismic response between the two types of greensand is due to the difference in greensand diagenesis. Small amounts of berthierine and microcrystalline quartz cement in Ty Formation greensands cause a difference in seismic response. Thus if difference between cemented greensand and weakly cemented greensand is ignored, their difference in AVO response could be interpreted as being due to pore fluid.

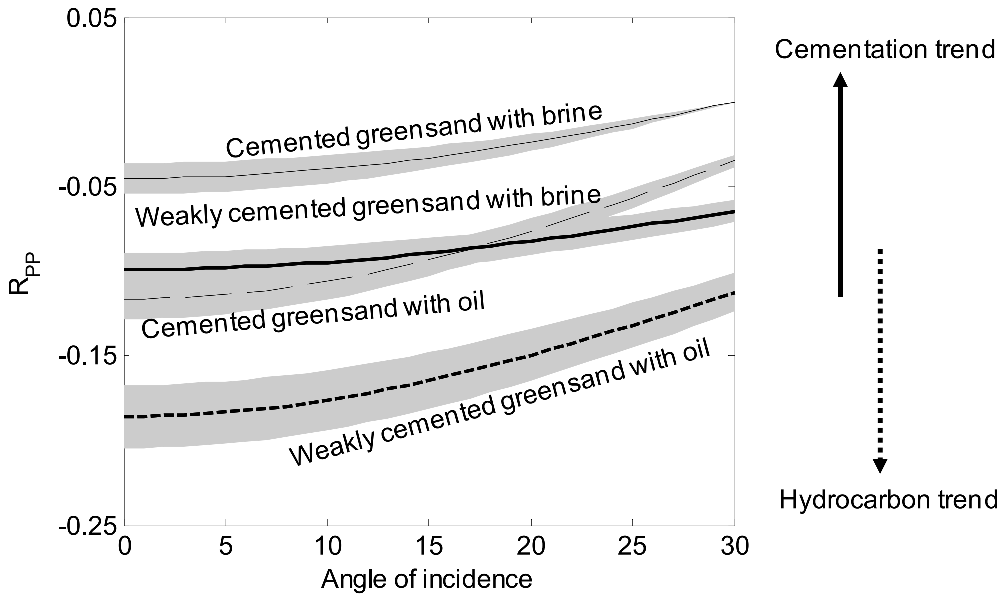

Figure 4.3. *AVO curves for weakly cemented greensand and cemented greensand capped by shale, in the brine and in the oil saturation condition. PP reflection coefficients were calculated by using Zoeppritz's equations. The brine saturated weakly cemented greensand has about the same AVO response as oil saturated cemented greensand. Errors in calculation of reflection coefficient are presented by shaded bands.*

Shale as a cap-rock was used during AVO modelling. Shale can be anisotropic and anisotropy of the cap rock would influence the AVO analysis. Blangy (1992) showed how transverse isotropy of shaly cap-rocks could drastically influence the AVO response of a reservoir. However, Avseth et al. (2008) studied the effect of shale intrinsic anisotropy on AVO signatures of sandstones reservoirs capped by shale and found that the anisotropy effect became significant beyond about 30^0 angles of incidence. Therefore, the effect of anisotropy on AVO was disregarded in this study.

5. Fluid substitution in greensand

Fluid substitution is the heart of rock physics. Fluid substitution is used to predict how the seismic velocity depends on pore fluids. Gassmann's equations (Gassmann, 1951) are simple, robust and widely used to predict rock moduli changes with a change of pore fluids. However, several studies show that the predictions from Gassmann's equations not always match observations (Fabricius et al., 2010; Adam et al., 2006; Coyer, 1984; Assefa et al., 2003; Røgen et al., 2005; Batzle et al., 2006; Baechle et al., 2009). Gassmann's equations generally work at low frequency and do not take into consideration the fluid related dispersion (Berryman, 1980). Biot's flow or global flow (Biot, 1956a, Biot, 1956a) is often used to describe the fluid related dispersion. At low frequency the fluids move with solid part of rock. While at high frequency the pore fluid lag behind the solid part and generate the Biot's flow. Biot's characteristic frequency (f_c) is used to describe the transition between high frequency and low frequency for the Biot's flow as cited by Mavko et al. (2009):

$$f_c = \frac{\phi\eta}{2\pi\rho_f k}, \qquad (5.1)$$

where, η is fluid viscosity and ρ_f is fluid density, ϕ is porosity and k is permeability. Biot's low frequency limiting velocities are the same as those Gassmann relations (Mavko et al., 2009).

However, several studies also showed that Biot's theory does not fully explain the frequency dispersion for natural saturated rocks and the calculated frequency dispersion is usually less than three percents for most reservoir rocks (Winkler, 1983; Winkler, 1985; Winkler, 1986; Wang and Nur, 1988 and Mavko and Jizba, 1991). Winkler (1983) studied the Berea sandstone and found a dispersion of two percent from low to high frequency by using Biot's theory. Fluid flow from compliant pores to less compliant pores can cause local flow or squirt flow (Mavko and Nur, 1979; Murphy, 1982; Murphy, 1984; Winkler, 1983; Winkler, 1985; Winkler, 1986). By squirt relations, Mavko and Jizba (1991) show that water saturated rock may have larger velocity dispersion than would be predicted from Gassmann's equations and even predicted from Biot's high frequency case. Mavko et al. (2009) suggested that in most crustal rocks the amount of squirt dispersion is comparable to or greater than Biot's dispersion, and thus using

Biot's theory alone will lead to poor predictions of high-frequency saturated velocities. Spencer (1981) described that total dispersion may be described by Biot's dispersion together with squirt dispersion.

5.1 Gassmann's method

Gassmann predicted saturated bulk modulus from dry bulk modulus should be equal to measured saturated bulk modulus if fluid related dispersion is insignificant. In the same way dry shear moduli should be equal to saturated shear moduli. However, there are some differences between them (Figure 5.1). Input parameters used in the Gassmann model are the dry bulk modulus, *K dry* computed from the dry P- and S-wave velocity data, the porosity, fluid bulk modulus and mineral bulk modulus (K_o). Fluid bulk modulus fluid is 2.9 GPa as calculated from Batzle and Wang (1992) relations as cited by Mavko et al. (2009). K_o is 33 GPa calculated as the effective mineral bulk modulus of greensand (Hossain et al., 2010d). Variation of the mineral bulk modulus within a reasonable range of ±5 percent has a negligible impact on the computed P- and S-wave velocities for sandstones (Mavko and Jizba, 1991). The sensitive analysis by Sengupta and Mavko (2003) also showed that Gassmann fluid substation method is only little sensitive to the mineral modulus of rock.

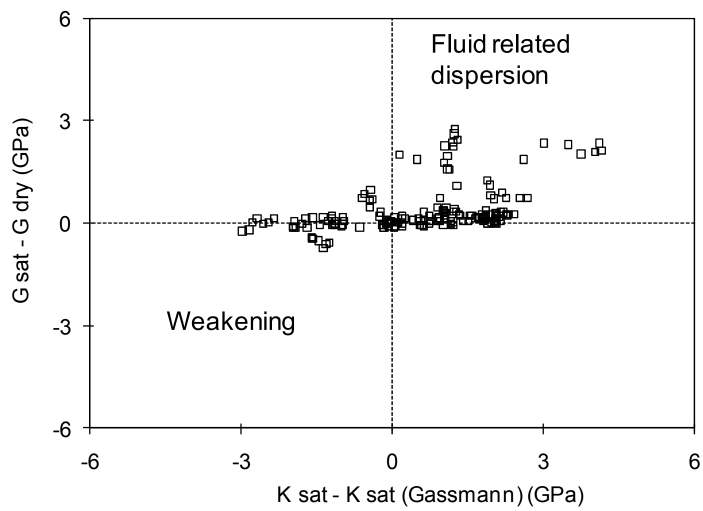

Figure 5.1. *Difference between measured and Gassmann's predicted bulk and shear moduli.*

Measured saturated moduli lower than Gassmann's predicted saturated moduli may be due to the water weakening effect of greensand. One of the assumptions of fluid substitution models is that the pore fluids do not interact with the matrix in such way that would soften the frame. In fact pore fluid may interact with solid matrix to changes the surface energy. Water weakening of saturated rocks is described by several authors (e.g. Wang, 2001; Røgen et al., 2005; Fabricius et al., 2010; Røgen et al., 2005). Gassmann's theory does not take into consideration the fluid related dispersion. Therefore measured saturated moduli higher than Gassmann's predicted saturated bulk moduli may be due to fluid related dispersion. Fluid related dispersions are expected if during the acoustic measurement due to high frequency the fluid would contribute to stiffen the rocks.

5.2 Biot's method

In order to check whether moduli dispersion will occur due to the high frequency Biot's flow, the characteristic frequency (f_c) for the Biot's flow was calculated. As Biot's flow occurs for wave frequency in the kHz to the MHz range, Biot's flow will occur in the North Sea greensand (Figure 5.2a). In Figure 5.2b however it is shown that Biot's flow will occur only in the large pores. Biot's flow should not occur in micro-pores. Fabricius et al. (2010) showed the relationship between Biot's reference frequency and specific surface of pores. In the same way a relationship between NMR T_{2i} and f_c may be obtained from Kozeny's equation (combining equation 2.7 and 5.1):

$$f_c = \frac{\eta}{2\pi\rho_f c(T_{2i}\rho_2)^2}. \qquad (5.2)$$

From equation (5.2) it is clear that each particular pore size has a characterized frequency and that can vary from GHz to kHz (Figure 5.3a). Even though cutoff time for micro-porosity is 5.1 ms, cutoff time for Biot's flow may be defined as 68 ms. Then it is clear that Biot's flow should occur only in the larger pores, whereas intermediate and micro-pores will not contribute to Biot's flow (Figure 5.3c). So Biot's flow should not occur in around in 18% porosity out of 38% porosity of this sample (Figure 5.3d).

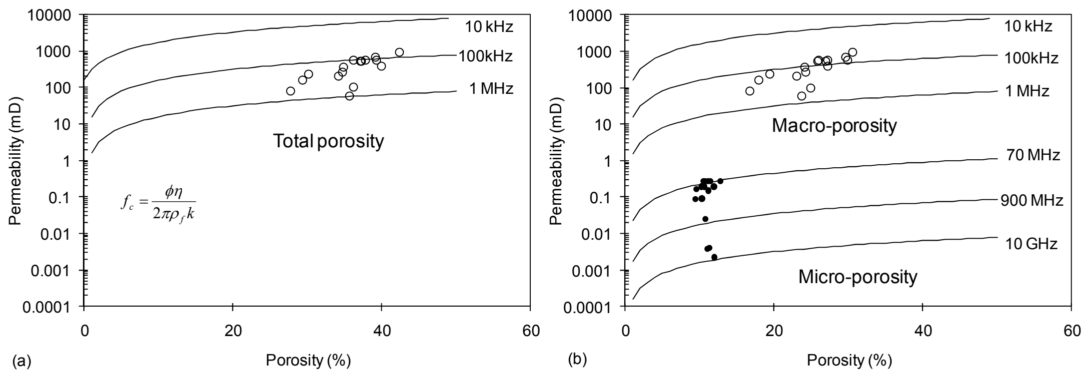

Figure 5.2. *(a) Cross plot of total porosity versus total permeability of greensand samples. Reference curves represent the permeability of Biot's flow as calculated by using Biot's critical frequency equation (5.1). As Biot's flow occurs for wave frequency in the kHz to the MHz range, Biot's flow will occur in the North Sea greensand. (b) Cross plot of macro-porosity versus permeability in large pores (open circles) and micro-porosity versus permeability in micro-pores (closed circles). Reference curves represent the permeability of Biot's flow as calculated by using Biot's critical frequency equation (5.1). Biot's flow will occur only in the macro-pores, while Biot's flow should not occur in the micro-pores.*

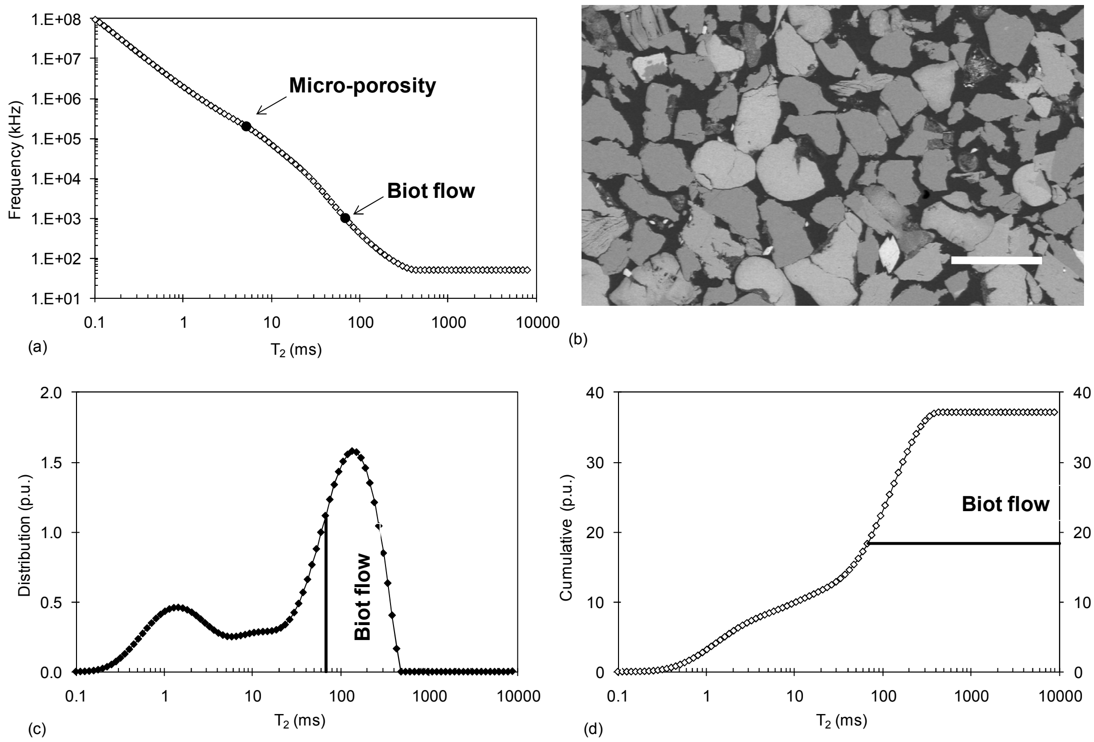

Figure 5.3. *(a) NMR T_2 distribution versus frequency as calculated by using Biot's critical frequency equation (5.2), (b) BSE image of this sample. (c) Porosity distribution from NMR measurement together with cutoff time of Biot's flow, (d) cumulative porosity from NMR measurement together with cutoff time of Biot's flow.*

5.3 Squirt method

In squirt flow mechanisms, the local flow in small cracks gives rise to a local stiffening pressure gradient in the fluid. A schematic diagram of squirt flow could be very similar to the greensand model if local flow in macro-porosity gives rise to local stiffening pressure gradient in the fluid (Figure 5.4).

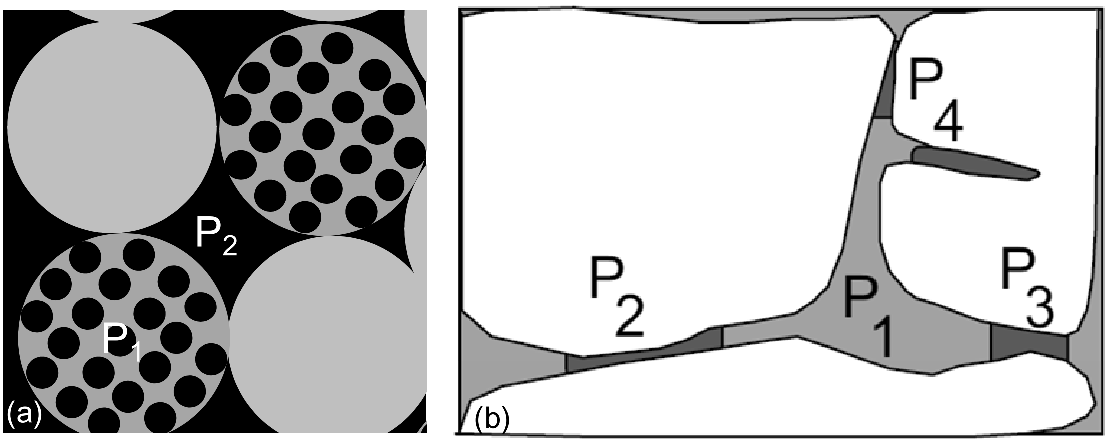

Figure 5.4. *(a) Greensand model, (b) schematic diagram of squirt flow (Mavko and Jizba, 1991).*

In order to check whether differences of fluid flow in macro-pores and micro-pores pores are related with local flow or squirt flow, the squirt model was used to predict high frequency unrelaxed saturated bulk modulus for sample 1-18 from dry bulk modulus. Figure 5.5 shows that comparison among the observed laboratory data, high-frequency predictions of Biot's (1956a, b), and low frequency predictions of Gassmann's (1951). Input parameters used in the Biot's model are the dry bulk modulus, *K dry* computed from the dry P- and S-wave velocity data, the porosity, fluid bulk modulus and mineral bulk modulus. In addition, a tortuosity factor set equal to 2 is used in the Biot's model. Variation of tortuosity within a typical range of one to three has a negligible impact on calculated moduli (Mavko and Jizba, 1991). Both Gassmann and Biot's methods under predicted the saturated bulk modulus (Figure 5.5). To calculate high-frequency saturated unrelaxed bulk moduli the unrelaxed frame bulk moduli were calculated, then these unrelaxed frame bulk moduli were used in Biot's model to estimate the high-frequency saturated unrelaxed bulk moduli. The high frequency unrelaxed bulk moduli agree with laboratory measured data when unrelaxed frame moduli are calculated by using micro-porosity of 20% as the soft porosity in a squirt model. It is clear that total fluid related dispersion in greensand may be explained by combining Biot's flow and squirt flow (Figure 5.5). Biot's dispersion is much lower than squirt dispersion. Biot model may not be enough to describe the fluid related dispersion of this greensand sample.

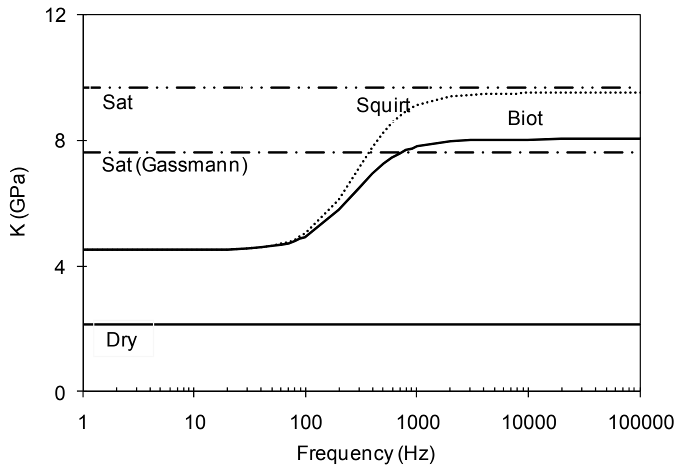

Figure 5.5. *Comparison of laboratory measured brine saturated bulk moduli with predicted saturated moduli from dry bulk moduli. Both Gassmann and Biot's methods are under predicted the saturated bulk modulus. Predictions by using squirt model are comparable with laboratory measured data when soft porosity is assumed around 20%.*

6. CO_2 injection effect on physical properties of greensand

At reservoir condition, CO_2 may affect the aquifer properties in two ways. Firstly, CO_2 dissolved in water is in equilibrium with carbonic acid. The acid may react with the rock thus changing its physical and mechanical properties. Secondly, when CO_2 is injected into a reservoir formation, the existing formation fluid in pore space will be partially displaced by CO_2 thus changing the compressibility and density of the reservoir rock.

Time-lapse seismic surveys currently provide the most attractive approach to monitoring compressibility and density of reservoir rocks. However, understanding the changes of seismic signature due to CO_2 injection is the key element in monitoring the injection of CO_2. Several studies show that based on rock physics modelling, it is possible to discuss how reservoir properties are affected seismically during CO_2 flooding (Wang et al., 1998; Xue and Ohsumi, 2004; Siggins, 2006; Brown et al., 2007; Lei and Xueb, 2009). Gassmann's equations (Gassmann 1951) are generally used to calculate the seismic response due to changing pore fluid. Gassmann's equations (Gassmann 1951) are also used to calculate the seismic response of CO_2 bearing rocks (McKenna et al., 2003; Lei and Xueb, 2009 and Wang et al., 1989; Wang, 2000; Kazemeini et al., 2010; Carcione et al., 2006). Compressibility and density of fluids are necessary input parameters for these calculations. When CO_2 is injected into water-saturated rock and CO_2 dissolves in the brine, it will change the physical properties of brine. Therefore, a correction of fluid properties is required based on compressibility and density as function of dissolve CO_2 in the brine. AVO is also used to calculate the CO_2 bearing rock's seismic response (Brown et al., 2007 and Morozov, 2010). AVO is a method that combines V_p, V_s and density, it will be more sensitive to changes in CO_2 saturation than a method that relies on V_p only. Therefore, since AVO depends on both the velocities and density, the AVO response should be sensitive to an extended range of CO_2 saturations.

6.1 Effect of CO_2 injection on petrophysical properties

In general, helium porosity, specific surface area by BET method, grain density and electrical resistivity before and after the CO_2 injection remain unchanged considering the error of measurements (Figure 5 in Paper IV).

The NMR T_2 distributions are presented in graphical form for one greensand sample before and after the CO_2 flooding experiment (Figure 6.1a). Sample 1A-142 shows that that the smaller peaks become slightly smaller whereas the larger peaks are shifted to larger time after CO_2 injection. Cutoff values 5.2 ms for the sample from Hermod Formation and 3.7 ms for the samples from Ty Formation were used to determine the macro-porosity and micro-porosity from NMR T_2 distribution. Micro-porosity remains largely unchanged from before to after CO_2 injection (Figure 6.1b). Whereas, macro-pore size tends to increase after CO_2 injection (Figure 6.1b).

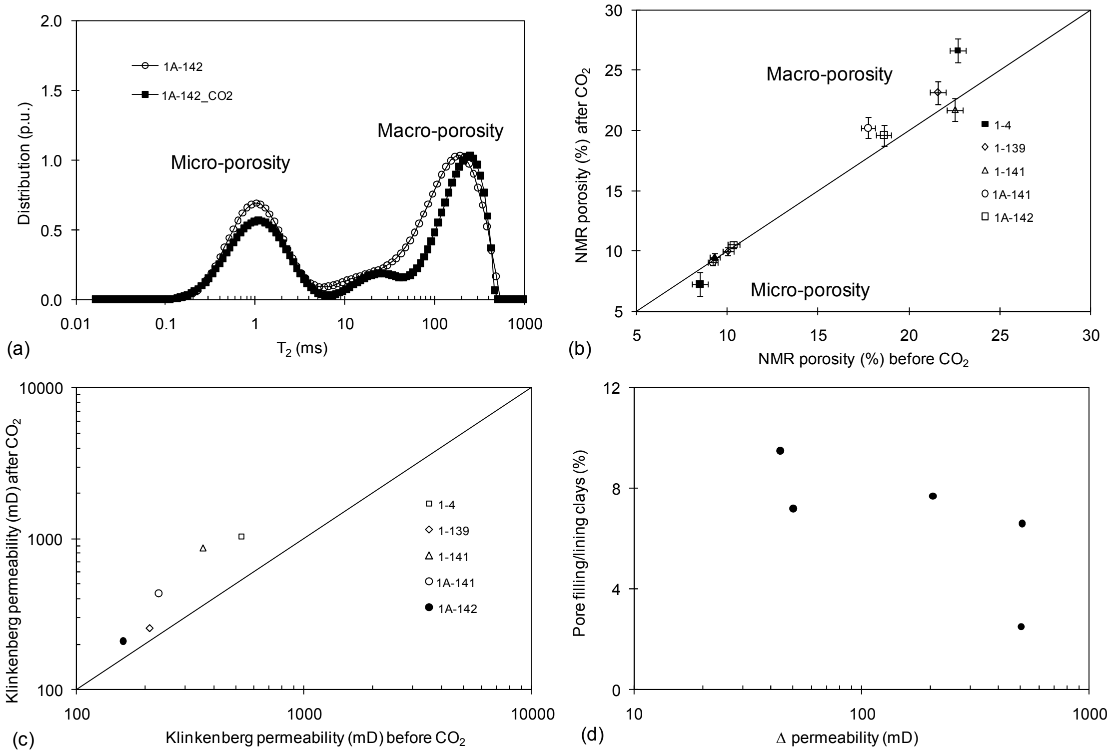

Figure 6.1. *(a) NMR T_2 distribution of a greensand in porosity units (p.u.) before and after CO_2 injection, (b) Macro-porosity and micro-porosity as determined from NMR measurements before and after CO_2 injection. (c) Laboratory measured Klinkenberg permeability before and after the CO_2 injection, (d) cross-plot of delta permeability (permeability after CO_2 injection minus permeability before CO_2 injection) versus amount of pore filling clay minerals.*

Klinkenberg permeability increased by a factor 1.26-2.4 due to the CO_2 flooding experiment (Figure 6.1c). The increased permeability could in principle be explained by sample fracturing and/or migration of fine particles during the CO_2 flooding experiment. Micro-crystalline quartz and pore-filling minerals (Fig. 1b) have significant effect on formation permeability (Stokkandel et al., 2009). During the CO_2 flooding experiment, lose fine particles of pore-filling or pore-lining clay could be shifted around which could cause the increase in permeability. This possibility is corroborated by the inverse trend between change in permeability and amount of pre-filling/lining clay minerals (Figure 6.1d).

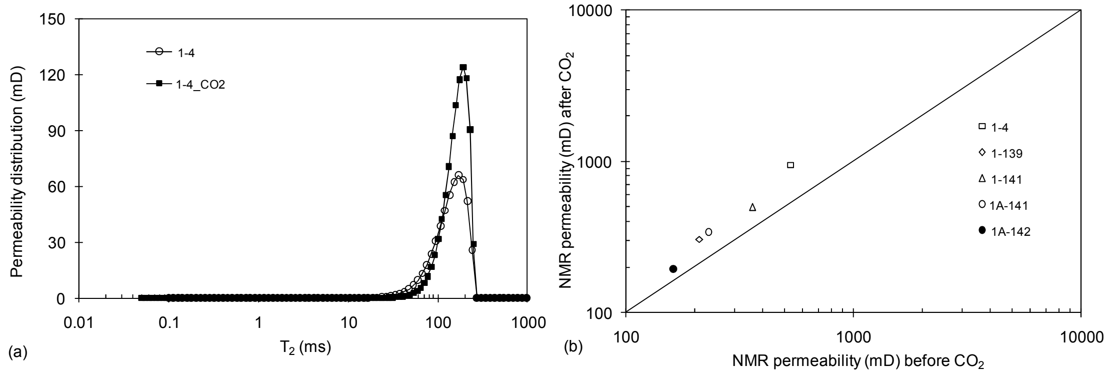

Figure 6.2. *(a) NMR permeability distribution in mD before and after CO_2 injection as calculated from permeability modelling. (b) NMR predicted permeability before and after CO_2 injection.*

In order to evaluate whether the permeability change is due to matrix effects alone, the NMR permeability model provided in section 2 was used to compare NMR predicted permeability before and after CO_2 injection. An example of predicted permeability distribution obtained by using Equation 2.8 is shown in Figure 6.2a. Below 5.2 ms, the amplitude of permeability is close to zero which means micro-porosity does not contribute significantly to fluid flow. From 5.2 ms to 100 ms, the amplitude of permeability is small but above 100 ms the contribution to permeability increases. NMR predicted permeability after CO_2 injection tends to increase (Figure 6.2). From NMR permeability distribution, it is clear that permeability is dominated by the size of macro-pores in the greensand. So NMR predicted permeability after CO_2 injection increases due to the increasing the size of macro-pores. The increase of macro-pores size is probably due to migration of fine pore-filling minerals. The increase in Klinkenberg permeability can thus not be explained by fracturing.

6.2 Effect of CO_2 injection on elastic properties

P-wave and S-wave velocity for the brine saturated condition are almost constant before and after the CO_2 flooding experiment (Figure 6.3a and Figure 6.3b). Even though P-wave and S-wave velocity for dry condition show more scatter before and after CO_2 injection, they probably remain unchanged (Figure 6.3c and Figure 6.3d).

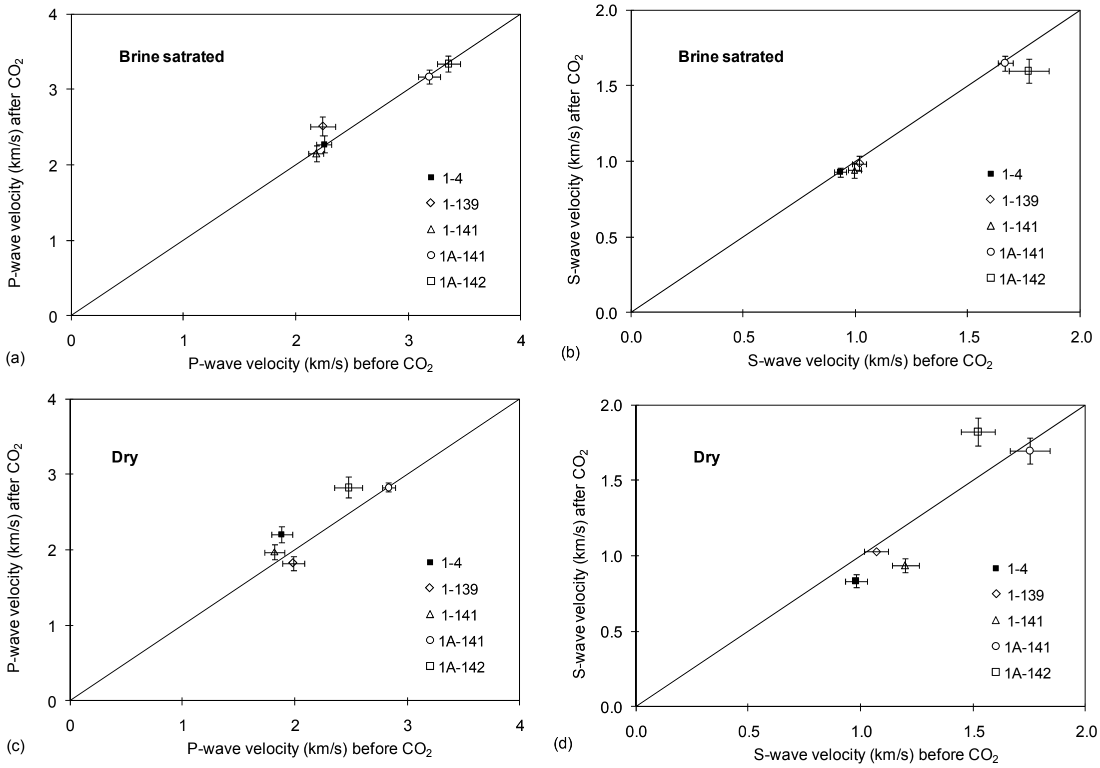

Figure 6.3. *Laboratory measured (a) P-wave velocity and (b) S-wave velocity of brine saturated greensand samples before and after the CO_2 injection. Laboratory measured (c) P-wave velocity and (d) S-wave velocity of dry greensand samples before and after the CO_2 injection.*

6.3 Rock physics and AVO modelling of CO_2 bearing greensand

By using Gassmann's equations calculated P-wave velocity and S-wave velocity of CO_2 bearing greensand samples are presented in Figure 6.4a. The modelling results demonstrate that the largest changes in CO_2 saturated properties occur when the first small amounts of CO_2 are injected into brine saturated greensand. At higher CO_2 saturation levels, the change in elastic properties is relatively small. Modelling results show that the effect of CO_2 flooding decreases V_p by 2%-41% relative to brine saturated V_p. CO_2 flooding also increases V_s, typically 1%-2% and decreases density by 3%-5%. The sensitivity analysis by Sengupta and Mavko (2003) indicates that Gassmann's equations are most sensitive to the brine saturated V_p while the sensitivity to shear wave velocity and bulk density is much lower.

In comparison with the Reuss model or uniform saturation, the Voigt model or patchy saturation shows a more gradual decrease in P-wave velocity with CO_2 content and always leads to higher velocities. Therefore, it is crucial to define whether the patchy or the uniform model should be used to calculate CO_2 saturated greensand properties.

For analysis of amplitude variation with offset, the PP (R_{PP}) reflection coefficients were calculated. Zoeppritz's equations as given in Mavko et al., (2009) were used to calculate the reflection coefficient as a function of reflection angle ranging from 0^o to 30^o. Shale data for AVO curves were obtained from the studied Nini 1A well. The shale represents the cap-rock for the greensand. The V_p, V_s and density of brine bearing greensand sample 1A-142 were used as input to calculate the reflection coefficient. Data representing the CO_2 bearing state were calculated by using Gassmann's equations (Gassmann, 1951).

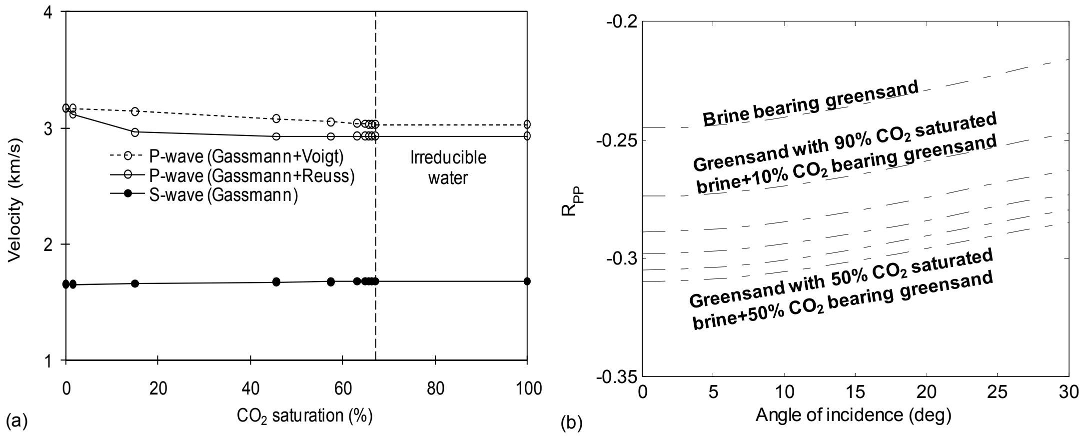

Figure 6.4. *(a) P-wave velocity and S-wave velocity of CO_2 bearing greensand samples as calculated from Gassmann's fluid substitution method, (b) PP refection coefficient (R_{pp}) versus incident angle of CO_2 bearing greensand.*

The corresponding AVO response shows a negative zero-offset reflectivity and a positive AVO gradient (Figure 6.4b). The AVO response of CO_2 saturated greensand is distinguishable both at zero and far offset. PP refection coefficients are monotonically decreasing with CO_2 saturation increase. Figure 6.4b demonstrates that the largest changes in the AVO responses occur when the first 10% CO_2 are injected into a brine saturated greensand. At higher CO_2 saturation levels, the change in AVO response is relatively small.

7. Conclusions

The total porosity of greensand measured by Archimedes method is close to Helium porosity, whereas NMR estimated porosity is lower the total porosity. The discrepancy between Archimedes porosity and NMR porosity may be due to the presence of iron bearing clay minerals in greensand.

Predicted permeability from NMR T_2 distribution by using Kozeny's equation agrees well with data when surface relaxivity is known. By using the traditional Timur-Coates model, predicting permeability works rather well if we optimize the constant to C=8.3. Permeability in greensand was found at two scales: permeability in large pores controlled by macro-porosity together with effective specific surface area and permeability in small pores controlled by micro-porosity together with specific surface measured by BET.

Predicted capillary pressure curves from NMR T_2 distribution overlay on measured capillary pressure curves for low permeability samples. The deviation between predicted capillary pressure curves from NMR T_2 distribution and measured capillary pressure curves for the high permeability samples is due to the contrasting relaxivity on the surface of quartz and glauconite.

Results of rock-physics modelling and thin section observations indicate that variations in elastic properties of greensand can be explained by two main diagenetic phases: silica cementation and berthierine cementation.

Initially, greensand is a mixture of quartz and glauconite grains; when weakly cemented, it has relatively low elastic moduli and can be modeled by the Hertz-Mindlin contact model for two types of grains.

Silica-cemented greensand has relatively high elastic moduli and can be modeled by an intermediate-stiff-sand or stiff-sand model.

Berthierine cement has a different growth pattern in the greensand formations, resulting in a soft-sand model and an intermediate-stiff-sand model.

New V_p-V_s relationships were derived by using data from the Paleocene greensand Nini oil field in the North Sea. A V_p-V_s relationship of greensand from the Iso-frame model was also derived and compared it with empirical V_p-V_s regressions from laboratory data as well as from well log data. Both simple empirical V_p-V_s regression of greensand and V_p-V_s relationship from modelling provide good prediction of V_s from the measured V_p.

AVO modelling indicates that an interface between shale and glauconitic greensand produces a stronger negative reflection coefficient than an interface between shale and quartzitic sandstone. Brine saturated greensand may have similar AVO response to oil saturated quartzitic sandstone. The observed difference in seismic response between the greensand and the quartzitic sandstone is due to the difference not only in mineralogy but also due to the compliant micro-porous glauconite grains.
AVO modelling also indicates that an interface between shale and weakly cemented greensand produces a stronger negative reflection coefficient than an interface between shale and cemented greensand. Cemented greensand with oil saturation can have similar AVO response to brine saturated weakly cemented greensand. The observed significant difference in the seismic response between the two types of greensands is due to a difference in greensand diagenesis.

Gassmann's equations are not enough to estimate the saturated elastic properties of greensand. This study shows that Biot's flow should occur only in large pores in greensand. Biot's flow should not occur in micro-pores. Differences of fluid flow in macro-pores and micro-pores pores are related to the high frequency squirt flow in greensand.

Laboratory results show that CO_2 injection has no major effect on porosity, electrical and elastic properties of greensand.
Klinkenberg permeability of greensand increased after CO_2 injection. An NMR T_2 distribution and NMR permeability modelling approach was tested to evaluate the effect on matrix permeability of CO_2 injection. It appears that permeability after CO_2 injection increased due to the increase of macro-pore size in the greensand. The increase of macro-pore size is probably due to migration of fine pore-filling minerals. The increased permeability is thus not caused by fracturing.
Rock physics modelling results show that the effect of CO_2 flooding alone decreases V_p by 2%-41%. CO_2 flooding also increases V_s, typically 1.9% and decreases density by 3%-5%. AVO modelling results shows that the largest change in the AVO response occurs when the first 10% CO_2 are injected into a brine saturated greensand.

8. Paper abstracts

Abstract from paper I

Nuclear magnetic resonance (NMR) is a useful tool in reservoir evaluation. The objective of this study is to predict petrophysical properties from NMR T_2 distributions. A series of laboratory experiments including core analysis, capillary pressure measurements, NMR T_2 measurements and image analysis were done on sixteen greensand samples from two formations in the Nini field of the North Sea. Hermod Formation is weakly cemented, whereas Ty Formation is characterized by microcrystalline quartz cement. The surface area measured by BET method and the NMR derived surface relaxivity are associated with the micro-porous glauconite grains. The effective specific surface area as calculated from Kozeny's equation and as derived from petrographic image analysis of Backscattered Electron Micrograph's (BSE), as well as the estimated effective surface relaxivity is associated with macro-pores. Permeability may be predicted from NMR by using Kozeny's equation when surface relaxivity is known. Capillary pressure drainage curves may be predicted from NMR T_2 distribution when pore size distribution within a sample is homogeneous.

Abstract from paper II

The relationship between V_p and V_s may be used to predict V_s where only V_p is known. V_p/V_s is also used to identify pore fluids from seismic data and amplitude variation with offset analysis. Theoretical, physical, as well as statistical empirical V_p-V_s relationships have been proposed for reservoir characterization when shear-wave data are not available. In published work, focus is primarily on the V_p-V_s relationship of quartzitic sandstone. In order to broaden the picture we present V_p-V_s relationships of greensand composed of quartz and glauconite by using data from the Paleocene greensand Nini oil field in the North Sea. A V_p-V_s relationship derived from modeling is compared with empirical V_p-V_s regressions from laboratory data as well as from well logging data. The quality of V_s prediction is quantified in terms of the rms error. We find that the V_p-V_s relationship derived from modeling works well for greensand shear-wave velocity prediction. We model seismic response of glauconitic greensand by using laboratory data from the Nini field with the goal of better understanding seismic response for this kind of rock. Our studies show that brine saturated glauconitic greensand may have similar seismic response to oil saturated

quartzitic sandstone and that strongly cemented greensand with oil saturation can have similar AVO response to brine saturated weakly cemented greensand.

Abstract from paper III

The objective of this study is to establish a rock-physics model of North Sea Paleogene greensand. The Hertz-Mindlin contact model is widely used to calculate elastic velocities of sandstone as well as to calculate the initial sand-pack modulus of the soft-sand, stiff-sand, and intermediate-stiff-sand models. When mixed minerals in rock are quite different e.g. mixtures of quartz and glauconite in greensand, the Hertz-Mindlin contact model of single type of grain may not be enough to predict elastic velocity. Our approach is first to develop a Hertz-Mindlin contact model for a mixture of quartz and glauconite. Next, we use this Hertz-Mindlin contact model of two types of grains as the initial modulus for a soft-sand model and a stiff-sand model. By using these rock-physics models, we examine the relationship between elastic modulus and porosity in laboratory and logging data and link rock-physics properties to greensand diagenesis. Calculated velocity for mixtures of quartz and glauconite from the Hertz-Mindlin contact model for two types of grains are higher than velocity calculated from the Hertz-Mindlin single mineral model using the effective mineral moduli predicted from the Hill's average. Results of rock-physics modeling and thin section observations indicate that variations in the elastic properties of greensand can be explained by two main diagenetic phases: silica cementation and berthierine cementation. These diagenetic phases dominate the elastic properties of greensand reservoir. Initially greensand is a mixture of mainly quartz and glauconite; when weakly cemented, it has relatively low elastic modulus and can be modeled by a Hertz-Mindlin contact model of two types of grains. Silica-cemented greensand has a relatively high elastic modulus and can be modeled by an intermediate-stiff-sand or a stiff-sand model. Berthierine cement has different growth patterns in different parts of the greensand, resulting in a soft-sand model and an intermediate-stiff-sand model.

Abstract from paper IV

The objective of this study is to investigate CO_2 injection effects on physical properties of greensand reservoir rocks from the North Sea Nini field. Greensands are sandstones composed of a mixture of clastic quartz grains and glauconite grains. A CO_2 flooding experiment was carried out by injecting supercritical CO_2 into brine saturated samples and subsequently flushing the CO_2

saturated samples with brine at reservoir conditions. Helium porosity, Klinkenberg permeability, and specific surface area by BET were measured on dry greensand samples before and after the CO_2 experiment. NMR T_2 distribution, electrical resistivity and ultrasonic P-and S-wave velocities were measured on brine saturated greensand samples before and after the CO_2 experiment. P-and S-wave velocities were also measured on dry samples. Our laboratory results indicate that CO_2 injection has no major effect on porosity, electrical and elastic properties of the greensand, whereas Klinkenberg permeability increased after CO_2 injection. An NMR permeability modeling approach was used to evaluate the effect on matrix permeability of CO_2 injection. It appears that permeability after CO_2 injection increased not due to fracturing but rather due to the increase of macro-pores in the greensand. The increase of macro-pore size is probably due to migration of fine pore-filling minerals. Rock physics modeling indicates that the presence of CO_2 in a greensand decreases V_p by 2%-41% relative to V_p of brine saturated greensand. CO_2 flooding would at the same time increase V_s, typically by 1%-2%, while decreasing density by 3%-5%. AVO modeling indicates that the largest change in the AVO response occurs when the first 10% CO_2 are injected into a brine saturated greensand.

9. References

Adam, L., Batzle, M. and Brevik, L., 2006. Gassmann's fluid substitution and shear modulus variability in carbonates at laboratory seismic and ultrasonic frequencies. *Geophysics*, **71**, no. 6, F173–F183.

Aki, K. and Richards, P.G., 1984. *Quantitative Seismology: Theory and Method*. San Francisco, CA: W.H. Freeman and Co.

Al-Mahrooqi S. H., Grattoni, C. A., Moss, A. K. and Jing, X. D., 2003. An investigation of the effect of wettability on NMR characteristics of sandstone rock and fluid systems. *Journal of Petroleum Science and Engineering,* **39**, 389-398.

Al-Mahrooqi, S. H., Grattoni, C. A., Muggeridge, A. H., Zimmerman, R. W. and Jing, X. D. , 2006. Pore-scale modeling of NMR relaxation for the characterization of wettability. *Journal of Petroleum Science and Engineering,* **52**, 172-186.

Assefa, S., McCann, C. and Sothcott, J., 2003. Velocities of compressional and shear waves in limestones. *Geophysical Prospecting*, **51**, 1–13.

Avseth, P., 2000. *Combining rock physics and sedimentlogy for seismic reservoir characterization of North Sea Turbidite systems*. Ph.D Thesis, Stanford University.

Avseth, P., Mukerji, T. and Mavko, G., 2005. *Quantitative seismic interpretation: applying rock physics tools to reduce interpretation risk*. Cambridge University Press.

Bachrach, R., Dvorkin, J. and Nur, A., 2000. Seismic velocities and Poisson's ratio of shallow unconsolidated sands. *Geophysics*, **65**, 559–564.

Backus, G.E., 1962. Long-wave elastic anisotropy produced by horizontal layering. *Journal of Geophysical Research*, **67**, 4427-4440.

Baechle, G. T., Eberli, G. P., Weger, R. J. and Massaferro, J. L., 2009. Changes in dynamic shear moduli of carbonate rocks with fluid substitution. *Geophysics*, **74**, 3, 135–147.

Batzle, M. and Wang, Z., 1992. Seismic properties of pore fluids. *Geophysics*, **57**, 1396-1408.

Batzle, M. L., Han, D. H. and Hofmann, R., 2006. Fluid mobility and frequency-dependent seismic velocity - Direct measurements. *Geophysics*, **71(1)**, 1–9.

Berryman, J. G., 1980. Confirmation of Biot's theory. *Applied Physics Letters*, **37**, 382–384.

Berryman, J.G., 1999. Origin of Gassmann's equations. *Geophysics*, **64**, 1627–1629.

Biot, M. A., 1956a. Theory of propagation of elastic waves in a fluid saturated porous solid. I. low-frequency range. *Journal of Acoustical Society of America*, **28**, 168-178.

Biot, M. A., 1956b. Theory of propagation of elastic waves in a fluid saturated porous solid. II. high-frequency range. *Journal of Acoustical Society of America*, **28**, 179-191.

Blangy, J.P., 1992. *Integrated seismic lithologic interpretation: The petrophysical basis*. Ph.D Thesis, Stanford University.

Borre, M., Lind, I. and Mortensen, J., 1997. Specific surface as a measure of burial diagenesis of chalk. *Zentralblatt fur Geologie und Palaontologie,* **1**, 1071–1078.

Brown, R. and Korringa, J., 1975. On the dependence of the elastic properties of a porous rock on the compressibility of the pore fluid. *Geophysics*, **40**, 608–616.

Brown, S., Bussod, G. and Hagin, P., 2007. AVO Monitoring of sequestration: A benchtop-modeling study. The Leading Edge, **26 (12)**, 1576-1583.

Budiansky, B., 1965. On the elastic moduli of some heterogeneous materials. *Journal of Mechanical Physics of Solids,* **13**, 223-227.

Cagatay, M. N., Saner, S., Al-Saiyed, I. and Carrigan W. J., 1996. Diagenesis of the Safaniya Sandstone Member (mid-Cretaceous) in Saudi Arabia. *Sedimentary Geology*, **105**, 221-239.

Carcione, J., Picotti, S., Gei, D. and Rossi, G., 2006. Physics and seismic modeling for monitoring CO_2 storage. *Pure and Applied Geophysics*, **163**, 175–207.

Castagna, J. P. and Smith, S. W., 1994. Comparison of AVO indicators: A modeling study. *Geophysics*, **59**, 1849-1855.

Castagna, J. P. and Swan, H. W., 1997. Principles of AVO cross-plotting. *The Leading Edge*, **16**, 337-342.

Castagna, J. P., 1993. Comparison of AVO indicators: A modeling study. *Geophysics*, **59**, 1849-1855.

Castagna, J., Batzle, M. and Eastwood, R., 1985. Relationships between compressional wave and shear-wave velocities in clastic silicate rocks. *Geophysics*, **50**, 571-581.

Castagna, J., Swan, H. W. and Foster, D. J., 1998. Framework for AVO gradient and intercept interpretation. *Geophysics*, **63**, 948-956.

Coates, G. R., Xiao, L. And Prammer, M., 1999. *NMR logging principles and applications*. Gulf Professional Publishing, Houston, Texas, 234.

Connolly, P., 1999. Elastic impedance. *The Leading Edge*, **18**, 438-452.

.

Coste, C., and Gilles, B., 1999. On the validity of Hertz contact law for granular material acoustics. *European Physical Journal*, **7**, 155–168.

Coyer, K. B., 1984. *Effects of stress, pore pressure, and pore fluids on bulk strain, velocity, and permeability in rocks*. Ph.D. thesis, Massachusetts Institute of Technology.

DeGennes, P., 1996. Static compression of a granular medium, the soft shell model. *Europhysics Letters*, **35**, 145–149.

Diaz, E., Prasad, M., Dvorkin, J. and Mavko, G., 2002. Effect of glauconite on the elastic properties, porosity, and permeability of reservoir rocks. AAPG Annual Meeting, March 10-13, Houston, Texas.

Diaz, E., Prasad, M., Mavko, G. and Dvorkin, J., 2003. Effect of glauconite on the elastic properties, porosity, and permeability of reservoir rocks. *The Leading Edge*, **22**, 42-45.

Digby, P. J., 1981. The effective elastic moduli of porous granular rocks. *Journal of Applied Mechanics*, **48**, 803–808.

Dodge, W. S., Shafer, J. L., Guzman-Garcia, A. G. and Noble, D. A., 1995. Core and Log NMR Measurements of an Iron-Rich, Glauconitic Sandstone Reservoir. *36th Annual Symposium of SPWLA*, Paris, France, June 26-29.

Dutta, T., 2009. *Integrating sequence stratigraphy and rock-physics to interpret seismic amplitudes and predict reservoir quality*. PhD Thesis, Stanford University.

Dvorkin, J. and Nur, A., 1996. Elasticity of high-porosity sandstones: Theory for two North Sea data sets. *Geophysics,* **61**, 1363-1370.

Dvorkin, J., Nolen-Hoeksema, R., and Nur, A., 1994. The squirt-flow mechanism: macroscopic description. *Geophysics,* **59**,428-438.

Fabricius, I. L., 2003. How burial diagenesis of chalk sediments controls sonic velocity and porosity. *AAPG Bulletin*, **87**, 1-24.

Fabricius, I. L., Høier, C., Japsen, P. and Korsbech, U., 2007. Modeling elastic properties of impure chalk from the South Arne Field, North Sea. *Geophysical Prospecting*, **55**, 487–506.

Fabricius, I.L., Bachle, G.T. and Eberli, G.P., 2010. Ealstic modulu of dry and water-saturated carbonates - Effect of depositional texture, porosity, permeability. *Geophysics*, **75**, 65-78.

Gassmann, F., 1951. Uber die elastizitat poroser medien. *Veirteljahrsschrift der Naturforschenden Gesellschaft*, **96**, 1–23.

Glover, P., Zadjali, I. and Frew, K., 2006. Permeability prediction from MICP and NMR data using an electrokinetic approach. *Geophysics,* **71**, 49-60.

Goddard, J. D., 1990. Nonlinear elasticity and pressure-dependent wave speeds in granular media: Proceedings of the Royal Society of London, Series A, Mathematical and Physical Sciences, **430**, 105–131.

Grattoni, C. A., Al-Mahrooqi, S. H., Moss, A. K., Muggeridge, A. H. and Jing, X. D., 2003. An improved technique for deriving drainage capillary pressure from NMR T2 distributions. *The International Symposium of the Society of Core Analysis,* **25,** 21-24 September, Pau, France.

Greenberg, M. and Castagna, J., 1992. Shear-wave velocity estimation in porous rocks: Theoretical formulation, preliminary verification and applications. *Geophysical Prospecting*, **40**, 195-209.

Gregory, A. R., 1976. Fluid saturation effects on dynamic elastic properties of sedimentary rocks. *Geophysics*, **4**, 895-921.

Hamada, G.M., Al-Blehed, M.S., and Al-Awad, M.N.J., 1999. Nuclear Magnetic Resonance Log Evaluation of Low-Resistivity Sandstone Reservoir. *Journal of Engineering Applied Science*, **46**, 951-970.

Hamada, G., Al-Blehed, M., Al-Awad, M. and Al-Saddique, M., 2001. Petrophysical evaluation of low-resistivity sandstone reservoirs with nuclear magnetic resonance log. *Journal of Petroleum Science and Engineering,* **29**, 129-138.

Han, D., 1986a. *Effects of porosity and clay content on acoustic properties of sandstones and unconsolidated sediments*. Ph.D.Thesis, Stanford University.

Han, D., Nur, A and Morgan, D., 1986b. Effect of porosity and clay content on wave velocities in sandstone. *Geophysics,* **51**, 2093-2107.

Hashin, Z. and Shtrikman, S., 1963. A variational approach to the theory of the elastic behaviour of multiphase materials. *Journal of Mechanics and Physics Solids*, **11**, 127-140.

Hertz, H., 1882. On the contact of rigid elastic solids and on hardness, Macmillan, paper 6.

Hidajat, I., Singh, M., Cooper, J. and Mohanty, K. K., 2002. Permeability of porous media from simulated NMR response. *Transport in Porous Media,* **48**, 225-247.

Hill, R., 1952. The elastic behavior of crystalline aggregate. *Proceeding of the Physical Society of London*, **65**, 349-354.

Hossain, Z., Fabricius, I. L. and Christensen, H. F., 2009. Elastic and nonelastic deformation of greensand. *The Leading Edge*, **28**, 260-262.

Hossain, Z., Mukerji, T. and Fabricius, I.L., 2010a. Vp-Vs relationship of glauconitic greensand. Extended abstracts, 72nd Annual EAGE conference, June 14-17, Barcelona, Spain.

Hossain, Z., Mukerji, T. and Fabricius, I.L., 2010b. Petrophysical properties of greensand as predicted from NMR measurements. Extended abstracts, 72nd Annual EAGE conference, June 14-17, Barcelona, Spain.

Hossain, Z., Mukerji, T., Dvorkin, J. and Fabricius, I.L., 2010c. Rock Physics model of glauconitic greensand from the North Sea. Extended abstract, 80th SEG annual conference, Denver October 17-25, Colorado, USA.

Hossain, Z., Mukerji, T., Dvorkin, J. and Fabricius, I.L., 2010d. Rock Physics model of glauconitic greensand from the North Sea. In: SRB Annual Meeting 23-25 June, 2010. Stanford Rock Physics & Borehole Geophysics Project. Annual Report Vol. 121, p. B1-B21, Stanford University, Stanford, CA.

Hossain, Z., Fabricius, I.L, Grattoni, A. C. and Solymar, M., 2011a. Petrophysical properties of greensand as predicted from NMR measurements. *Petroleum Geoscience* (in Press).

Hossain, Z. and Fabricius, I.L., 2011b. Effect of CO_2 injection on Physical properties of greensand. Extended abstracts, 73th Annual EAGE conference, May 23-26, Barcelona, Spain.

Hossain, Z., Mukerji, T. and Fabricius, I.L., 2011c. Vp-Vs relationship and AVO modeling of glauconitic greensand. *Geophysical Prospecting* (in Press).

Howard, J. J., Kenyon, W. E. and Straley, C., 1993. Proton magnetic resonance and pore size variations in reservoir sandstones. *SPE Formation Evaluation,* **1**, 194-200.

Jenkins, J., D. Johnson, L. La Ragione, and Makse, H., 2005. Fluctuations and the effective moduli of an isotropic, random aggregate of identical, frictionless spheres. *Journal of the Mechanics and Physics of Solids*, **53**, 197–225.

Johnson, K.L., 1985., *Contact Mechanics*. Cambridge University Press.

Jørstad, A., Mukerji, T. and Mavko, G., 1999. Model-based shear-wave velocity estimation versus empirical regressions. *Geophysical Prospecting*, **47**, 785-797.

Kazemeini, S.H., Juhlin, C. and Fomel, S., 2010. Monitoring CO_2 response on surface seismic data; a rock physics and seismic modeling feasibility study at the CO_2 sequestration site, Ketzin, Germany. *Journal of Applied Geophysics*, **71**, 109–124.

Kenyon, B., Kleinberg, R., Straley, C. and Morriss, C., 1995. Nuclear Magnetic Resonance Imaging—Technology for the 21st Century. *Oilfield Review,* **7**, 19–30.

Kenyon, W. E., 1997. Petrophysical principles of applications of NMR logging. *The Log Analyst,* **38**, 21-43.

Kewan, W. and Ning, L., 2008. Numerical simulation of rock pore-throat structure effects on NMR T_2 distribution. *Applied Geophysics,* **5**, 86-91.

Kleinberg, R., 1996. Utility of NMR T2 distributions, connection with capillary pressure, clay effect, and determination of the surface relaxivity parameter ρ_2. *Magnetic resonance imaging,* **14**, 761-767.

Kozeny, J., 1927. Ueber kapillare Leitung des Wassers im Boden. *Sitzungsber.Akad.Wiss.Wien,* **136**, 271-306.

Krief, M., Garat, J., Stellingwerff, J. and Ventre, J., 1990. A petrophysical interpretation using the velocities of P and S waves (full-waveform sonic). *Log Analyst*, **31**, 355-369.

Kuster, G.T. and Toksoz, M.N., 1974. Velocity and attenuation of seismic waves in two phase media. *Geophysics,* **39**, 587-618.

Lei, X. and Xueb, Z., 2009. Ultrasonic velocity and attenuation during CO_2 injection into water-saturated porous sandstone: Measurements using difference seismic tomography. *Physics of the Earth and Planetary Interiors*, **176**, 224-234.

Li, Y., Downton, J. and Xu, Y., 2007. Practical aspects of AVO modeling. *The Leading Edge*, **26**, 295-311

Ma, J. and Morozov, I., 2010. AVO modeling of pressure-saturation effect in Weyburn CO_2 sequestration. *The Leading Edge*, **29**, 178-183.

Makse, A., Gland, N., Johnson, D. and Schwartz, L., 2004. Granular packings: Nonlinear elasticity, sound propagation, and collective relaxation dynamics. *Physics Review*, **70**, 061302.

Marion, D., 1990. *Acoustical, mechanical and transport properties of sediments and granular materials*. Ph.D.Thesis, Stanford University.

Marion, D., Nur, A., Yin, H. and Han, D., 1992. Compresional velocity and porosity in sand-clay mixture. *Geophysics,* **57**. 554-563.

Marschall, D., Gardner, J. S., Mardon, D. and Coates, G. R., 1995. Method for correlating NMR relaxometry and mercury injection data. *Proceeding of the 1995 International Symposium of Society of core Analysts,* papers 9511.

Mavko, G. and Jizba, D., 1991. Estimating grain-scale fluid effects on velocity dispersion in rocks. *Geophysics*, **56**, 1940-1949.

Mavko, G., Mukerji, T. and Dvorkin, J., 2009. The Rock Physics Handbook. Tools for Seismic Analysis of Porous Media. Cambridge University press. Second Edition.

McKenna, J.J., Gurevich, B., Urosevic, M. and Evans, B.J., 2003. Rock physics-application to geological storage of CO_2. APPEA Journal 43, 567–576.

Milholland, P., Manghnani, M.H., Schlanger, S.O. and Sutton, G.H., 1980. Geo-acoustic modelling of deep-sea carbonates sediments. *Journal of Acoustical Society of America*, **59**, 2368-2375.

Mindlin, R. D., 1949. Compliance of elastic bodies in contact. *Journal of Applied Mechanics*, **16**, 259–268.

Mindlin, R. D., Mason, W. P., Osmer, I. F. and Deresiewicz, H., 1951. Effects of an oscillating tangential force on the contact surfaces of elastic spheres. Proceedings of the First U. S. *National Congress of Applied Mechanics*, 203–208.

Morgan, J.T. and Gordon, D.T., 1970. Influence of pore geometry on water-oil relative permeability. *Journal of Petroleum Technology*, **22**, 1199-1208.

Mortensen, J., Engstrøm, F. and Lind, I., 1998. The relation among porosity, permeability, and specific surface of chalk from the Gorm field, Danish North Sea. *SPE Reservoir Evaluation and Engineering,* **1**, 245-251.

Mukerji, T., Berryman, J.G., Mavko, G. and Berge, P.A., 1995. Differential effective medium modeling of rock elastic moduli with critical porosity constraints. *Geophysics Research Letter,* **22**, 555-558.

Mukerji, T., Jorstad, A., Avseth, P., Mavko, G., and Granli, J. R., 2001. Mapping lithofacies and pore fluid probabilities in a North Sea reservoir: Seismic inversions and statistical rock physics. *Geophysics*, **66**, 988-1001.

Murphy, W. F., 1982. *Effects of microstructure and pore fluids on the acoustic properties of granular sedimentary materials*. Ph.D. Thesis, Stanford University.

Murphy, W. F., 1984. Acoustic measures of partial gas saturation in tight sandstones. *Journal of Geophysical Research*, **89(13)**, 549-11,559.

Norris, A. N., and Johnson, D. L., 1997. Non-linear elasticity of granular media. *Journal of Applied Mechanics*, **64**, 39–49.

Pickett, G.R., 1963. Acoustic character logs and their applications in formation evaluation. *Journal of Petroleum Technology*, **15**, 650-667.

Ranganathan, V. and Tye, R. S., 1986. Petrography, diagenesis, and facies controls on porosity in Shannon Sandstone, Hartzog Draw Field, Wyoming. *AAPG Bulletin,* **70**, 56-69.

Raymer, L.L., Hunt, E.R. and Gardner, J.S., 1980. An improved sonic transit time-to-porosity transform. Trans. Society of Professional Well Log Analysts, 21st Annual Logging Symposium, Paper P.

Reuss, A., 1929. Berechnung der Fliessgrenzen von Mischkristallen auf Grund der Plastizitatsbedingung fur Einkristalle, *Zeitschrift fur Angewandte Mathematik und Mechanik,* **9**,49-58.

Riepe, L., 1998. Specific internal surface: the "forgotten?" petrophysical measurement! *Proceeding of the 1998 International Symposium of Society of core Analysts,* papers 9540.

Røgen, B. and Fabricius, I.L., 2002. Influence of clay and silica on permeability and capillary entry pressure of chalk reservoir in the North Sea. *Petroleum Geopscience*, **8**, 287-293.

Røgen, B., Fabricius, I. L., Japsen, P. Høier, C., Mavko, G. and Pedersen, J. M., 2005. Ultrasonic velocities of North Sea chalk samples—Influence of porosity, fluid content and texture. *Geophysical Prospecting*, **53**, 481–496.

Rueslåtten, H., Eidesmo, T., Lehne, K. A. and Relling, O. M., 1998a. The use of NMR spectroscopy to validate NMR logs from deeply buried reservoir sandstones. *Journal of Petroleum Science and Engineering,* **19**, 33-44.

Rueslåtten, H., Eidsemo, T. and Slot-Petersen, C., 1998b. NMR studies of iron-rich sandstone oil reservoir. *Proceeding of the 1998 International Symposium of Society of core Analysts,* papers 9821.

Schiøler, P., Andsbjerg, J., Clausen, O. R., Dam, G., Dybkjær, K., Hamberg, L., Heilmann-Clausen, C., Johannessen, E. P., Kristensen, L. E. and Prince, I., 2007. Lithostratigraphy of the Paleocene: Lower Neogene succession of the Danish North Sea. *Geological Survey of Denmark and Greenland Bulletin*, **12**, 77.

Sengupta, M.and Mavko, G., 2003. Impact of flow-simulation parameters on saturation scales and seismic velocity. *Geophysics*, **68**, 1267–1280.

Shuey, R.T., 1985. A simplification of the Zoeppritz equation. *Geophysics,* **50**, 609-614.

Siggins A. F., 2006. Velocity-effective stress of CO_2-saturated sandstone. *Exploration Geophysics,* **37**, 60-66.

Slot-Petersen, C., Eidsemo, T., White, J. and Rueslatten, H. G., 1998. NMR formation evaluation application in a complex low resistivity hydrocarbon reservoir. *Transactions of the SPWLA 39th Annual Logging Symposium*, Paper 1998-TT .

Solymar, M., 2002. Influence *of composition and pore geometry on immiscible fluid flow through greensand*. Ph.D.Thesis, Chalmers University of Technology.

Solymar, M., Fabricus, I.L. and Middleton, M.F., 2003. Flow characterization of glauconitic sandstones by interated Dynamic Neutron Radiagraphy and image analysis of backscattered electron micrographs. *Petroleum Geoscience*, **9**, 175-183.

Spencer, J.W., 1981. Stress relaxations at low frequencies in fluid-saturated rocks: Attenuation and modulus dispersion. *Journal of Geophysical Research*, **86**, 1803–1812.

Stokkendal, J., Friis, H., Svendsen, J. B., Poulsen, M. L. K. and Hamberg, L., 2009. Predictive permeability variations in a Hermod sand reservoir, Stine Segments, Siri Field, Danish North Sea. *Marine and Petroleum Geology*, **26**, 397-415.

Straley, C., Roosini, D., Vinegar, H., Tutunjian, P. and Morriss, C., 1997. Core analysis by low-field NMR. *The Log Analyst,* **38**, 84-94.

Tilley, B. J. and Longstaffe, F. J., 1984. Controls on hydrocarbon accumulation in glauconitic sandstone, Suffield heavy oil sands, southern Alberta. *AAPG Bulletin*, **68**, 1004-1023.

Tsuneyama, F., 2005. *Quantitative detection of fluid distribution using time-lapse seismic*. Ph.D Thesis, Stanford University.

Vernik, L., Fisher, D., and Bahret, S., 2002. Estimation of net-to-gross from P and S impedance in deepwater turbidites. *The Leading Edge*, **21**, 380-387.

Voigt, W., 1910. *Lehrbuch der Kirstallphysik*: B. G. Teubner-Verlag.

Volokitin, Y., Looyestijn, W. J., Slijkerman, W. F. J. and Hofman, J. P., 1999. A Practical Approach to Obtain 1st Drainage Capillary Pressure Curves From NMR Core and Log Data. *The International Symposium of the Society of Core Analysts,* **24**, 1–4.

Walton, K., 1987. The effective elastic moduli of a random pack of spheres. *Journal of the Mechanics and Physics of Solids*, **35**, 213–226.

Wang, Z. Michael E. C., and Robert T. L., 1998, Seismic monitoring of a CO_2 flood in carbonate reservoir: A rock physics study. *Geophysics*, 63, 1604-1617.

Wang, Z., 2000. Dynamic versus static properties of reservoir rocks, in seismic and acoustic velocities in reservoir rocks. *SEG Geophysics Reprint Series,* **19**, 531-539.

Wang, Z., 2001. Fundamentals of seismic rock physics. *Geophysics*, **66**, 398–412

Wang, Z., and Nur, A., 1988. Velocity dispersion and the "local flow" mechanism in rocks: 58th Annual International Meeting, SEG, Expanded Abstracts, 548–550.

Wang, Z., and Nur, A., 1992, Seismic and acoustic velocities in reservoir rocks. *SEG Geophysics Reprint Series*, **10**.

Winkler, K. W., 1983. Frequency dependent ultrasonic properties of high-porosity sandstone. *Journal of Geophysical Research*, **88**, 9493-9499.

Winkler, K. W., 1985. Dispersion analysis of velocity and attenuation in Berea sandstone. *Journal of Geophysical Research*, **90**, 6793-6800.

Winkler, K. W., 1986. Estimates of velocity dispersion between seismic and ultrasonic frequencies. *Geophysics*, **51**, 183-189.

Winn, R. D., 1994. Shelf Sheet-Sand Reservoir of the Lower Cretaceous Greensand, North Celtic Sea Basin, Offshore Ireland. *AAPG Bulletin*, **78**, 1775-1789.

Wyllie, M., Gardner, G., and Gregory, A., 1963. Studies of elastic wave attenuation in porous media. *Geophysics*, **27**, 569-589.

Wyllie, M., Gardner, R. J. and Gregory, A. R., 1962. Studies of elastic wave attenuation in porous media, *Geophysics*, **2,** 569-589.

Wyllie, M., Gregory, A., and Gardner, G., 1956. Elastic wave velocities in heterogeneous and porous media. *Geophysics*, **21**, 41-70.

Wyllie, M., Gregory, A., and Gardner, G., 1958. An experimental investigation of factors affecting elastic wave velocities in porous media. *Geophysics*, **23**, 459-493.

Xie, R. H., Xiao, L. Z., Wang, Z. D. and Dunn, K. J., 2008. The influence factors of NMR logging porosity in complex fluid reservoir. *Science in China Series D: Earth Sciences*, **51**, 212-217.
Xu, S. and White, R. E., 1995. A new velocity model for clay-sand mixtures. *Geophysical Prospecting*, **43**, 91-118.

Xu, S. and White, R. E., 1996. A physical model for shear-wave velocity prediction. *Geophysical Prospecting*, **44**, 687-718.
Xue, Z., Ohsumi, T., 2004. Seismic wave monitoring of CO_2 migration in water-saturated porous sandstone. *Exploration Geophysics*, **35**, 25–32.

Zimmer, M., 2003. *Seismic velocities in unconsolidated sands: Measurements of pressure, sorting, and compaction effects*. Ph.D. Thesis, Stanford University.

Zimmerman, R.W., 1991. *Compressibility of Sandstones,* Elsevier, New York, 173 pp.

10. Papers

I. **Hossain, Z.**, Fabricius, I.L., Grattoni, A. C. and Solymar, M. (2011): Petrophysical properties of greensand as predicted from NMR measurements. *Petroleum Geoscience,* vol 17, No. 2, pp 111-125.

II. **Hossain, Z.**, Fabricius, I.L., Mukerji, T. and Dvorkin, J. (2011): Rock Physics model of glauconitic greensand from the North Sea. *Geophysics* (submitted revised version).

In: SRB Annual Meeting 23-25 June, 2010. Stanford Rock Physics & Borehole Geophysics Project. Annual Report Vol. 121, p. B1-B21, Stanford University, Stanford, CA.

III. **Hossain, Z.**, Fabricius, I.L. and Mukerji, T. (2011): V_p-V_s relationship and AVO modeling for glauconite bearing sandstone. *Geophysical Prospecting* (in press).

IV. **Hossain, Z.** and Fabricius, I.L. (2011). Effect of CO_2 injection of physical properties of greensand. *Journal of Petroleum science and Engineering* (submitted).

V. **Hossain, Z.**, and Mukerji, T (2011). Statistical rock physics and Monte Carlo simulation of seismic attributes for greensand (Accepted for EAGE annual meeting, Vienna, May 23-26, 2011).

VI. **Hossain, Z.**, Fabricius, I.L. and Christensen, H.F. (2009): Elastic and non-elastic deformation of greensand. *The Leading Edge*, Volume 28, Issue 1, pp.86-88.

I

Journal paper

Hossain, Z., Fabricius, I.L, Grattoni A. C. and Solymar M. (2011): Petrophysical properties of greensand as predicted from NMR measurements. *Petroleum Geoscience,* vol 17, No. 2, pp 111-125.

Petrophysical properties of greensand as predicted from NMR measurements

Zakir Hossain[1,*], Carlos A. Grattoni[2], Mikael Solymar[3] and Ida L. Fabricius[1]

[1]*Department of Environmental Engineering, Technical University of Denmark, Miljøvej, Building 113, DK-2800 Lyngby, Denmark*

[2]*Rock Deformation Research Ltd, School of Earth and Environment, University of Leeds, Leeds LS2 9JT, UK*

[3]*Statoil ASA, Oslo, Norway*

[*]*Corresponding author (e-mail: zaho@env.dtu.dk)*

ABSTRACT: Nuclear magnetic resonance (NMR) is a useful tool in reservoir evaluation. The objective of this study is to predict petrophysical properties from NMR T_2 distributions. A series of laboratory experiments including core analysis, capillary pressure measurements, NMR T_2 measurements and image analysis were carried out on sixteen greensand samples from two formations in the Nini field of the North Sea. Hermod Formation is weakly cemented, whereas Ty Formation is characterized by microcrystalline quartz cement. The surface area measured by the BET method and the NMR derived surface relaxivity are associated with the micro-porous glauconite grains. The effective specific surface area as calculated from Kozeny's equation and as derived from petrographic image analysis of backscattered electron micrograph's (BSE), as well as the estimated effective surface relaxivity, is associated with macro-pores. Permeability may be predicted from NMR by using Kozeny's equation when surface relaxivity is known. Capillary pressure drainage curves may be predicted from NMR T_2 distribution when pore size distribution within a sample is homogeneous.

KEYWORDS: *greensand, glauconite, porosity, permeability, capillary pressure, NMR*

Greensands are glauconite-bearing sandstones composed of a mixture of stiff clastic quartz grains and soft glauconite grains. Glauconite grains are porous and composed of aggregates of iron-bearing smectitic or illitic clay. Porosity occurs at two scales: macro-porosity between grains and micro-porosity within grains (Fig. 1). Greensand petroleum reservoirs occur world-wide, e.g. the mid-Cretaceous Safaniya Sandstone member in Saudi Arabia (Cagatay *et al.* 1996), the Cretaceous Mardi Greensand in Australia (Hocking *et al.* 1988), the Lower Cretaceous glauconitic sandstone in Alberta, Canada (Tilley & Longstaffe 1984), the Upper Cretaceous Shannon Sandstone in Wyoming, USA (Ranganathan & Tye 1986), a Lower Cretaceous greensand offshore Ireland (Winn 1994) and a late Paleocene greensand in the central part of the North Sea (Slot-Petersen *et al.* 1998). However, the evaluation of greensand reservoirs has challenged geologists, engineers and petrophysicsts. Glauconite has an effect on porosity, permeability and the elastic properties of reservoir rocks (Diaz *et al.* 2003). It is also ductile (Ranganathan & Tye 1986) and may cause non-elastic deformation of greensand (Hossain *et al.* 2009) and thus affect the reservoir quality. Greensands generally show low resistivity in the reservoir zone due to the large amount of bound water in the glauconite, yet free hydrocarbons can be produced because glauconite rather than being pore-filling is part of the sand grain framework (Slot-Petersen *et al.* 1998). Core analysis of greensand thus shows a poor relationship between porosity and permeability. Furthermore, greensand paramagnetic glauconite or pore-filling berthierine may induce magnetic gradients on the pore level causing the NMR T_2 relaxation time to be shortened dramatically (Rueslåtten *et al.* 1998*a*).

Nuclear magnetic resonance (NMR) is a non-invasive technique, and NMR measurements on reservoir core samples are carried out to obtain an improved interpretation of logging data. NMR measures the net magnetization of a hydrogen atom (^{1}H) in the presence of an external magnetic field. Hydrogen has a relatively large magnetic moment and is abundant in both the water and hydrocarbons that exist in the pore space of sedimentary rocks. NMR spectrometry involves a series of manipulations of the hydrogen protons found in fluids. A measurement sequence starts with proton alignment to a magnetic field followed by spin tipping, and decay. The quantities measured include signal amplitude which is proportional to the number of hydrogen nuclei and decay, also called relaxation time (Kenyon *et al.* 1995). Longitudinal relaxation time (T_1) measures the decay of spin alignment; transverse relaxation time (T_2) measures the decay of precession. Although T_1 measurements are more common in the literature, they are more time consuming than T_2 measurements. Hence, pulsed NMR logging tools preferentially measure T_2 for faster logging speeds (Straley *et al.* 1997). NMR transverse relaxation (T_2) of fluids confined in a porous rock is affected by pore

DOI 10.1144/1354-079309-038

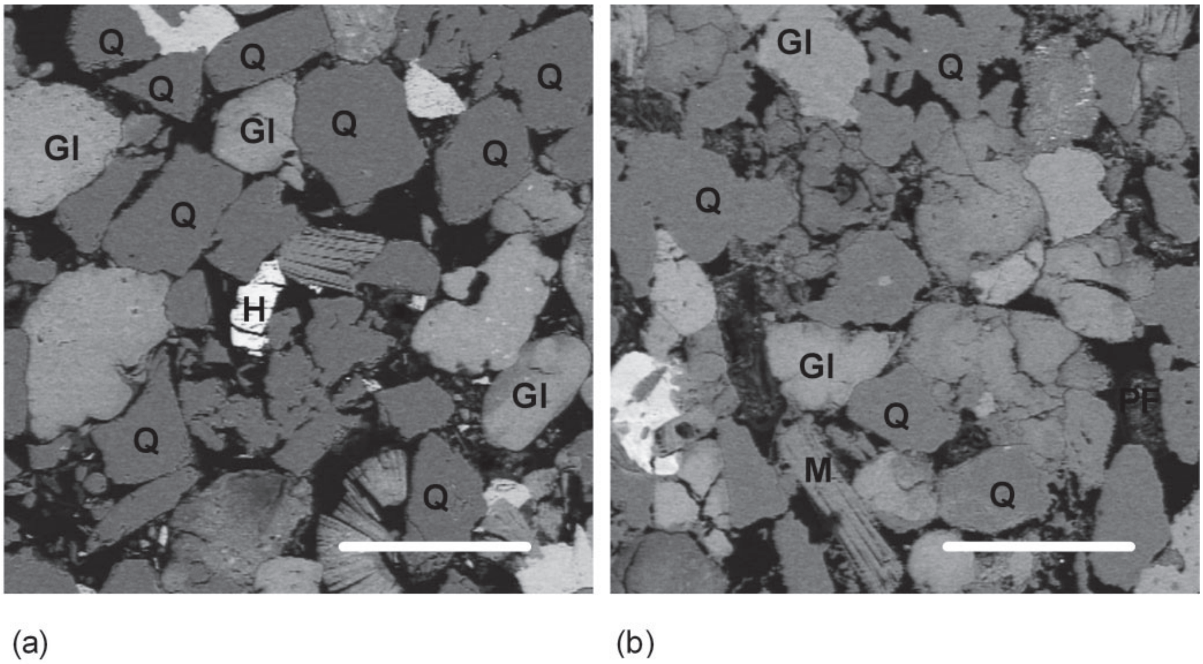

Fig. 1. BSE images of greensand samples. (**a**) Sample 1–4 from Hermod Formation and (**b**) sample 1A-142 from Ty Formation. Scale bar is 200 µm. Q, quartz; Gl, glauconite; H, heavy minerals, M, mica; PF, pore-filling clay minerals. Porosity, permeability and irreducible water saturation are 37 p.u., 530 mD and 26% for sample 1-4 and 29 p.u., 150 mD and 38% for sample 1A-142.

surface, by the bulk relaxation process in the fluid and additionally by dephasing in case of molecular diffusion. T_2 may be expressed by the fundamental equation governing the NMR relaxation spectrum (Coates *et al.* 1999):

$$\frac{1}{T_2} = \frac{1}{T_{2Surface}} + \frac{1}{T_{2Bulk}} + \frac{1}{T_{2Diffusion}}. \quad (1)$$

Surface relaxation ($T_{2Surface}$) is the dominating mechanism in porous media, controlled by pore surface area. The relation between NMR relaxation and pore surface area results from strong interaction between the protons and the surface because the surface relaxivity (ρ) causes rapid alignment of hydrogen protons on the pore wall, perhaps only a monolayer or two thick, whereas protons in the remaining fluid decay through itself (bulk relaxation), which is much slower (Howard *et al.* 1993). Bulk relaxation (T_{2Bulk}) is thus significantly smaller than the surface relaxation and so where relaxation of diffusion ($T_{2Diffusion}$) is slow, the relaxation ($1/T_2$) may be related to surface relaxivity and surface to volume ratio of pores (Sp):

$$\frac{1}{T_2} = \rho_2 S_P. \quad (2)$$

NMR measurements provide information about the pore structure (Sp), the amount of fluid *in situ* and interactions between the pore fluids and surface of pores. Thus, laboratory NMR measurements can be used to obtain porosity and correlate pore size distribution, clay-bound water, and to estimate permeability and potentially predict capillary pressure curves from longitudinal relaxation time (T_1) and transverse relaxation time (T_2) distribution (Kenyon 1997). Numerous authors have explored the link between NMR measurements and petrophysical properties, e.g. the wettability investigation by NMR measurements by Al-Mahrooqi *et al.* (2003, 2006).

Porosity is one of the key parameters for hydrocarbon reservoir evaluation, and NMR is an effective tool for the determination of porosity. However, several authors have reported that there are significant differences between NMR porosity and core analysis porosity. Factors influencing the T_2 measurements include paramagnetic minerals in the reservoir rock which may cause $T_{2Diffusion}$ and hence reduce the T_2 relaxation time (Xie *et al.* 2008). Additionally, iron and other paramagnetic minerals affect the surface relaxivity and produce a shift of the relaxation distribution to shorter times (Dodge *et al.* 1995). Rueslåtten *et al.* (1998) studied NMR of iron-rich sandstone from the North Sea and found a detrimental effect of iron-bearing minerals on porosity estimation by NMR T_2.

Specific surface area is another significant petrophysical parameter for understanding the physics of porous media and for permeability prediction. It was never fully integrated into standard or special core analysis programs due to lack of petrophysical understanding and concepts for correct evaluation (Riepe 1998). Nitrogen adsorption methods (BET) yield high specific surface value as nitrogen enters the pores in the sample. By using image analysis to determine the specific surface area, usually a much smaller value is derived, and the value depends upon the resolution (Solymar *et al.* 2003). The results of different methods reflect the different properties of pores at different scales. By using a high resolution BET surface or a highly smoothed surface derived from image analysis, the calculated permeability can be varied several orders of magnitude (Riepe 1998). This is a concern because specific surface plays a vital role in understanding and calibrating the T_2 spectra by estimating surface relaxivity (equation (2)).

NMR relaxation is not only affected by the pore dimensions but also by the relaxivity of the rock surface. Quantitative knowledge of the surface relaxivity is needed when T_2

distributions are interpreted. Surface relaxivity is required in order to convert T_2 distribution into specific surface area, to calculate permeability and to convert T_2 time to capillary pressure curves. It is not easy to measure surface relaxivity directly. Surface relaxivity may be estimated by scaling the normalized capillary pressure curve to the normalized T_2 distribution (Kleinberg 1996); or by comparing NMR T_2 distributions to specific surface area from nitrogen BET adsorption (Hidajat *et al.* 2002). Alternatively, it can be estimated by comparing NMR pore size distribution to pore size distribution from image analysis of thin sections (Howard *et al.* 1993; Kenyon 1997). Kleinberg (1996) concluded that the NMR effective specific surface area is closely associated with hydraulic radius of the sedimentary rock and calculated effective surface relaxivity from capillary pressure curves and T_2 distribution.

Permeability is a difficult property to determine from logging data, yet it is essential for reservoir characterization. Laboratory measurements provide absolute permeability at core scale which could be different from reservoir permeability. NMR is the only tool that attempts to estimate *in-situ* formation permeability (Hidajat *et al.* 2002; Glover *et al.* 2006). One of the most popular NMR derived permeability correlations is the Timur-Coates formula (Coates *et al.* 1999), and is implemented as:

$$k_{NMR} = (\mathrm{C}\phi)n\left(\frac{FFI}{BFI}\right)^n, \tag{3}$$

where, ϕ is the porosity, *FFI* is the free fluid volume and *BFI* is the bound irreducible fluid, as determined from NMR measurements. Formation dependent constants *C, m* and *n* may be assumed to be 10, 4 and 2 for sandstones respectively, where NMR permeability, k_{NMR} is given in mD. However, this equation is simply an empirical derived relationship that links various NMR-derived parameters to permeability. Especially for diagenetically altered consolidated reservoir rocks, the complicated internal pore structures may not be described by this model, causing unrealistic permeability estimates, unless empirically calibrated parameters are used, which have no general physical meaning and thus are only valid for special facies types and for local investigations. Timur-Coates formula also indicates that porosity or pore volume strongly controls the permeability together with the effective specific surface area as expressed by FFI/BFI in accordance with the equation of Kozeny (1927). For homogeneous sediments like chalk, the effective specific surface is equivalent to the one measured by nitrogen adsorption (BET) and Kozeny's equation works well without introducing empirical factors (Mortensen *et al.* 1998). However, for less homogenous sediments, like greensand, we can calculate an effective surface area (*Sp(Kozeny)*) from permeability and porosity by using Kozeny's equation. We infer that it is this effective surface that controls permeability.

Capillary pressure (P_c) curves can be determined only from core analysis, but NMR derived P_c curves provide a fast, cheap and non-destructive estimation. Until now, most authors have focused on the relationship between T_2 distribution and P_c curves (Marschall *et al.* 1995; Kleinberg 1996; Volokitin *et al.* 1999; Grattoni *et al.* 2003) and the general conclusion is that, if the bulk relaxation and diffusion effects are ignored, a simple relationship between P_c and T_2 becomes:

$$P_c = \frac{K}{T_2}, \tag{4}$$

where, K is an empirical scaling factor introduced to predict capillary pressure curves. However, several authors, e.g. Kleinberg (1996) concluded that the match between capillary pressure and NMR relaxation curves are not universal. The simple relationship (equation (4)) reflects that both the T_2 distribution and P_c curves are affected by pore structures but overlooks the difference between the physics of the processes. Kewan & Ning (2008) discussed that in a pore and throat model of the pore space, the capillary pressure is sensitive to the pore throat, whereas NMR measures the pore body size. The technique gives the same information only when there is a constant ratio between them.

The combination of conventional core analysis, such as helium porosity, gas permeability, specific surface area by BET and image analysis of thin sections micrographs is very effective in the evaluation of normal reservoir rocks. However, for glauconite-bearing greensand where a high proportion of micro-porosity in glauconite grains creates an uncertainty with respect to fluid distribution and fluid saturation, an accurate determination of petrophysical properties by using conventional core analysis is difficult (Rueslåtten *et al.* 1998*b*). The objective of this study is to predict petrophysical properties from NMR T_2 distributions which can be applied to *in-situ* well logging. Estimates of porosity, permeability, irreducible water saturation derived from NMR measurement were corrected with measurements from core analysis. The porosity obtained by using the different methods was compared for the greensand samples. The potential use of surface area data is also described and illustrated. Kozeny's equation was used for NMR permeability prediction and P_c curves were estimated from NMR measurements.

GEOLOGICAL SETTING OF NINI FIELD

The Nini field is located in Siri Canyon which is part of a larger system of submarine canyons in the Paleocene in the Norwegian–Danish Basin running in an east–west to NE–SW direction towards the Central Graben (Fig. 2) (Stokkendal *et al.* 2009). The Nini accumulation is defined by a combined structural and stratigraphic trap, the anticlinal structure being induced through salt tectonics. The reservoir consists of sands deposited in the Siri Fairway (Schiøler *et al.* 2007).

The glauconite-bearing sandstone in the Nini field was recognized by stratigraphic work in Statoil in the mid-1990s (Schiøler *et al.* 2007). It is formally included in the Hermod Formation and in the older Ty Formation. These Paleocene reservoir sands are characterized by glauconite rich (20–30 vol %) fine grained, well sorted sand, embedded in hemiplegic to pelagic mud- and marl-stones, in which both quartz grains and glauconite pellets are part of the load-bearing matrix. The greensand beds thus occur in a shale sequence. In the Nini wells, the Hermod sand was found to be more massive, more porous and more permeable than the Ty sand (Fig. 3).

METHOD

We studied sixteen one and half inch horizontal core plugs from the two greensand formations of the Nini-1 well (7 samples from Hermod Formation and 9 samples from Ty Formation). The samples had already been used for routine core analysis and were chosen so as to cover the range of variation in porosity (25–40%) and air permeability (60–1000 mD). All cores were cleaned from brine and hydrocarbons by soxhlet extraction with methanol and toluene prior to analysis. Thin sections were prepared from the end of each

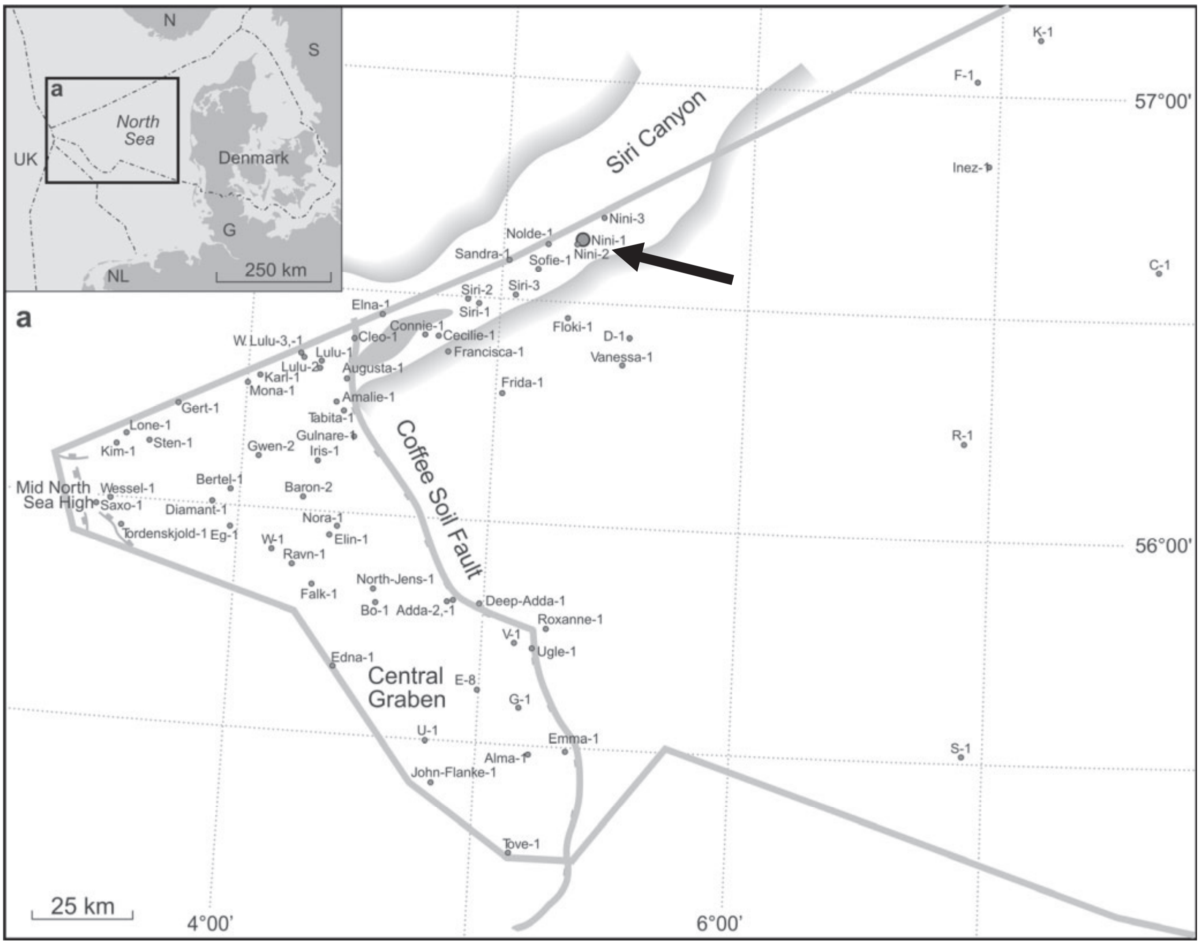

Fig. 2. Location map showing the position of the Nini-1 well used in this study (arrow). The margins of the Siri Canyon are shown by grey shading. An area of positive relief within the canyon is also shown by grey shading. G, Germany; N, Norway; NL, Netherlands; S, Sweden; UK, United Kingdom (Figure modified after Schiøler *et al*. 2007).

plug and material from the end trimmings were used for X-ray diffraction (XRD) and BET analysis.

ROUTINE CORE ANALYSIS

Helium porosity (ϕ_H) of the samples was measured by the gas expansion method. Helium porosity is a good measure of total porosity, including porosity in clay minerals, as no pores are so small that helium cannot enter. Buoyancy of the cores in brine (Archimedes) was also used to determine bulk volume on a fully saturated sample and pore volume was calculated from grain density as measured by the gas expansion method. Complete saturation was verified by comparing porosity measured by helium expansion and by Archimedes method. As porosity data from the two methods are within experimental error, all samples were assumed to be fully brine saturated.

Klinkenberg-corrected permeability was derived from permeability at a series of nitrogen gas pressures. Specific surface area of the grain (S_g) was measured by BET method by using nitrogen gas adsorption. Specific surface of pores from BET method (*Sp(BET)*) was calculated by dividing S_g by porous fraction, (ϕ_H) and multiplying by grain fraction, ($1-\phi_H$) as:

$$Sp(BET) = S_g\left(\frac{1-\phi_H}{\phi_H}\right)\rho_g, \tag{5}$$

where, ρ_g is grain density.

The effective bulk specific surface (S) was obtained from Klinkenberg permeability (k) and macro-porosity (ϕ) by using Kozeny's equation (Kozeny 1927) as:

$$k = c\frac{\phi^3}{S^2}, \tag{6}$$

where, c is Kozeny's factor which can be estimated from porosity via a simple model of linear 3D interpenetrating tubes (Mortensen *et al*. 1998):

$$c = \left[4\cos\left\{\frac{1}{3}\arccos\left(\phi\frac{8^2}{\pi^2}-1\right)+\frac{4}{3}\pi\right\}+4\right]^{-1}. \tag{7}$$

According to equation (7), c increases from 0.15 to 0.25 as porosity increases from 0.05 to 0.5. Specific surface of pores from Kozeny's equation (*Sp(Kozeny)*) can then be calculated:

$$Sp(Kozeny) = \frac{S}{\phi}. \tag{8}$$

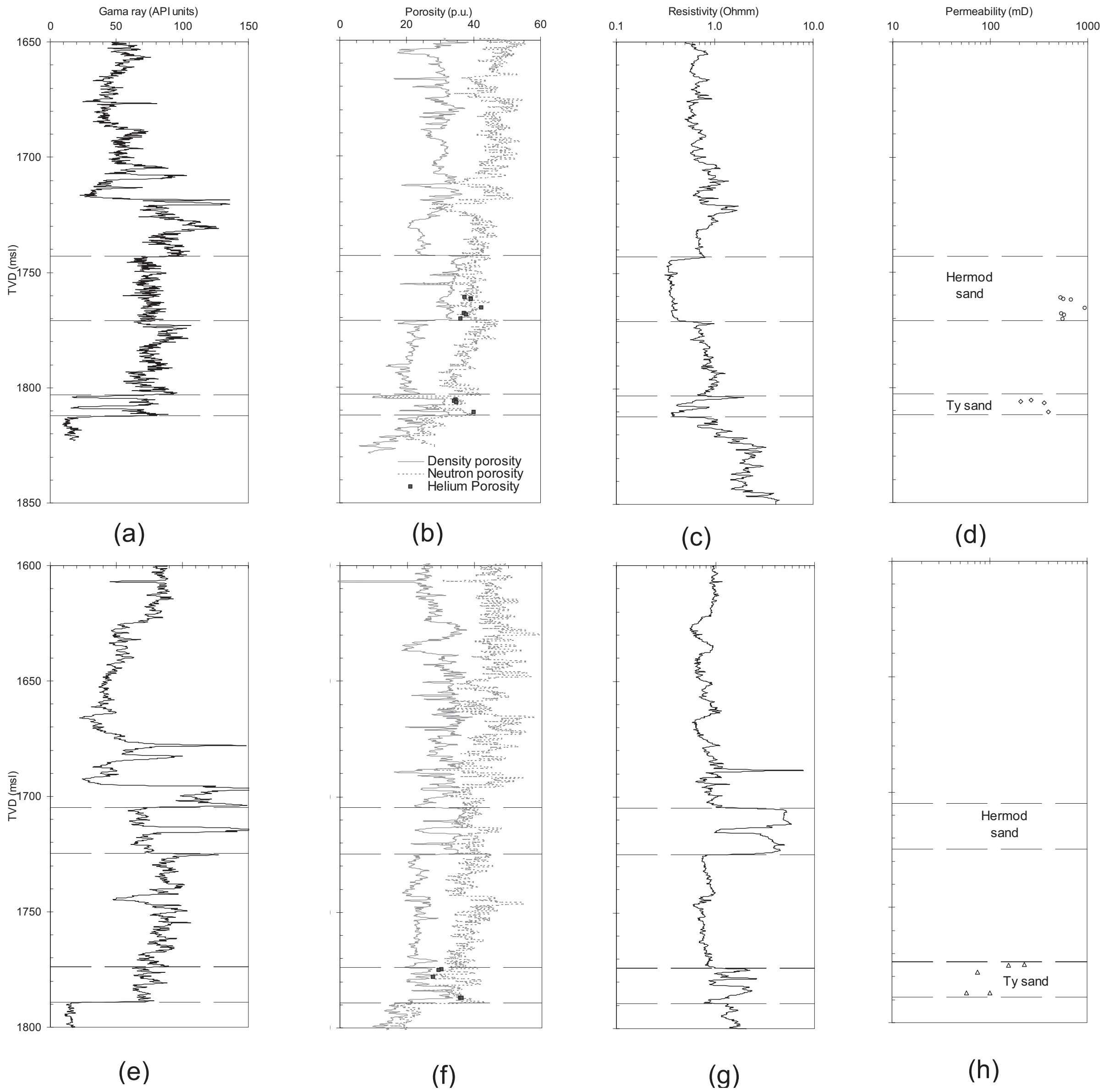

Fig. 3. Gamma ray, porosity and resistivity logs for wells Nini-1 (top) and Nini-1A (bottom). The glauconite-bearing reservoir intervals (Hermod sand and Ty sand) have relatively low separation between neutron- and density porosity. Horizontal dashed lines indicate the studied core intervals. Core data are shown for reference. Permeability is higher in Hermod sand than in Ty sand.

$1/Sp(Kozeny)$ is equivalent to hydraulic radius and thus should be related to capillary pressure and T_2 relaxation, so we base the remaining analysis on $Sp(Kozeny)$.

CAPILLARY PRESSURE

The capillary pressure may be expressed by the fundamental equation:

$$P_c = \frac{2\sigma \cos\theta}{r_c}, \tag{9}$$

where, r_c is the radius of pore throat, σ is the surface tension and θ is the contact angle. For water-wet conditions $\cos\theta$ becomes one, and in terms of specific surface of pore (Sp) equation (9) may be rewritten as:

$$P_c = S_P \sigma. \tag{10}$$

Air brine drainage capillary pressure measurements were done on brine saturated greensand samples by using the porous plate method at room temperature. Initially each sample was saturated with simulated formation brine. The brine has a density of 1.06 g cm^{-3} and a viscosity of 1.054 cP. Irreducible water saturation (S_{wi}) including clay-bound water was determined from capillary pressure curves and macro-porosity was calculated as porosity above irreducible water saturation (Fig. 4b).

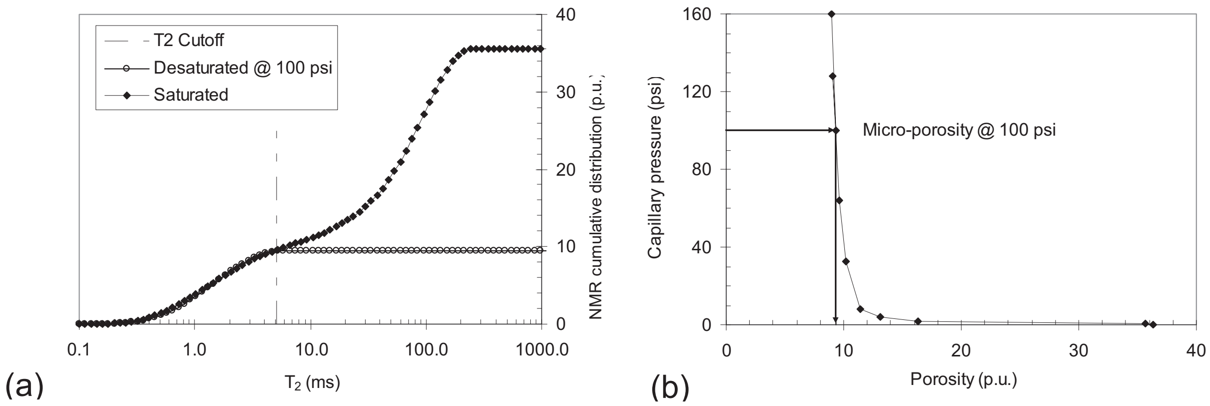

Fig. 4. Macro-porosity and micro-porosity determination for sample 1–4 (**a**) from NMR T_2 distribution (**b**) from the capillary pressure curve. The cumulative distribution for the fully saturated sample is compared to the cumulative distribution after centrifuging at 100 psi. The cutoff time which separates the T_2 distribution into macro-porosity and micro-porosity is defined as the relaxation time at the point where the cumulative porosity of the fully saturated sample equals the irreducible water saturation. The dashed vertical line is shown a cutoff of 5.21 ms. The capillary pressure of 100 psi corresponds to a micro-porosity of 9.1%.

IMAGE ANALYSIS

Polished thin sections were prepared from all samples in a plane perpendicular to the flow direction during core analysis. A Philips XL40 scanning electron microscope was used for acquisition of back scattered electron (BSE) images. The images are 1024 x 1024 byte greyscale images with a pixel length of 1.78 µm. This magnification resolves the intergranular macro-porosity and leaves the micro-porosity unresolved. Each image was filtered to remove the noise and a threshold used to create a binary image prior to analysis. Porosity determined in the images is called image porosity (ϕ_{image}). The image analysis procedure is sensitive to porosity threshold, so image porosity was determined when they are equal to macro-porosity determined from P_C measurements. The macro-porosity determined by image analysis is within a narrow range (±2.5 p.u.) obtained by image analysis along. The specific surface area or strictly speaking the specific perimeter (*S(image)*) of the solid grains was determined by using the method of Borre *et al.* (1995). According to Underwood (1970) and Solymar & Fabricius (1999) the specific perimeter (*S(image)*) may be approximated to the 3D specific surface (*S*) by:

$$S = \frac{4}{\pi} S(image). \tag{11}$$

Image specific surface of pores (S_p *(image)*) is thus calculated by using equation (8) where porosity is defined as macro-porosity determined from capillary pressure measurements.

NMR MEASUREMENTS

For NMR measurements all samples were saturated with brine (7.6 % NaCl). Complete saturation was verified by using the dry weight, the saturated weight, grain volume by helium expansion, and brine density. All samples attained full brine saturation. All the measurements were performed with the samples sleeved in PTFE heat shrink as several were poorly consolidated. The weights and volumes of the heat shrink material were accounted for in the measurements.

The laboratory NMR measurements were performed using a Resonance Instruments MARAN 2 spectrometer at ambient pressure and 34°C at a proton resonance frequency of 2.2 MHz. T_2 relaxation was measured using Carr-Purcel-Meiboom-Gill (CPMG) pulse sequence. The T_2 relaxation curves were measured by using a recycle delay (repetition time) of 10 s, number of echos 8000, CPMG inter echo spacing (τ) 200 µs and 100 scans. The $\pi/2$ and π pulses were 14.8 µs and 29.6 µs, respectively.

NMR porosity of the fully saturated samples was determined by using the total signal amplitude of each sample (by summing the amplitudes of the T_2 distribution) and known standard of similar diameter. In this case the reference standard was a sealed glass vial, containing 3 cm^3 of 50 000 ppm NaCl and 17 cm^3 of deuterium oxide. Deuterium oxide does not have an NMR signal therefore this reference standard has an equivalent porosity of 15%. The same number of scans was used for the reference and the sample. NMR porosity is then calculated using the, total signal amplitude, the bulk volume, hydrogen index of both plug and reference and the equivalent porosity of the reference.

For determining the macro-porosity and micro-porosity we need a cutoff value from the T_2 distribution. For two samples (one from Hermod and one from Ty), the T_2 cutoff was determined in the laboratory by obtaining the T_2 distribution at two saturations, fully brine saturated and at irreducible water saturation as determined from capillary pressure curves. The analysis of the air–water systems is relatively easy as there is no NMR response from the air and the relaxation time is exclusively due to the protons in the water. The cutoff time is defined as the relaxation time at the point where the cumulative porosity of the fully saturated sample equals the irreducible water saturation (Fig. 4a). As the T_2 cutoff is determined from capillary pressure equilibrium experiments includes capillary bound fluid and trapped in micro-pores. A single T_2 cutoff value for each formation was used for all samples of that formation. The cumulative porosity over the range $T_2 > T_{2\mathrm{cutoff}}$ was the macro-porosity and below the range $T_2 < T_{2\mathrm{cutoff}}$ was the micro-porosity or irreducible water saturation.

The NMR permeability model used in this work was obtained by combining equation (2), (6), and (8):

$$k = c\phi(T_2\rho_2)^2. \tag{12}$$

In a similar way the capillary pressure NMR model was obtained combining equation (2) and (10):

Table 1. *Core plug porosity data. Helium porosity was measured by Helium gas expansion, Archimedes porosity was measured by immersing, and NMR porosity was measured by the signal amplitude of* T_2 *measurements respectively. Archimedes macro-porosity and NMR macro-porosity were determined from capillary pressure curves and* T_2 *distributions respectively.*

Formation	Measured depth (m)	TVD (msl)	Sample ID	Helium porosity (p.u.)	Error ±	Archimedes porosity (p.u.)	Error ±	NMR porosity (p.u.)	Error ±	Archimedes macro-porosity (p.u.)	NMR macro-porosity (p.u.)
Hermod	1761.1		1-4	37.3	1.5	35.3	1.1	31.2	0.4	27.0	22.7
	1761.7		1-6	39–3	1.3	37.2	1.1	33.8	0.5	29.9	25.4
	1762.1		1-7	39.2	0.4	37.9	1.1	35.5	0.5	29.6	26.7
	1765.7		1-18	42.4	0.5	40.2	1.2	37.2	0.5	30.5	28.8
	1768.1		1-25	37.1	0.5	36.7	1.1	33.3	0.5	25.9	23.7
	1768.7		1-27	37.8	1.1	37.0	1.1	32.7	0.5	27.2	23.0
	1770.4		1-32	36.2	0.9	35.5	1.1	32.6	0.5	26.0	24.3
Ty	1805.5		1-137	34.7	0.8	36.0	1.1	31.6	0.4	24.2	22.2
	1806.1		1-139	34.2	0.5	34.3	1.0	31.6	0.4	23.1	21.6
	1806.7		1-141	34.2	0.3	34.6	1.0	31.8	0.4	24.1	22.5
	1810.7		1-153	40.0	0.4	38.6	1.2	33.6	0.5	27.2	23.0
	1972.1	1774.7	1A-141	30.1	0.1	29.5	0.9	27.0	0.4	19.4	17.7
	1972.4	1775.0	1A-142	29.3	0.7	29.0	0.9	29.0	0.4	19.9	18.6
	1975.8	1778.1	1A-152	27.7	0.3	28.1	0.8	26.6	0.4	16.7	17.5
	1985.7	1787.0	1A-182	35.7	0.1	35.3	1.1	33.7	0.5	23.7	23.9
	1986.0	1787.2	1A-183	36.2	0.4	35.5	1.1	33.3	0.5	24.9	24.5

Table 2. *Core plug data. Specific surface area of grains (SSA) was measured using the BET method and the effective specific surface of pores (Sp(Kozeny)) was calculated by using Kozeny's equation. Image specific perimeter of pores (Sp(image)) was determined by image analysis by using the method of* Borre et al. *(1997). The cutoff time which separates the* T_2 *distribution into macro-porosity and micro-porosity is defined as the relaxation time at the point where the cumulative porosity of the fully saturated sample equals the irreducible water saturation.*

Sample ID	Klinkenberg permeability (mD)	SSA (BET) (m^2/g)	Sp (Kozeny (μm^{-1})	Sp (image) (μm^{-1})	T_2 Cutoff (ms)	Irreducible water saturation from P_c (%)	Irreducible water saturation from NMR (%)
1-4	530	21	0.34	0.32	5.2	25.6	27.2
1-6	560	21	0.35	0.33		19.6	24.9
1-7	680	21	0.31	0.35		22.1	24.9
1-18	940	19	0.27	0.32		24.2	22.6
1-25	540	20	0.33	0.35		29.4	28.8
1-27	570	22	0.33	0.33		26.5	29.8
1-32	550	21	0.32	0.36		26.7	25.5
1-137	260	20	0.45	0.34		33.0	29.8
1-139	210	22	0.49	0.38		32.8	31.8
1-141	360	20	0.38	0.39		30.5	29.2
1-153	390	23	0.39	0.33		29.6	31.61
1A-141	230	17	0.43	0.35	3.7	34.4	34.2
1A-142	160	19	0.49	0.35		38.4	35.7
1A-152	80	20	0.68	0.36		40.7	34.4
1A-182	60	22	0.95	0.46		32.9	28.9
1A-183	100	19	0.74	0.41		29.9	26.4

$$P_c = \frac{\sigma}{\rho_2 T_2}. \qquad (13)$$

The assumption of this model is that: (1) the pore structure controlling the T_2 distribution and capillary pressure is a bundle of capillary tubes and the drainage is controlled by the hierarchy of pore sizes; (2) the surface relaxivity is constant overall the sample; and (3) diffusion relaxation is negligible.

RESULTS

The helium porosity of greensand ranges from 28–42 p.u. (porosity units) with a maximum uncertainty 1.5 p.u. (Table 1). Klinkenberg corrected permeability ranges from 60–940 mD (Table 2). Permeabilities of Hermod samples are larger than Ty samples and correlates with porosity, whereas Ty data are more scattered (Fig. 5).

Petrographic thin section analysis indicates that the studied Paleocene greensands are well to very well sorted, dominated by grains of quartz but also large volumes of glauconite (20–25 vol %) (Fig. 6). Samples from the Hermod Formation contain glauconite grains of size between 100–200 µm, some glauconite grains are larger (300–400 µm) (Fig. 1a). Samples from the Ty Formation contain glauconite grains of 100–150 µm, although some glauconite grains are larger (200–300 µm) (Fig. 1b). The grains are subangular to sub-rounded for both formations. The Hermod Formation is only weakly cemented, whereas samples from the Ty Formation contain cement of berthierine or microcrystalline quartz cement resulting in a relatively low permeability (Table 2). In both formations XRD analyses of separate glauconite grains show the presence of some expanding layers in the predominantly illitic glauconite.

The capillary pressure was obtained assuming 72 mN m^{-1} for the brine surface tension. Capillary pressure curves show

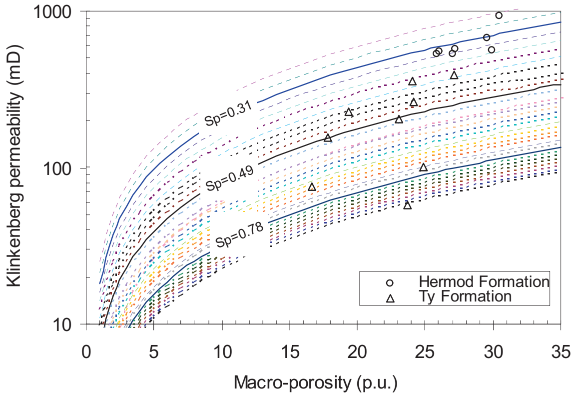

Fig. 5. Cross plot of macro-porosity from capillary pressure measurement and permeability. Samples from the Hermod sand have similar porosity and permeability, whereas the samples from Ty sand are more scattered. The reference lines represent equal specific surface of pores (*Sp (Kozeny)*) in μm^{-1} as calculated by using Kozeny's equation. The data indicate that *Sp* is lower in Hermod sand than in Ty sand.

that for the higher permeability Hermod Formation samples, the P_c curves are shifted toward low irreducible water saturation, whereas P_c curves for the lower permeability Ty Formation samples are shifted towards high irreducible water saturation (Fig. 7a, c). Irreducible water saturation from capillary pressure was obtained at P_c 100 psi, and varied between 25% and 42% of the total porosity (Table 2).

The NMR T_2 distributions are presented in graphical form for each sample and the population is expressed in porosity units in Figure 7(b, d). All T_2 distributions are bimodal. Each T_2 time corresponds to a particular pore size. If the rock has a single pore size then instead of a broader distribution there will be a single vertical line. Thus broader distributions reflect a greater variability in pore size. We have determined a time cutoff of 5.21 ms for the sample 1-4 from Hermod Formation and 3.68 ms for sample 1A-141 from the Ty Formation. The short relaxation time component in a T_2 distribution of a rock is attributed to the water in glauconite. For these greensand samples, a peak close to 1 ms should correspond to glauconite water, whereas all samples also exhibit a second peak close to 100 ms that corresponds to movable fluid. Higher permeability Hermod Formation samples show larger amplitude in the movable fluid than samples from the Ty Formation; whereas lower permeability bearing Ty Formation samples show a slightly larger amplitude in capillary bound and glauconite water (Fig. 7b, d).

DISCUSSION

Porosity

Helium porosity, Archimedes porosity and NMR porosity are compared in Figure 8. Helium porosity is associated with the total porosity of the sample including micro- porosity in glauconite and it shows the highest values among the three types of porosity data. In principle, Archimedes and NMR porosity should also represent the total porosity of a sample, but it could be lower if water saturation is below 100%. Although the Archimedes porosity is close to helium porosity, NMR porosity tends to be lower. Both macro-porosity and micro-porosity are underestimated by NMR measurements (Fig. 8c, d). The discrepancy between Archimedes porosity and NMR porosity could be due to several factors. First, NMR and Archimedes porosity depend on the saturation condition of the sample. We cannot rule out the possibility that during NMR measurement the saturation condition was lower than that during the Archimedes measurements. Second, paramagnetic iron-bearing minerals in reservoir rock may be an important factor influencing T_2 measurements as shown by Dodge *et al.* (1995). The presence of paramagnetic ions increases the rate of relaxation of the hydrogen proton. This is expected for greensand because both glauconite and berthierine contain iron. These clay minerals have a large surface area and high magnetic susceptibilities, leading to large internal gradients and short T_2 (Straley *et al.* 1997). Rueslåtten *et al.* (1998) illustrated the influence of chlorite (berthierine) and glauconite on the difference between helium porosity and NMR T_2 derived porosity (delta porosity) and found a broad positive correlation between delta porosity and chlorite content, whereas they found no correlation with glauconite content. Thus they pointed to the detrimental effect of chlorite or berthierine on porosity estimated by NMR. We found only a vague negative correlation between delta porosity and bulk mineral composition (glauconite, clay coating and pores filling) (Fig. 8b).

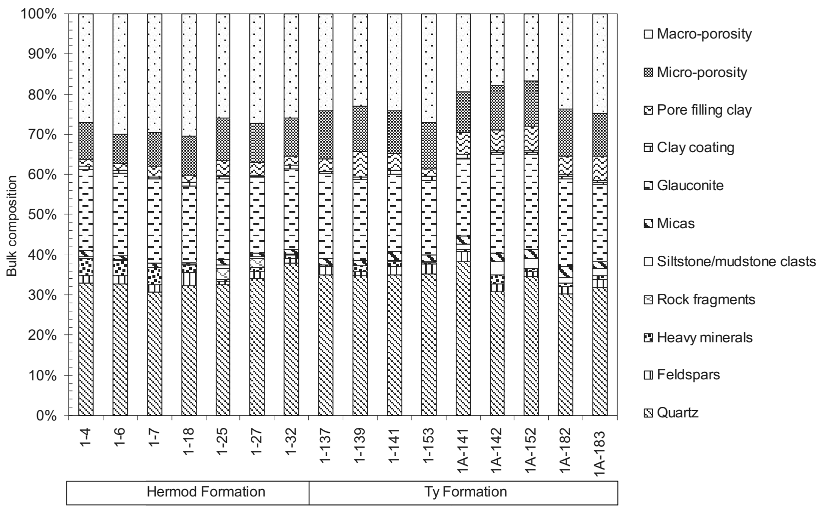

Fig. 6. Bulk composition of investigated samples from the Hermod and Ty formations of the Nini Field. Mineral composition was determined by point counting of 500 points across each entire thin section. Macro-porosity was determined by image analysis when porosity threshold is equal to macro-porosity determined from P_c measurements. Micro-porosity is the difference between helium porosity and image porosity.

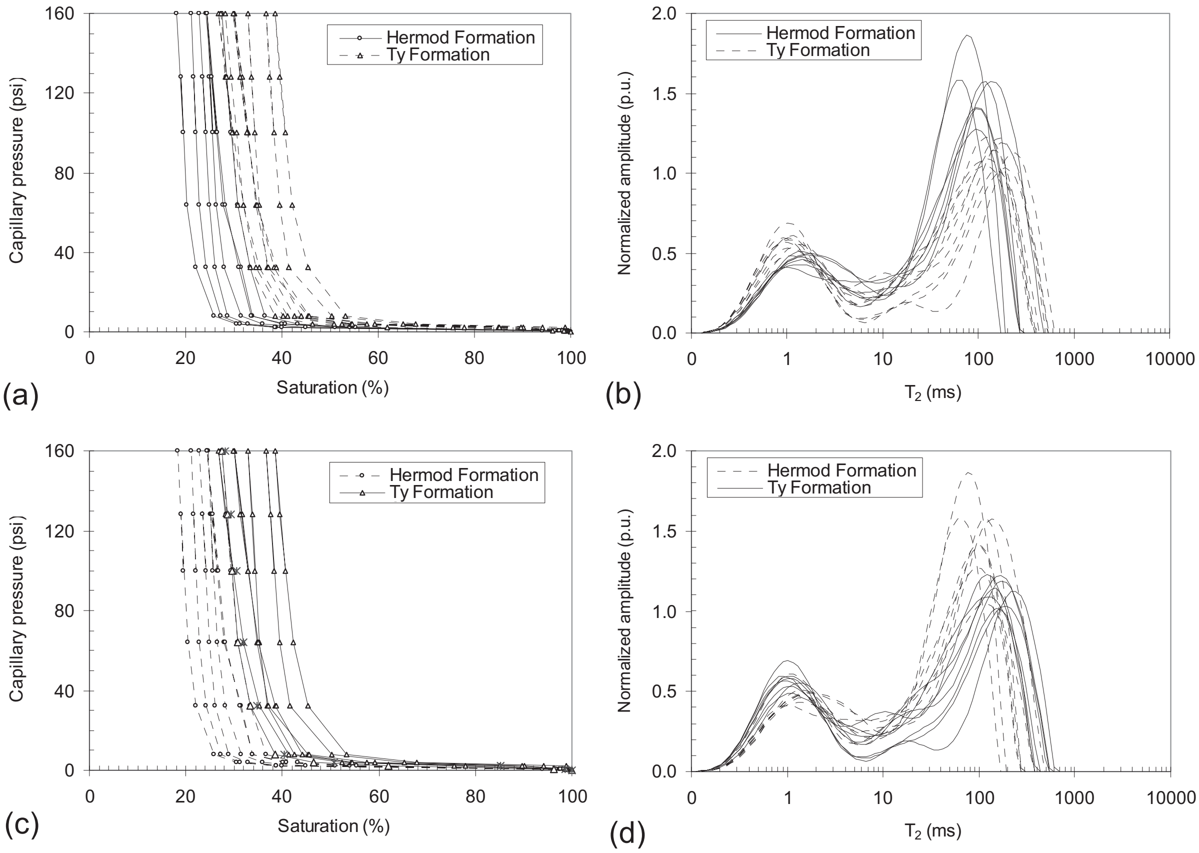

Fig. 7. (**a**), (**c**) Capillary pressure curves and (**b**), (**d**) NMR T_2 distribution curves of greensand samples. (a) P_c curves of Hermod Formation samples are shifted towards low irreducible water saturation, whereas (c) the Ty Formation samples have relatively high irreducible water saturation. This pattern compares to the relatively high permeability of Hermod sand relative to the low permeability of Ty sand (Fig. 3). T_2 distribution of all samples shows two peaks. The peak close to 1 ms represents micro-porosity and the peak close to 100 ms represents macro-porosity.

Specific surface area

Specific surface area with respect to pore (*Sp*) was determined by three methods which are compared in Figure 10a. We found a large difference between the specific surface areas as measured by BET method (*Sp(BET)*, 76–141 μm^{-1}) and calculated by Kozeny's equation (*Sp(Kozeny)*, 0.27–0.95 μm^{-1}) and that determined by image analysis (*Sp(image)*, 0.32–0.46 μm^{-1}). Nitrogen adsorption has a very high resolution; therefore this method determines the specific surface of the total porosity, including micro-porosity. Based on the Kozeny's equation, we estimated *Sp(Kozeny)* by using permeability determined on the cores and macro-porosity. *Sp* determination by image analysis depends on the resolution of the image (Solymar *et al*. 2003). However, *Sp* from image analysis at the present pixel size and *Sp* from Kozeny's equation are in same order of magnitude which tells us that the resolution of the image is sufficient and that the pixel size is small enough to determine *Sp* by image analysis. The specific surface area of separated glauconite grains are in order of 1300–1600 μm^{-1}, whereas the specific surface area of quartz grains is less than 1 μm^{-1}. So rather than quartz grains, specific surface of glauconite grains are measured by BET method. Thus, *Sp* by BET method is mainly reflected by the micropores of glauconite grains and pore filling/lining clays, whereas *Sp* from Kozeny's equation and image analysis is associated with effective surface and related to macro-porosity. We found that *Sp* measured by the BET method is well correlated with the fraction of glauconite plus pore-filling clay minerals (Fig. 9c).

We found that irreducible water saturation ranges from 22–41% from capillary pressure measurements and from 23–36% from NMR measurements. Considering the errors associated with these two methods, irreducible water saturations are similar. The high value of irreducible water saturation is due to the high specific surface of glauconite. The micropores of glauconite remain brine filled even at a capillary pressure of 100 psi. We found a positive correlation between irreducible water saturation determined from P_c and NMR with *Sp* determined from BET method (Fig. 9a, b). In addition Figure 9 (a, b) also shows a tendency for low surface area samples to approach minimum irreducible water saturation and for high surface area samples to remain more saturated. A relationship between specific surface and irreducible water saturation has been noted by several authors e. g. Hamada *et al.* (2001) where authors reported an excellent correlation (R^2=0.98) between irreducible water saturation and specific surface of pores.

Surface relaxivity

We compare four ways of estimating surface relaxivity in Figure 10b. Equation (2) shows that surface relaxivity for the NMR T_2 distribution is related to the specific surface of pores. Thus in the absence of laboratory data, surface relaxivity may be evaluated by comparing T_2 distributions with *Sp(BET),*

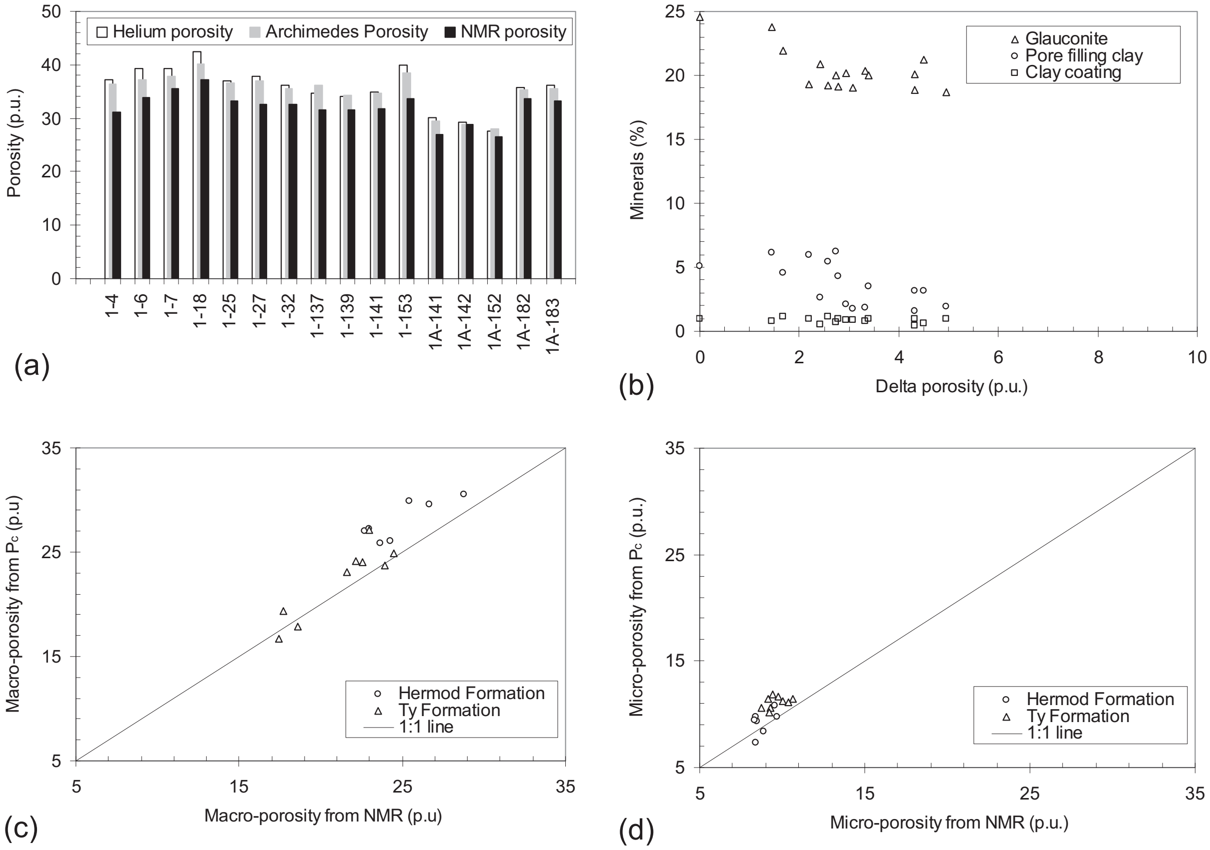

Fig. 8. (**a**) Helium porosity, Archimedes porosity and NMR porosity of investigated samples. Helium porosity tends to be the highest, whereas NMR porosity is underestimated due to iron-bearing minerals in greensand. (**b**) Cross plot of delta porosity (Archimedes porosity–NMR porosity) and minerals bulk composition (glauconite, pore-filling clay and clay coating). Cross plots of (**c**) macro-porosity and (**d**) micro-porosity from NMR T_2 distribution and capillary pressure curves.

Sp(Kozeny) or *Sp(image)*. This results in relaxivity value ranges in the order of 2.7–4.2 μm s^{-1} from *Sp(BET)*, 7–58 μm s^{-1} from *Sp(Kozeny)*, and 10–35 μm s^{-1} from *Sp(image)*. As an alternative, we used P_c curves and found that a surface relaxivity of 20.4 μm s^{-1} for the Hermod and of 28.4 μm s^{-1} for the Ty formations are needed to generate P_c curves from NMR measurements. The surface relaxivity estimated based on *Sp(BET)* would be controlled by micro-porosity in glauconite. We found an average surface relaxivity using *Sp(BET)* of 3.42 μm s^{-1}, which is close to the 3.3 μm s^{-1} for glauconite reported by Matteson *et al.* (1996). Surface relaxivity estimated from *Sp(Kozeny)* and *Sp(image)* should also be effective surface relaxivity as it was calculated from effective specific surface area.

Permeability

Kozeny's equation (equation (12)) was used to predict permeability from NMR T_2 distributions. Before applying this equation we highlight the similarities and differences within T_2 distribution among samples (Fig. 11). The T_2 distribution of sample 1–18 peaks for longer than for sample 1–6, thus the larger porosity of sample 1–18 is due to the larger pores which also cause higher permeability (Fig. 11a). The comparison of three samples with similar distributions for shorter periods of time is shown in Figure 11b. When the larger peak (around 100 ms) becomes smaller and is shifted to larger times due to a small number of intermediate pores, there is a small increase of the number of larger pores. Thus, for these samples although porosity is higher, the permeability is not high. We cannot use average T_2 time or final T_2 time in equation (12) for the permeability calculation, so we modified equation (12) by summing the total permeability among the T_2 distribution and only including the macro-porosity. Thus resulting:

$$k = c\phi\rho_2^2 \sum_{i=1}^{N} f_i \, (T_{2i})^2 \, , \tag{14}$$

where, f_i is a fraction of the total amplitude of each T_{2i}. The Kozeny factor c was calculated using equation (7).

The predicted permeability distribution obtained by using equation (14) is shown in Figure 11(c, d). Below the cutoff time, the amplitude of permeability is zero which means that micro-porosity does not contribute to fluid flow. From the cutoff time to 100 ms, the amplitude of permeability is small but above 100 ms the contribution of permeability increases.

Predicted permeability and measured permeability are compared in Figure 12a by using surface relaxivity from *Sp(Kozeny)*, average surface relaxivity for each depth interval in Figure 12b by using surface relaxivity from *Sp*(*image*), in Figure 12c by using surface relaxivity from equation (13), and in Figure 12d by using surface relaxivity from *Sp(BET)*. Predicted permeability is close to 1:1 line of measured permeability for cases 1 and 2. The estimated permeability from

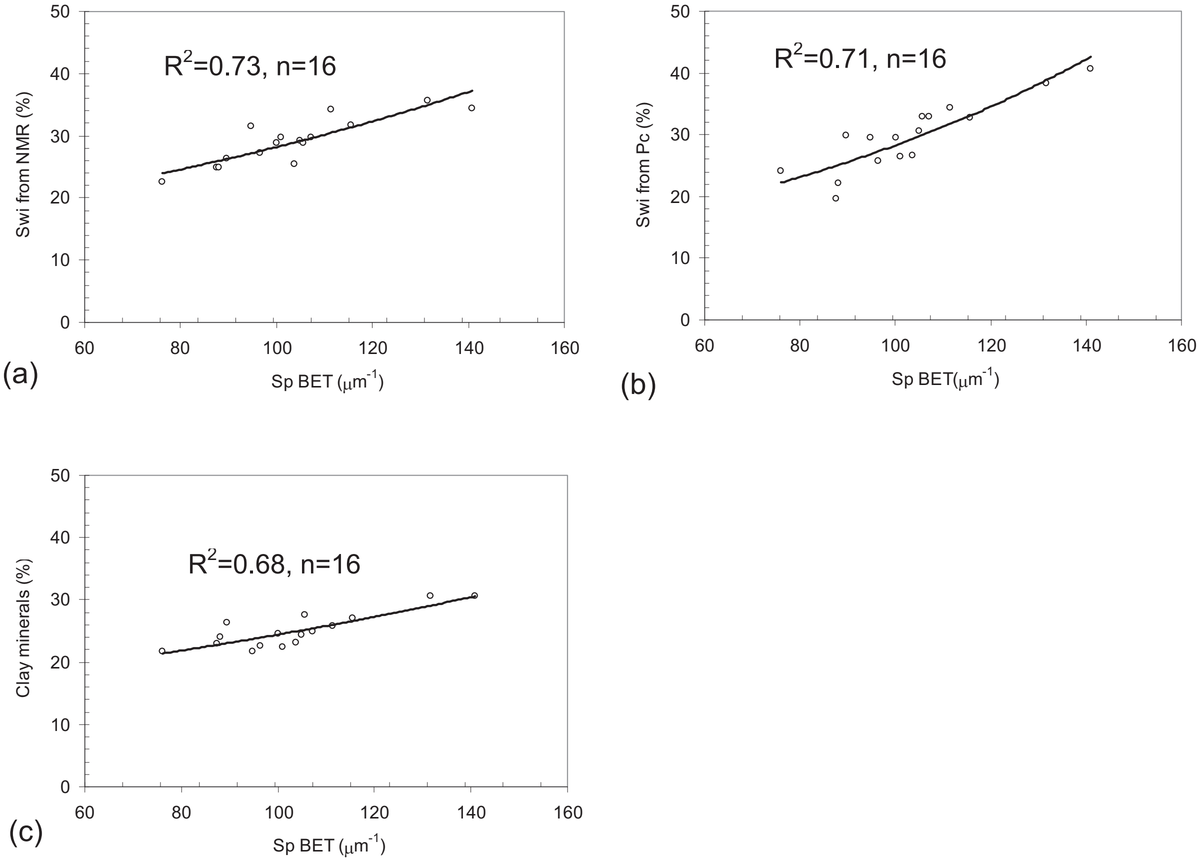

Fig. 9. Correlation between specific surface of pores as measured by BET (*Sp (BET)*) and (**a**) irreducible water saturation as determined from NMR measurements, (**b**) irreducible water saturation as determined from capillary pressure measure as well as (**c**) clay minerals (glauconite, clay coating and pore-filling clay) as percentage of bulk composition.

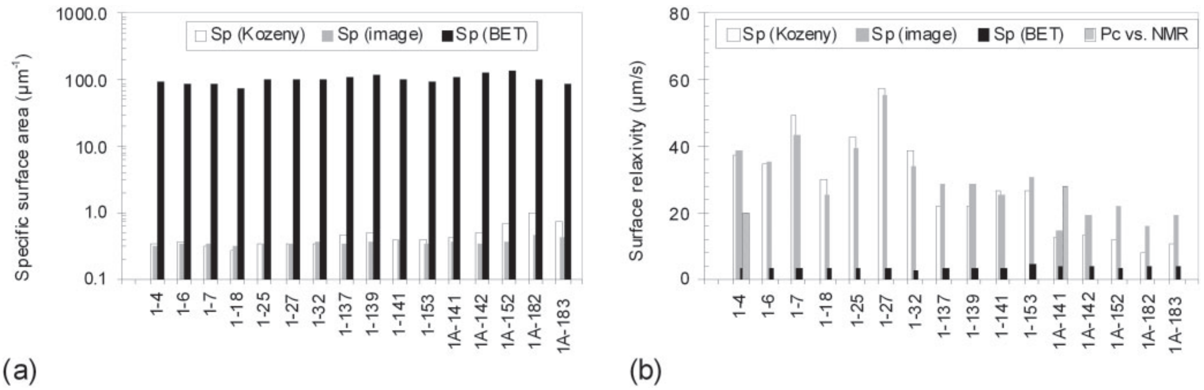

Fig. 10. (**a**) Specific surface area with respect to pore (*Sp*) determined by BET nitrogen adsorption (*Sp (BET)*), estimated from Kozeny's equation (*Sp (Kozeny)*) and determined by image analysis of the BSE images (*Sp (image)*). (**b**) Surface relaxivity determined comparing T_2 distribution with *Sp (BET)*, *Sp (Kozeny)*, and *Sp (image)*. For two samples, surface relaxivity are also determined from capillary pressure versus NMR T_2 distribution.

Timur-Coates model is illustrated in Figure 12e. Predicted permeability using this model works well if we use C=8.3 which was optimized in a least-squares sense such that the sum of the squared error between the measured and predicted permeability is minimized. Predicted permeability from image analysis and measured permeability are compared in Figure 12f. Image permeability and NMR predicted permeability by using surface relaxivity from *Sp*(*image*) are equal.

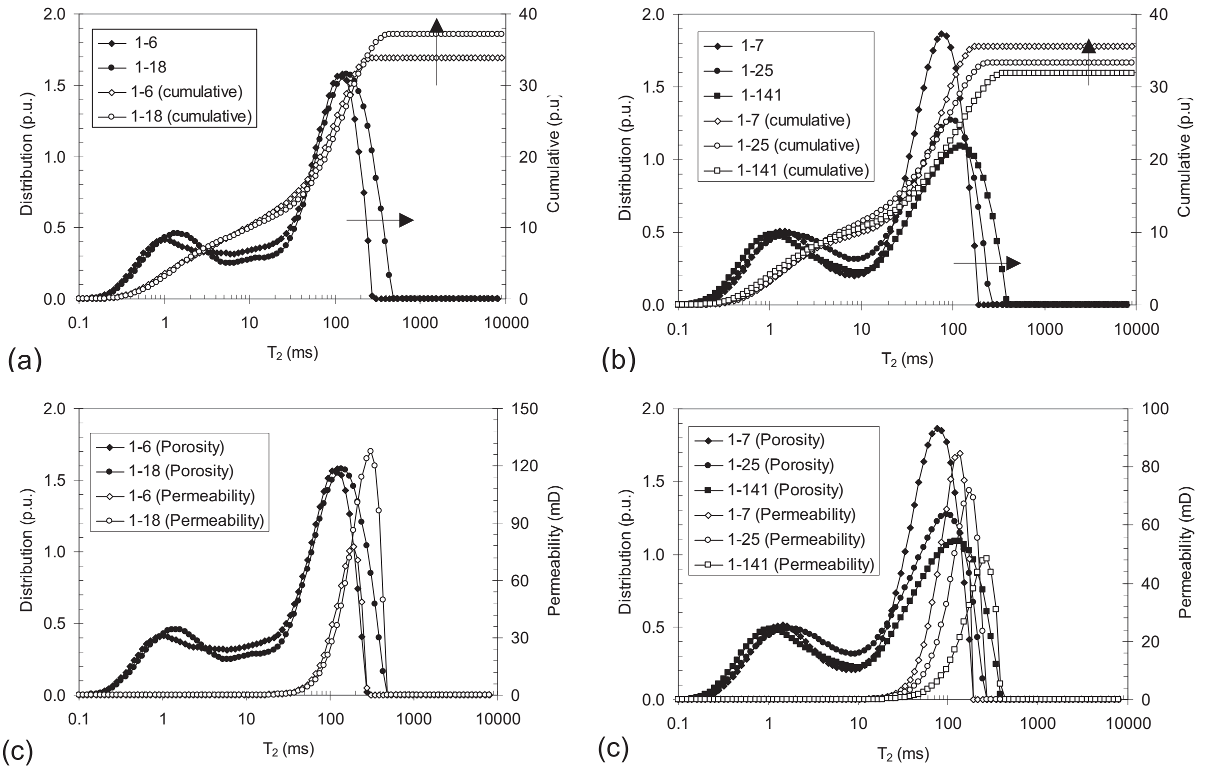

Fig. 11. (**a**), (**b**) Porosity distribution and cumulative porosity for five greensand samples. (**c**), (**d**) Permeability distribution of five greensand samples obtained from Kozeny's equation.

Capillary pressure curves

We applied the value of surface relaxivity of 20.3 μm s^{-1} and 28.4 μm s^{-1} for the Hermod Formation and Ty Formation samples respectively to generate the capillary pressure curves directly from the T_2 distribution by using equation (13) (Fig. 13). Capillary pressure curves overlie each other for low permeability samples. However, we found deviation between the P_c NMR and P_c lab for the high permeability sample from Hermod Formation. A deviation is to be expected because we assumed uniform surface relaxivity within a sample and ignored diffusion relaxation. The calculated surface relaxivity is shown in Figure 13e for a sample from Hermod Formation and in Figure 13f for a sample from Ty Formation. A good match between P_c curves from laboratory and NMR measurement is found when average surface relaxivity is equal to surface relaxivity applied to predict P_c curves from NMR. In contrast, there is deviation between P_c curves from the laboratory and NMR measurements when average surface relaxivity is not equal to the surface relaxivity need to match P_c curves. This variation of surface relaxivity within the sample is probably due to the large pores and higher permeability in the greensands of Hermod Formation.

CONCLUSIONS

The objective of this study is to predict petrophysical properties from NMR T_2 distributions. Based on laboratory experiments and image analysis on sixteen greensand samples from the two formations in the Nini field of the North Sea, we found that the Hermod Formation is only weakly cemented, whereas samples from Ty Formation contain cement of berthierine or microcrystalline quartz cement resulting in relatively lower permeability than in the Hermod samples.

We found that the total porosity measured by the Archimedes method is to close to helium porosity, whereas NMR porosity tends to be lower. The discrepancy between Archimedes porosity and NMR porosity may be due to several factors, including the presence of glauconite grains in the greensand.

This study shows that the surface area measured by the BET method and the derived surface relaxivity are associated with micro-porous glauconite grains. The effective surface area as calculated by Kozeny's equation and as determined from petrographic image analysis of backscattered electron micrographs and the estimated effective surface relaxivity is associated with macro-pores. We found that *Sp* measured by the BET method is well correlated with the fraction of glauconite plus pore-filling clay minerals.

Irreducible water saturation in the studied greensands ranges from 22–41% and these high values are due to the high specific surface area of glauconite. The micro-pores of glauconite remain brine filled even at a capillary pressure of 100 psi.

We found that the predicted permeability from NMR by using Kozeny's equation agrees well when surface relaxivity is known. By using Timur-Coates model, predicting permeability works well if we optimize the constant to C=8.3.

This study shows that predicted capillary pressure curves from NMR T_2 distribution agree with measured capillary pressure curves for low permeability samples. The deviation between the P_c NMR and P_c lab for the high permeability samples is due to the contrasting relaxivity on the surface of quartz and glauconite.

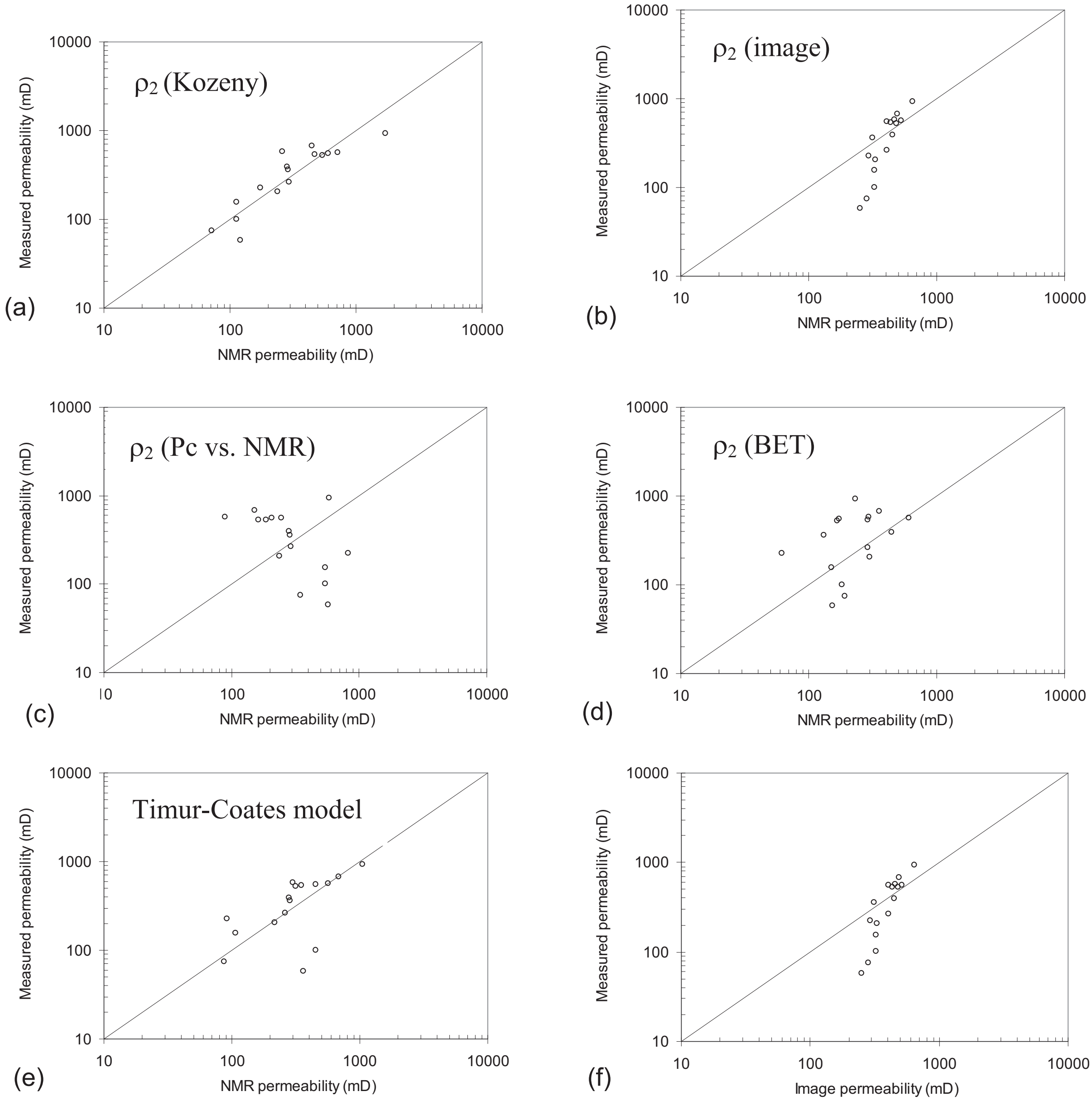

Fig. 12. Measured permeability versus NMR predicted permeability by using surface relaxivity from (**a**) *Sp(Kozeny)*, (**b**) *Sp(image)*, (**c**) *Sp(BET)*, (**d**) P_c versus NMR and (**e**) from Timur-Coates model. (**f**) Measured permeability versus predicted permeability from image analysis. Image permeability and NMR predicted permeability by using surface relaxivity from *Sp(image)* are equal.

Niels Springer and Hans Jørgen Lorentzen (GEUS, DK) are thanked for help with the core analysis. Sinh Hy Nguyen (DTU, DK) performed XRD and BET measurements, Hector Ampuero Diaz (DTU, DK) prepared polished thin sections. DONG Energy A/S is acknowledged for financial support.

APPENDIX

Nomenclature

BFV	Bound fluid volume
C	Formation dependent constant
c	Kozeny factor
f_i	Amplitude of each T_{2i}
FFI	Free fluid volume
k	Klinkenberg permeability
K	Scaling factor
S	Specific surface area of bulk
S_g	Specific surface area of grains
Sp	Specific surface of pores
$T_{2\ Bulk}$	Relaxation of fluids
$T_{2\ Diffisionk}$	Relaxation of molecular diffusion
$T_{2\ Surface}$	Relaxation of surface

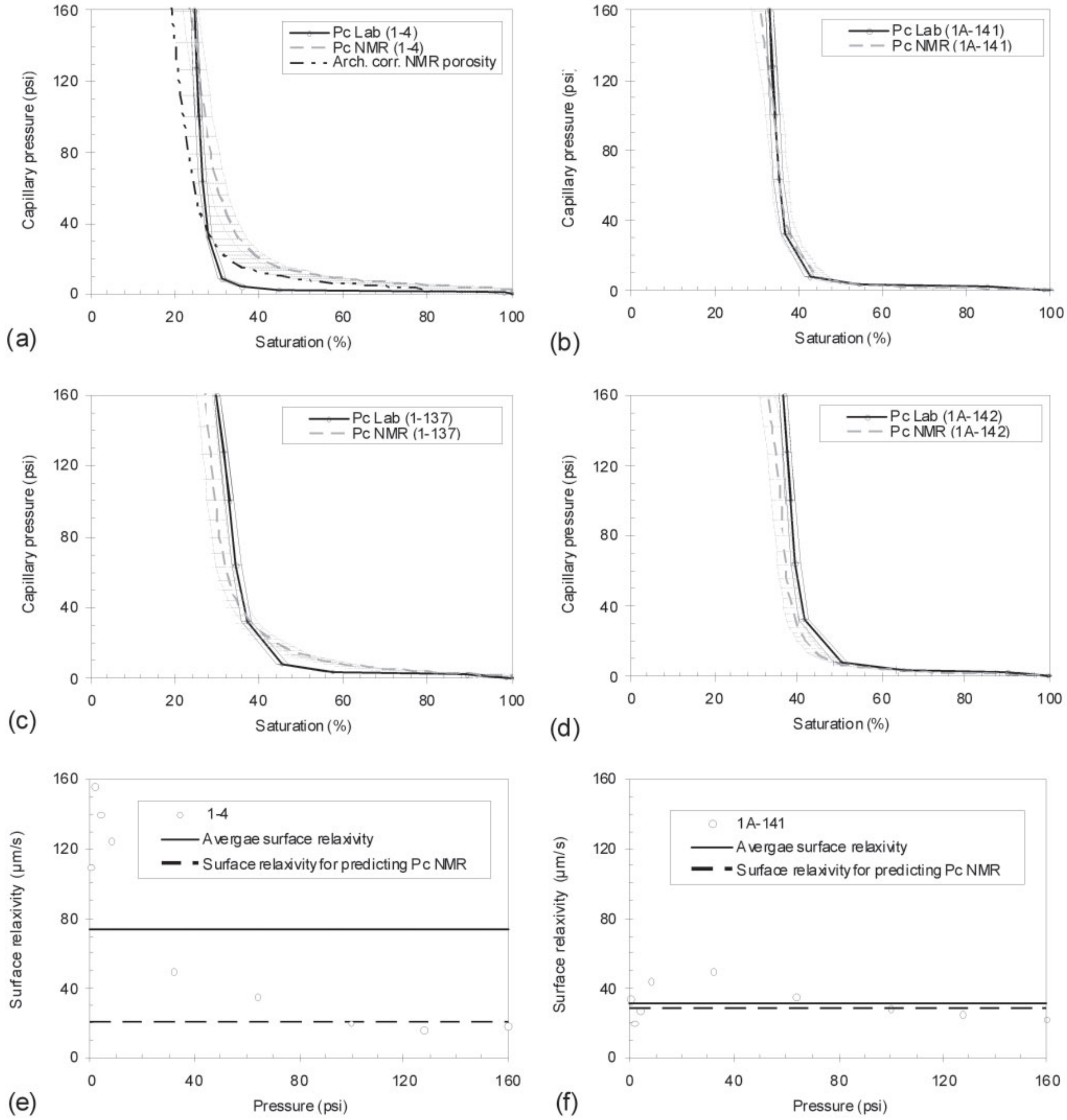

Fig. 13. Air brine capillary pressure curves including saturation error compared with NMR derived capillary pressure including saturation error. Saturation error corresponds to the error associated with porosity measurements. The NMR derived capillary pressure curves are based on surface relaxivity value of 20.4 µm s^{-1} for Hermod Formation and 28.4 µm s^{-1} for Ty formation. Deviation between average surface relaxivity (solid line) and surface relaxivity for predicting P_c NMR (dashes line) are shown (**e**) for Hermod Formation and (**f**) for Ty Formation.

Greek symbols

ϕ	Porosity (fraction)
ρ	Surface relaxivity
τ	Inter echo spacing

Unit conversion

1 mD = 0.9869 10^{-15} m^2
1 psi = 6.89 kPa

REFERENCES

Al-Mahrooqi, S. H., Grattoni, C. A., Moss, A. K & Jing, X. D 2003. An investigation of the effect of wettability on NMR characteristics of sandstone rock and fluid systems. *Journal of Petroleum Science and Engineering*, **39**, 389–398.

Al-Mahrooqi, S. H., Grattoni, C. A., Muggeridge, A. H., Zimmerman, R. W & Jing, X. D 2006. Pore-scale modeling of NMR relaxation for the characterization of wettability. *Journal of Petroleum Science and Engineering*, **52**, 172–186.

Borre, M., Lind, I & Mortensen, J 1997. Specific surface as a measure of burial diagenesis of chalk. *Zentralblatt fur Geologie und Palaontologie*, **1**, 1071–1078.

Cagatay, M. N., Saner, S., Al-Saiyed, I & Carrigan, W. J 1996. Diagenesis of the Safaniya Sandstone Member (mid-Cretaceous) in Saudi Arabia. *Sedimentary Geology*, **105**, 221–239.

Coates, G. R., Xiao, L. *et al.* 1999. *NMR Logging Principles and Applications*. Gulf Professional Publishing, Houston, Texas.

Diaz, E., Prasad, M., Mavko, G & Dvorkin, J 2003. Effect of glauconite on the elastic properties, porosity, and permeability of reservoir rocks. *The Leading Edge*, **22**, 42–45.

Dodge, W. S., Shafer, J. L., Guzman-Garcia, A. G. & Noble, D. A 1995. Core and Log NMR Measurements of an Iron-Rich, Glauconitic Sandstone Reservoir. 36th Annual Symposium of SPWLA, Paris, France, 26–29 June.

Glover, P., Zadjali, I & Frew, K 2006. Permeability prediction from MICP and NMR data using an electrokinetic approach. *Geophysics*, **71**, 49–60.

Grattoni, C. A., Al-Mahrooqi, S. H., Moss, A. K., Muggeridge, A. H & Jing, X. D 2003. An improved technique for deriving drainage capillary pressure from NMR T_2 distributions. *The International Symposium of the Society of Core Analysis*, **25**, 21–24 September, Pau, France.

Hamada, G., Al-Blehed, M., Al-Awad, M & Al-Saddique, M 2001. Petrophysical evaluation of low-resistivity sandstone reservoirs with nuclear magnetic resonance log. *Journal of Petroleum Science and Engineering*, **29**, 129–138.

Hidajat, I., Singh, M., Cooper, J & Mohanty, K. K 2002. Permeability of porous media from simulated NMR response. *Transport in Porous Media*, **48**, 225–247.

Hocking, R., Voon, J & Collins, L 1988. Stratigraphy and sedimentology of the basal Winning Group, northern Carnarvon Basin. *In:* Purcell, P.G & Purcell, R.R (eds) *The North West Shelf*. Proceedings of Petroleum Exploration Society Australia Symposium, Perth, 203–224.

Hossain, Z., Fabricius, I. L & Christensen, H. F 2009. Elastic and nonelastic deformation of greensand. *The Leading Edge*, **28**, 260–262.

Howard, J. J., Kenyon, W. E & Straley, C 1993. Proton magnetic resonance and pore size variations in reservoir sandstones. *SPE Formation Evaluation*, **1**, 194–200.

Kenyon, B., Kleinberg, R., Straley, C & Morriss, C 1995. Nuclear Magnetic Resonance Imaging—Technology for the 21st century. *Oilfield Review*, **7**, 19–30.

Kenyon, W. E 1997. Petrophysical principles of applications of NMR logging. *The Log Analyst*, **38**, 21–43.

Kewan, W & Ning, L 2008. Numerical simulation of rock pore-throat structure effects on NMR T_2 distribution. *Applied Geophysics*, **5**, 86–91.

Kleinberg, R 1996. Utility of NMR T_2 distributions, connection with capillary pressure, clay effect, and determination of the surface relaxivity parameter ρ_2. *Magnetic Resonance Imaging*, **14**, 761–767.

Kozeny, J 1927. Ueber kapillare Leitung des Wassers im Boden. *Sitzungsberichte der Kaiserlichen Akademie der Wissenschaften, Wien*, **136**, 271–306.

Marschall, D., Gardner, J. S., Mardon, D & Coates, G. R 1995. Method for correlating NMR relaxometry and mercury injection data. *Proceedings of the 1995 International Symposium of Society of Core Analysts*, papers, 9511.

Mortensen, J., Engstrøm, F & Lind, I 1998. The relation among porosity, permeability, and specific surface of chalk from the Gorm field, Danish North Sea. *SPE Reservoir Evaluation and Engineering*, **1**, 245–251.

Ranganathan, V & Tye, R. S 1986. Petrography, diagenesis, and facies controls on porosity in Shannon Sandstone, Hartzog Draw Field, Wyoming. *AAPG Bulletin*, **70**, 56–69.

Riepe, L 1998. Specific internal surface: the 'forgotten?' petrophysical measurement! *Proceeding of the 1998 International Symposium of Society of Core Analysts*, papers, 9540.

Rueslåtten, H., Eidesmo, T., Lehne, K. A & Relling, O. M 1998*a*. The use of NMR spectroscopy to validate NMR logs from deeply buried reservoir sandstones. *Journal of Petroleum Science and Engineering*, **19**, 33–44.

Rueslåtten, H, Eidsemo, T & Slot-Petersen, C 1998*b*. NMR studies of iron-rich sandstone oil reservoir. *Proceeding of the 1998 International Symposium of Society of Core Analysts*, papers, 9821.

Schiøler, P., Andsbjerg, J. *et al.* 2007. *Lithostratigraphy of the Paleocene: Lower Neogene succession of the Danish North Sea*. Geological Survey of Denmark and Greenland, Danish Ministry of the Environment Report **77**.

Slot-Petersen, C., Eidsemo, T., White, J & Rueslatten, H. G 1998. NMR formation evaluation application in a complex low resistivity hydrocarbon reservoir. *Transactions of the SPWLA 39th Annual Logging Symposium*, Paper 1998-TT.

Solymar, M & Fabricius, I. L 1999. Image analysis and estimation of porosity and permeability of Arnager Greensand, Upper Cretaceous, Denmark. *Physics and Chemistry of the Earth Part A-Solid Earth and Geodesy*, **24**, 587–591.

Solymar, M., Fabricius, I. L & Middleton, M 2003. Flow characterization of glauconitic sandstones by integrated Dynamic Neutron Radiography and image analysis of backscattered electron micrographs. *Petroleum Geoscience*, **9**, 175–183.

Stokkendal, J., Friis, H., Svendsen, J. B., Poulsen, M. L. K & Hamberg, L 2009. Predictive permeability variations in a Hermod sand reservoir, Stine Segments, Siri Field, Danish North Sea. *Marine and Petroleum Geology*, **26**, 397–415.

Straley, C., Rossini, D., Vinegar, H., Tutunjian, P & Morriss, C 1997. Core analysis by low-field NMR. *The Log Analyst*, **38**, 84–94.

Tilley, B. J & Longstaffe, F. J 1984. Controls on hydrocarbon accumulation in glauconitic sandstone, Suffield heavy oil sands, southern Alberta. *AAPG Bulletin*, **68**, 1004–1023.

Underwood, E. E 1970. *Quantitative Stereology*. Addison-Wesley, Reading, Massachusetts.

Volokitin, Y., Looyestijn, W. J, Slijkerman, W. F. J & Hofman, J. P 1999. A practical approach to obtain 1st drainage capillary pressure curves from NMR core and log data. *The International Symposium of the Society of Core Analysts*, **24**, 1–4.

Winn, R. D 1994. Shelf Sheet-Sand Reservoir of the Lower Cretaceous Greensand, North Celtic Sea Basin, Offshore Ireland. *AAPG Bulletin*, **78**, 1775–1789.

Xie, R. H., Xiao, L. Z., Wang, Z. D & Dunn, K. J 2008. The influence factors of NMR logging porosity in complex fluid reservoir. *Science in China Series D: Earth Sciences*, **51**, 212–217.

Received 10 February 2010; revised typescript accepted 15 October 2010.

II

Journal paper

Hossain, Z., Fabricius, I.L, Mukerji T. and Jvorkin J. (2011): Rock Physics model of glauconitic greensand from the North Sea. *Geophysics* (submitted revised version).

Published In: SRB Annual Meeting 23-25 June, 2010. Stanford Rock Physics & Borehole Geophusics Project. Annual Report Vol. 121, p. B1-B21. Stanford University, Stanford, CA.

Rock physics model of glauconitic greensand from the North Sea

Zakir Hossain
Technical University of Denmark

Tapan Mukerji
Stanford Center for Reservoir Forecasting

Jack Dvorkin
Stanford Rock Physics Laboratory

Ida L. Fabricius
Technical University of Denmark

Abstract

The objective of this study is to establish a rock-physics model of North Sea Paleogene greensand. The Hertz-Mindlin contact model is widely used to calculate elastic velocities of sandstone as well as to calculate the initial sand-pack modulus of the soft-sand, stiff-sand, and intermediate-stiff-sand models. When mixed minerals in rock are quite different e.g. mixtures of quartz and glauconite in greensand, the Hertz-Mindlin contact model of single type of grain may not be enough to predict elastic velocity. Our approach is first to develop a Hertz-Mindlin contact model for a mixture of quartz and glauconite. Next, we use this Hertz-Mindlin contact model of two types of grains as the initial modulus for a soft-sand model and a stiff-sand model. By using these rock-physics models, we examine the relationship between elastic modulus and porosity in laboratory and logging data and link rock-physics properties to greensand diagenesis. Calculated velocity for mixtures of quartz and glauconite from the Hertz-Mindlin contact model for two types of grains are higher than velocity calculated from the Hertz-Mindlin single mineral model using the effective mineral moduli predicted from the Hill's average. Results of rock-physics modeling and thin section observations indicate that variations in the elastic properties of greensand can be explained by two main diagenetic phases:

silica cementation and berthierine cementation. These diagenetic phases dominate the elastic properties of greensand reservoir. Initially greensand is a mixture of mainly quartz and glauconite; when weakly cemented, it has relatively low elastic modulus and can be modeled by a Hertz-Mindlin contact model of two types of grains. Silica-cemented greensand has a relatively high elastic modulus and can be modeled by an intermediate-stiff-sand or a stiff-sand model. Berthierine cement has different growth patterns in different parts of the greensand, resulting in a soft-sand model and an intermediate-stiff-sand model.

Introduction

Greensands are sandstones composed of a mixture of stiff clastic quartz grains and soft glauconite grains. Glauconite grains are porous and composed of aggregates of iron-bearing clay. Porosity in this sediment is found at two scales: macro-porosity between grains and micro-porosity within grains (Figure 1). Greensand petroleum reservoirs occur world-wide, e.g., the Mid-Cretaceous Safaniya Sandstone Member in Saudi Arabia (Cagatay et al., 1996), the Lower Cretaceous Glauconitic sandstone in Alberta, Canada (Tilley and Longstaffe, 1984), the Upper Cretaceous Shannon sandstone in Wyoming, USA (Ranganathan and Tye, 1986), a Lower Cretaceous Greensand offshore Ireland (Winn, 1994) and a late Paleocene Greensand in central part of the North Sea (Solymar, 2002; Solymar et al., 2003; Hossain et al., 2009; Hossain et al., 2010; Stokkendal et al., 2009). However, evaluation of greensand reservoirs has challenged geologists, engineers and petrophysicsts. Glauconite affects the elastic properties, porosity, and permeability of reservoir rocks (Diaz et al., 2003). Glauconite is also ductile (Ranganathan and Tye, 1986), so it can cause non-elastic deformation of greensand (Hossain et al., 2009) and, hence, can affect reservoir quality. Greensands generally show low resistivity in the reservoir zone due to the large amount of bound water in the glauconite, yet free hydrocarbons can be produced because rather than being pore-filling, glauconite is part of the sand-size grains of the framework (Slot-Petersen et al., 1998).

Rock-physics modeling becomes an integral part of geophysics, petrophysics and geology. Rock-physics modeling helps to establish a quantitative link between sedimentological parameters and elastic properties. The seismic reflections depend on contrasts in elastic properties, rock-physics modeling allows us to link seismic properties to geologic properties. Avseth et al. (2005) showed that rock physics models are particularly useful for testing multiple possible geological scenarios using well logs, and, when integrated with rock texture properties, can be useful for interpreting observed seismic amplitudes away from well control.

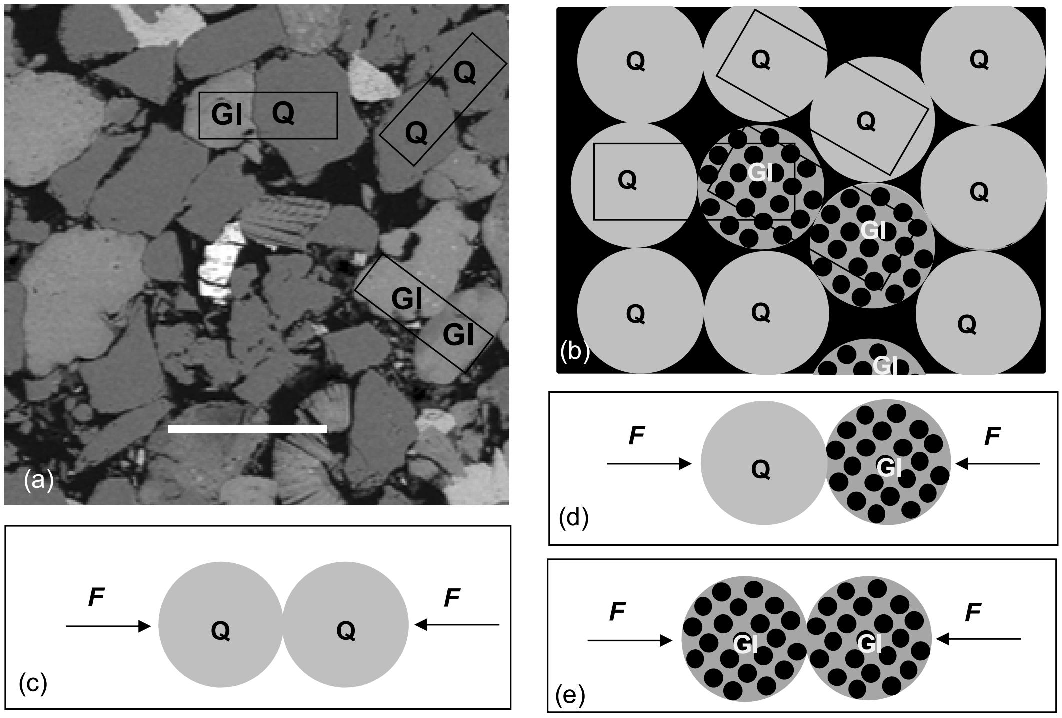

Figure 1. *(a) BSE (Backscattered Electron Micrograph) image of North Sea greensand represents macro-porosity between grains of quartz (Q), and glauconite (Gl). Scale bar for the image is 200 µm. (b) Greensand idealized model. Micro-pores reside within glauconite grains. (c) Schematic representation of Hertz-Mindlin contact model considering quartz and glauconite grains as load bearing, (c) quartz-quartz contacts, (d) quartz-glauconite contacts, and (e) glauconite-glauconite contacts.*

Granular-medium rock-physics models include the Hertz-Mindlin contact model (Mindlin 1949); the Walton model (Watlon 1987); Digby's model (Digby 1981); the model of Jenkins (Jenkins et al. 2005); the model of Johnson (Norris and Johnson 1997); the cemented-sand model (Dvorkin and Nur 1996); the soft-sand model (Dvorkin and Nur, 1996); as well as the stiff-sand and intermediate stiff-sand models (Mavko et al., 2009). Some of the existing granular media models are summarized by Wang and Nur (1992). Commonly used granular-medium models for sandstone are the soft-sand and the stiff-sand models (Dvorkin and Nur, 1996; Mavko et al., 2009). These models are used to infer rock microstructure from elastic modulus-porosity relations. Such techniques are conducted by adjusting an effective-medium theoretical model curve to a trend in the data, assuming that the microstructure of the sediment is similar to that used in the model (Avseth, 2000).

The soft-sand model was introduced by Dvorkin and Nur (1996) for high-porosity sands. The soft-sand model assumes that porosity reduces from the initial sand-pack value due to the deposition of the solid matter away from the grain contacts (Figure 2). The soft-sand model line is represented by the modified lower Hashin-Shtrikman bound (Hashin and Shtrikman, 1963; Dvorkin and Nur, 1996), and connects the sand-pack porosity end-point and the pure mineral end-point. The lower Hashin-Shtrikman bound, which is an iso-stress model for suspensions, is always the elastically softest way to mix multiple mineral phases. In the soft-sand model, the effective moduli of the initial sand-pack are computed by the Hertz-Mindlin contact theory (Mindlin, 1949; Mavko et al., 2009), whereas the elastic moduli at the zero-porosity end member are defined by the elastic moduli of the minerals. The porosity reduction between these points will be a gradual stiffening of the rock, as smaller grains fill the pore-space between the larger grains.

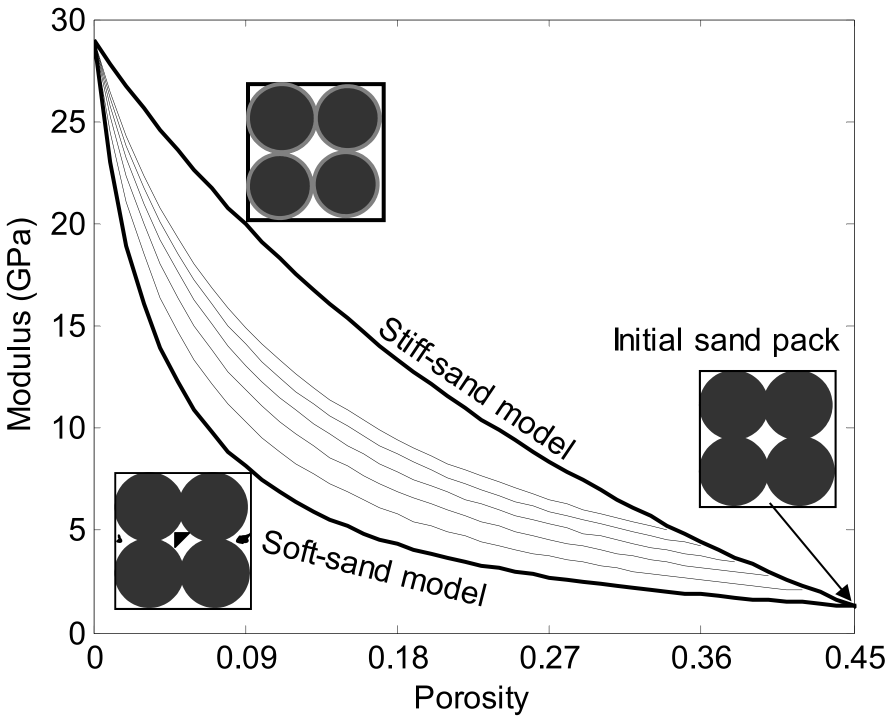

Figure 2. *Illustration of the soft-sand model (modified Hashin-Shtrikman lower bound) and stiff-sand model (modified Hashin-Shtrikman upper bound). The curves between the bounds are the intermediate-stiff-sand model that uses the soft-sand model equation with artificial coordination number.*

A counterpart to the soft-sand model is the stiff-sand model. The stiff-sand model assumes that porosity reduces from the initial sand-pack value due to the deposition of cement at the grain contacts (Figure 2). The stiff-sand model line is represented by the modified upper Hashin-Shtrikman bound (Hashin and Shtrikman, 1963; Mavko et al., 2009), and connects the initial sand-pack porosity end-point and the pure mineral end-point. Like in the soft-sand model, the initial sand-pack modulus of the stiff-sand model is determined by the Hertz-Mindlin theory (Mindlin, 1949), whereas the mineral end-point is defined by the elastic moduli of the minerals. The porosity reduction from the initial sand-pack will stiffen of the rock, as the contacts between the grains grow.

The intermediate-stiff-sand model fills the interval between the stiff-sand and soft-sand model (Mavko et al., 2009). This model uses the function from the soft-sand model, but the high porosity end-point is situated on the stiff-sand model curve (Figure 2). The easiest way to generate these curves is by simply increasing the coordination number of the Hertz-Mindlin theory in the soft-sand model (Mavko et al., 2009). The stiff-sand model explains the theoretically stiffest way to add cement with initial sand-pack, while the soft-sand model explains the theoretically softest way to add pore-filling minerals. However, rocks with very little initial contact cement are not well described by either the stiff-sand or the soft-sand model. In this case, the intermediate-stiff-sand model can be used, because it takes into account the initial cementation effect.

The Hertz-Mindlin contact model (Mindlin 1949) calculates the normal and shear contact stiffnesses of two spherical grains in contact. In this model, grain contacts are first exposed to normal loading, with tangential forces applied afterwards. The effective elastic moduli of the granular assembly are then estimated by taking averages of contact forces corresponding to an assumed distribution of strain over all the contacts (e.g. Walton 1987). Several authors (e.g., Goddard, 1990; Bachrach et al., 2000; Zimmer, 2003; Makse et al., 2004) have explained the discrepancies between measured data and predictions from the Hertz-Mindlin contact model. Makse et al. (2004) found that the relation between coordination number and porosity from molecular dynamics simulations usually predicts a lower coordination number than Murphy's empirical relation (Murphy, 1982). Sain (2010) has shown using granular dynamics simulations that the cause for the discrepancies between measured data and predictions from Hertz-Mindlin contact models are due to heterogeneities in coordination number and stress distributions in the granular pack. To mitigate the overprediction from effective medium models, the modeled effective modulus at the critical porosity is often divided by an ad hoc correction factor, and another ad hoc constant is applied in order to use the frictionless versions of the contact models combined with unrealistically high coordination numbers (Dutta, 2009). DeGennes (1996) suggested that the Hertz model is not valid for granular media. However, Coste and Gilles (1990) have experimentally confirmed the validity of the Hertz single contact model.

Still, the Hertz-Mindlin model appears to be the most commonly used contact model for sandstone. Although the Hertz-Mindlin theory is only applicable to perfect elastic contacts of spherical bodies, it works fairly well for sands (Avseth et al., 2005). This model is used to calculate the initial sand-pack modulus of the soft-sand, stiff-sand, and intermediate-stiff-sand models. For the initial sand-pack for sandstone, it is assumed that only quartz grains are packed together, and the normal and shear stiffness are calculated based on the contact of two quartz grains. For rocks with mixed mineralogy, a homogeneous mineral modulus is assumed, typically derived using Hill's average (Hill, 1952). Then the normal and shear stiffnesses are calculated based on the contact of two average-mineralogy grains. However, this is probably only adequate when the moduli of mixed minerals are quite similar. When the mixed minerals are quite different (such as quartz and glauconite) we may lose some of the predictive value (Avseth et al., 2005).

For greensands, the initial sand-pack is a mixture of quartz and glauconite, and because both of them are load bearing, elastic properties between those of quartz and glauconite are anticipated. To address this, we present a Hertz-Mindlin contact model for mixtures of quartz and glauconite.

The objective of this study is to establish a rock physics model of North Sea Paleogene greensand. In published work, laboratory ultrasonic measurements have been performed in quartz sandstone (Han et al., 1986) and shaly sandstone (Marion, 1990), and various theoretical models have been developed (see overview in Mavko et al., 2009). However, rock-physics models for greensand are not well defined yet. Achieving this objective will improve the understanding and interpretation of seismic signatures of greensand. First, our approach is to develop a Hertz-Mindlin contact model for a mixture of quartz and glauconite grains. Next, we use this Hertz-Mindlin contact model of two types of grains as initial modulus for a soft-sand model and a stiff-sand model. Using these rock-physics models, we explore the effect of microstructure on the elastic properties of greensand.

Elastic properties are controlled by a wide range of factors, including porosity, lithology, pore fluids and pressure. In this study, we superimpose the elastic-modulus–porosity relations of laboratory and logging data on the rock-physics model and finally link the rock-physics properties to greensand diagenesis by thin section analysis.

Contact Model for Mixture of Quartz and Glauconite Grains

We investigate the effective elastic properties of a granular pack of spheres, for which each pair of grains in contact under normal and tangential load determines the fundamental mechanics. Typically in granular media models for unconsolidated sand, all grains are taken to be of the same material. Here we consider the contact deformation of two grains made of two different minerals, quartz and glauconite, each with the same radius *R,* to calculate the effective bulk, and shear modulus for a dry pack. The mineral's effective Young's modulus of quartz and glauconite, $E_{Eff(2)}$ is calculated from the elastic properties of the two minerals as (Johnson, 1985)

$$E_{Eff(QG)} = \left(\frac{1-\nu_q^2}{E_q} + \frac{1-\nu_g^2}{E_g}\right)^{-1}, \tag{1}$$

where ν_q, and E_q are the Poisson's ratio and Young's modulus of quartz, respectively, and ν_g, and E_g are the Poisson's ratio and Young's modulus of glauconite, respectively. The relation between Young's modulus E, Poisson's ratio ν, and the shear modulus μ in an isotropic material is $E = 2\mu(1+\nu)$. By using this relationship, Eqn. 1 can be written as

$$E_{Eff(QG)} = \left(\frac{1-\nu_q}{2\mu_q} + \frac{1-\nu_g}{2\mu_g}\right)^{-1}, \tag{2}$$

where μ_q, and μ_g are the shear moduli of quartz and glauconite, respectively. If the materials of the two grains are the same, the mineral's effective Young's modulus, E_{Eff} is calculated from the elastic properties of this mineral, and then Eqn. 1 can be written as:

$$E_{Eff} = (2\frac{1-\nu^2}{E})^{-1} = \frac{E}{2(1-\nu^2)} = \frac{2\mu\ (1+\nu\ )}{2(1-\nu^2)} = \frac{\mu}{1-\nu}. \tag{3}$$

$$E_{Eff(QQ)} = \frac{\mu_q}{1-\nu_q}, \tag{4}$$

$$E_{Eff(GG)} = \frac{\mu_g}{1-\nu_g}, \tag{5}$$

where $E_{Eff(QQ)}$ is the effective Young's modulus of quartz-quartz contacts, and $E_{Eff(GG)}$ is the effective Young's modulus of glauconite-glauconite contacts. Effective Young's modulus in Eqn. 1 describes the exactly contacts between quartz and glauconite. For unequal mixtures, the effective Young's modulus may be calculated by balancing contacts among quartz-quartz (QQ), quartz-glauconite (QG), and glauconite-glauconite (GG) (Figure 1b). Adding the solid volume fractions of quartz, f_q, and glauconite, f_g, the mineral's effective Young's modulus mixture of quartz and glauconite, $E_{Eff(2)}$ can be written as:

$$E_{Eff(2)} = f_q(f_q \cdot E_{Eff(QQ)} + f_g \cdot E_{Eff(QG)}) + f_g(f_g \cdot E_{Eff(GG)} + f_q \cdot E_{Eff(QG)}) \tag{6}$$

$$E_{Eff(2)} = f_q^{\ 2} \cdot E_{Eff(QQ)} + 2f_g \cdot f_q \cdot E_{Eff(QG)}) + f_g^{\ 2} \cdot E_{Eff(GG)} \tag{7}$$

In the Hertz model of normal compression of the two identical grains, the radius of contact area, *a,* is (Mavko et al., 2009)

$$a = \left[\frac{3FR(1-\nu\ )}{8\mu}\right]^{1/3} = \left[\frac{3FR}{8E_{Eff}}\right]^{1/3}, \tag{8}$$

where F is the compressing force between the two grains. For two different grains, the radius of the resulting Hertzian contact is:

$$a(2) = \left[\frac{3FR}{8E_{Eff(2)}} \right]^{1/3} \qquad (9)$$

If P is the effective pressure applied to a dry pack of grains, the external stress applied to the solid phase is $P/(1-\phi)$, where ϕ is the porosity of the grain pack. Next, because the surface area of each grain is $4\pi R^2$, the total force applied to a single grain is $4\pi R^2 P/(1-\phi)$. This force is distributed among C contacts, where C is the coordination number, which is sometimes related to porosity. Here we take the C-ϕ relation according to Murphy (1982), though other relations, e.g., from granular dynamics simulations, could also be used. If the effective pressure P is applied to a random, identical-sphere packing, the effective force acting between two particles is (Mavko et al., 2009):

$$F = \frac{4\pi R^2 P}{C(1-\phi)}. \qquad (10)$$

If the material only contains one types of grain, the radius of the resulting Hertzian contact is (combining Eqn. 10 and Eqn. 8)

$$a = R\left[\frac{3\pi P}{2C(1-\phi)E_{Eff}} \right]^{1/3}. \qquad (11)$$

Now, by combining Eqn. 9 and Eqn. 11, we find the radius of the resulting Hertzian contact for two types of grains made of different elastic materials:

$$a(2) = R\left[\frac{3\pi P}{2C(1-\phi)E_{Eff(2)}} \right]^{1/3}. \qquad (12)$$

If the material only contains one types of grain, the effective bulk modulus of a dry pack is (Mavko et al., 2009)

$$K_{Eff} = \left[\frac{C^2(1-\phi)^2 \mu_s^{\ 2}}{18\pi^2(1-\nu_s)^2} P\right]^{1/3} = \left[\frac{C^2(1-\phi)^2 E_{Eff}^2}{18\pi^2} P\right]^{1/3}. \quad (13)$$

If the material contains two types of grains, the effective elastic bulk modulus of the dry pack is

$$K_{Eff(2)} = \left[\frac{C^2(1-\phi)^2 E_{Eff(2)}^2}{18\pi^2} P\right]^{1/3}. \quad (14)$$

If the material only contains one types of grain, the effective shear modulus of a dry pack is (Mavko et al., 2009):

$$\mu_{Eff} = \frac{(5-4\nu)}{5(2-\nu)}\left[\frac{3C^2(1-\phi)^2 \mu^{\ 2}}{2\pi^2(1-\nu\ )^2} P\right]^{1/3} = \frac{(5-4\nu)3K_{Eff}}{5(2-\nu)} \quad (15)$$

If the material contain two types of grains, the effective shear modulus of a dry pack is

$$\mu_{Eff(2)} = \frac{(5-4\nu_{Eff})3K_{Eff(2)}}{5(2-\nu_{Eff})}, \quad (16)$$

where, ν_{Eff} is the effective Poisson's ratio of the grain mixture.

A soft-sand model is a heuristically modified Hashin-Shtrikman lower bound. The bulk (K_{Dry}) and shear moduli (G_{Dry}) of such dry sand at porosity ϕ can be calculated (Dvorkin and Nur, 1996) as follows:

$$K_{Dry} = \left[\frac{\phi}{K_{HM} + 4G_{HM}/3} + \frac{1-\phi}{K + 4G_{HM}/3} \right]^{-1} - 4G_{HM}/3 \tag{17}$$

$$G_{Dry} = \left[\frac{\phi}{G_{HM} + z} + \frac{1-\phi}{G + z} \right]^{-1} - z \tag{18}$$

$$z = \frac{G_{HM}}{6} \left[\frac{9K_{HM} + 8G_{HM}}{K_{HM} + 2G_{HM}} \right]. \tag{19}$$

The stiff-sand model (a heuristic modified Hashim-Shtrikman upper bound) is a counterpart to the soft sand model. The bulk (K_{Dry}) and shear (G_{Dry}) moduli of such dry sand at porosity ϕ can be calculated (Mavko et al., 2009) as

$$K_{Dry} = \left[\frac{\phi}{K_{HM} + 4G/3} + \frac{1-\phi}{K + 4G/3} \right]^{-1} - 4G/3 \tag{20}$$

$$G_{Dry} = \left[\frac{\phi}{G_{HM} + z} + \frac{1-\phi}{G + z} \right]^{-1} - z \tag{21}$$

$$z = \frac{G}{6} \left[\frac{9K + 8G}{K + 2G} \right], \tag{22}$$

where K and G are the bulk and shear moduli of grains, respectively; and K_{HM} and μ_{HM} are respectively the effective bulk and shear moduli of the dry grain pack calculated from Hertz-Mindlin theory. For a single type of the grain material, K_{HM} and μ_{HM} are calculated by using Eqn. 13 and Eqn. 15, respectively. For two different types of grains, K_{HM} and μ_{HM} are calculated by using Eqn. 14 and Eqn.16, respectively.

Geological setting of Nini Field and data available

Nini field is located in Siri Canyon, which is part of a larger system of submarine canyons in the Paleocene in the Norwegian-Danish Basin running in the E-W to NE-SW direction towards the Central Graben (Figure 3). The Nini accumulation is defined by a combined structural and stratigraphic trap, the anticlinal structure being induced through salt tectonics. The reservoir consists of sands deposited in the Siri Fairway. The glauconite-bearing sandstone in the Nini field was recognized as the Paleocene greensand. The Paleocene greensand is characterized by thick beds of olive-green to greenish grey, very fine to fine-grained, well-sorted sandstone in which both quartz grains and glauconite pellets are part of the load-bearing matrix. Rounded and translucent quartz grains dominate, but the content of glauconite grains is 20%-30% (Schiøler et al., 2007).

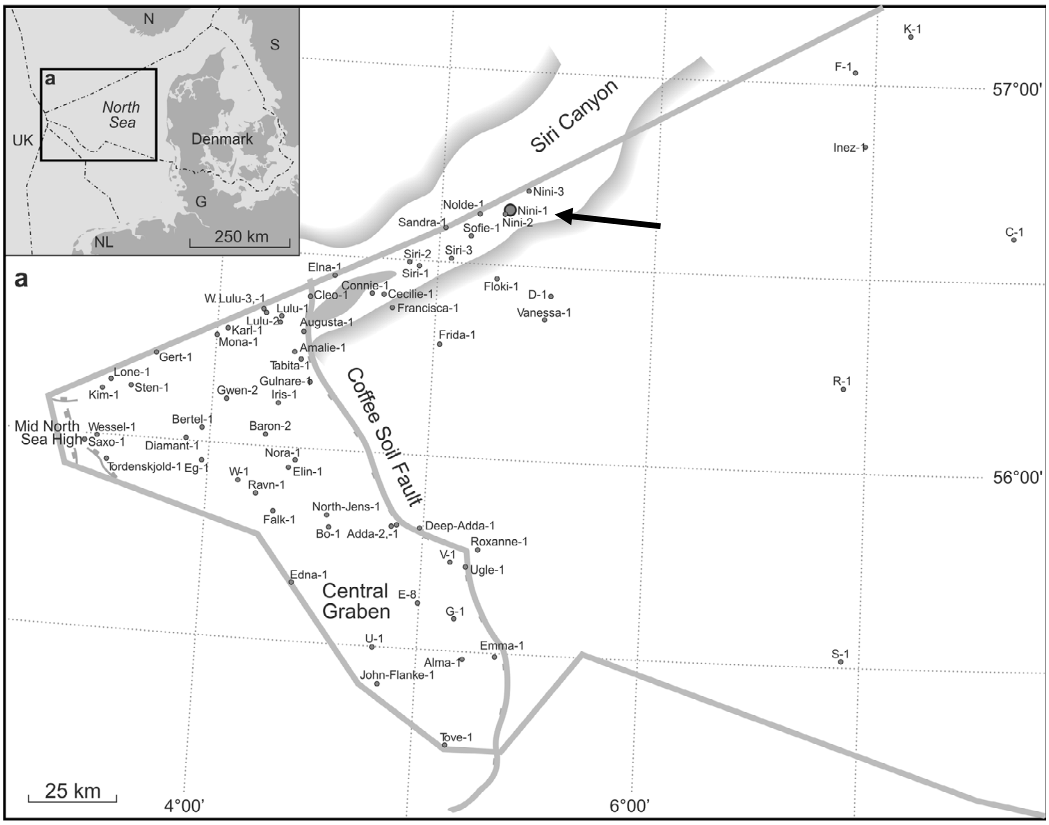

Figure 3. Map showing location of Nini field in the Danish North Sea (arrow). Grey shading on this map indicates the margins of the Siri Canyon; grey shading inside the canyon indicates an area of positive relief within the canyon. Germany (G), Norway (N), Netherlands (NL), Sweden (S), and United Kingdom (UK) (Figure modified after Schiøler et al., 2007).

A series of log data including compressional wave velocity (Vp), shear wave velocity (Vs), and density (ρ), as well as laboratory measured Vp, Vs, ρ, and porosity on sixteen 1.5 inch horizontal core plugs are included in this study. These data represent the two greensand formations of the Nini field. The samples have already been used for routine core analysis and were chosen to cover the range of variation in porosity (25%-40%) and air permeability (60 mD-1000 mD). All cores were cleaned of brine and hydrocarbons by soxhlet extraction with methanol and toluene prior to analysis. Thin sections were prepared from the end of each plug. Backscattered Electron Micrographs (BSE) from thin sections are also available for this study. The mineralogical composition has been determined by point counting of thin sections (Solymar, 2002). We estimate the glauconite grain bulk modulus to be about 7 GPa and shear modulus to be about 5 GPa (Hossain et al., 2010). The effective mineral moduli are then calculated by using the Voigt-Reuss-Hill average (Mavko et al., 2009), and the effective density is calculated using the arithmetic average. The effective bulk modulus is 33 GPa, shear modulus is 29 GPa and density is 2.71 g/cc at 30% glauconite content. The brine and oil properties were computed by using Batzle and Wang's relations (Batzle and Wang, 1992). We calculate the brine bulk modulus and density to be 2.97 GPa and 1.05 g/cc, and the oil bulk modulus and density to be 1.53 GPa and 0.84 g/cc.

The ultrasonic P- and S-wave velocities were measured on all dry samples using the pulse-transmission technique with an approximate center frequency of 132 kHz. The ultrasonic measurements were done at hydrostatic confining pressure with steps from 1 MPa to 15 MPa. The ultrasonic velocities of the samples were calculated from the transit time to travel the sample length. The system delay time was subtracted from the transit time. The system delay time was determined by measuring the transit time on three aluminum plugs of different lengths. The transit times for the P- and S-waves were measured on a digital oscilloscope and saved digitally for a later manual analysis. Using error propagation, the estimated standard deviations, σ are as follows: $\sigma(Vp) < 0.05$ km/s, $\sigma(Vs) < 0.1$ km/s and $\sigma(\rho) < 0.08$ g/cm3. The dry-rock density was calculated from the dry weight and volume of the samples.

We studied the oil- and brine-bearing greensand interval to establish the rock-physics model from the logging data. To correct Vp, Vs, and density for full brine saturation conditions prior to the rock-physics modeling, we applied Gassmann's fluid substitution method (Gassmann, 1951) in the oil-bearing greensand interval by assuming a homogenous mixture of oil and brine.

Hertz-Mindlin modeling for quartz and glauconite

The P- and S-wave velocities calculated by using Hertz-Mindlin contact model for two types of grains are presented in Figure 4. We notice that, in the limit, the Hertz-Mindlin contact model for a single grain type as reported in Mavko et al. (2009) has the same solution as our Hertz-Mindlin model for two types of grains when the fraction of one constituent is 1 and the other is 0 and vice-versa. Calculated velocity for mixtures of quartz and glauconite are higher than velocity predicted from averages of 100% quartz velocity and 100% glauconite velocity. Calculated velocity for mixtures of quartz and glauconite are even higher than velocity calculated from the Hertz-Mindlin contact model for a single grain type by using the effective minerals predicted from Hill's average (Hill, 1952). This demonstrates that the Hertz-Mindlin model with two types of grains may not be approximated by the Hertz-Mindlin single mineral model for a mixture of quartz and glauconite.

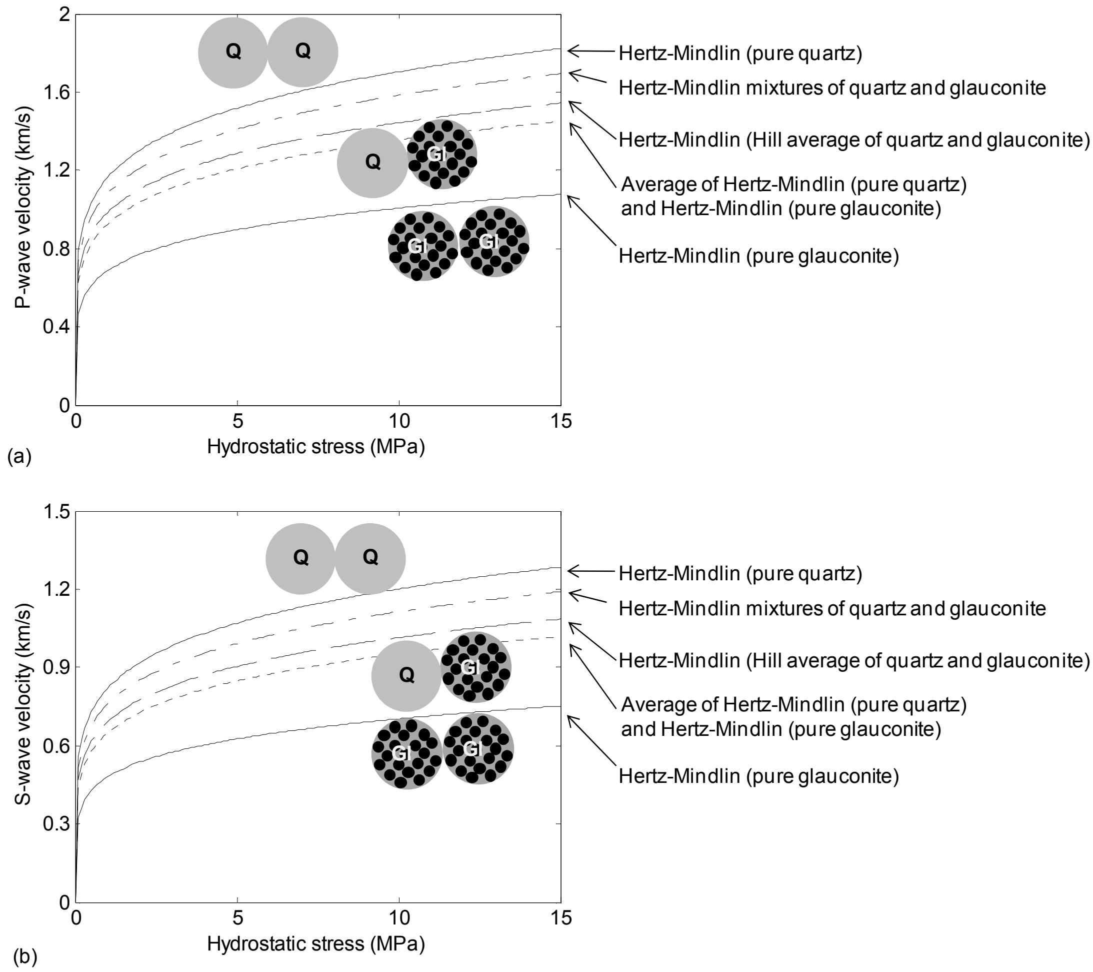

Figure 4. *(a) P-wave and (b) S-wave velocity calculated using Hertz-Mindlin contact model with two types of grains. Upper curves are calculated for a quartz fraction of 1 and glauconite fraction of 0. Lower curves are calculated for a quartz fraction of 0 and glauconite fraction of 1. The middle dotted curves are the average of the upper and lower curves. The middle dash-dot curves are calculated for 70% quartz and 30% glauconite. The middle dashed curves represent the Hill average of minerals to get effective minerals and then the effective minerals used in Hertz-Mindlin single mineral model.*

Next, we verify the Hertz-Mindlin model for two types of grains by laboratory experimental results. Figure 5a represents the experimental results and results from the Hertz-Mindlin model for two types of grains. From the porosity-coordination number relationship given by Murphy (1982) we used coordination number of 8 for this calculation. Thin section analysis shows that this greensand sample is only weakly cemented (Figure 5b). For weakly cemented greensand, the Hertz-Mindlin contact model for two types of grains has good agreement with laboratory measured data.

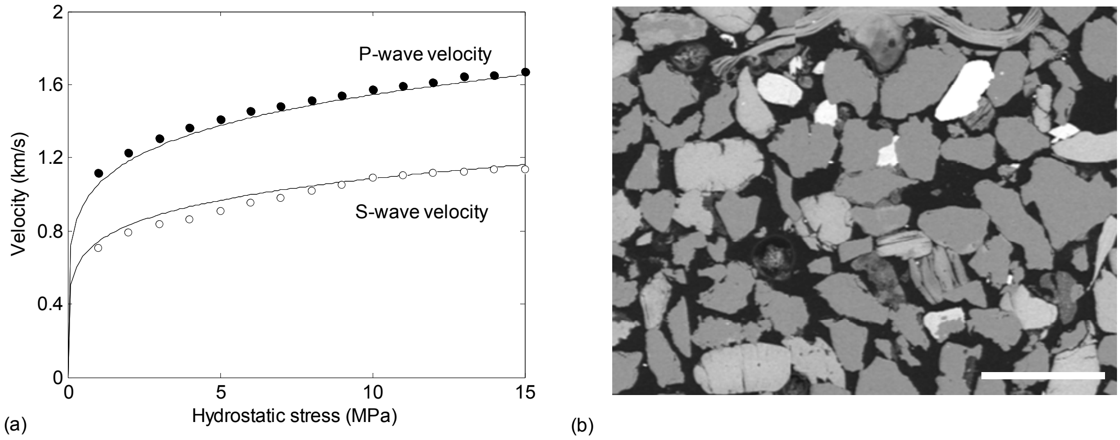

Figure 5. *(a) Laboratory measured P-wave velocity (filled circles) and S-wave velocity (open circles) of a weakly cemented greensand and predicted velocity (solid lines) by using the Hertz-Mindlin contact model of two types of grains for 70% quartz and 30% glauconite. (b) BSE image of weakly cemented greensand sample.*

However, for cemented greensand, the Hertz-Mindlin contact model of two types of grains underestimates the velocity (Figure 6). From the porosity-coordination number relationship given by Murphy (1982), we used a coordination number of 8 for this calculation. Due to cementation of greensand, the area of contacts between grains increase, thus to match velocity prediction with experimental results we artificially increase the coordination number to 18. The Hertz-Mindlin model is designed to describe the properties of precompacted granular rocks (Mavko et al., 2009). Thus one may debate the applicability of the Hertz-Mindlin contact model for cemented samples. The theory behind the model is based on the normal and shear contact stiffness of two spherical grains due to external applied pressure. Cementation of greensand certainly causes a higher contact area. However, when calculating the effective bulk and shear moduli of a dry sphere pack, the coordination number to some degree takes into account the shape of the grains (Avseth et al., 2005). Unconsolidated sand tends to have high porosity and low coordination number, while cemented sand will have lower porosity and high coordination number. Hence, for cemented greensand the experimental results can be fitted by using a higher coordination number as a fitting parameter in the Hertz-Mindlin contact model.Modeling of Laboratory and Log Data

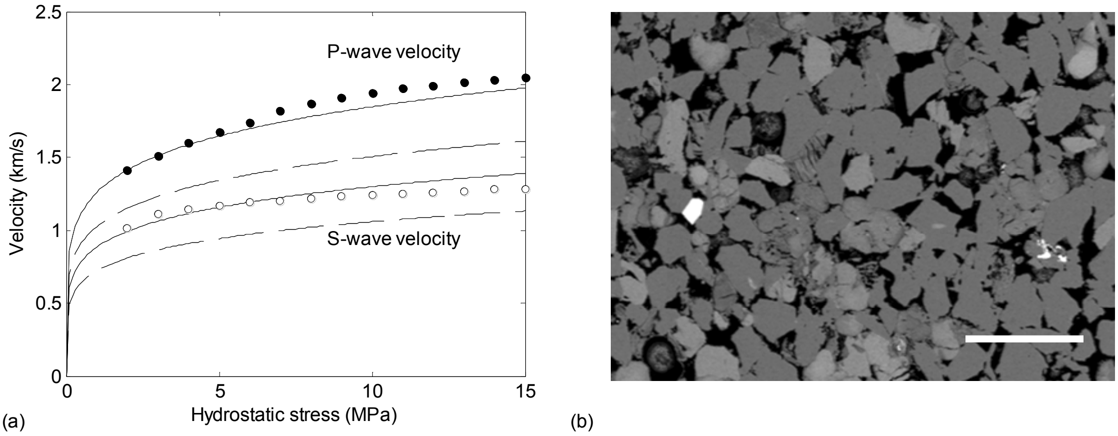

Figure 6. *(a) Laboratory measured P-wave velocity (filled circles) and S-wave velocity (open circles) of a cemented greensand and predicted velocity (solid and dashed lines) by using Hertz-Mindlin contact model of two types of grains for 70% quartz and 30% glauconite. Dashed lines represent calculated velocity using a coordination number of 8. Solid lines represent calculated velocity using an artificial coordination number of 18. (b) BSE image of cemented greensand.*

Modeling of laboratory and log data

We used the Hertz-Mindlin contact model for two types of grains to calculate the initial sand-pack modulus for a soft-sand and a stiff-sand model. The elastic-modulus–porosity cross plots of laboratory and logging data are presented in Figures 7 and 8. To understand the observed elastic modulus difference in greensand, we superimpose the model lines on the elastic-modulus–porosity cross-plot. The rock-physics models shown in Figure 7 for laboratory data imply that these greensand data have two general trends: "berthierine cementation" and "silica cementation." For the compressional modulus, the rock-physics model shown in Figure 7a implies that the greensand has a small initial contact cementation. However, for shear modulus, the rock-physics model shown in Figure 7b implies that the greensand has no initial contact cementation.

For logging data, the rock-physics model curves shown in Figure 8 also imply that the greensand has two general trends: "berthierine cementation" and "silica cementation." The "berthierine cementation" trends in Figure 7 and Figure 8 are likely due to the increasing amount of pore-filling minerals in the pore space between larger grains. These pore-filling minerals have small effect on the elastic modulus but a large effect on the porosity. Hence, the porosity in greensands decreases from initial quartz-glauconite pack porosity due to the increasing amount of pore-filling minerals. The cementation trend goes from the soft-sand model to the stiff-sand model. Cementation has a very strong effect on elastic properties and a weaker effect on porosity.

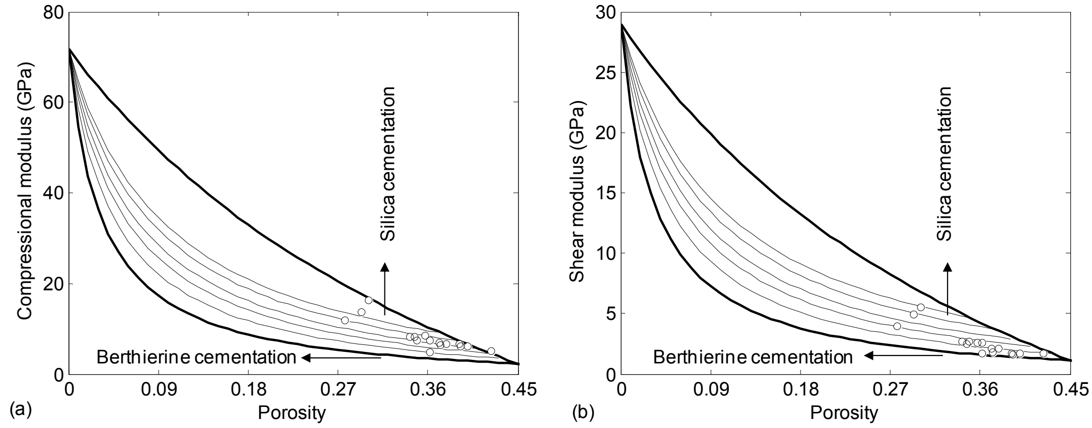

Figure 7. *Modeling of laboratory measured greensand samples, (a) for compressional modulus and (b) for shear modulus. Model curves represent the soft-sand (lower), stiff-sand (upper), and intermediate-stiff-sand (middle) models. "Berthierine cementation" is due to increasing amount of pore filling minerals in the pore space between larger grains. Initial sand-pack modulus of these models was calculated by using the Hertz-Mindlin contact model for two types of grains*

Unlike the laboratory data, the logging data fall into two clusters: one cluster follows the soft-sand model curve, while the other follows the stiff-sand model. Although some data points lie on the intermediate stiff-sand model curves, these data points are few and do not form a cluster.

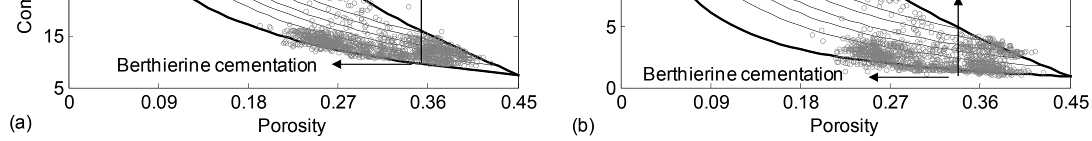

Figure 8. *Modeling of greensand logging data, (a) for compressional modulus and (b) for shear modulus. Model curves are the soft-sand (lower), stiff-sand (upper), and intermediate-stiff-sand (middle) models. "Berthierine cementation" is due to increasing amount of pore filling minerals in the pore space between larger grains. Initial sand-pack modulus of these models was calculated by using the Hertz-Mindlin contact model for two types of grains.*

Silica and pore-filling berthierine cementation

BSE images of sixteen greensand samples from two reservoir formations are used for this study. Petrographic thin section analysis indicates that these Paleocene greensands are well to very well sorted and dominated by quartz grains. However, large volumes of glauconite are present in the samples as well: Greensand from the North Sea Nini field exhibits glauconite volumes in excess of 30% of the total mineral composition, as determined by quantitative analysis of sixteen thin-sections (Solymar, 2002). These results come from point counting on 500-cell grids for each thin-section. Glauconite occurs mainly as grains, but also as glauconitized illite, which is generally strongly expanded and may contain micro-porosity. It can also act as cement, together with the glauconite coating on quartz and feldspar. All greensands are fine–grained, with the average grain size of the detrital quartz between 100 and 200 μm. BSE images of four greensand samples are shown in Figure 9. We observed marked variations in the character of these BSE images: the upper two images (Figure 9a and 9b) show only weak cementation, whereas the two lower images (Figure 9c and 9d) reveal substantial cementation.

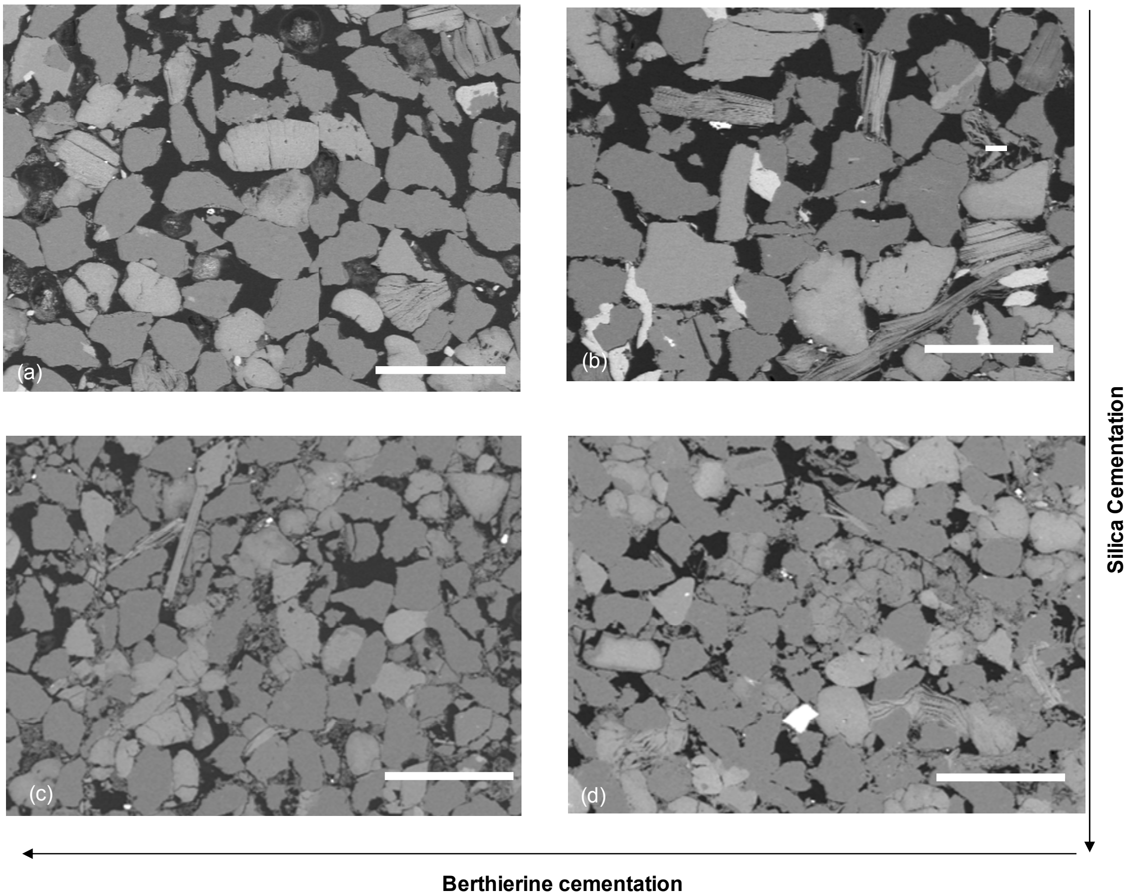

Figure 9. *BSE images of greensand samples show the variation of microcrystalline quartz and berthierine cement. Scale bar for the image is 200 µm. (a) Weakly cemented greensand, with 3.7% pore-filling berthierine, (b) weakly cemented greensand, with 2.2% pore-filling berthierine, (c) Microcrystalline quartz cemented greensand, with pore-filling berthierine of about 8%. (d) Microcrystalline quartz cemented, greensand with pore-filling berthierine of about 4.7%.*

To this end, we can define the two main diagenetic phases in the greensand: silica cementation and berthierine cementation, as illustrated in Figure 10. The silica cement appears in the form of microcrystalline quartz, with crystals about 2 µm in diameter, probably formed as an opal rim on the surface of the grains (Figure 10a). Microcrystalline quartz coating on detrital grains is located at the grain contacts. As a result, this quartz cement acts to stiffen the rock (Stokkendal et al. 2009). Hence, the presence of the microcrystalline quartz cement should have a major effect on the elastic properties of greensand.

The pore-filling berthierine cement is randomly oriented and precipitates in the pores between the large grains (Figure 10b). The main mineralogical difference between these two types of diagenetic phases is in that microcrystalline-quartz–

cemented samples may contain more SiO_2 than berthierine-cemented samples (Stokkendal et al., 2009).

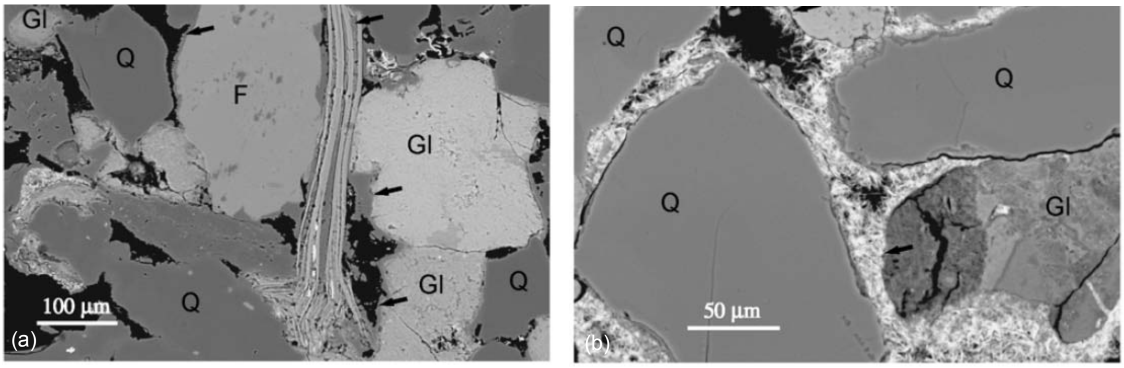

Figure 10. *Micrographs of microcrystalline quartz and berthierine cemented greensand samples. (a) BSE image of silica linings on grains (arrowed). Quartz (Q), glauconite (Gl), and feldspar (F). (b) BSE image of berthierine cemented greensand (arrowed). Quartz (Q) and glauconite (Gl). (Images modified after Stokkendal et al., 2009).*

Our next step is to understand the effects of these pore-filling minerals on the elastic properties and porosity of the rock. Along these lines, we observe a correlation between pore-filling berthierine and total porosity, where total porosity of greensand linearly decreases when the amounts of pore-filling berthierine are increased (Figure 11a). We also observe a correlation between sonic velocity and pore-filling berthierine, where velocity linearly increases when the amounts of pore-filling berthierine are increased (Figure 11b). Hence, this thin-section analysis is consistent with our choice of rock-physics models.

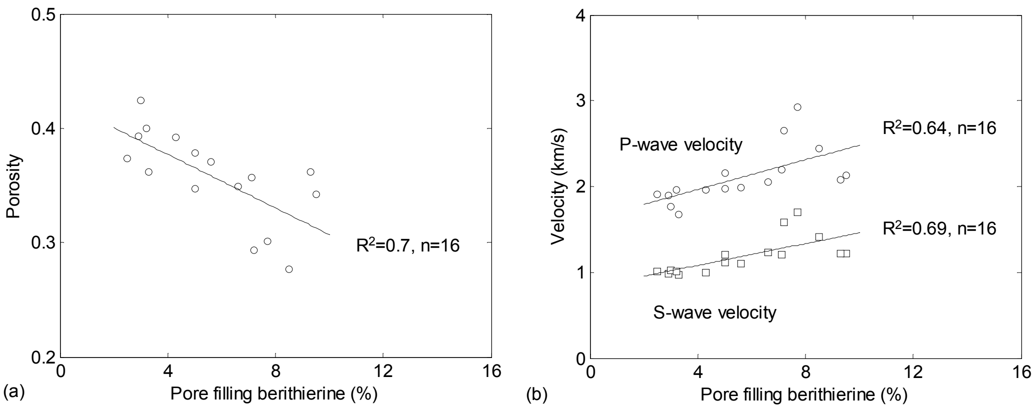

Figure 11. *(a) Correlation between pore-filling berthierine and Helium porosity and (b) correlation between pore-filling berthierine with laboratory measured sonic velocity. Pores-filling berthierine determined by point counting of thin sections, obtained from Solymar (2002).*

Disscusion

We provided a Hertz-Mindlin model for two types of mineral grains. Our modeling results demonstrate that the Hertz-Mindlin model with two types of grains may not be approximated by the Hertz-Mindlin single mineral model. Velocity calculated from the Hertz-Mindlin single mineral model by using effective mineral moduli predicted from the Hill's average (Hill, 1952) of quartz and glauconite are lower than calculated velocity from the Hertz-Mindlin contact model for two types of grains. This is probably due to higher moduli contrasts between quartz and glauconite. So for rocks when mixed minerals are quite different, we may lose some of the predictive value by using the Hertz-Mindlin contact model with single grain type, though a fit to data may be obtained by using an unphysically high coordination number.

We have discussed rock-physics modeling for greensand with emphasis on the effect of pore-filling versus pore-lining cementation. It appears that such texture identification is crucial in the sands under examination: the reservoir zone can produce drastically different seismic responses depending on whether the sands are weakly or strongly cemented. Also, if such textural changes are not properly identified, seismic data may be misinterpreted. Based on laboratory data, log data, and thin section analysis, we present a schematic rock-physics model of the North Sea greensand. This model is subdivided into several parts (Figure 12):

1. Depositional stage: During the deposition of greensand, quartz and glauconite grains are packed together. In clean greensand, where no diagenetic processes have occurred, the elastic properties of greensand can be calculated by using the Hertz-Mindlin contact model for two types of grains (Figure 4).

2.1. Lack of silica cementation: At first the marginal parts of the reservoir may have received a major flux of silica from the Sele Formation located in the Siri Canyon in the North Sea (Stokkendal et al., 2009). The silica flux did not influence all parts of the greensand reservoir. For this reason, during this stage, some of the greensand remained unchanged compared to the depositional stage. Elastic properties of this kind of greensand can be calculated by using Hertz-Mindlin contact model for two types of grains (Figure 5).

2.2. Early silica cementation: The first diagenetic mineral to form in the greensand was probably the silica cement. Silica may have formed as an opal rim so that the opal-derived microcrystalline quartz covers all grains. Microcrystalline quartz derived from the opal coating on detrital grains are found in close contact between grains, so this quartz cement has a stiffening effect on the elastic properties of the greensand. The elastic properties of this type of greensand can be calculated from the Hertz-Mindlin contact model by increasing the artificial coordination number (Figure 6). Elastic properties of this kind of greensand may be modeled by an intermediate-stiff-sand or a stiff-sand model.

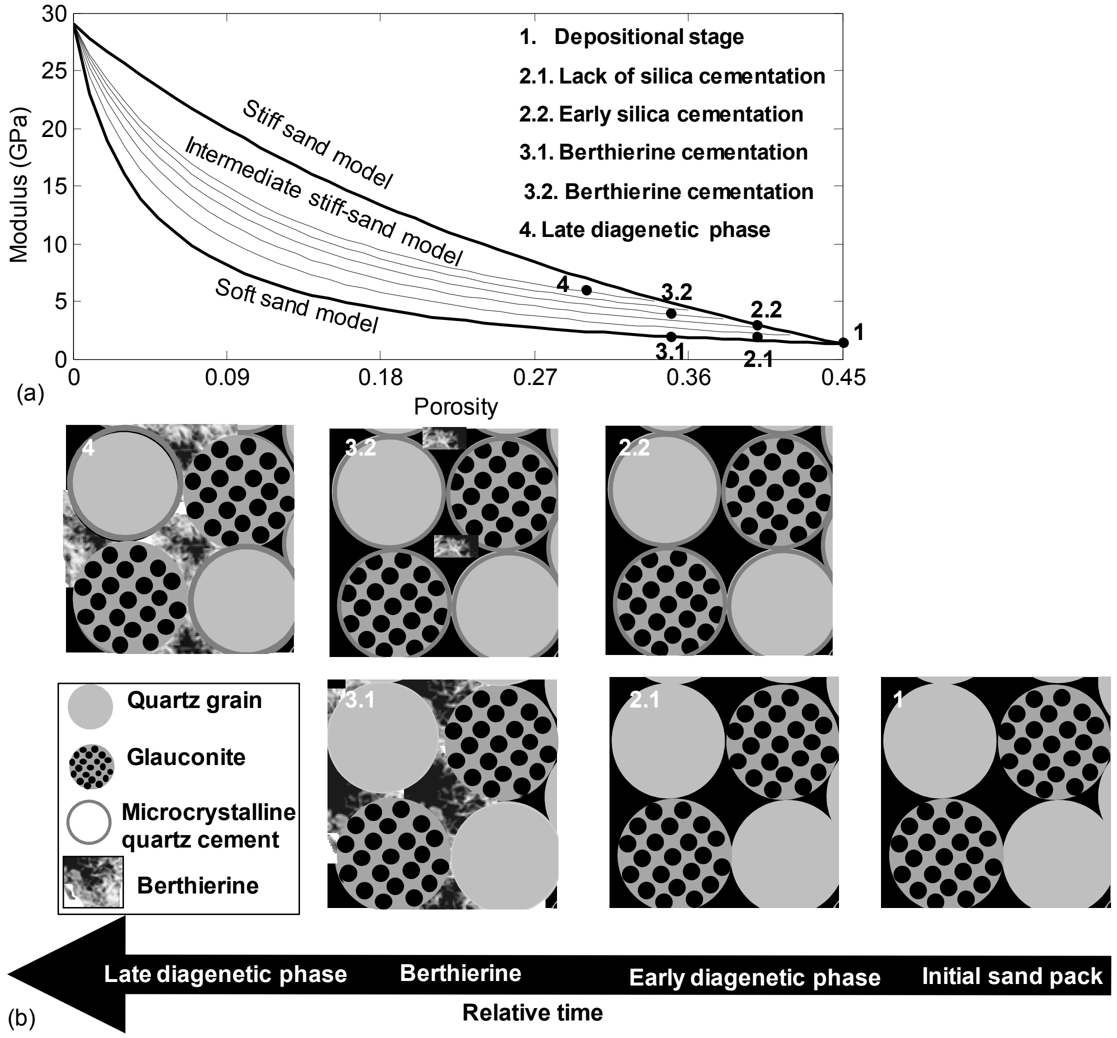

Figure 12. Schematic rock physics model for the North Sea greensand shows the link between rock- physics model and greensand diagenesis.

3.1. Pore-filling berthierine cementation: In the greensand reservoir, where microcrystalline quartz cement is absent, berthierine precipitates between the

grains, so porosity of this kind of greensand decreases from the initial sand-pack porosity. This kind of greensand can be modeled by a soft-sand model.
3.2. Berthierine in early silica-cemented greensand: Berthierine also precipitates in greensand, where microcrystalline quartz cement is present. Berthierine precipitation between the grains causes major porosity reduction. Elastic properties of this kind of greensand may be modeled by an intermediate-stiff-sand or a stiff-sand model.

4. Late diagenetic phase: If berthierine continues its growth in the pore space, the elastic properties of this kind of greensand may be modeled by an intermediate-stiff-sand or a stiff-sand model.

Conclusion

Calculated velocity for mixtures of quartz and glauconite from the Hertz-Mindlin contact model for two types of grains are higher than velocity calculated from the Hertz-Mindlin single mineral model using the effective mineral moduli predicted from the Hill's average.

Results of rock-physics modeling and thin section observations indicate that variations in elastic properties of greensand can be explained by two main diagenetic phases: silica cementation and berthierine cementation. These diagenetic phases dominate in different parts of reservoir bodies.

Initially, greensand is a mixture of quartz and glauconite grains; when weakly cemented, it has relatively low elastic moduli and can be modeled by the Hertz-Mindlin contact model for two types of grains.

Silica-cemented greensand has relatively high elastic moduli and can be modeled by an intermediate-stiff-sand or stiff-sand model.

Berthierine cement has a different growth pattern in the greensand formations, resulting in a soft-sand model and an intermediate-stiff-sand model.

Acknowledgements

We acknowledge the Stanford Rock Physics laboratory and the department of Energy Resources Engineering, Stanford University, for their hospitality in summer, 2009. Gary Mavko (Stanford University) is kindly acknowledged for his discussion on this work. Mikael Solymar is acknowledged for recording the BSE images. DONG Energy A/S is acknowledged for financial support.

References

Avseth, P., 2000, Combining rock physics and sedimentology for seismic reservoir characterization of North Sea turbidite systems: PhD Thesis, Stanford University.

Avseth, P., Mukerji, T. and Mavko, G., 2005, Quantitative seismic interpretation: Applying rock physics tools to reduce interpretation risk: Cambridge University Press.

Bachrach, R., J. Dvorkin, and A. Nur, 2000, Seismic velocities and Poisson's ratio of shallow unconsolidated sands: Geophysics, **65**, 559–564.

Batzle, M. and Wang, Z., 1992, Seismic properties of pore fluids: Geophysics, **57**, 1396-1408.

Cagatay, M. N., Saner, S., Al-Saiyed, I. and Carrigan, W. J., 1996, Diagenesis of the Safaniya Sandstone Member (mid-Cretaceous) in Saudi Arabia: Sedimentary Geology, **105**, 221-239.

Coste, C., and B. Gilles, 1999, On the validity of Hertz contact law for granular material acoustics: European Physical Journal B, **7**, 155–168.

De Gennes, P., 1996, Static compression of a granular medium, The soft shell model: Europhysics Letters, **35**, 145–149.

Diaz, E., Prasad, M., Mavko, G. and Dvorkin, J., 2003, Effect of glauconite on the elastic properties, porosity, and permeability of reservoir rocks: The Leading Edge, **22**, 42-45.

Digby, P. J. 1981. The effective elastic moduli of porous granular rocks. Journal of Applied Mechanics, **48**, 803–808.

Dutta, T., 2009, Integrating sequence stratigraphy and rock-physics to interpret seismic amplitudes and predict reservoir quality: PhD Thesis, Stanford University.

Dvorkin, J., and Nur, A., 1996, Elasticity of High-Porosity Sandstones: Theory for Two North Sea Datasets: Geophysics, **61**, 1363-1370.

Gassmann, F., 1951, Uber die elastizitat poroser medien: Veirteljahrsschrift der Naturforschenden Gesellschaft, **96**, 1–23.

Goddard, J . D., 1990, Nonlinear elasticity and pressure-dependent wave speeds in granular media: Proceedings of the Royal Society of London, Series A, Mathematical and Physical Sciences, **430**, 105–131.

Han, D., 1986, Effects of porosity and clay content on acoustic properties of sandstones and unconsolidated sediments: Ph.D.Thesis, Stanford University.

Hashin, Z., and Shtrikman, S., 1963, A variational approach to the elastic behavior of multiphase materials: Journal of Mechanics and Physics Solids, **11**, 127-140.

Hill, R., 1952, The elastic behavior of crystalline aggregate: Proceeding of the Physical Society of London, **A65**, 349-354.

Hossain, Z., Fabricius, I. L. and Christensen, H. F., 2009, Elastic and nonelastic deformation of greensand: The Leading Edge, **28**, 260-262.

Hossain, Z., Mukerji, T. and Fabricius, I.L., 2010, Vp-Vs relationship of glauconitic greensand: 72nd Annual Conference & Exhibition, EAGE.

Jenkins, J., D. Johnson, L. La Ragione, and Makse, H. 2005. Fluctuations and the effective moduli of an isotropic, random aggregate of identical, frictionless spheres. Journal of the Mechanics and Physics of Solids, **53**, 197–225.

Johnson, K.L., 1985, Contact Mechanics: Cambridge University Press.

Makse, A., N. Gland, D. Johnson, and L. Schwartz, 2004, Granular packings: Nonlinear elasticity, sound propagation, and collective relaxation dynamics Physical Review E, **70**, 061302.

Marion, D., 1990, Acoustical, mechanical and transport properties of sediments and granular materials: Ph.D.Thesis, Stanford University.

Mavko, G., T. Mukerji, and J. Dvorkin, 2009, The rock physics handbook: Cambridge University Press.

Mindlin, R. D., 1949, Compliance of elastic bodies in contact: Journal of Applied Mechanics, **16**, 259–268.

Murphy, W. F., 1982, Effects of microstructure and pore fluids on the acoustic properties of granular sedimentary materials: Ph.D. Thesis, Stanford University.

Norris, A. N., and Johnson, D. L. 1997. Non-linear elasticity of granular media. Journal of Applied Mechanics, **64**, 39–49.

Ranganathan, V. and Tye, R. S., 1986, Petrography, diagenesis, and facies controls on porosity in Shannon Sandstone, Hartzog Draw Field, Wyoming: AAPG Bulletin, **70**, 56-69.

Sain, R., 2010, numerical simulation of pore-scale heterogeneity and its effects on elastic, electrical and transport properties, Ph.D. dissertation, Stanford University.

Schiøler, P., Andsbjerg, J., Clausen, O. R., Dam, G., Dybkjær, K., Hamberg, L., Heilmann-Clausen, C., Johannessen, E. P., Kristensen, L. E. and Prince, I., 2007, Lithostratigraphy of the Paleocene: Lower Neogene succession of the Danish North Sea: Geological Survey of Denmark and Greenland Bulletin, **12**, 77pp.

Slot-Petersen, C., Eidsemo, T., White, J. and Rueslatten, H. G., 1998, NMR formation evaluation application in a complex low resistivity hydrocarbon reservoir: Transactions of the SPWLA 39th Annual Logging Symposium, Paper 1998-TT

Solymar, M., 2002, Influence of composition and pore geometry on immiscible fluid flow through greensand: Ph.D.Thesis, Chalmers University of Technology.

Solymar, M., Fabricus, I.L. and Middleton, M.F., 2003, Flow characterizatiob of glauconitic sandstones by interated Dynamic Neutron Radiagraphy and image analysis of backscattered electron micrographs: Petroleum Geoscience, **9**, 175-183.

Stokkendal, J., Friis, H., Svendsen, J. B., Poulsen, M. L. K. and Hamberg, L., 2009, Predictive permeability variations in a Hermod sand reservoir, Stine Segments, Siri Field, Danish North Sea: Marine and Petroleum Geology, **26**, 397-415.

Tilley, B. J. and Longstaffe, F. J., 1984, Controls on hydrocarbon accumulation in glauconitic sandstone, Suffield heavy oil sands, southern Alberta: AAPG Bulletin, **68**, 1004-1023.

Wang, Z., and Nur, A. 1992. Seismic and acoustic velocities in reservoir rocks, SEG Geophysics Reprint Series **10(2)**.

Walton, K., 1987, The effective elastic moduli of a random pack of spheres: Journal of the Mechanics and Physics of Solids, **35**, 213–226.

Winn, R. D., 1994, Shelf Sheet-Sand Reservoir of the Lower Cretaceous Greensand, North Celtic Sea Basin, Offshore Ireland: AAPG Bulletin, **78**, 1775-1789.

Zimmer, M., 2003, Seismic velocities in unconsolidated sands: Measurements of pressure, sorting, and compaction effects: Ph.D. Thesis, Stanford University.

III

Journal paper

Hossain, Z., Fabricius, I.L and Mukerji T. (2011): *V_p-V_s* relationship and AVO for glauconite bearing sandstone. *Geophysical Prospecting* (in press).

V_p-V_s relationship and AVO for glauconite bearing sandstone

Zakir Hossain
Technical University of Denmark

Tapan Mukerji
Stanford Center for Reservoir Forecasting

Ida L. Fabricius
Technical University of Denmark

Abstract

The relationship between V_p and V_s may be used to predict V_s where only V_p is known. V_p/V_s is also used to identify pore fluids from seismic data and amplitude variation with offset analysis. Theoretical, physical, as well as statistical empirical V_p-V_s relationships have been proposed for reservoir characterization when shear-wave data are not available. In published work, focus is primarily on the V_p-V_s relationship of quartzitic sandstone. In order to broaden the picture we present V_p-V_s relationships of greensand composed of quartz and glauconite by using data from the Paleocene greensand Nini oil field in the North Sea. A V_p-V_s relationship derived from modeling is compared with empirical V_p-V_s regressions from laboratory data as well as from well logging data. The quality of V_s prediction is quantified in terms of the rms error. We find that the V_p-V_s relationship derived from modeling works well for greensand shear-wave velocity prediction. We model seismic response of glauconitic greensand by using laboratory data from the Nini field with the goal of better understanding seismic response for this kind of rock. Our studies show that brine saturated glauconitic greensand may have similar seismic response to oil saturated quartzitic sandstone and that strongly cemented greensand with oil saturation can have similar AVO response to brine saturated weakly cemented greensand.

Keywords: Greensand, glauconite, AVO, velocity analysis

Introduction

Greensands are sandstones composed of a mixture of stiff clastic quartz grains and soft glauconite grains. Glauconite grains are porous aggregates of iron-bearing clay. Porosity in greensand is thus found in two scales: macro-porosity between grains and micro-porosity within grains (Fig. 1). Greensand petroleum reservoirs occur world-wide, e.g. the mid-Cretaceous Safaniya Sandstone Member in Saudi Arabia (Cagatay *et al.* 1996), a Lower Cretaceous Glauconitic sandstone in Alberta, Canada (Tilley and Longstaffe 1984), the Upper Cretaceous Shannon sandstone in Wyoming, USA (Ranganathan and Tye 1986), a lower Cretaceous Greensand offshore Ireland (Winn 1994) and a late Paleocene Greensand in central part of the North Sea (Solymar 2002; Solymar *et al.* 2003; Hossain *et al.* 2009; Stokkendal *et al.* 2009; Hossain *et al.* 2010; Hossain *et al.* 2011). However, evaluation of greensand reservoirs has challenged geologists, engineers and petrophysicists. Glauconite affects the elastic properties, porosity and permeability of reservoir rocks (Diaz *et al.* 2003). Because glauconite is ductile (Ranganathan and Tye 1986) it can cause non-elastic deformation of greensand (Hossain *et al.* 2009) and thus affect the reservoir quality. Greensands have relatively low electrical resistivity in reservoir zones due to the large amount of bound water in the glauconite, yet free hydrocarbons can be produced because glauconite, rather than being pore-filling, is part of the sand size framework grains (Slot-Petersen *et al.* 1998).

The relationship between V_p (compressional wave velocity) and V_s (shear wave velocity) may be used to predict V_s where only V_p is known. V_p/V_s is also used to identify pore fluids from seismic data and AVO (Amplitude Variation with Offset) analysis. Adding S-wave (shear-wave) information to P-wave (compressional-wave) information often allows us to better separate the seismic signature of lithology, pore fluids, and pore pressure. Information on V_s may also provide a strategy for distinguishing between pressure and saturation change in 4D seismic data and can provide the means for obtaining images in gassy sediments where the P-wave is attenuated (Avseth *et al.* 2005). However, when S-wave data are not available or difficult to obtain, V_s is calculated from V_p. Even when S-wave velocity is available, comparison with V_s as predicted from V_p logs can be a useful quality control.

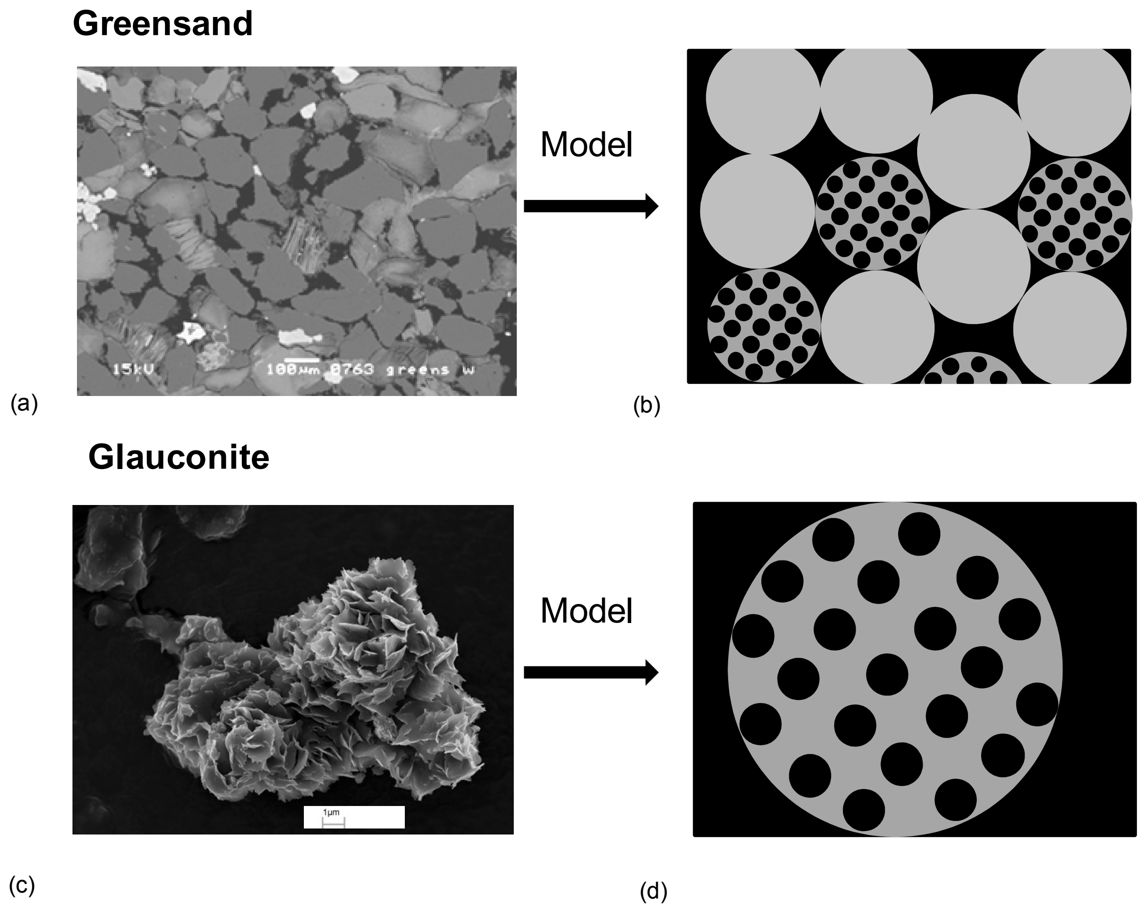

Figure 1. *(a) BSE image of the North Sea greensand and (b) idealized greensand model. (c) Glauconite grain from Arnager greensand (courtesy of Egil Nybakk) and (d) its idealized model. Scale bar for greensand is 100 µm. The image represents macro-porosity, quartz and glauconite grains. Scale bar for glauconite grain is 1 µm. Micro-pores reside within the glauconite grain (Figure modified after Hossain et al. 2009).*

Therefore theoretical, physical, as well as statistical empirical V_p-V_s relationships for estimation of V_s have been developed by several authors e.g. (Castagna *et al.* 1985; Krief *et al.* 1990; Greenberg and Castagna 1992; Han *et al.* 1986; Xu and White 1995, 1996; Vernik *et al.* 2002). The most widely used empirical V_p-V_s relationships was published by Castagna *et al.* (1985) for rock types including sandstone, mudrock, limestone and dolomite. In most practical cases, Castagna's regressions provide us with reasonable results in terms of calculating V_s from the measured V_p for consolidated rocks with P-wave velocities greater than about 2.6 km/s. The relation by Vernik *et al.* (2002) works better for low velocity sandstones. A regression was proposed by Greenberg and Castagna (1992), taking into account complex lithologies. Xu and White (1995) demonstrated a method to determine the V_p-V_s relationship of shaly sandstone by mixing two inclusion models with different aspect ratios, which represent respectively sandstone and shale portions. Jørstad *et al.* (1999) compared the method of Xu and White (1995) to linear regressions using a dataset from the North Sea. They concluded that the inclusion models need to be calibrated well by well, whereas the simple regression tuned to the target wells provide good prediction of V_s from the measured V_p. However, there is no systematic explanation why a linear regression works well in most cases. Tsuneyama (2005) presented theoretical assessments of the validity of several known regressions by using effective medium theory and discussed how one should consider modifying the known relationship depending on the character of the target rock.

AVO modeling is an important step in multidisciplinary integration of petrophysics, rock physics, seismic data, geology and petroleum engineering as AVO interpretation provides information about reservoir characteristics and reduces risk in hydrocarbon exploration (Li and Xue 2007). Using AVO technique one can physically explain the seismic amplitudes in terms of rock physics (Avseth *et al.* 2005). The main objective for AVO analysis is to predict lithology and pore fluid from seismic data (Castagna 1993; Castagna and Smith 1994; Castagna *et al.* 1998). However, lithology and pore fluid are not the only factors affecting the AVO. Due to a variety factors affecting the amplitudes, the extraction of correct reflection coefficient from seismic interface may not a simple procedure (Norris and Evans 1993). Therefore, AVO modeling is used to examine the potential use of AVO. Avseth *et al.* (2005) pointed out that in many cases AVO has been applied without success and that lack of V_s information and the use of a too simple geological model are some of the common reasons for failure. Therefore, it is necessary to improve the physical understanding of seismic information before using it for reservoir characterization. Avseth (2000) described that lithology has significant impact on AVO response which may mask or induce AVO anomalies. Therefore before interpreting fluid content from AVO analysis, it is necessary to know what type of rock is expected for a given prospect, and how much one expects the rock to change locally due to textural changes. Thus during AVO analysis it is critical to understand the seismic properties of greensand based on local geology and petrophysical properties. Rock properties and AVO reflectivity models could be the tools used to understand the seismic properties of greensand before pre-processing, inversion and interpretation of pre-stack data.

The objectives of our study are to predict the velocity of the elastic shear wave (V_s) from velocity of the elastic compressional wave (V_p) and to investigate the AVO response of greensand. In published work, focus is primarily on the V_p- V_s relationship and AVO analysis of quartzitic sandstone. However, the V_p- V_s relationship of greensand has not yet been well defined. Furthermore, the elastic moduli of micro-porous glauconite grains and their effect on the V_p-V_s relationship are also unknown. Thus we study V_p-V_s relationships of glauconitic greensand by using log and laboratory data from the Paleocene greensand Nini oil field in the North Sea. We also model AVO response of these glauconitic greensands with the goal of better understanding AVO behavior for this kind of rock.

Geological setting of Nini-1 Field

The Nini field is located in Siri Canyon which is part of a larger system of submarine canyons in the Paleocene in the Norwegian-Danish Basin running in an E-W to NE-SW direction towards the Central Graben (Fig. 2). The Nini accumulation is defined by a combined structural and stratigraphic trap, the anticlinal structure being induced through salt tectonics. The reservoir consists of sands deposited in the Siri Fairway (Stokkendal *et al.* 2009).

The Paleocene greensand of Nini field is characterized by thick beds of olive-green to greenish grey, very fine to fine grained and well sorted sandstone in which both quartz grains and glauconite grains are part of the load-bearing matrix. Quartz grains dominate, with the content of glauconite grains being about 20%-30%. (Schiøler *et al.* 2007).

The two main greensand formation of the Nini field are the Hermod Formation and the Ty Formation. Petrographic studies by Solymar (2002) show that samples from Hermod Formation contain glauconite grains of size between 100 and 200 µm, with some glauconite grains even larger (300 to 400 µm) . Samples from Ty Formation contain glauconite grains of size between 100 and 150 µm, although some glauconite grains are larger (200 to 300 µm). The grains are subangular to subrounded for both formations. However, the main difference between the two formations is that Hermod Formation is only weakly cemented, whereas samples from Ty formation contain cement of berthierine and microcrystalline quartz.

Method

A series of log data including V_p, V_s, and density as well as laboratory V_p, V_s, density, and porosity data of sixteen one and half inch horizontal core plugs are included in this study. The data represent the two greensand formations of the Nini field. The samples had already been used for routine core analysis and were chosen so as to cover the range of variation in porosity (25%-40%) and air permeability (60 mD-1000 mD). All cores were cleaned from brine and hydrocarbons by soxhlet extraction with methanol and toluene prior to analysis. Thin sections had been prepared from the end of each plug. Backscattered Electron Micrographs (BSE) from thin sections are also available for this study. Mineralogical composition has been determined from X-ray diffractiometry and from point counting of thin sections (Solymar 2002). The moduli of each mineral used in our modeling are shown in Table 1. The effective mineral moduli are then calculated using Voigt-Reuss-Hill average (Mavko *et al.* 2009), and the effective grain density is calculated using arithmetic average. Calculated effective mineral bulk modulus is 33 GPa, shear modulus is 29 GPa and mineral density is 2.71 g/cm^3. The brine and oil properties were calculated by using the Batzle and Wang's relations as cited in Mavko *et al.* (2009).

Laboratory Vp-Vs measurement

Ultrasonic P-and S-wave velocities (V_p and V_s) were measured on all brine saturated samples by using the pulse transmission technique with an approximate centre frequency of 132 kHz. The ultrasonic measurements were done at a hydrostatic confining pressure with steps from 1 to 12 MPa. The ultrasonic velocity of the samples was calculated from the transit time through the sample length, where the system delay time was subtracted from the transit time. The system delay time was determined by measuring the transit time on three aluminum plugs of different lengths. Transit times for P- and S-waves were measured on a digital oscilloscope and saved digitally for later manual analysis. Saturated density (ρ) was calculated from saturated weight and volume of the samples. Using error propagation, the estimated standard deviations, σ are as follows: $\sigma(V_p)<50$ m/s, $\sigma(V_s)<100$ m/s and $\sigma(\rho)<0.08$ g/cm^3.

Vp-Vs regression from log data

We derived a V_p-V_s regression from well log data of the oil and brine bearing greensand intervals in the Nini field. We recalculated both V_p and V_s to brine saturated condition using Gassmann's equations before estimating a V_p- V_s regression. We used Archie's equation (Archie 1942) to calculate water saturation (S_w) from the deep resistivity log data:

$$S_w^n = \frac{a}{\phi^m} \frac{R_w}{R_t} \tag{1}$$

where R_t is the true resistivity, R_w is formation brine resistivity, S_w is water saturation, ϕ is porosity, the a factor corrects for clay and other conducting minerals, m is the cementation factor and n is the saturation exponent. In our procedure for calculating water saturation, we applied a=1.67, m=1.81, n=2.4, and R_w =0.077 Ωm. Porosity was calculated from the density log. We determined a and m based on laboratory data for sixteen greensand samples, whereas n was measured on two greensand samples (Appendix A1).

Once the saturation was calculated, we applied Gassmann's fluid substitution equations (Gassmann 1951) to calculate the brine saturated P-and S-wave velocity. Bulk modulus and density of the pore-fluid mixtures in partially saturated rock were calculated by using Reuss model and arithmetic average respectively:

$$\frac{1}{K_f} = \frac{S_o}{K_o} + \frac{S_w}{K_w} \tag{2}$$

$$\rho_f = \rho_o S_o + \rho_w S_w \tag{3}$$

where K_f, K_w, K_o are the bulk moduli of fluid, brine and oil and ρ_f, ρ_w, ρ_o are the corresponding densities. S_o denotes the saturation of oil. Parameters used for this procedure are summarized in Table1.

__Table 1.__ Mineral and fluid properties. Mineralogical composition was determined from XRD and point counting of thin sections. Micro-porous glauconite grain modulus was modeled by using effective medium theory. The brine and oil properties are calculated from the empirical relationship of Batzle and Wang (1992) as cited by Mavko et al. (2009), assuming in situ conditions.

		Composition (% Wt.)	Bulk modulus (GPa)	Shear modulus (GPa)	Density (g/cm^3)	Reference
Minerals	Quartz	56±6	36.6	45	2.65	Citation in Mavko *et al.* (2009)
	Glauconite	30±5	15	10	2.71	Diaz *et al.* (2002)
	Feldspar	3±1	75.6	25.6	2.63	Citation in Mavko *et al.* (2009)
	Micas	2±1	61.5	41.1	2.79	Citation in Mavko *et al.* (2009)
	Pryrite	2±1	147.4	132.5	4.93	Citation in Mavko *et al.* (2009)
	Pore filling minerals	7±3	95.3	45	2.65	Katahara (1996)
Grains	Glauconite		7	5	2.01	
Fluids	Brine		2.97	0	1.05	
	Oil		1.53	0	0.84	
	air		0.000014	0	0.12	

Modeling of a porous glauconite grain

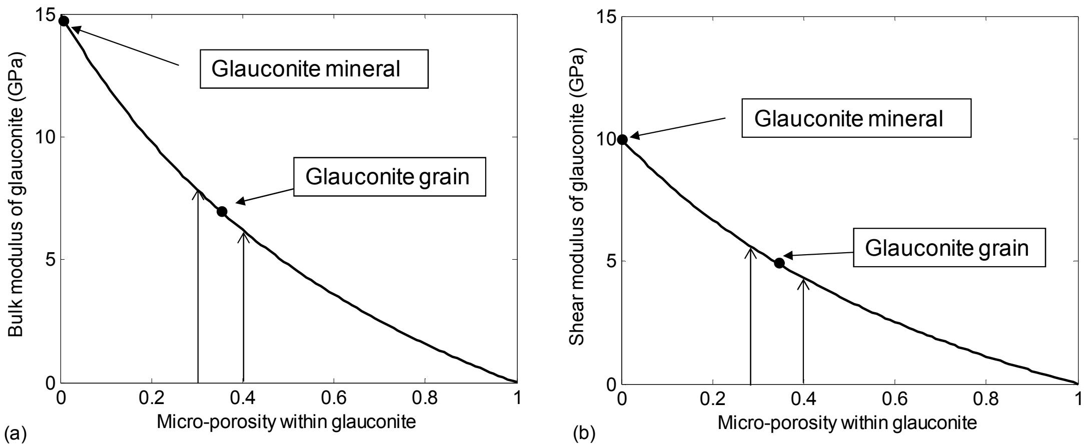

Figure 3. *Effective medium modeling of micro-porous glauconite. (a) Bulk modulus and (b) shear modulus of glauconite grain as function of micro-porosity within glauconite by using Hashin-Shtrikman (HS) upper bound. Micro-porosity within glauconite ranges from 30% to 40% for 16 greensand samples and this information was applied to determine the bulk and shear modulus of a micro-porous glauconite grain. Glauconite mineral bulk modulus (15 GPa) and shear (10 GPa) was obtained from Diaz et al. (2002).*

Bulk modulus (15 GPa) and shear modulus (10 GPa) of the glauconite mineral are reported by Diaz *et al.* (2002). Because glauconite grains are micro-porous, we need to calculate the glauconite grain modulus, which is different from the solid glauconite mineral modulus. For this purpose we applied the Hashin-Shtrikman (HS) upper bound (Hashin and Shtrikman, 1963) for mixtures of glauconite mineral and the micro-porosity within glauconite grains. Micro-porosity was calculated as the differences between Helium porosity and image porosity as determined by image analysis method. Porosity of glauconite grains was determined as micro-porosity divided by the amount of glauconite grains as determined by image analysis of petrographic thin sections (Solymar, 2002). Micro-porosity within glauconite varies from 30% to 40% for the 16 greensand samples. By applying these micro-porosities to the HS upper bound, we estimated the glauconite grain bulk modulus to be about 7 GPa and shear modulus to be about 5 GPa (Fig. 3).

Modeling of Vp-Vs relationship

We investigated V_p-V_s relationships empirically as well as by effective medium models and bounds. The Hashin-Shtrikman bounds (Hashin and Shtrikman 1963) describe the narrowest possible range for an isotropic, linear elastic composite, when only the volume fractions are known. Tighter bounds exist when volume fractions and spatial correlations are known. The Hashin-Shtrikman bounds give us the upper and lower limits of the data distribution for bulk and shear moduli as a function of the volume fractions of mixing materials (Appendix A2). These bounds are narrower than those defined by the Reuss lower bound and the Voigt upper bound (Mavko *et al*. 2009). The Reuss bound is the harmonic average of the elastic moduli of individual components of a composite, while the Voigt bound is the arithmetic average. Consider greensand whose grains are mainly quartz and micro-porous glauconite. The V_p and V_s of this quartz and glauconite mixture according to Hashin-Shtrikman and Voigt-Reuss elastic bounds are plotted in Fig. 4. Elastic moduli applied for these bounds are listed in Table 1.

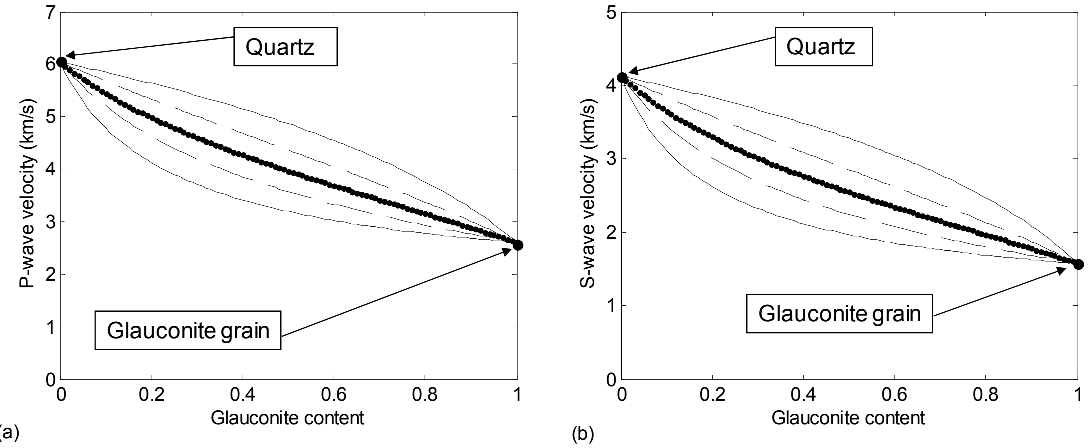

Figure 4. *Plots of solid grain elastic wave velocity of quartz-glauconite mixtures (a) P-wave velocity and (b) S-wave velocity as a function of glauconite fraction. In each figure, the outer two curves represent the Voigt and Reuss Bounds (citation in Mavko et al. 2009). The dashed curves are Hashin-Shtrikman bounds (Hashin and Shtrikman 1963). The dotted curve in the middle is calculated from Hill's average (Hill 1952).*

The separation between upper and lower bound depends on how elastically different the constituents are. The elastic bounds are far apart from each other and from Hill's average (Hill 1952) because of the large elastic contrast between quartz and glauconite grains (Fig. 4). This implies that the effect of micro-porous glauconite may be critical for seismic greensand interpretation.

Next we calculated the effective minerals moduli of greensand by using the Voigt-Reuss-Hill average (Mavko *et al.* 2009), and the effective density is calculated using the arithmetic average. Greensand from the North Sea Nini field has glauconite content around 30%, as determined by petrographic thin sections analysis. Thus by considering 70% quartz and 30% glauconite, we can determine the effective mineral modulus of greensand. So in Fig. 5, glauconite point corresponds to the micro-porous glauconite grain and greensand point corresponds to the effective minerals of quartz and micro-porous glauconite at zero macro-porosity.

Having obtained the mineral modulus of greensand, we constructed Hashin-Shtrikman bounds for greensand-brine and quartz-brine in the V_p -porosity plane, in the V_s-porosity plane, and V_p-V_s plane (Fig. 5). The Iso-frame (IF) model by Fabricius (2003) is based on Hashin-Shtrikman bounds (Hashin and Shtrikman 1963), and describes the rock as composed of solids partly in suspension and partly in the frame (Appendix A2). We derived V_p -V_s relationship of greensand by using Hashin-Shtrikman bounds and the Iso-frame model. We made Iso-frame curves under assumption of a critical porosity of 100% for mixtures of greensand-brine in the velocity-porosity plane and in the V_p-V_s plane. For simplicity of IF modeling, we assumed a critical of 100% (Fabricius *et al.* 2007). To obtain a V_p-V_s relationship from the Iso-frame model, that would be independent of the Iso-frame parameter, we regress all the points of Iso-frame curves in the V_p-V_s plane to derive a linear equation of V_s as a function of V_p (Fig. 5c):

$$Vs = 0.95Vp - 1.27 \text{ (km/s)} \tag{4}$$

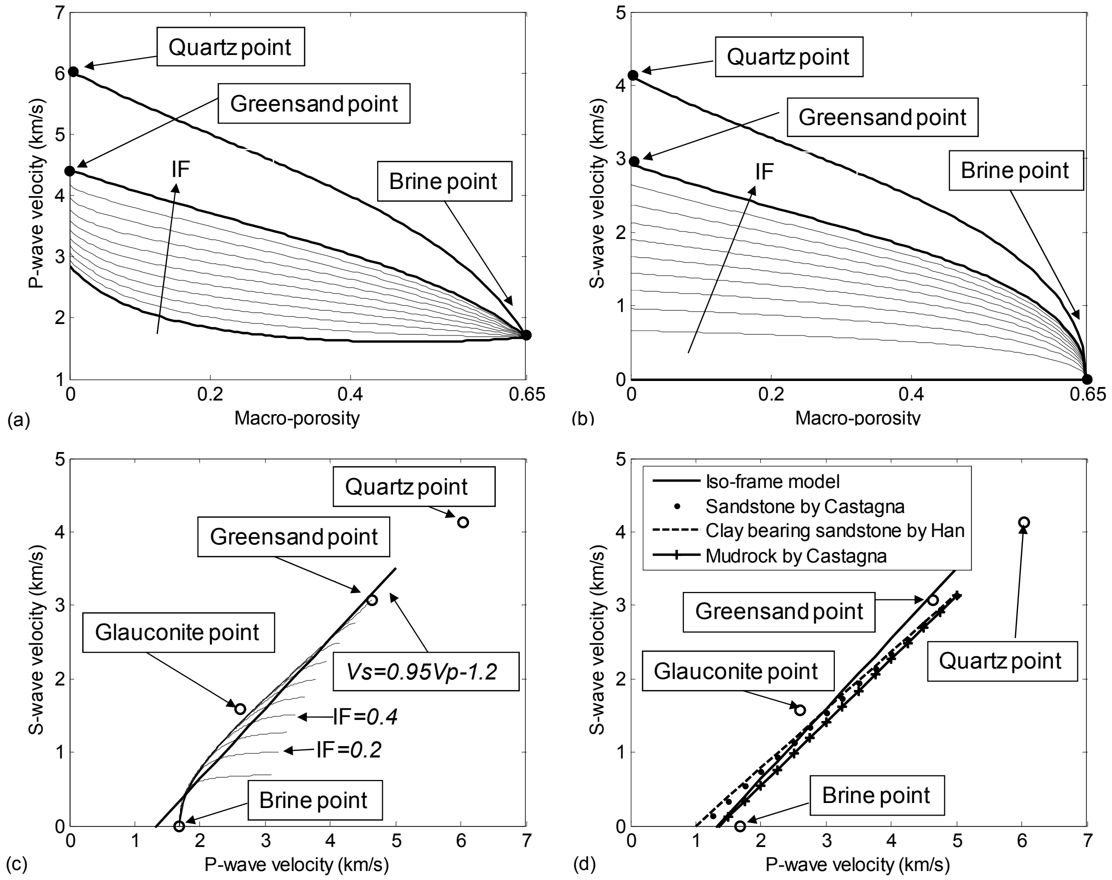

Figure 5. *Hashin-Shtrikman bounds and Iso-frame (IF) curves for greensand (a) in the V_p-porosity plane, (b) in the V_s-porosity plane, (c) in the V_p-V_s plane. Greensand moduli were calculated by using Hill's average for mixture of 70% quartz and 30% glauconite grain. The quartz point, greensand point, glauconite grain point, and brine point are shown for reference. A linear V_p-V_s regression for greensand was derived from all points of the IF curves in the V_p-V_s plane. (d) Comparison among the V_p-V_s relations derived from Iso-frame model, sandstone and mudrock by Castagna et al. (1985) and clay bearing sandstone by Han et al. (1986).*

We also used the empirical V_p-V_s relationship for sandstone offered by Castagna *et al.* (1985):

$$Vs = 0.80Vp - 0.86 \text{ (km/s)} \qquad (5)$$

and the mudrock line of Castagna *et al.* (1985), which was derived from in situ data:

$$Vs = 0.86Vp - 1.17 \text{ (km/s)} \qquad (6)$$

and the empirical relationship of Han *et al.* (1986) based on ultrasonic laboratory measurements for clay bearing sandstone:

$$Vs = 0.79Vp - 0.79 \text{ (km/s)} \qquad (7)$$

Fig. 5d shows a comparison of the above V_p-V_s relations. Derived V_p-V_s relation from Iso-frame model for greensand is slightly different from V_p-V_s relations presented by Han *et al.* (1986) and Castagna *et al.* (1985). Castagna *et al.* (1985) pointed out that for a clay bearing sandstone, the V_p-V_s trend is controlled in part by the location of the clay point relative to a line joining the quartz point. They also noted that P-wave and S-wave velocities decrease in a nearly linear fashion as the water point is approached; similarly, as quartz is added to clay, velocities increase in a nearly linear fashion as the quartz point is approached. Greensand is composed of a mixture of quartz and glauconite grains, rather than quartz and clay particles, thus the mineral point of greensand should be between the glauconite grain point and the quartz point. As porosity for greensand approaches the micro-porosity, the velocity must approach the value for greensand grains, instead of the pure quartz point (Fig. 5d).

Results and discussion

V_p-V_s relationship from laboratory measured data

Fig. 6 shows V_s versus V_p plot of laboratory measured dry and brine saturated greensand samples (Table 2). From these data an empirical V_p-V_s regression of laboratory measured dry greensand can be approximated by the least-square linear fit:

$$Vs = 0.65Vp - 0.05 \text{ (km/s)} \qquad (8)$$

***Table 2.** Laboratory measured V_p, V_s in km/s and bulk density on saturated greensand samples.*

Sample	Brine saturation	Density g/cm^3	1 MPa V_p(km/s)	1 MPa V_s(km/s)	3 MPa V_p(km/s)	3 MPa V_s(km/s)	7 MPa V_p(km/s)	7 MPa V_s(km/s)	12 MPa V_p(km/s)	12 MPa V_s(km/s)
1-4	0.97	2.13	1.98	0.75	2.15	0.86	2.25	0.93	2.25	0.93
1-6	0.98	2.08	2.50	1.20	2.80	1.42	2.95	1.49	3.04	1.54
1-7	1.00	2.04	2.42	1.13	2.57	1.20	2.68	1.33	2.77	1.38
1-18	1.00	1.95	2.31	0.95	2.43	1.04	2.50	1.08	2.57	1.11
1-25	0.99	2.08	2.35	0.97	2.55	1.11	2.63	1.14	2.69	1.19
1-27	0.98	1.98	2.40	0.87	2.53	1.00	2.55	1.03	2.58	1.04
1-32	0.98	2.07	2.17	0.95	2.23	0.99	2.25	1.02	2.38	1.03
1-137	1.04	2.05	2.07	0.86	2.35	0.94	2.51	1.06	2.63	1.15
1-139	1.00	2.11	1.94	0.80	2.15	1.00	2.24	1.02	2.24	1.02
1-141	0.99	2.20	1.90	0.71	2.08	0.91	2.18	1.00	2.18	1.00
1-153	0.96	2.00	2.18	0.80	2.35	0.86	2.40	0.87	2.60	1.02
1A-141	0.98	2.20	2.90	1.43	3.13	1.61	3.18	1.66	3.18	1.66
1A-142	0.99	2.21	3.01	1.47	3.25	1.68	3.36	1.77	3.36	1.77
1A-152	0.98	2.22	2.85	1.47	2.94	1.48	3.05	1.63	3.19	1.74
1A-182	0.99	2.12	2.25	0.85	2.33	0.91	2.43	0.99	2.53	1.07
1A-183	0.98	2.10	1.95	0.81	2.17	0.92	2.33	1.00	2.39	1.04

Whereas an empirical V_p-V_s regression of laboratory measured brine saturated greensand can be approximated by the least-square linear fit:

$$Vs = 0.76Vp - 0.76 \text{ (km/s)} \qquad (9)$$

We observe that all data fall along a narrow trend, in spite of variation in porosity, variation in greensand cementation and confining pressure ranging from 1 to 12 MPa (Fig. 6a,b). However, the dry greensand data are more scattered than brine saturated greensand data. We know porosity tends to decrease velocity; clay also tends to lower velocity and confining pressure tends to increase velocity. However, from Han *et al.* (1986) data discussed in Avseth *et al.* (2005) we know that for clay bearing sandstone, porosity, clay and confining pressure act approximately similarly on V_p and V_s so that the data stay tightly clustered within the same V_p-V_s trend. Greensand data at individual stress levels can also be approximated by the least-square linear equation (8) (Fig. 6). These results indicate that the confining pressure act similarly on both V_p and V_s and that there is no hydrostatic stress effect on the V_p-V_s relationship of greensand.

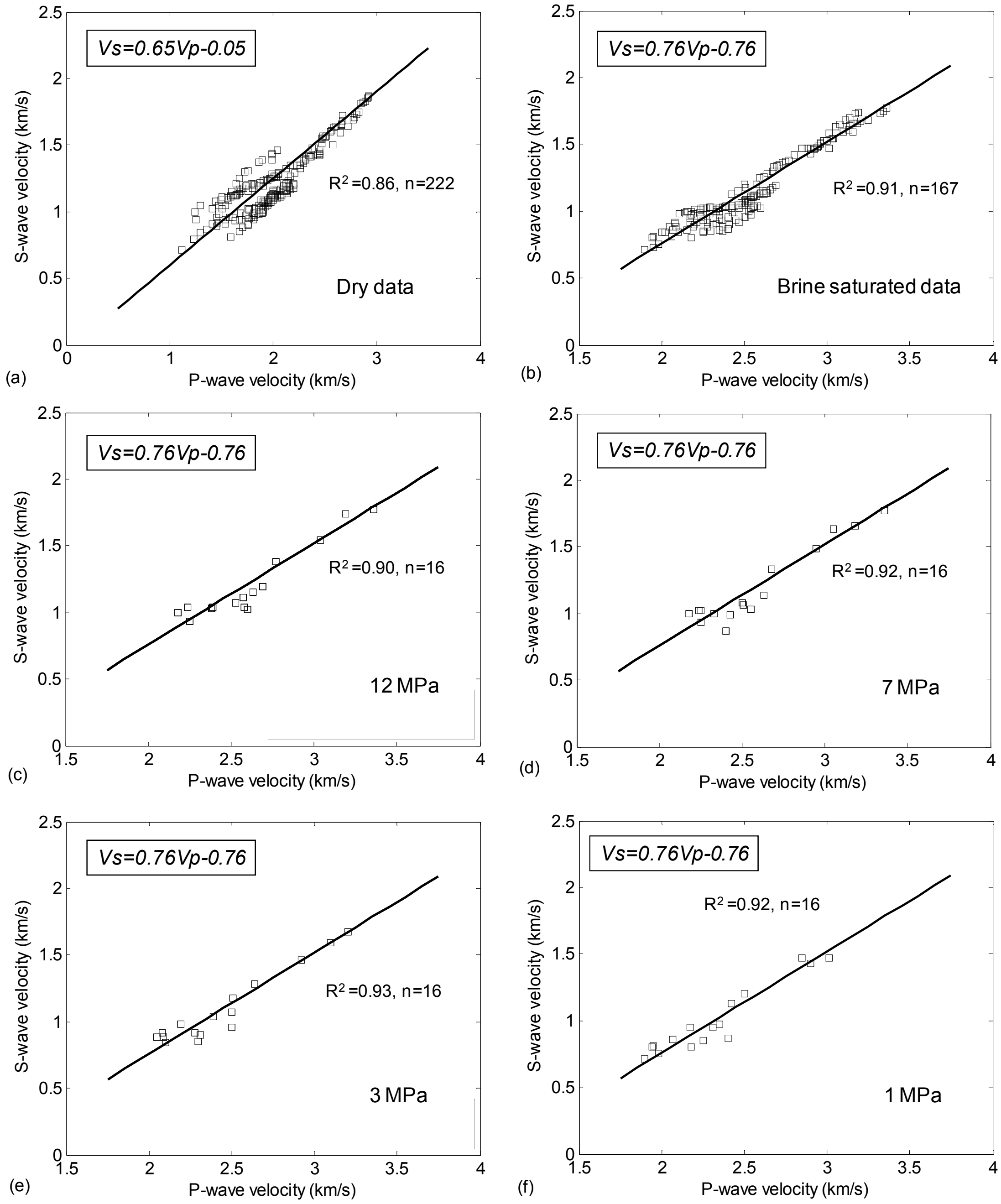

Figure 6. *Linear regression between laboratory V_p and V_s data (a) on dry greensand samples at hydrostatic confining pressure with steps 1 MPa to 12 MPa, (b) on saturated greensand samples at hydrostatic confining pressure with steps 1 MPa to 12 MPa, (c) on saturated greensand samples at hydrostatic confining pressure of 12 MPa, (d) on saturated greensand samples at hydrostatic confining pressure of 7 MPa, (e) on saturated greensand samples at hydrostatic confining pressure of 3 MPa, (f) on saturated greensand samples at hydrostatic confining pressure of 1 MPa.*

Fig. 7 shows the comparison of measured and predicted V_s velocity by using different V_p- V_s regressions including histogram of the residuals. Predictions using the Iso-frame model are quite well although high V_s tend to be overpredicted and low V_s tend to be under predicted (Fig. 7c). The regression reported by Han *et al.* (1986) for clay bearing sandstone underestimates the velocity prediction (Fig. 7e) while the mudrock line by

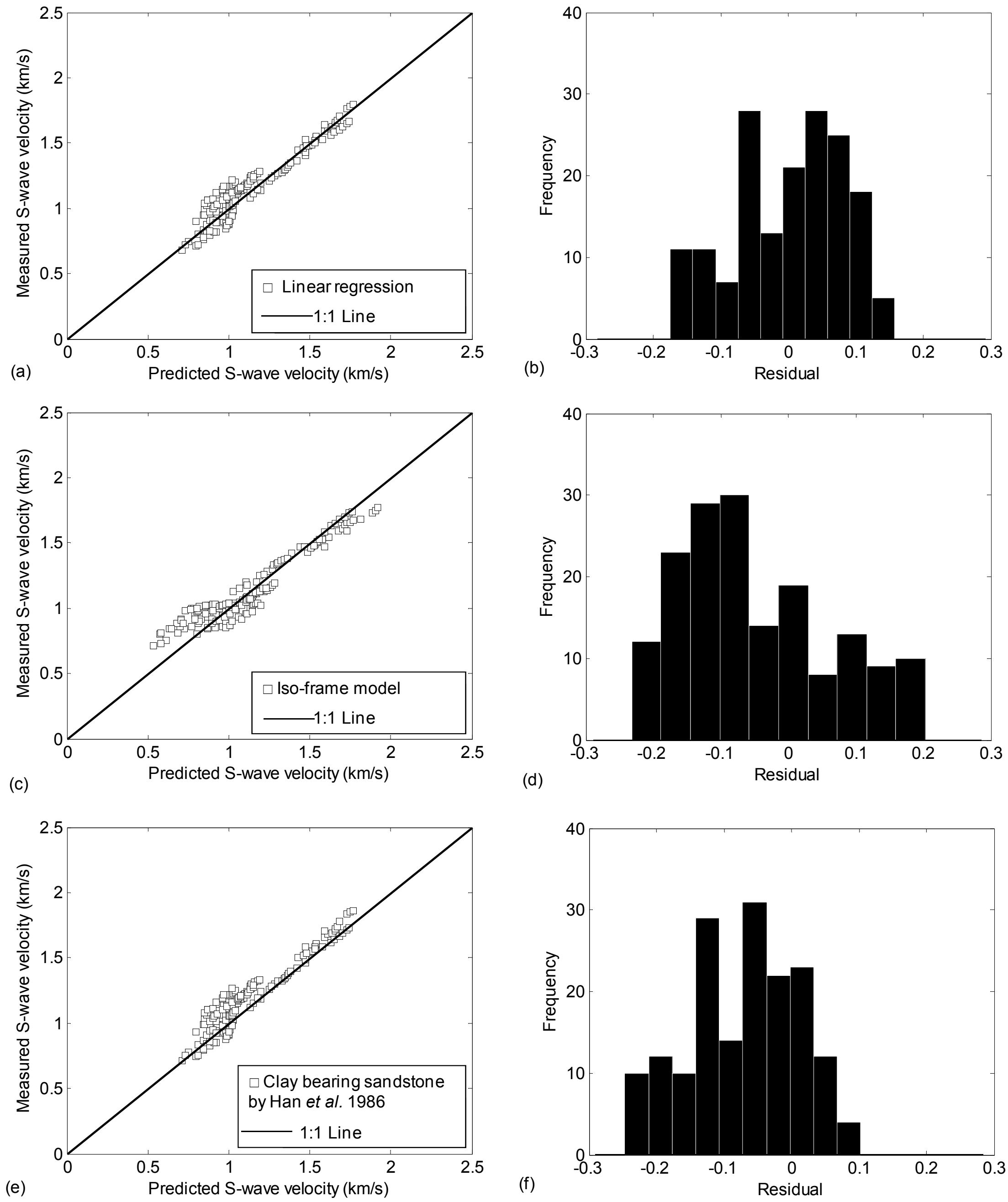

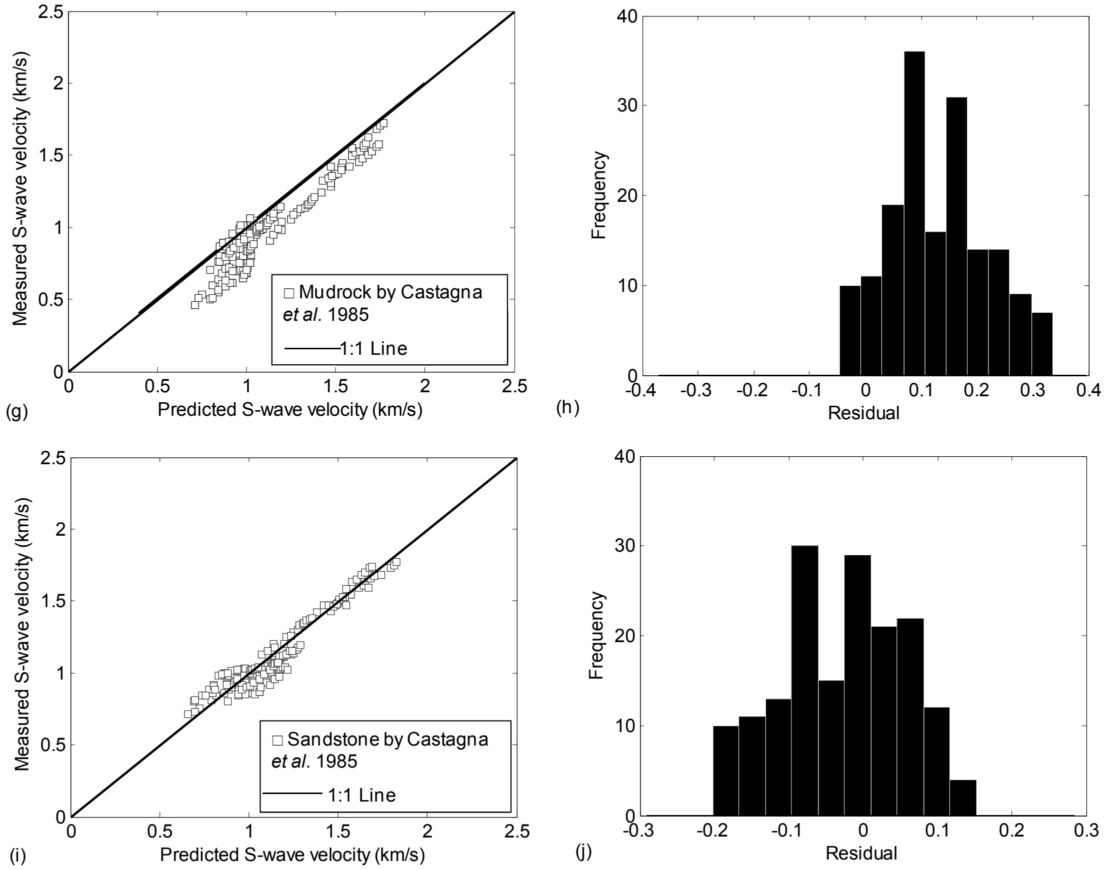

Figure 7. *Comparison between predicted and measured shear wave velocity including histogram of the residuals: (a), (b) by using V_p-V_s relationship obtained from laboratory measured brine saturated greensands, (c), (d) by using V_p-V_s relationship obtained from the effective medium Iso-frame model, (e), (f) by using regression by Han et al. (1986) for clay bearing sandstone, (g), (h) by Mudrock line by Castagna et al. (1985), and (i), (j) by using sandstone regression by Castagna et al. (1985).*

Table 3. *RMS errors and coefficient of determination (r^2) for predicting shear wave velocity from compressional wave velocity from laboratory data and from logging data.*

Methods	**Lab data rms error (%)**	**Lab data r^2**	**Log data rms error (%)**	**Log data r^2**
Linear regression	8.6	0.90	12.0	0.79
Iso-Frame model based	10.6	0.82	11.5	0.75
Sandstone by Castagna *et al.* (1985)	8.8	0.88	12.0	0.72
Mudrock line by Castagna et al. (1985)	15.9	0.63	21.8	0.35
Sandstone by Han et al. (1986)	11.0	0.81	10.0	0.78

Castagna *et al.* (1985) over-estimates the velocity prediction (Fig. 7g). However, predictions are quite good when using the regression reported by Castagna *et al.* (1985) for sandstone (Fig. 7i). We quantified these comparisons by using rms (root mean square) error and r^2 (coefficient of determination). The rms error is 8% and r^2 is 0.9 in the empirical V_p-V_s regression obtained from laboratory data. The rms error is also 8% and r^2 is 0.88 for the regression reported for sandstone (Castagna *et a.* 1985). However, the rms errors are comparatively higher when using the relation derived from the Iso-frame model (10%), when using the regression for clay bearing sandstone reported by Han *et al.* 1986 (11%) and for the mudrock line (Castagna *et al.* 1985) (16%). Moreover, the r^2 are comparatively lower when using the relation derived from the Iso-frame model (0.82), when using the regression for clay bearing sandstone reported by Han *et al.* (1986) (0.81) and for the mudrock line (Castagna *et al.* 1985) (0.63). Obviously the mudrock line was derived for shales and should not be used for greensands.

V_p-V_s relation from logging data

Fig. 8a shows the V_s versus V_p plot of log measured greensand data from the Nini field. An empirical V_p -V_s regression of log measured greensand (after fluid substitution to 100 % brine saturation) can be approximated by the least-square linear fit to these data:

$$Vs = 0.86Vp - 0.96 \text{ (km/s)} \qquad (10)$$

Fig. 8 also shows the comparison of logging data and predicted V_s velocity using different V_p-V_s regressions. Predictions are quite good (rms error = 12% and r^2 = 0.72) with the empirical regression derived from lab measured data (Fig. 8d). Predictions using the Iso-frame model are quite well (rms error = 11% and r^2 = 0.75) although V_s tend to be under predicted (Fig. 8f). Unlike for the laboratory measured data, the regression reported by Han *et al.* 1986 for clay bearing sandstone predicts V_s velocity quite well (rms error = 10% and r^2 = 0.78) (Fig. 8l), whereas the mudrock line and regression reported by Castagna *et al.* 1985 for sandstone under-estimate the velocity (Fig. 8h, 8j). The rms error is 12% and r^2 = 0.72 when using the regression reported for sandstone (Castagna *et al.* 1985). However, the rms errors is quite high (22%) for the mudrock line of Castagna *et al.* 1986.

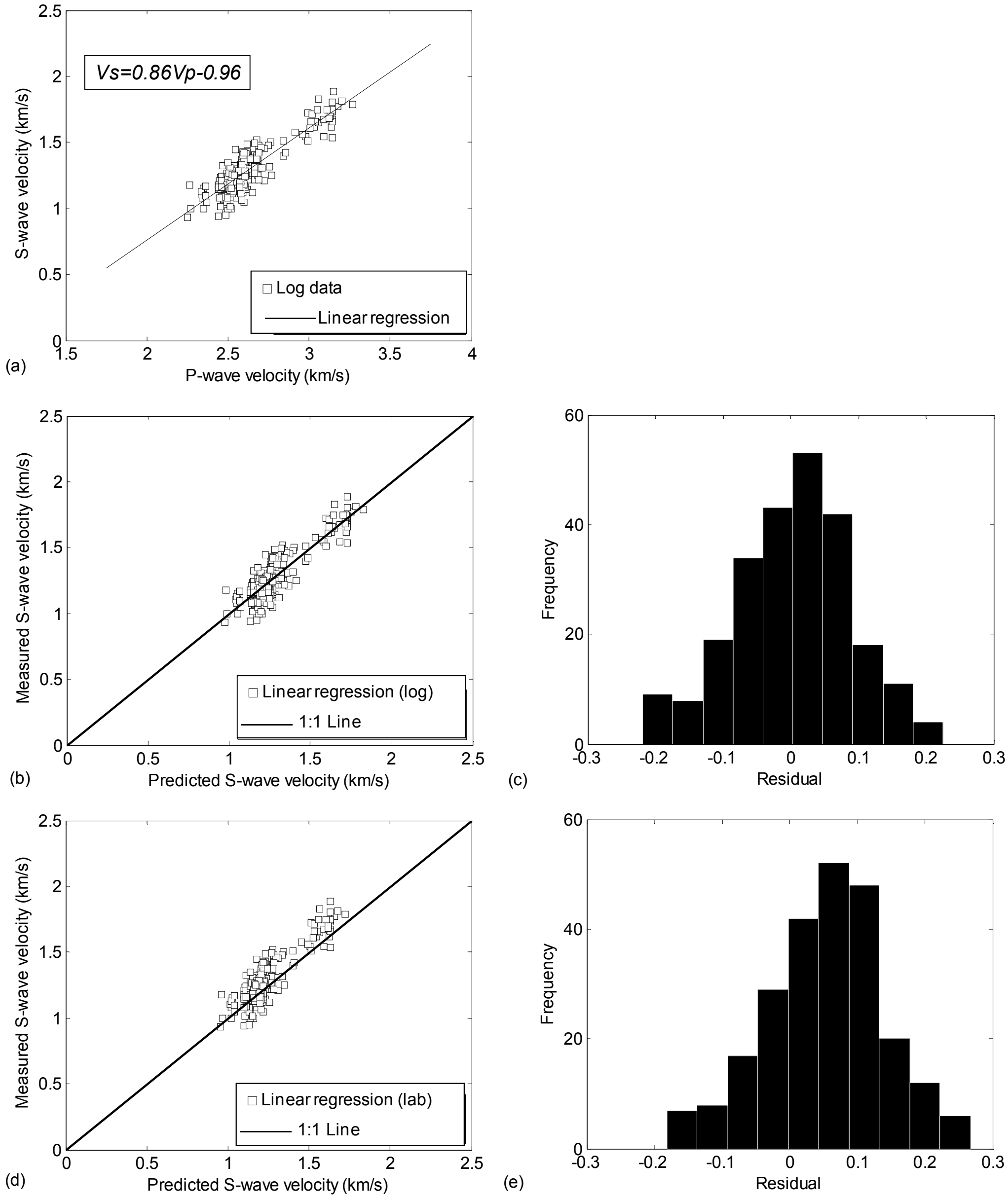
Vs=0.86Vp-0.96
Log data
Linear regression
S-wave velocity (km/s)
P-wave velocity (km/s)
(a)
Linear regression (log)
1:1 Line
Measured S-wave velocity (km/s)
Predicted S-wave velocity (km/s)
(b)
Frequency
Residual
(c)
Linear regression (lab)
1:1 Line
Measured S-wave velocity (km/s)
Predicted S-wave velocity (km/s)
(d)
Frequency
Residual
(e)

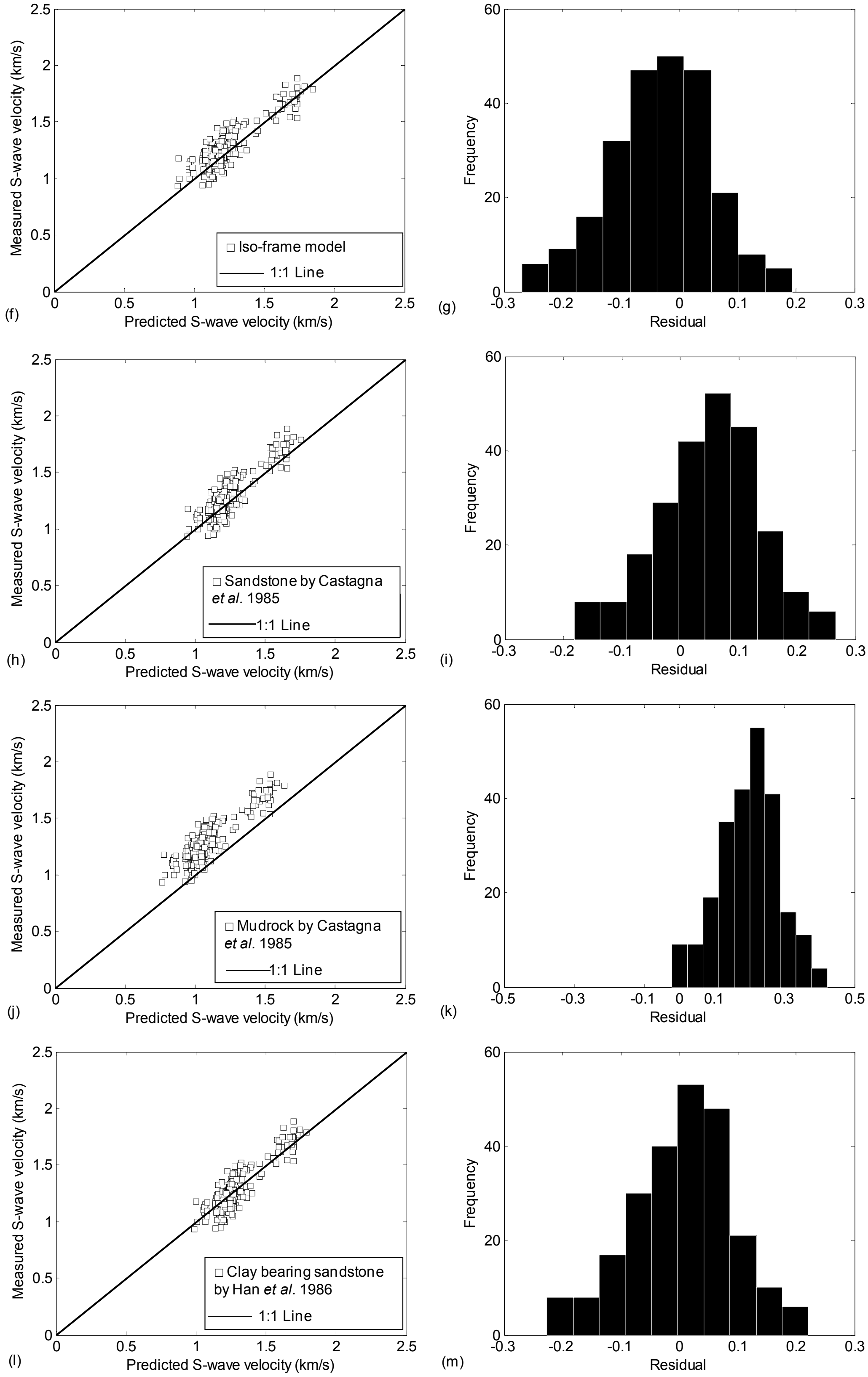

Figure 8. *(a) Linear regression between logging V_p and V_s data. Comparison between predicted and measured shear wave velocity including histogram of the residuals: (b), (c) by using V_p-V_s relationship obtained from log measured brine saturated greensands, (d), (e) by*

using regression obtained from laboratory data, (f), (g) by using V_p-V_s relationship obtained from the effective medium Iso-frame model, (h), (i) by using sandstone regression by Castagna et al. (1985), (j), (k) by Mudrock line by Castagna et al. (1985) and (l), (m) by using regression by Han et al. (1986) for clay bearing sandstone

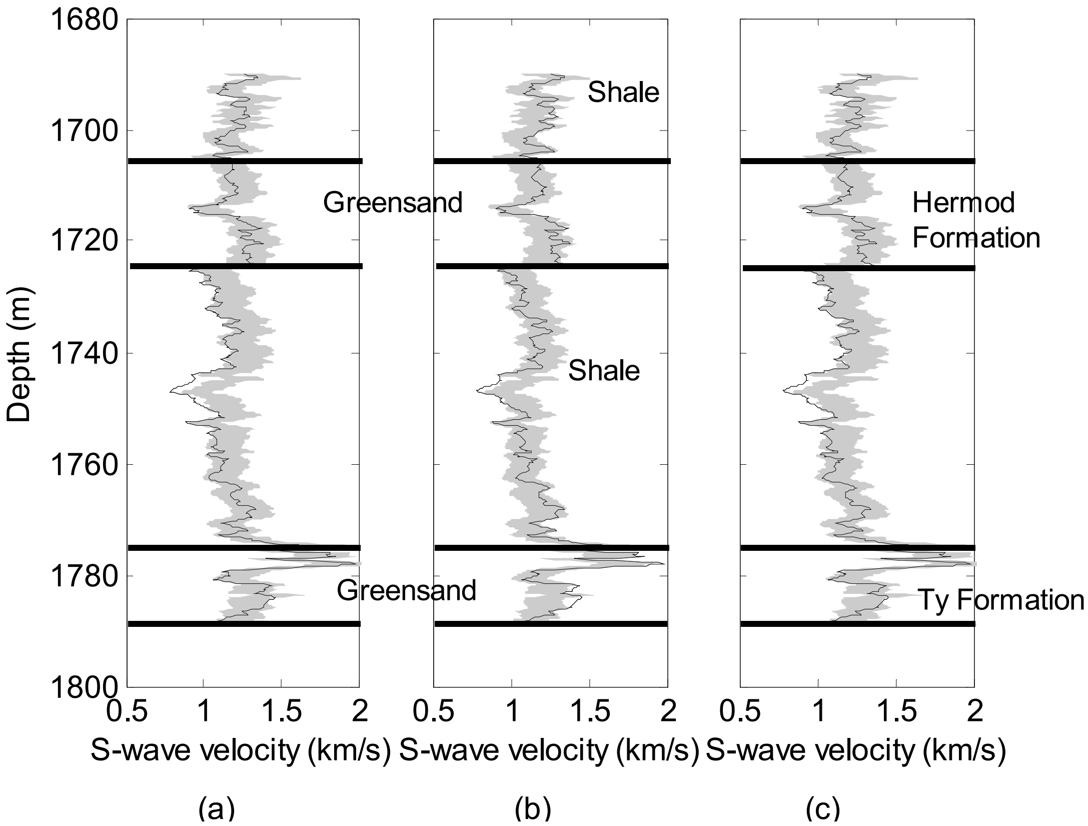

Figure 9. *Comparison between predicted (rms error band) and measured shear wave velocity from logging measurements (thin black line), (a) by using regression obtained from logging data, (b) by using regression obtained from laboratory data, (c) by using regression based on Iso-frame model. V_s in the shale intervals are also predicted according to the greensand model.*

Both simple empirical V_p-V_s regression of greensand and V_p-V_s relationship from modeling provide good prediction of V_s from the measured V_p. Although published V_p-V_s relationships for clay bearing sandstone by Han *et al.* (1986), and for sandstone and mudrock by Castagna *et al.* (1985) are useful in deriving shear wave velocity when other alternative relationships are unavailable, for greensand they are not consistent, in some cases they underestimate and in other cases they overpredict V_s with known V_p. However, the statistical analysis shows that rms error and r^2 for greensand, for clay bearing sandstone by Han *et al.* (1986) and for sandstone by Castagna *et al.* (1985) are close to each other. Therefore, these three may be used to predict the shear wave velocity for greensand.

Fig. 9 illustrates the measured versus predicted shear wave velocity for logging data on a depth scale, by using the regression obtained from logging data (Fig. 9a), the regression obtained from laboratory data (Fig. 9b), and the regression based on Iso-frame model (Fig. 9c). V_s in the shale intervals are also predicted according to the greensand V_p- V_s relations. The gray band of average rms prediction error represents the estimated shear-wave velocity. The measured shear-wave velocity is displayed as the thin line on the plot. We derive a single V_p-V_s relationship both for cemented (Ty Formation) and weakly cemented greensand (Hermod Formation) without considering any cementation effect. Fig. 9 demonstrates that V_p-V_s relationships without considering the cementation effect may be used to predict shear wave velocity in greensand formations. However, these V_p-V_s relations poorly predict the shear wave velocity in shale between the two greensand formations.

AVO model of sandstone and greensand

For analysis of amplitude variation with offset, we calculated the PP (R_{PP}) and PS (R_{PS}) reflection coefficients. We used Knott-Zoeppritz's equations and the approximation by Aki and Richards as given in Mavko *et al.* (2009). PP and PS reflection coefficients link the seismic data with elastic parameters that are sensitive to possible hydrocarbons existing in the rock (Avseth, 2000). We calculated the reflection coefficient as a function of reflection angle ranging from 0^o to 30^o. Data for sandstone with brine and oil were obtained from Castagna and Swan (1997). Shale data for AVO curves were obtained from the studied Nini 1A well. The shale represents the cap-rock for both greensand and quartzitic sandstone. For greensand, the mean values of V_p, V_s and density of laboratory measured sixteen dry greensand samples were used as input to calculate the reflection coefficient. Data representing the brine and oil saturated state were calculated by using Gassmann's equation (Gassmann, 1951).

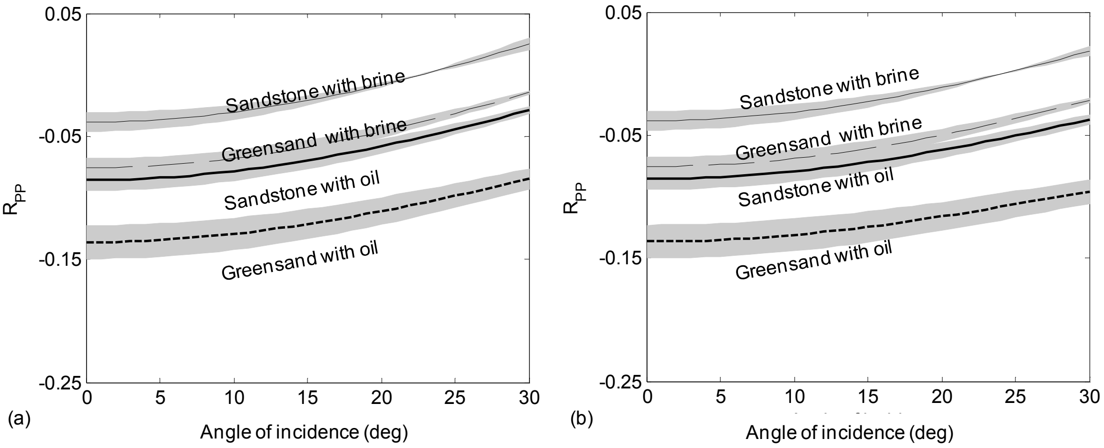

Figure 10. *AVO curves for sandstone and greensand capped by shale, in the brine saturated and in the oil saturated states. (a) PP Reflection coefficients were calculated by using Zoeppritz's equations and (b) by using Aki and Richard's approximation. The input rock physics properties are given in Table 4. The oil saturated sandstone and brine saturated greensand have almost similar AVO response. Shaded bands represent errors in calculation of reflection coefficients.*

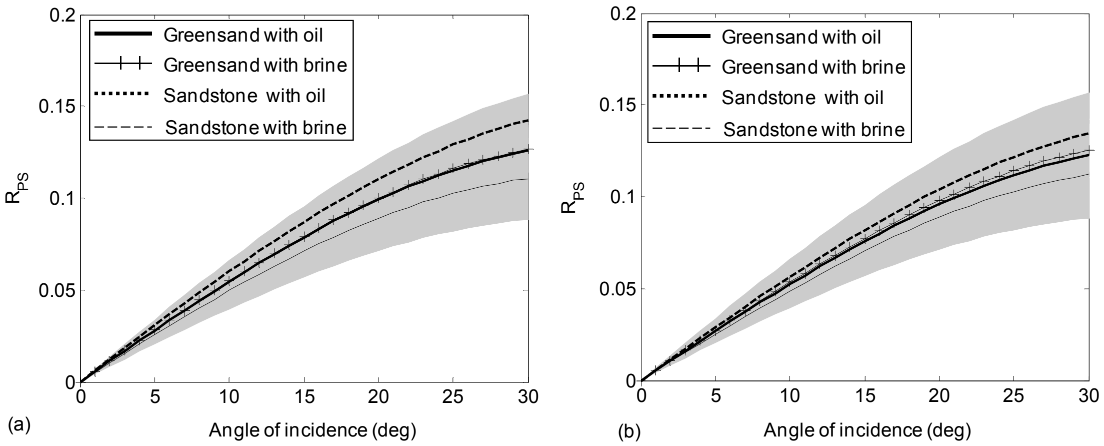

Figure 11. *AVO curves for sandstone and greensand capped by shale, in the brine saturated and in the oil saturated states. (a) PS Reflection coefficients were calculated by using Zoeppritz's equations and (b) by using Aki and Richard's approximation. The input rock physics properties are given in Table 4. The oil saturated sandstone and brine saturated greensand have almost similar AVO response according to Zoeppritz's equations. Shaded bands represent errors in calculation of reflection coefficients.*

Table 4. *Input parameters for AVO reflectivity modeling. P-wave velocity (**V_p**), shear wave velocity (**V_s**) and density of dry greensand are the mean value of sixteen samples. Brine versus oil saturated density and velocity was calculated using Gassmann's equation (Gassmann 1951).*

Lithology	Vp (km/s)	Vs (km/s)	Density (g/cm^3)	Reference
Shale	2.64	1.37	2.34	
Brine sand	2.59	1.06	2.21	Castagna and Swan (1997)
Oil sand	2.45	1.08	2.13	
Brine greensand	2.52	1.05	2.09	
Oil greensand	2.3	1.06	2.02	
Weakly cemented greensand with brine	2.36	0.94	2.08	
Weakly cemented greensand with oil	2.13	0.96	1.98	
Cemented greensand with brine	2.67	1.21	2.21	
Cemented greensand with oil	2.47	1.23	2.05	

We used single interface modeling to show theoretical AVO responses of greensand. In the first example, AVO curves were calculated for glauconitic greensand and quartzitic sandstone each capped by shale. Fig. 10 represents the PP reflection coefficient as a function of incident angle, whereas Fig. 11 represents the PS reflection coefficient as a function of incident angle. Calculated reflection coefficient is displayed as the thin line on the plot as calculated from mean value of V_p, V_s and density, whereas the gray band represents the range of reflection coefficient as calculated from the maximum and minimum value of V_p, V_s and density. We compared the reflection coefficients from Zoeppritz's equations (Fig. 10a and Fig. 11a) and by using Aki and Richard's approximation (Fig. 10b and Fig. 11b). For the PP reflectivity (Fig. 10), the corresponding AVO response shows a negative zero-offset reflectivity and a positive AVO gradient. AVO responses of brine saturated quartzitic sandstone and brine saturated greensand are distinguishable both at zero and far offset. Oil saturated sandstone and oil saturated greensand are also distinguishable both at zero and at far offset. For the PS reflectivity coefficient, AVO responses of sandstone and greensand with brine and oil saturation are distinguishable at far offset only, all curves are ambiguous at zero offsets, as the P-to-S reflection coefficient goes to zero for normal incidence (Fig. 11). Although both greensand and quartzitic sandstone are capped by elastically similar shale, greensand produces a stronger negative reflector. However, we also observe that brine saturated greensand may have similar AVO response to oil saturated quartzitic sandstone (both in PP and PS reflection coefficient). The observed differences are significant in PP reflection coefficient, but not in PS reflection coefficient as the gray bands overlap each other. The observed difference in seismic response between the greensand and the quartzitic sandstone is due to the difference in grain composition. Thus if the difference between greensand and quartzitic sandstone is ignored, their difference in AVO response could be interpreted as being due to pore fluid.

AVO model of weekly cemented and cemented greensand

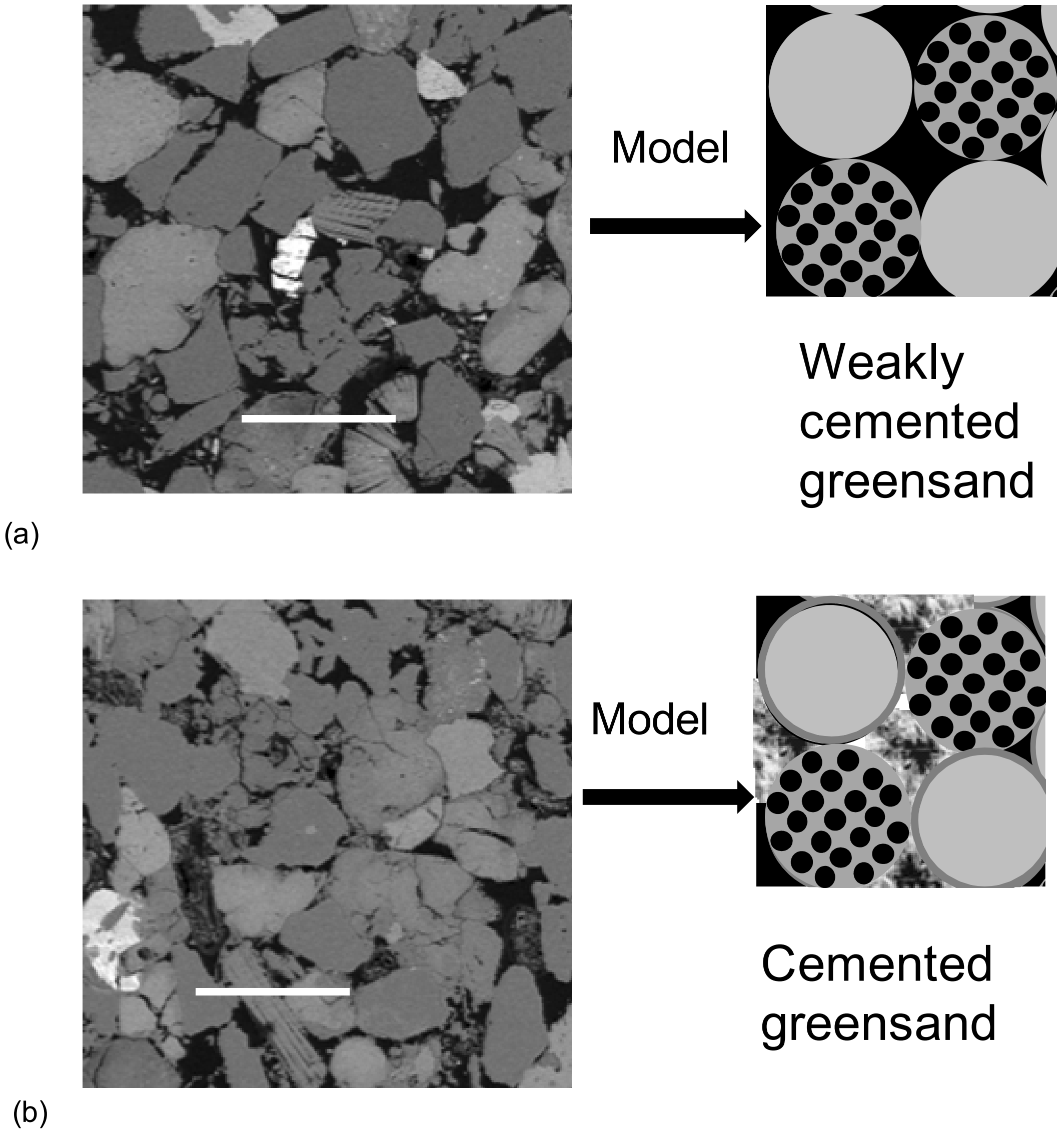

Figure 12. *BSE images of two types of greensand samples (courtesy of Mikael Solymar). Scale bar is 200 µm. (a) Weakly cemented greensand and its idealized model and (b) cemented greensand and its idealized model.*

Next, we do AVO modeling of two types of greensand (the weakly cemented and the cemented) defined by petrographic image analysis and core analysis (Fig. 12). Fig. 13 and Fig. 14 show the AVO curves for weakly cemented greensand capped by shale and cemented greensand capped by shale, in the brine and in the oil saturated state. Fig. 13 represents the PP reflection coefficient as a function of incident angle, whereas Fig. 14 represents the PS reflection coefficient as a function of incident angle. Parameters applied for this calculation are summarized in Table 4. The mean values of V_p, V_s and density of the laboratory measured four greensand samples from Hermod Formation are used as input to calculate reflection coefficient of weakly cemented greensand, whereas the mean values of V_p, V_s and density of the laboratory measured four samples from Ty Formation are used as input to calculate reflection coefficient of cemented greensand. Data for the brine and the oil saturated state were calculated using Gassmann's equation (Gassmann 1951). We compared the reflection coefficients from Zoeppritz's equations (Fig. 13a, and Fig. 14a) and by using Aki and Richard's approximation (Fig. 13b and Fig. 14b). Calculated reflection coefficient is displayed as the thin line on the plot as calculated from mean value of V_p, V_s and density, whereas the gray band represents the range of of reflection coefficient as calculated from the maximum and minimum value of V_p, V_s and density.

AVO responses of brine saturated weakly cemented greensand and brine saturated cemented greensand are distinguishable both at zero and far offset. Oil saturated weakly cemented greensand and oil saturated cemented greensand are also distinguishable both at zero and far offset. Hydrocarbons cause stronger negative reflection coefficient, whereas cementation causes a more positive reflection coefficient. We also observe that oil saturated cemented greensand may have similar AVO response to brine saturated weakly cemented greensand. The observed difference in the seismic response between the two types of greensand is due to the difference in greensand diagenesis. Small amounts of berthierine and microcrystalline quartz cement in Ty Formation greensands cause a difference in seismic response. Thus if difference between cemented greensand and weakly cemented greensand is ignored, their difference in AVO response could be interpreted as being due to pore fluid.

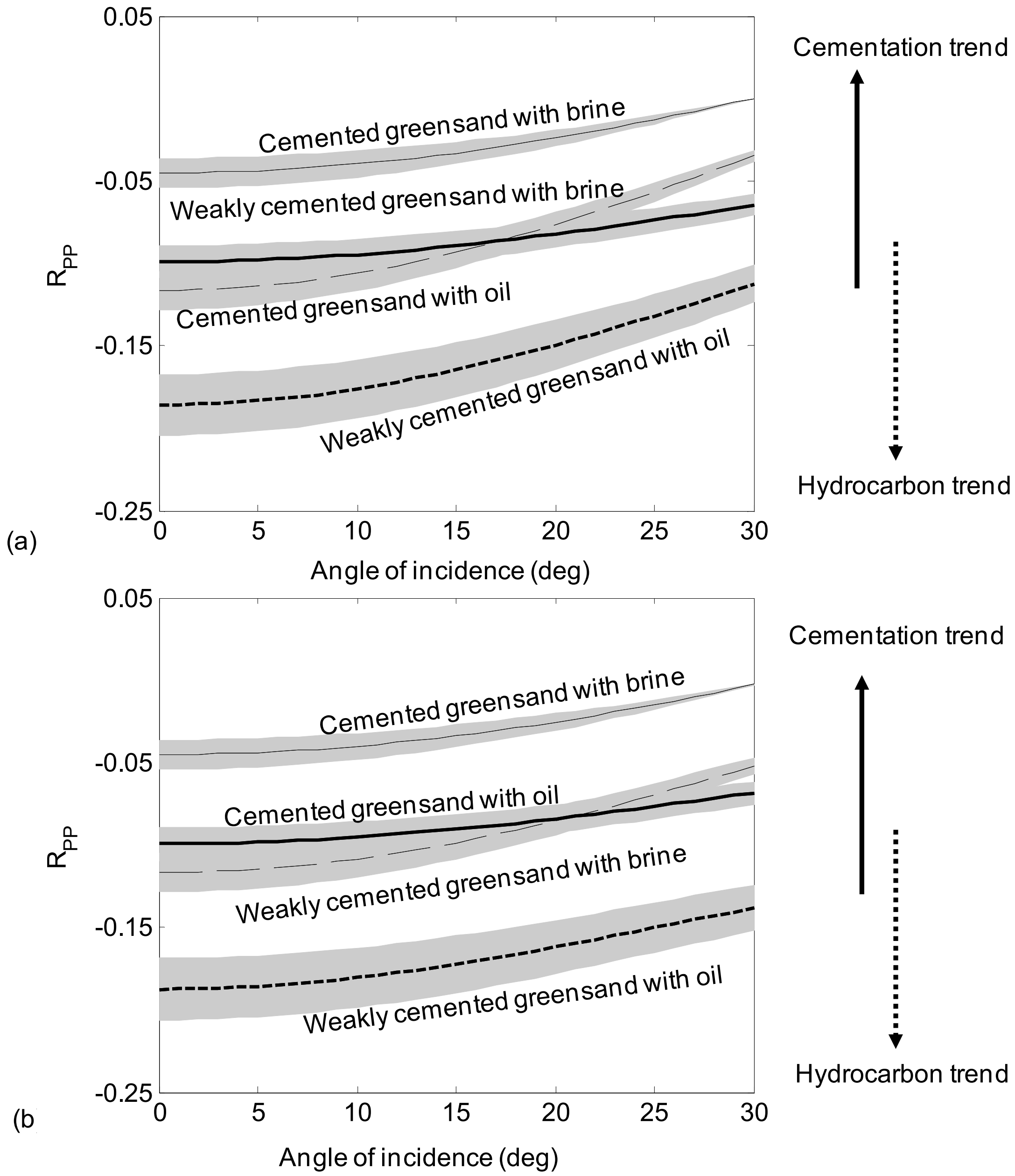

Figure 13. *AVO curves for weakly cemented greensand and cemented greensand capped by shale, in the brine saturated and in the oil saturated states. (a) PP Reflection coefficients were calculated by using Zoeppritz's equations and (b) by using Aki and Richard's approximation. The oil saturated cemented greensand has about the same AVO response as brine saturated weakly cemented greensand. Shaded bands represent errors in calculation of reflection coefficients.*

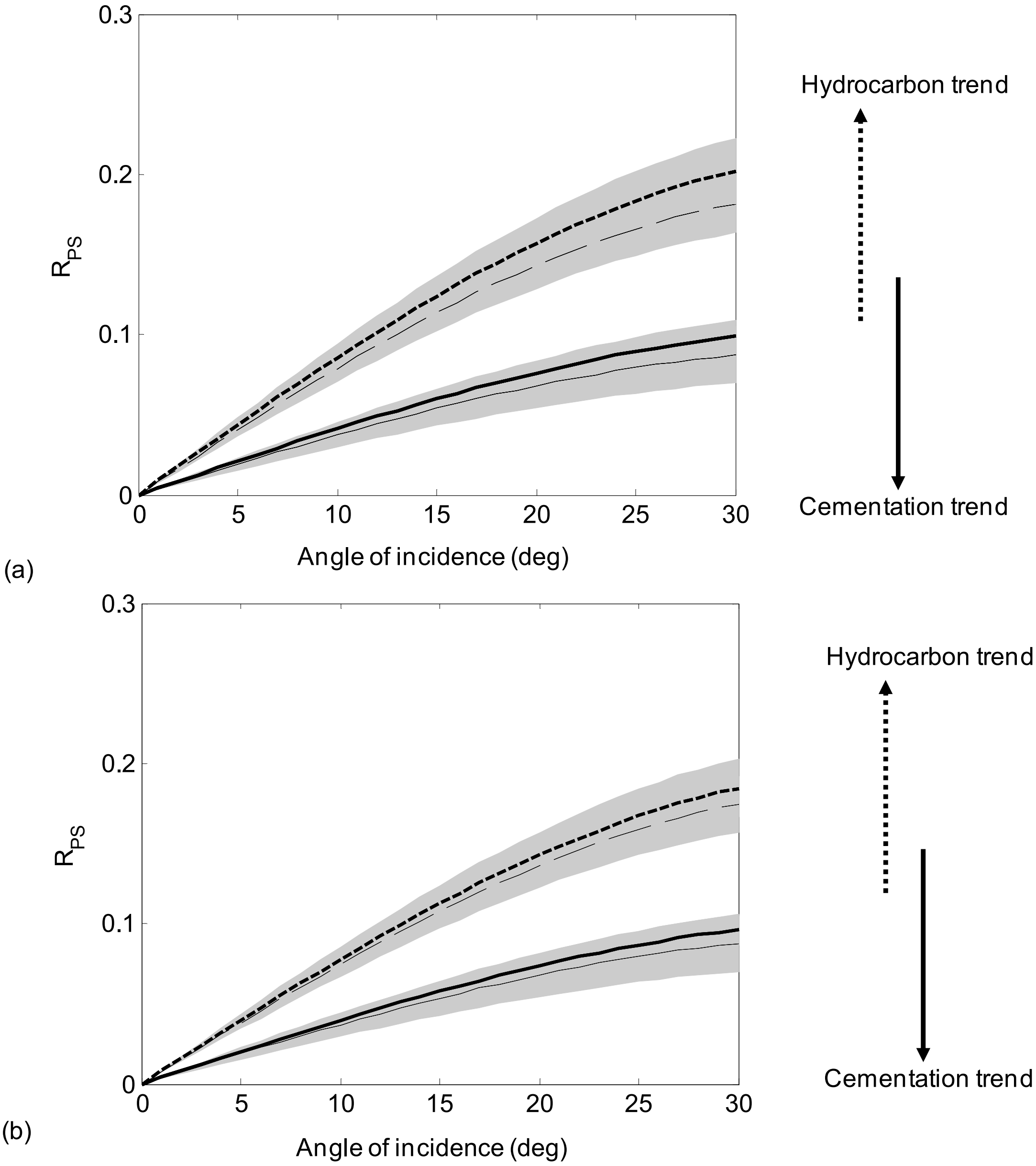

Figure 14. *AVO curves for weakly cemented greensand and cemented greensand capped by shale, in the brine saturated and in the oil saturated states. (a) PS Reflection coefficients were calculated by using Zoeppritz's equations and (b) by using Aki and Richard's approximation. The oil saturated greensand has about the same AVO response as brine saturated greensand. Shaded bands represent errors in calculation of reflection coefficients.*

For the PS reflectivity coefficient (Fig. 14), we observe that AVO responses of weakly cemented and cemented greensand, with brine versus oil saturation are distinguishable at far offset only and all curves are ambiguous at zero offset. Hydrocarbon and cementation trends show the opposite direction to the PP reflection coefficient. In this case the reflection coefficient for brine and oil saturation shows similar seismic response for each rock type.

Reflection coefficients obtained from both Zoeppritz equation and from Aki and Richards's approximation are slightly different at high incident angle, where the approximation becomes poor. However, they give the same overall information.

We used shale as a cap-rock during our AVO modeling. Shales can be anisotropic and anisotropy of the cap rock would influence the AVO analysis. Blangy (1992) showed how transverse isotropy of shaly cap-rocks could drastically influence the AVO response of a reservoir. However, Avseth *et al.* (2008) studied the effect of shale intrinsic anisotropy on AVO signatures of sandstones reservoirs capped by shale and found that the anisotropy effect starts becoming significant beyond about 30^0 angle of incidence. Therefore, we disregarded the effect of anisotropy in this study.

Conclusion

Although published V_p-V_s relationships for clay bearing sandstone by Han *et al.* (1986), and for sandstone and mudrock by Castagna *et al.* (1985) are useful in deriving shear wave velocity when other alternative relationships are unavailable, for greensand they are not consistent, in some cases they underestimate and in other cases they overpredict V_s with known V_p.

We present new V_p-V_s relationships derived by using data from the Paleocene greensand Nini oil field in the North Sea. We also derived a V_p-V_s relationship of greensand from the Iso-frame model and compared it with empirical V_p-V_s regressions from laboratory data as well as from well log data. Both simple empirical V_p-V_s regression of greensand and V_p-V_s relationship from modeling provide good prediction of V_s from the measured V_p.

AVO modeling indicates that an interface between shale and glauconitic greensand produces a stronger negative reflection coefficient than an interface between shale and quartzitic sandstone. Brine saturated greensand may have similar AVO response to oil saturated quartzitic sandstone. The observed difference in seismic response between the greensand and the quartzitic sandstone is due to the difference not only in mineralogy but also due to the compliant micro-porous glauconite grains.

AVO modeling also indicates that an interface between shale and weakly cemented greensand produces a stronger negative reflection coefficient than an interface between shale and cemented greensand. We found that cemented greensand with oil saturation can have similar AVO response to brine saturated weakly cemented greensand. The observed significant difference in the seismic response between the two types of greensands is due to a difference in greensand diagenesis.

Acknowledgements

We acknowledge Stanford Rock Physics project and department of Energy Resources Engineering, Stanford University for their hospitality during the summer, 2009. Gary Mavko (Stanford University) is kindly acknowledged for his valuable discussions. Egil Nybakk and Mikael Solymar are acknowledged for BSE images and mineralogical analysis from thin sections. DONG Energy A/S is acknowledged for financial support.

References

Archie G. E. 1942. Electrical resistivity log as an aid in determining some reservoir characteristics. *Journal of Petroleum Technology* **5(1)**, 54-62.

Avseth P. 2001. *Combining rock physics and sedimentlogy for seismic reservoir characterization of North Sea Turbidite systems*. PhD thesis, Stanford University.

Avseth P., Mukerji T. and Mavko G. 2005. *Quantitative Seismic Interpretation: Applying Rock Physics Tools to Reduce Interpretation Risk.* Cambridge University Press, ISBN: 9780521816014.

Avseth O., Dræge A., Wijngaarden A.J., Johansen T.A. and Jørstand A. 2008. Shale rock physics and implications for AVO analysis: A North Sea demonstration. *The Leading Edge* **27**, 788-797.

Batzle M. and Wang Z. 1992. Seismic properties of pore fluids. *Geophysics* **57**, 1396-1408.

Blangy J.P. 1992. *Integrated seismic lithologic interpretation: The petrophysical basis*. PhD Thesis, Stanford University.

Cagatay M. N., Saner S., Al-Saiyed I. and Carrigan W. J. 1996. Diagenesis of the Safaniya Sandstone Member (mid-Cretaceous) in Saudi Arabia. *Sedimentary Geology* **105**, 221-239.

Castagna J., Batzle M. and Eastwood R. 1985. Relationships between compressional wave and shear-wave velocities in clastic silicate rocks. *Geophysics* **50**, 571-581.

Castagna J. P. 1993. Comparison of AVO indicators: A modeling study. *Geophysics* **59**, 1849-1855.

Castagna J. P. and Smith S. W. 1994. Comparison of AVO indicators: A modeling study. *Geophysics* **59**, 1849-1855.

Castagna J. P. and Swan H. W. 1997. Principles of AVO crossplotting. *The Leading Edge* **16**, 337-342.

Castagna J., Swan H. W. and Foster D. J. 1998. Framework for AVO gradient and intercept interpretation. *Geophysics* **63**, 948-956.

Diaz E., Prasad M., Dvorkin J. and Mavko G. 2002. Effect of glauconite on the elastic properties, porosity, and permeability of reservoir rocks. AAPG Annual Meeting, March 10-13, Houston, Texas, Extended Abstracts.

Diaz E., Prasad M., Mavko G. and Dvorkin J. 2003. Effect of glauconite on the elastic properties, porosity, and permeability of reservoir rocks. *The Leading Edge* **22**, 42-45.

Fabricius I. L. 2003. How burial diagenesis of chalk sediments controls sonic velocity and porosity. *AAPG Bulletin* **87**, 1-24.

Fabricius I. L., Høier C., Japsen P. and Korsbech U. 2007. Modelling elastic properites of impure chalk from South Arne Field, North Sea. *Geophysical Prospecting* **55**, 487-506.

Gassmann F. 1951. Elastic waves through a packing of spheres. *Geophysics* **16**, 673-685.

Greenberg M. and Castagna J. 1992. Shear-wave velocity estimation in porous rocks: Theoretical formulation, preliminary verification and applications. *Geophysical Prospecting* **40**, 195-209.

Han D., Nur A and Morgan D. 1986. Effect of porosity and clay content on wave velocities in sandstone. *Geophysics* **51**, 2093-2107.

Hashin Z. and Shtrikman S. 1963. A variational approach to the theory of the elastic behaviour of multiphase materials. *Journal of Mechanics and Physics Solids* **11**, 127-140.

Hill R. 1952. The elastic behavior of crystalline aggregate. *Proceeding of the Physical Society of London* A65, 349-354.

Hossain Z., Fabricius I. L. and Christensen H. F. 2009. Elastic and nonelastic deformation of greensand. *The Leading Edge* **28**, 260-262.

Hossain Z., Mukerji, T. and Fabricius I.L. 2010. V_p- V_s relationship of glauconitic greensand. 72th EAGE meeting, Barcelona, Spain, Extended abstract, I1016.

Hossain, Z., Fabricius, I.L, Grattoni, A. C. and Solymar, M. 2011. Petrophysical properties of greensand as predicted from NMR measurements. *Petroleum Geoscience* (in Press).

Jørstad A., Mukerji, T. and Mavko, G. 1999. Model-based shear-wave velocity estimation versus empirical regressions. *Geophysical Prospecting* **47**, 785-797.

Katahara W. 1996. Clay minerals elastic properties. SEG 66th Annual meeting, Expanded abstracts 66, 1691-1694.

Krief M., Garat J., Stellingwerff J. and Ventre J. 1990. A petrophysical interpretation using the velocities of P and S waves (full-waveform sonic). *Log Analyst* **31**, 355-369.

Li Y. Downton J. and Xu Y. 2007. Practical aspects of AVO modeling. *The Leading Edge* **26**, 295-311

Mavko G., Mukerji T. and Dvorkin J. 2009. *The Rock Physics Handbook: Tools for Seismic Analysis of Porous Media*. Second edition. Cambridge University Press, ISBN 9780521861366.

Norris J.S., Evans B.J. (1993) Seismic interface modelling: a physical approach to Zoeppritz Theory. *Exploration Geophysics* **24**, 733–742.

Ranganathan V. and Tye R. S. 1986. Petrography, diagenesis, and facies controls on porosity in Shannon Sandstone, Hartzog Draw Field, Wyoming. *AAPG Bulletin* **70**, 56-69.

Schiøler P., Andsbjerg J., Clausen O. R., Dam G., Dybkjær K., Hamberg L.,Heilmann-Clausen C., Johannessen E. P., Kristensen L. E. and Prince I. 2007. Lithostratigraphy of the Paleocene: Lower Neogene succession of the Danish North Sea. *Geological Survey of Denmark and Greenland Bulletin* **12**, 77-99.

Solymar M. 2002. *Influence of composition and pore geometry on immiscible fluid flow through greensand*. PhD. Thesis, Chalmers University of Technology.

Solymar M., Fabricus I.L. and Middleton M.F. 2003. Flow characterization of glauconitic sandstones by interated Dynamic Neutron Radiagraphy and image analysis of backscattered electron micrographs. *Petroleum Geoscience* **9**, 175-183.

Slot-Petersen C., Eidsemo T., White J. and Rueslatten H. G. 1998. NMR formation evaluation application in a complex low resistivity hydrocarbon reservoir. Transactions of the SPWLA 39th Annual Logging Symposium.

Stokkendal J., Friis H., Svendsen J. B., Poulsen M. L. K. and Hamberg L. 2009. Predictive permeability variations in a Hermod sand reservoir, Stine Segments, Siri Field, Danish North Sea. *Marine and Petroleum Geology* **26**, 397-415.

Tilley B. J. and Longstaffe F. J. 1984. Controls on hydrocarbon accumulation in glauconitic sandstone, Suffield heavy oil sands, southern Alberta. *AAPG Bulletin* **68**, 1004-1023.

Tsuneyama F. 2005. *Quantitative detection of fluid distribution using time-lapse seismic*. PhD thesis, Stanford University.

Vernik, L., Fisher, D., and bahret, S., 2002, Estimation of net-to-gross from P and S impedance in deepwater turbidites. *The Leading Edge* **21**, 380-387.

Winn R. D. 1994. Shelf Sheet-Sand Reservoir of the Lower Cretaceous Greensand, North Celtic Sea

Basin, Offshore Ireland. *AAPG Bulletin* **78**, 1775-1789.
Xu S. and White R. E. 1995. A new velocity model for clay-sand mixtures. *Geophysical Prospecting* **43**, 91-118.

Xu S. and White R. E. 1996. A physical model for shear-wave velocity prediction. *Geophysical Prospecting* **44**, 687-718.

Appendix A1

Resistivity measurements

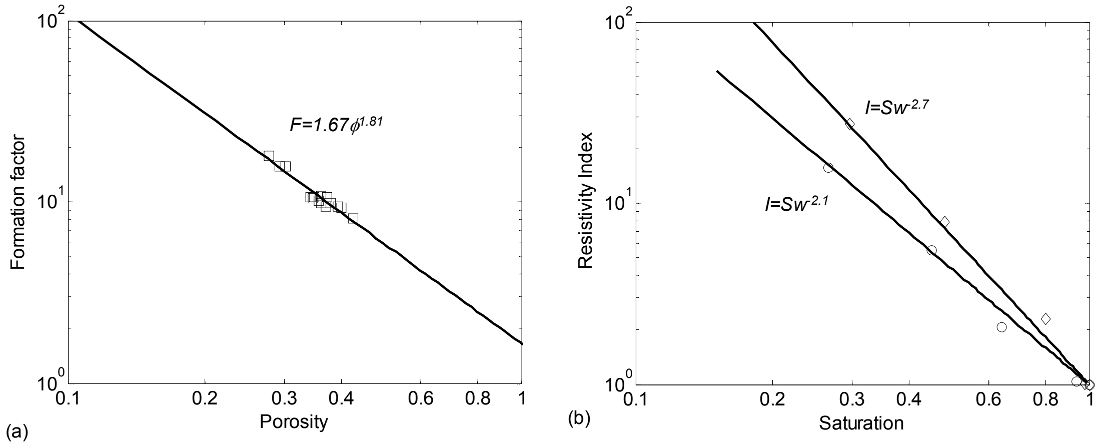

Figure A1 *Laboratory resistivity measured data. (a) Porosity-formation factor plot for 16 greensand samples. Y-intercept and slope define a=1.67 and cementation factor, m=1.81. (b) Resistivity index-saturation plot of two greensand samples. Average saturation exponent, n is 2.4.*

Resistivity was measured in the same triaxial Hoek cell and under the same condition as the acoustic measurement was done. Both acoustic and resistivity data were recorded simultaneously at hydrostatic confining pressure with steps from 1 to 12 MPa. Samples saturations are given in Table A1. Considering the error in saturation calculation, the greensand samples were assumed fully saturated prior to resistivity measurements. The sample was place in between the pistons and the Hoek cell was installed in an AC current circuit with variable resistance in series. To isolate electrical influence from the load frame, a plastic film was attached between the pistons. The supply voltage was 1 V and the frequency 1 kHz. The variable resistance was adjusted so that the voltage over the variable resistance is half of the supplied voltage. Then the resistance of the sample is equal to the resistance of the variable resistance. Frequency is adjusted from power supply frequency in such a way that the phase shift between the two voltage waves is minimal and always below 1 degree. The resistivity (*Rt*) is defined as the resistance multiplied by as geometric factor, (*A/l*), where *A* and *l* are the cross sectional area and length of the sample respectively. The resistivity of pore water was measured by a conductivity meter. The uncertainty for the resistivity measurements is assessed to be maximally 3%.

The ratio of the pore fluid resistivity of, R_w to bulk resistivity of the fully saturated rock, *Ro* is known is known as the formation factor, *F* (Archie 1942):

$$F = \frac{R_O}{R_W} \tag{A1}$$

Archie's low is an empirical relation relating the formation factor and cementation factor, m to the porosity in brine saturated reservoir rock:

$$F = \frac{a}{\phi^m} \tag{A2}$$

Where ϕ is porosity of rock, *a* factor corrects for clay and other conducting minerals. Equation A2 was applied to measured resistivity results (Table A1) to define the m=1.81 and a=1.67 (Fig. A1).

In the case of partially saturated rock with resistivity R_t, the resistivity index is define as:

$$I = S_w^n = \frac{R_O}{R_t} \tag{A3}$$

In order to define n, we measured resistivity of two greensand samples in four saturation conditions (Fig. A1). Average n was calculated as 2.4.

Appendix A2

Hashin- Shtrikman bounds

The best bounds for isotropic mixtures, when only the volume fractions and constituent moduli are known, are the Hashin and Shtrikman bounds (Hashin and Shtrikman, 1963). For a mixture of two constituents, the Hashin and Shtrikman bounds are given by:

$$K^{HS\pm} = K_1 + \frac{f_2}{(K_2 - K_1)^{-1} + f_1(K_1 + 4\mu_1/3)^{-1}} \quad \text{(A4)}$$

$$\mu^{HS\pm} = \mu_1 + \frac{f_2}{(\mu_2 - \mu_1)^{-1} + 2f_1(K_1 + 2\mu_1)/[5\mu_1(K_1 + 4\mu_1/3)]} \quad \text{(A5)}$$

where K_1 and K_2 are bulk modulus of each constituent; μ_1 and μ_2 are shear modulus of each constituent; f_1 and f_2 are volume fraction of each constituent. Upper and lower bound are calculated by interchanging which material is subscripted 1 and which is subscripted 2.

In the Iso-frame model by Fabricius (2003) only a part (IF) of the solid constitutes the frame whereas the remaining solids (1-IF) are assumed in suspension. The volume fractions f_1 and f_2 of the H-S model are then given as:

$$f_1 = IF(1-\phi) \quad \text{(A6)}$$

$$f_2 = (\phi + (1-IF)(1-\phi)) \quad \text{(A7)}$$

IV

Journal paper

Hossain, Z., and Fabricius, I.L. (2011): CO_2 injection effect on physical properties of greensand from the North Sea (submitted to Journal of Petroleum Science and Engineering).

CO_2 injection effect on physical properties of greensand from the North Sea

Zakir Hossain
Technical University of Denmark

Ida L. Fabricius
Technical University of Denmark

Abstract

The objective of this study is to investigate CO_2 injection effects on physical properties of greensand reservoir rocks from the North Sea Nini field. Greensands are sandstones composed of a mixture of clastic quartz grains and glauconite grains. A CO_2 flooding experiment was carried out by injecting supercritical CO_2 into brine saturated samples and subsequently flushing the CO_2 saturated samples with brine at reservoir conditions. Helium porosity, Klinkenberg permeability, and specific surface area by BET were measured on dry greensand samples before and after the CO_2 experiment. NMR T_2 distribution, electrical resistivity and ultrasonic P-and S-wave velocities were measured on brine saturated greensand samples before and after the CO_2 experiment. P-and S-wave velocities were also measured on dry samples. Our laboratory results indicate that CO_2 injection has no major effect on porosity, electrical and elastic properties of the greensand, whereas Klinkenberg permeability increased after CO_2 injection. An NMR permeability modeling approach was used to evaluate the effect on matrix permeability of CO_2 injection. It appears that permeability after CO_2 injection increased not due to fracturing but rather due to the increase of macro-pores in the greensand. The increase of macro-pore size is probably due to migration of fine pore-filling minerals. Rock physics modeling indicates that the presence of CO_2 in a greensand decreases V_p by 2%-41% relative to V_p of brine saturated greensand. CO_2 flooding would at the same time increase V_s, typically by 1%-2%, while decreasing density by 3%-5%. AVO modeling indicates that the largest change in the AVO response occurs when the first 10% CO_2 are injected into a brine saturated greensand.

Keywords: CO_2, greensand, porosity, permeability, NMR, resistivity, velocity

Introduction

Greensands are sandstones mainly composed of a mixture of clastic quartz grains and glauconite grains. Glauconite grains are porous aggregates of iron-bearing clay. Therefore porosity in greensand is found in two scales: macro-porosity between grains and micro-porosity within grains (Fig. 1). Greensand petroleum reservoirs occur world-wide, e.g. the mid-Cretaceous Safaniya Sandstone Member in Saudi Arabia (Cagatay et al., 1996), a Lower Cretaceous Glauconitic sandstone in Alberta, Canada (Tilley and Longstaffe 1984), the Upper Cretaceous Shannon sandstone in Wyoming, USA (Ranganathan and Tye 1986), and late Paleocene Greensand in central part of the North Sea (Solymar, 2002; Solymar et al., 2003; Hossain et al., 2009; Hossain et al., 2010a; Hossain et al., 2010b; Schiøler et al. 2007; Stokkendal et al. 2009). The Paleocene greensands of the Nini field in the Danish North Sea are recognized in the young Hermod Formation and in the older Ty Formation. Greensand from Hermod Formation is only weakly cemented, whereas greensand from Ty formation contains cement of berthierine or microcrystalline quartz (Fig. 1).

CO_2 capture and storage (CCS) is a technique designed to reduce CO_2 emission, and CO_2 is also used in EOR (enhanced oil recovery). It may increase oil production by 15-25% from an oil field. CO_2 may be stored either as gas or dissolved in an aqueous solution in aquifers or in depleted oil or gas reservoirs. The consequence of CO_2 injection into a geological formation needs to be considered including the physical and chemical interaction of CO_2 with rock minerals and pore fluids. At reservoir condition, CO_2 may affect the aquifer properties in two ways. Firstly, CO_2 dissolved in water is in equilibrium with carbonic acid. The acid may react with the rock thus changing its physical and mechanical properties. Secondly, when CO_2 is injected into a reservoir, the existing formation fluid in the pore space will be partially displaced by CO_2 thus changing the compressibility and density of the reservoir rock.

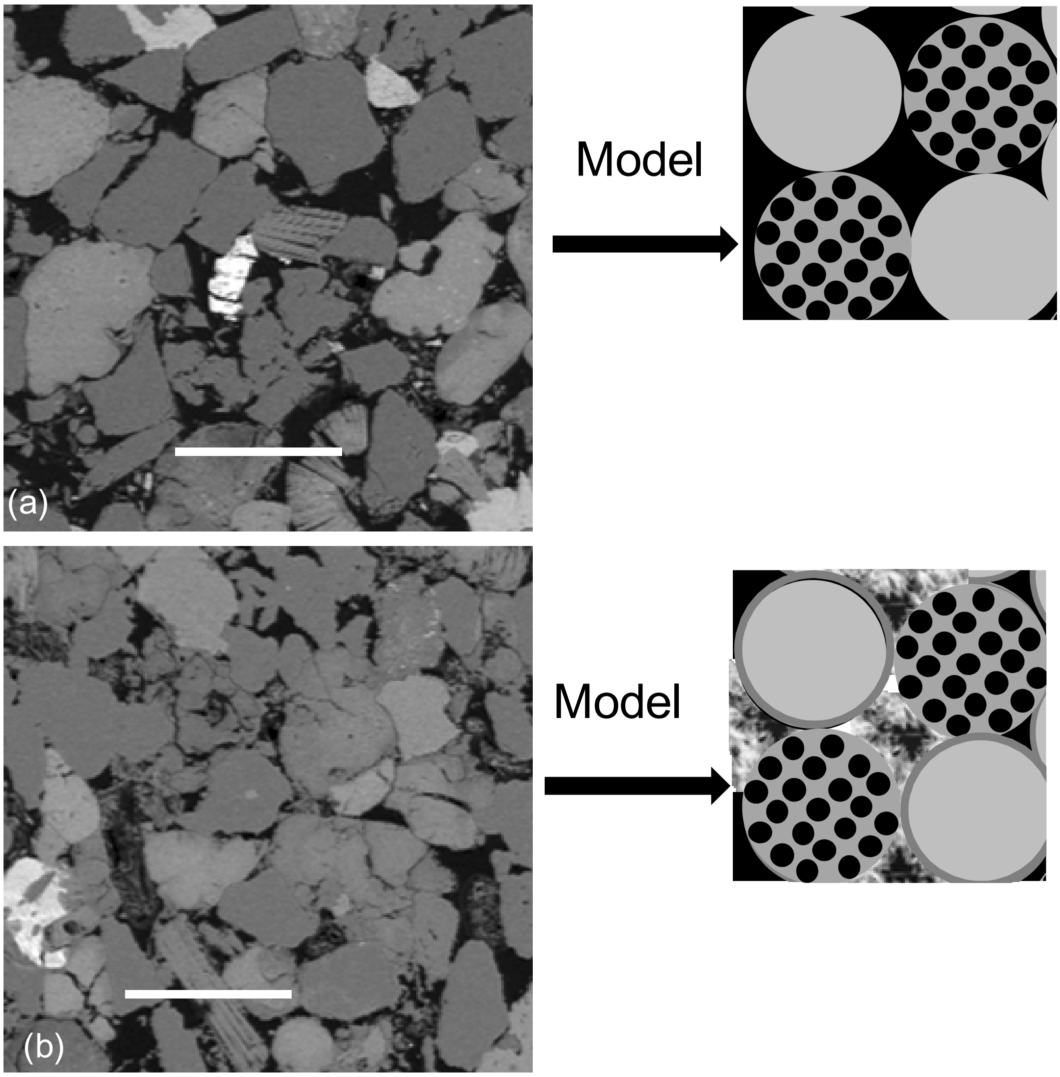

Figure 1. *BSE images and conceptual models of two types of greensands from the North Sea Nini field. Scale bar of these images is 200 μm and the images represent macro-porosity, quartz and glauconite grains and micro-porosity within glauconite. (a) Weakly cemented greensand (b) Micro crystalline quartz and pore filling berthierine cemented greensand (Modified after Hossain et al., 2010b).*

Time-lapse seismic surveys currently provide the most attractive approach to monitoring changes in compressibility and density of reservoir rocks. However, understanding the changes of seismic signature due to CO_2 injection is the key element in monitoring the injection of CO_2. Several studies show that based on rock physics modeling, it is possible to discuss how during CO_2 flooding changes in reservoir properties are affected in seismic data (Wang et al., 1998; Xue and Ohsumi 2004; Siggins, 2006; Brown et al., 2007; Lei and Xueb 2009). Gassmann's equations (Gassmann 1951) are generally used to calculate the seismic response due to changing pore fluid. Gassmann's equations (Gassmann

1951) are also used to calculate the seismic response of CO_2 bearing rocks (McKenna et al., 2003; Lei and Xueb 2009 and Wang et al., 1989; Wang 2000; Kazemeini et al., 2010; Carcione et al., 2006). Compressibility and density of fluids are necessary input parameters for these calculations. When CO_2 is injected into water-saturated rock and CO_2 dissolves in the brine, it will change the physical properties of the brine. Therefore, a correction of fluid properties is required based on compressibility and density as a function of amount of dissolved CO_2 in the brine.

AVO modeling is a step in the multidisciplinary integration of petrophysics, rock physics, seismic data, geology as well as petroleum engineering. To predict the lithology and pore fluid from seismic data are the main objective for AVO analysis (Castagna and Smith, 1994; Castagna et al. 1993; Castagna et al. 1998; Lie et al., 2007). Therefore, AVO is also used to calculate the CO_2 bearing rock's seismic response (Brown et al., 2007; Ma and Morozov, 2010). AVO is a method that combines V_p , V_s and density, it will be more sensitive to changes in CO_2 saturation than a method that relies on V_p only. Since AVO depends on both the velocities and density, the AVO response should be sensitive to an extended range of CO_2 saturations.

The objective of this study is to investigate CO_2 injection effects on physical properties of greensand reservoir rocks from the North Sea Nini field. The CO_2 injection processes in greensand could be more complicated than in quartz sand, because in greensands interaction of CO_2 with glauconite is expected rather than with quartz. Furthermore, greensand from the North Sea contains micro-crystalline quartz and pore-filling clay (berthierine) cement (Solymar et al., 2002; Hossain et al., 2011b). Moreover, in the case of Nini field a question is whether injected CO_2 can be detected seismically. To address these issues, we did laboratory CO_2 injection in greensand samples to detect the effect on physical properties. We also used rock physics-based models to predict the changes of seismic properties due to CO_2.

Greensand sample characterization and method

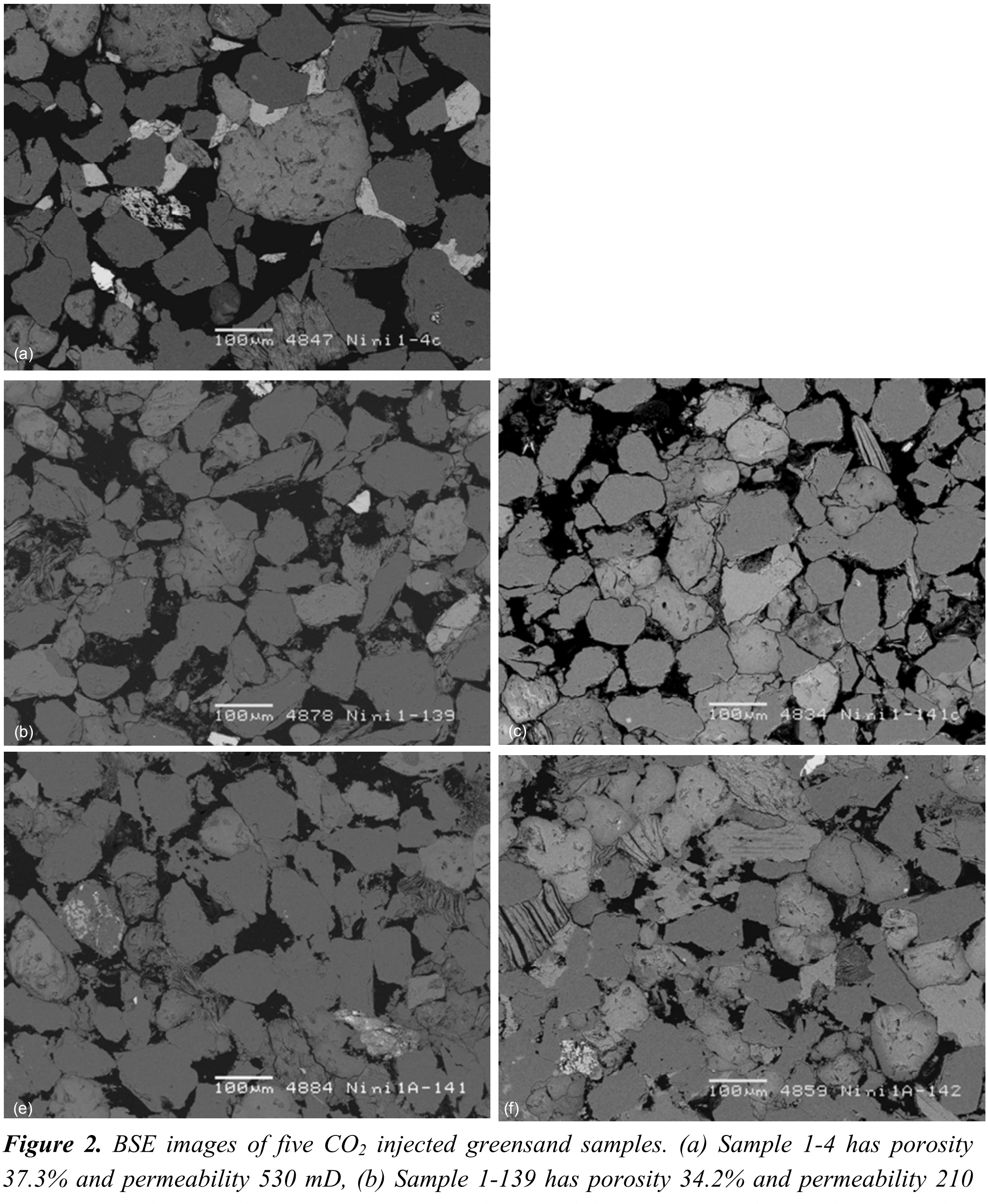

Figure 2. *BSE images of five CO_2 injected greensand samples. (a) Sample 1-4 has porosity 37.3% and permeability 530 mD, (b) Sample 1-139 has porosity 34.2% and permeability 210 mD, (c) Sample 1-141 has porosity 34.9% and permeability 360 mD , (d) Sample 1A-141 has porosity 30.1% and permeability 230 mD and (e) Sample 1A-142 has porosity 29.3% and permeability 160 mD. The images represent macro-porosity, quartz and glauconite grains.*

To investigate the effect of CO_2 injection, we used five horizontal greensand plug samples from two greensand formations of the North Sea Paleogene Nini field (Fig. 2). The Nini field is located in Siri Canyon which is part of a larger system of submarine canyons in the Paleocene in the Norwegian-Danish Basin running in an E-W to NE-SW direction towards the Central Graben (Schiøler et al. 2007). Porosity and permeability of the studied greensand vary from 29% to 37% and 160 mD to 530 mD respectively. Porosity and permeability of greensand from Hermod Formation are higher than from Ty Formation (Table 1).

CO_2 flooding experiment

A CO_2 flooding experiment was carried out on the five greensand samples at reservoir conditions. At reservoir conditions fluid pressure is 38 MPa, hydrostatic confining pressure is 50 MPa and temperature is 115°C.

The CO_2 flooding experiments were conducted in a reservoir condition rig that utilized a Hassler-type core holder for 0.038 m plug samples and a high pressure pump system. The reservoir rig together with a number of pressure cylinders and pressure transducers were situated in a large thermostated oven. The oven provided temperature control with stability significantly better than 1°C. The rig was equipped with a densitometer that measures the density of the fluid produced from the core sample at reservoir conditions.

The five greensand samples were mounted in the core holder in sequence according to permeability such that the sample with lowest permeability was positioned at the inlet of the core holder. The core holder was then mounted in a vertical position so that both CO_2 and brine flooding took place from the bottom towards top of the core holder. The core holder was also equipped with a floating end piece to determine the changes in sample length during the flooding experiments.

After mounting the samples in the core holder, the core holder was mounted in the reservoir condition rig. The fluid pressure and the hydrostatic confining pressure were increased simultaneously until reservoir pressure conditions. During the pressure increase, the difference between the fluid pressure and the confining pressure was kept below 12 MPa and then the reservoir rig was heated to 115°C, where the rig remained to attain equilibrium for a week. Then water was injected into the samples in order to determine the CO_2 injection rate.

The subsequent CO_2 injection experiment lasted five days. Before breakthrough the densitometer log showed that the produced fluid was mainly water with density 1.03 g/cm^3. After breakthrough the density of the non-water phase gradually decreased which indicates a gradual increase in the CO_2 contents of the produced fluid. At the end of the flooding the fluid density had dropped to 0.694 g/cm^3 which indicated that the produced fluid was CO_2 which would have a density of 0.686 g/cm^3 at 38 MPa and 115°C.

After the CO_2 flooding, the core samples were flushed with brine. After breakthrough the density of the water phase gradually increased. At the end of the brine flushing the fluid density had increased to 1.03 g/ cm^3 which indicated that the produced fluid was brine which ideally would have a density of 1.04 g/cm^3. After the CO_2 flooding experiment, samples did not show visible signs of dissolution.

Routine core analysis

Before and after the CO_2 flooding experiment, porosity of the samples was measured by the helium gas expansion method. Helium porosity represents the total porosity of greensand as no pores are so closed that helium cannot enter. Buoyancy of the cores in brine (Archimedes) was also used to determine bulk volume of a fully saturated sample and pore volume was calculated from grain density as measured by the gas expansion method. As porosity data from the two methods are within experimental error, all samples were assumed to be fully brine saturated. Klinkenberg-corrected permeability was derived from permeability at a series of nitrogen gas pressures. Specific surface area (SSA) of grains was measured by the BET method by using nitrogen gas adsorption. Before and after the CO_2 flooding experiments, polished thin sections were prepared from a slice of the end of each plug and backscattered electron micrographs were made.

Capillary pressure

Air brine drainage capillary pressure measurements were done on brine saturated greensand samples by using the porous plate method at room temperature (Hossain et al. 2011). Initially each sample was saturated with simulated formation brine. The brine has a density of 1.06 g/cm^3 and a viscosity of 1.054 cP. Irreducible water saturation (S_{wi}) including clay bound water was determined from capillary pressure curves and macro-porosity was calculated as porosity above irreducible water saturation (Fig. 3b). The capillary pressure (P_c) may be expressed by the fundamental equation:

$$P_c = \frac{2\sigma \cos\theta}{r_c}, \tag{1}$$

where, r_c is the pore radius, σ is the fluid interface tension and θ is the contact angle. For water-wet conditions $cos\theta$ becomes one.

The Buckley and Leverett (1942) dimensionless capillary pressure term was used to convert air brine capillary pressure curve to a CO_2 brine capillary pressure curve:

$$\frac{P_c(air - brine)}{\sigma(air - brine)} = \frac{P_c(CO_2 - brine)}{\sigma(CO_2 - brine)}. \tag{2}$$

Surface tension is $72 \cdot 10^{-3}$ N/m for an air brine system and $50 \cdot 10^{-3}$ N/m for a CO_2 brine system as obtained by Bennion and Bachu (2006).

NMR measurements

NMR measurements and porosity determined from NMR T_2 distributions were described in Hossain et al. (2011). For determining the macro-porosity and micro-porosity we used cutoff values determined from the T_2 distribution. For two samples (one from Hermod and one from Ty), the T_2 cutoff was determined in the laboratory by obtaining the T_2 distribution at two saturations, fully brine saturated and at irreducible water saturation as determined from capillary pressure curves. The analysis of the air-water systems is relatively easy as there is no NMR response from the air and the relaxation time is exclusively due to the protons in the water. The cutoff time is defined as the relaxation time at the point where the cumulative porosity of the fully saturated sample equals the irreducible water saturation (Fig. 3a). As the T_2 cutoff is determined from capillary pressure equilibrium experiments it mainly represents capillary bound fluid in micro-pores. The cumulative porosity over the range $T_2 > T_{2cutoff}$ then represents the macro-porosity, and the range $T_2 < T_{2cutoff}$ represents the micro-porosity or irreducible water saturation. Macro-porosity and micro-porosity represents the total NMR porosity which is lower than Helium porosity due to the effect of paramagnetic iron bearing minerals in greensand (Hossain et al., 2010b).

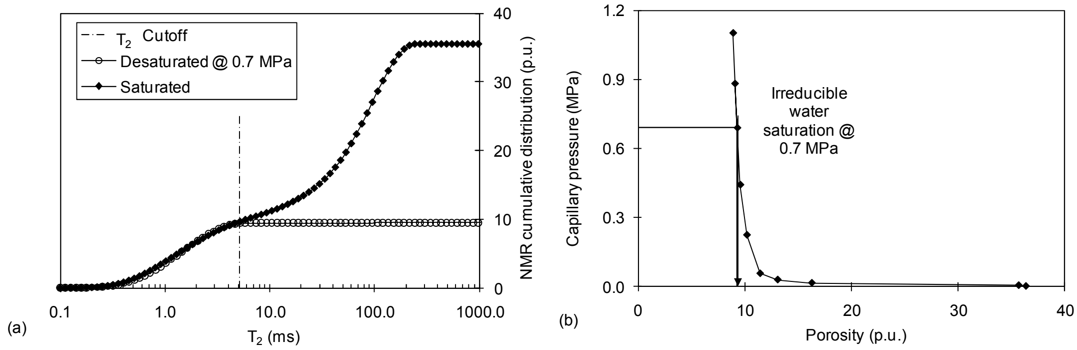

Figure 3. *Macro-porosity and micro-porosity determination for sample 1-4 (a) from NMR T_2 distribution (b) from the capillary pressure curve. The cumulative distribution for the fully saturated sample is compared to the cumulative distribution after centrifuging at 0.7 MPa. The cutoff time which separates the T_2 distribution into macro-porosity and micro-porosity is defined as the relaxation time at the point where the cumulative porosity of the fully saturated sample equals the irreducible water saturation. The dashed vertical line indicates a cutoff of 5.21 ms. The capillary pressure of 0.7 MPa corresponds to a micro-porosity of 9.1% (Hossain et al., 2011).*

We used the cutoff free permeability model of Hossain et al. (2011) to calculate the permeability from NMR T_2 distribution:

$$k = c\phi R_2^2 \sum_{i=1}^{N} f_i (T_{2i})^2 , \qquad (3)$$

where, f_i is the fraction of the total amplitude of each T_{2i}. Kozeny's factor c may be calculated from porosity, ϕ (Mortenseen et al., 1998). R_2 is the surface relaxivity. Surface relaxivity depends on the mineralogical composition and for each sample we used a constant surface relaxivity of 27µm/s (Hossain et al. 2011) before and after CO_2 injection to calculate permeability by using this model.

Resistivity measurements

Resistivity and acoustic data were measured in the same triaxial Hoek cell. Both acoustic and resistivity data were recorded simultaneously at hydrostatic confining pressure with steps from 1 to 12 MPa. Each sample was placed in between the pistons and the Hoek cell was installed in an AC current circuit with variable resistance in series. To isolate electrical influence from the load frame, a plastic film was attached between the pistons. The supply voltage was 1 V and the frequency 1 kHz. The variable resistance was adjusted so that the voltage over the variable resistance is half of the supplied voltage. Then the resistance of the sample is equal to the resistance of the variable resistance. Frequency is adjusted from power supply frequency in such a way that the phase shift between the two voltage waves is minimal and always below 1 degree. The resistivity (R_t) is defined as the resistance multiplied by as geometric factor, (A/l), where A and l are the cross sectional area and length of the sample respectively. The uncertainty for the resistivity measurements is assessed to be maximally 3%.

Laboratory Vp-Vs measurement

Ultrasonic P-and S-wave velocities (V_p and V_s) were measured on all brine saturated and dry samples by using the pulse transmission technique with an approximate centre frequency of 200 kHz. The ultrasonic measurements were done at a hydrostatic confining pressure with steps from 1 to 12 MPa. The ultrasonic velocity of the samples was calculated from the transit time through the sample length, where the system delay time was subtracted from the transit time. The system delay time was determined by measuring the transit time on three aluminum plugs of different lengths. Transit times for P- and S-waves were measured on a digital oscilloscope and saved digitally for later manual analysis. Using error propagation, the estimated standard deviations are less than 50 m/s for V_p and less than 100 m/s for V_s.

Physical properties of fluid

For fluid substitution models, the bulk modulus of the fluid is a basic input parameter. Therefore for modeling purpose, we first need to investigate the physical properties of CO_2 and brine at variable temperature and pressure. We derived the CO_2 properties as a function of temperature and pressure based on data from Wang (2000), and calculated brine properties from equations of Batzle and Wang (1992) as cited in Mavko et al. (2009).

CO_2 saturated brine density was calculated according to Garcia (2001). Based on thermodynamic theory, the density of CO_2 saturated brine (ρ_{brine}) may be expressed as (Garcia, 2001):

$$\rho_{brine} = \rho_b + M_2 c_1 - \rho_b V_M c_1. \tag{4}$$

where M_2 is the molecular weight of CO_2, where ρ_b is the density of pure brine, c_1 is the CO_2 concentration expressed by the number of moles of solute in 1 m^3 of solution and V_M is the apparent molar volume of dissolved CO_2 as expressed as function temperature, t in °C:

$$V_M = 37.51 - 9.585 \cdot 10^{-2} t + 8.740 \cdot 10^{-4} t^2 - 5.5044 \cdot 10^{-7} t^3. \tag{5}$$

Equations 4 and 5 were used to calculate density of aqueous solutions of CO_2 at a pressure of 10 MPa for mole fractions from 0.02 to 0.05. A maximum density increase of 2.5 % was obtained for a solution with a CO_2 mole fraction of 0.05. By using the above mentioned method Garcia (2001) found a very good correlation between measured and calculated CO_2 saturated brine density. Bulk modulus of CO_2 saturated brine (K_{brine}) is the reciprocal of the compressibility of brine saturated CO_2 (β_{brine}):

$$K_{brine} = \frac{1}{\beta_{brine}}. \tag{6}$$

In thermodynamics, compressibility measures the relative volume changes of a fluid as a response to pressure changes. At a constant temperature (T), compressibility of brine saturated CO_2 (β_{brine}) can be written as:

$$\beta_{brine} = -\frac{1}{V_{brine}}\left(\frac{\partial V_{brine}}{\partial P}\right)_T = -\frac{m}{V_{brine}}\left(\frac{\partial \frac{V_{brine}}{m}}{\partial P}\right)_T, \tag{7}$$

where, V_{brine}, is volume and m is mass of CO_2 saturated brine. Then β_{brine} with respect to density changes can be written as:

$$\beta_{brine} = -\rho_{brine}\left(\frac{\partial \frac{1}{\rho_{brine}}}{\partial P}\right)_T = \frac{1}{\rho_{brine}}\left(\frac{\partial \rho_{brine}}{\partial P}\right)_T. \tag{8}$$

$\frac{\partial \rho_{brine}}{\partial P}$ is obtained from the relations of CO_2 saturated brine density versus pressure as shown in Fig. 4.

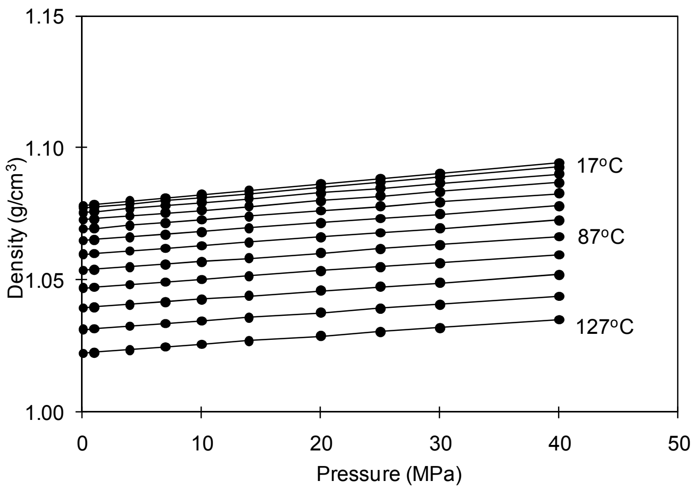

Figure 4. *CO_2-saturated brine density as function of pressure. Brine density was calculated based on equations of Batzle and Wang (1992) as cited in Mavko et al., (2009). CO_2 saturated brine density was calculated based on Garcia (2001).*

CO_2 bearing greensand properties

Initially greensands are saturated with brine. In order to calculate the CO_2 bearing greensand properties we used Gassmann's fluid substitutions equations (Gassmann, 1951). For two types of pore fluids Gassmann's equations are rewritten as (Mavko et al., 2009):

$$\frac{K_{sat1}}{K_0 - K_{sat1}} - \frac{K_{fl1}}{\phi(K_0 - K_{fl1})} = \frac{K_{sat2}}{K_0 - K_{sat2}} - \frac{K_{fl2}}{\phi(K_0 - K_{fl2})}, \ \mu_{sat1} = \mu_{sat2}, \qquad (9)$$

where K_{sat1} and K_{sat2} are bulk modulus of the brine and CO_2 bearing rock respectively, K_{fl1} is bulk modulus of the brine, K_{fl2} is bulk modulus of brine and CO_2 mixtures, K_o is effective bulk modulus of the solid making up the rock, ϕ is porosity, μ_{sat1}, μ_{sat2} are shear modulus of the brine saturated rock and shear modulus of CO_2 bearing rock. A mineral modulus of 33 GPa is estimated for the studied greensand (Hossain et al. 2010b). For isotropic linear elastic materials, the elastic moduli are expressed by the P-wave and S-wave velocities, V_p and V_s, and the bulk density, ρ. The P-wave modulus M is given by $M = \rho V_p^2$, the shear modulus G is given by $G = \rho V_s^2$, and the bulk modulus K is given by $K = M - 4/3G$. Bounds for bulk modulus of brine and CO_2 mixtures (K_{fl2}) was calculated by using the Voigt and Reuss models as cited in Mavko et al. (2009):

$$K_{fl2} = S_{CO_2} K_{CO_2} + S_{brine} K_{brine}, \qquad (10)$$

$$\frac{1}{K_{fl2}} = \frac{S_{CO_2}}{K_{CO_2}} + \frac{S_{brine}}{K_{brine}}, \qquad (11)$$

where K_{brine} and K_{CO_2} are the bulk moduli of CO_2 saturated brine and CO_2. S_{brine} and S_{CO_2} demote the saturations of CO_2 saturated brine and CO_2. Density of brine and CO_2 mixtures (ρ_{fl2}) was calculated by linear combination:

$$\rho_{fl2} = S_{CO_2} \rho_{CO_2} + S_{brine} \rho_{brine}, \qquad (12)$$

where ρ_{brine} and ρ_{CO2} are the density of CO_2 saturated brine and CO_2.

AVO modeling

For analysis of amplitude variation with offset, we calculated the PP (R_{PP}) and PS (R_{PS}) reflection coefficients. We used Zoeppritz's equations as given in Mavko et al. (2009). We calculated the reflection coefficient as a function of reflection angle ranging from 0^o to 30^o. Shale data for AVO curves were obtained from the studied Nini 1A well. The corresponding shale properties are: P-wave velocity of 2.64 km/s, S-wave velocity of 1.37 km/s, and density of 2.34 g/cm^3. The shale represents the cap-rock for the greensand. The V_p, V_s and density of brine bearing greensand sample 1A-142 were used as input to calculate the reflection coefficient. Data representing the CO_2 bearing state were calculated by using Gassmann's equations (Gassmann, 1951).

Results and discussion

Effect of CO_2 injection on porosity, grain density, resistivity and permeability

In general, helium porosity, specific surface area by BET method, grain density and electrical resistivity before and after CO_2 injection remain unchanged considering the error of measurements (Fig. 5, Table 1 and Table 2).

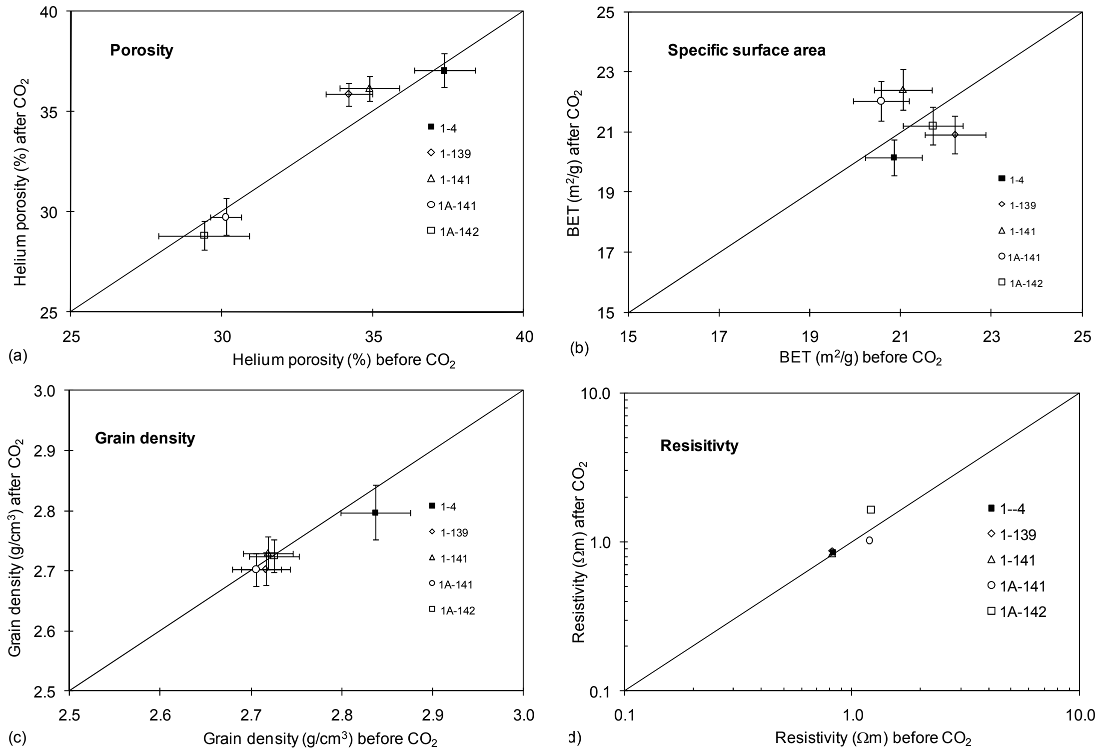

Figure 5. *Laboratory measured (a) Helium porosity, (b) specific surface area by BET method, (c) grain density and (d) resistivity of greensand samples before and after CO_2 injection.*

Table 1. *Porosity, grain density and permeability of greensand samples before and after CO_2 injection experiment.*

	Sample ID	Formation	Porosity (%)	Grain density (g/cm^3)	BET (m^2/g)	Permeability (mD)
Before CO_2 injection	1-4	Hermod	37.4	2.84	20.9	530
	1-141	Ty	34.2	2.72	22.2	360
	1A-141	Ty	34.9	2.72	21.1	230
	1-139	Ty	30.1	2.71	20.6	210
	1A-142	TY	29.4	2.72	21.7	160
After CO_2 injection	1-4	Hermod	37.1	2.80	20.2	1032
	1-141	Ty	35.9	2.71	20.9	254
	1A-141	Ty	36.2	2.73	22.4	867
	1-139	Ty	29.8	2.71	22.0	436
	1A-142	TY	28.8	2.72	21.2	210

Table 2. *Resistivity of samples saturated with a brine with resistivity 0.077 Ωm before CO_2 and after CO_2 injection as a function of confining stress.*

	Sample / Confining stress (MPa)	1-4 Resistivity (Ωm)	1-139 Resistivity (Ωm)	1-141 Resistivity (Ωm)	1A-141 Resistivity (Ωm)	1A-142 Resistivity (Ωm)
Before CO_2 injection	1	0.80	0.81	0.81	1.33	1.19
	2	0.80	0.80	0.81	1.28	1.16
	3	0.81	0.80	0.81	1.22	1.14
	4	0.81	0.82	0.82	1.17	1.16
	5	0.82	0.82	0.83	1.15	1.18
	6	0.83	0.83	0.83	1.15	1.18
	7	0.84	0.83	0.83	1.15	1.18
	8	0.84	0.83	0.83	1.15	1.18
	9	0.84	0.83	0.83	1.15	1.18
	10	0.84	0.83	0.83	1.15	1.18
	11	0.84	0.83	0.83	1.15	1.18
	12	0.84	0.83	0.83	1.15	1.18
After CO_2 injection	1	0.95	0.93	0.85	1.37	1.90
	2	0.89	0.91	0.85	1.27	1.87
	3	0.87	0.91	0.84	1.14	1.81
	4	0.85	0.87	0.84	1.10	1.62
	5	0.85	0.87	0.84	1.06	1.59
	6	0.84	0.86	0.84	1.02	1.55
	7	0.84	0.86	0.84	1.02	1.52
	8	0.83	0.85	0.84	1.02	1.52
	9	0.82	0.85	0.83	1.02	1.52
	10	0.82	0.85	0.83	1.02	1.52
	11	0.82	0.85	0.83	1.02	1.52
	12	0.82	0.85	0.83	1.02	1.52

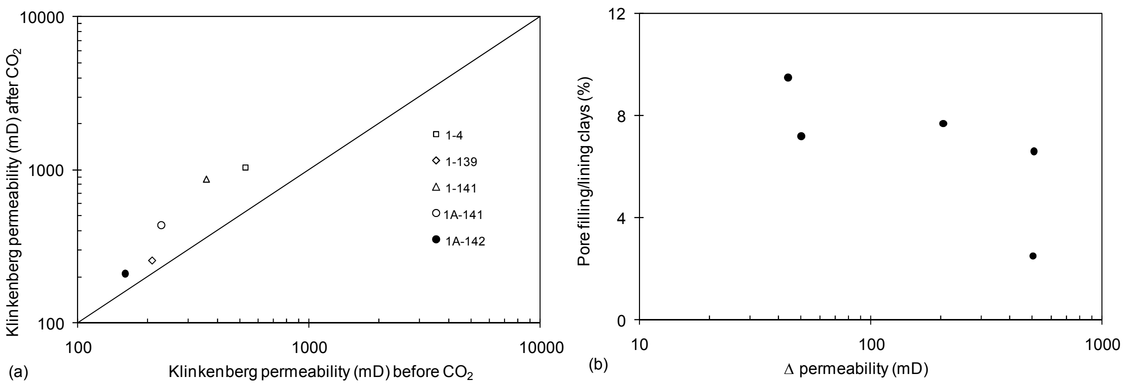

Figure 6. *(a) Laboratory measured Klinkenberg permeability before and after CO_2 injection, (b) cross-plot of delta permeability (permeability after CO_2 injection minus permeability before CO_2 injection) versus pores filling-lining clay minerals.*

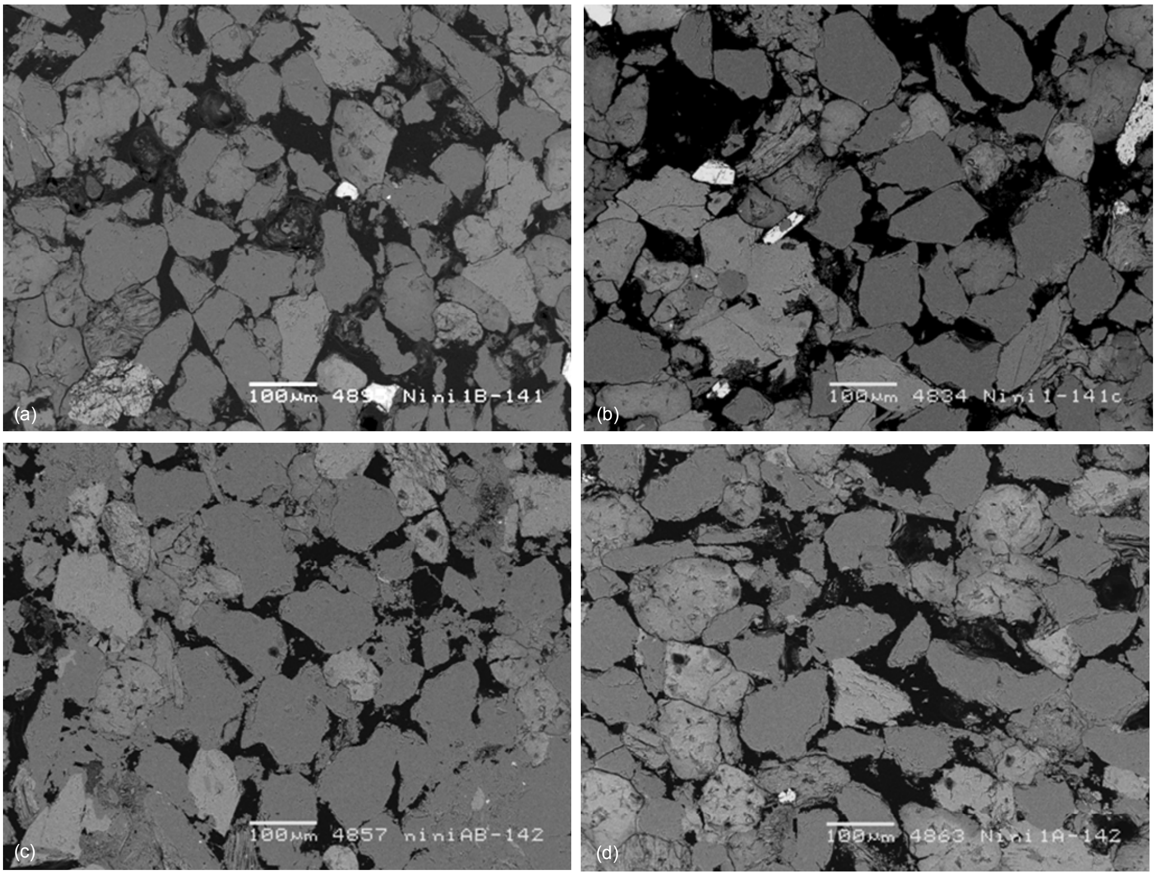

Figure 7. *BSE images of sample 1A-141 (a) before CO_2 injection and (b) after CO_2 injection. BSE images of sample 1A-142 (c) before CO_2 injection and (d) after CO_2 injection.*

By contrast Klinkenberg permeability increases by a factor 1.26-2.4 due to the CO_2 flooding experiment (Fig. 6a and Table 1). The increased permeability could in principle be explained by sample fracturing and/or migration of fine particles during the CO_2 flooding experiment. Micro-crystalline quartz and pore-filling minerals (Fig. 1b) have significant effect on formation permeability (Stokkandel et al., 2009). During the CO_2 flooding experiment, lose fine particles of pore-filling or pore-lining clay could be shifted around which could cause the increase in permeability. This possibility is corroborated by the inverse trend between change in permeability and amount of pre-filling/lining clay minerals (Fig. 6b). CO_2 injection effects are not noticeable from the BSE images (Fig. 7).

Effect of CO_2 injection on NMR T_2 distribution

The NMR T_2 distributions are presented in graphical form for each sample before and after the CO_2 flooding experiment (Fig. 8). All greensand have bimodal T_2 distributions. Each T_2 time corresponds to a particular pore specific surface. If the rock has a single pore specific surface then instead of a broader distribution there will be a single vertical line. Thus broader distributions reflect greater variability in pore shape. The short relaxation time component in a T_2 distribution of a rock is attributed to the water in glauconite. For the present greensand samples a peak close to 1 ms should correspond to glauconite water, whereas all samples also present a second peak close to 100 ms that corresponds to movable fluid (Hossain et al., 2010). The effect of CO_2 flooding on T_2 distribution differs among the samples. T_2 distribution of sample 1-4 after the CO_2 flooding experiment shows that the smaller peak (at around 1 ms) is shifted to larger times, whereas the larger peak (at around 100 ms) becomes narrower. In sample 1-139 the smaller peak becomes slightly smaller, whereas the larger peak is shifted to larger time after CO_2 injection. In sample 1-141 the smaller peaks are overlapping before and after the CO_2 flooding experiment, whereas the larger peak is shifted to larger time. Sample 1A-141 and 1A-142 show that that the smaller peaks become slightly smaller whereas the larger peaks are shifted to larger time. Cumulative porosity is unchanged from before to after CO_2 injection except for sample 1-4. To determine the macro-porosity and micro-porosity from NMR T_2 distribution, we used a cutoff value of 5.2 ms for the sample from Hermod formation and 3.7 ms for the samples from Ty formation (Hossain et al., 2010). Porosity below cutoff corresponds to micro porosity, whereas porosity above cutoff corresponds to macro-porosity. Micro-porosity remains largely unchanged from before to after CO_2 injection (Fig. 9). Whereas, macro-porosity tends to be larger after CO_2 injection (Fig. 9).

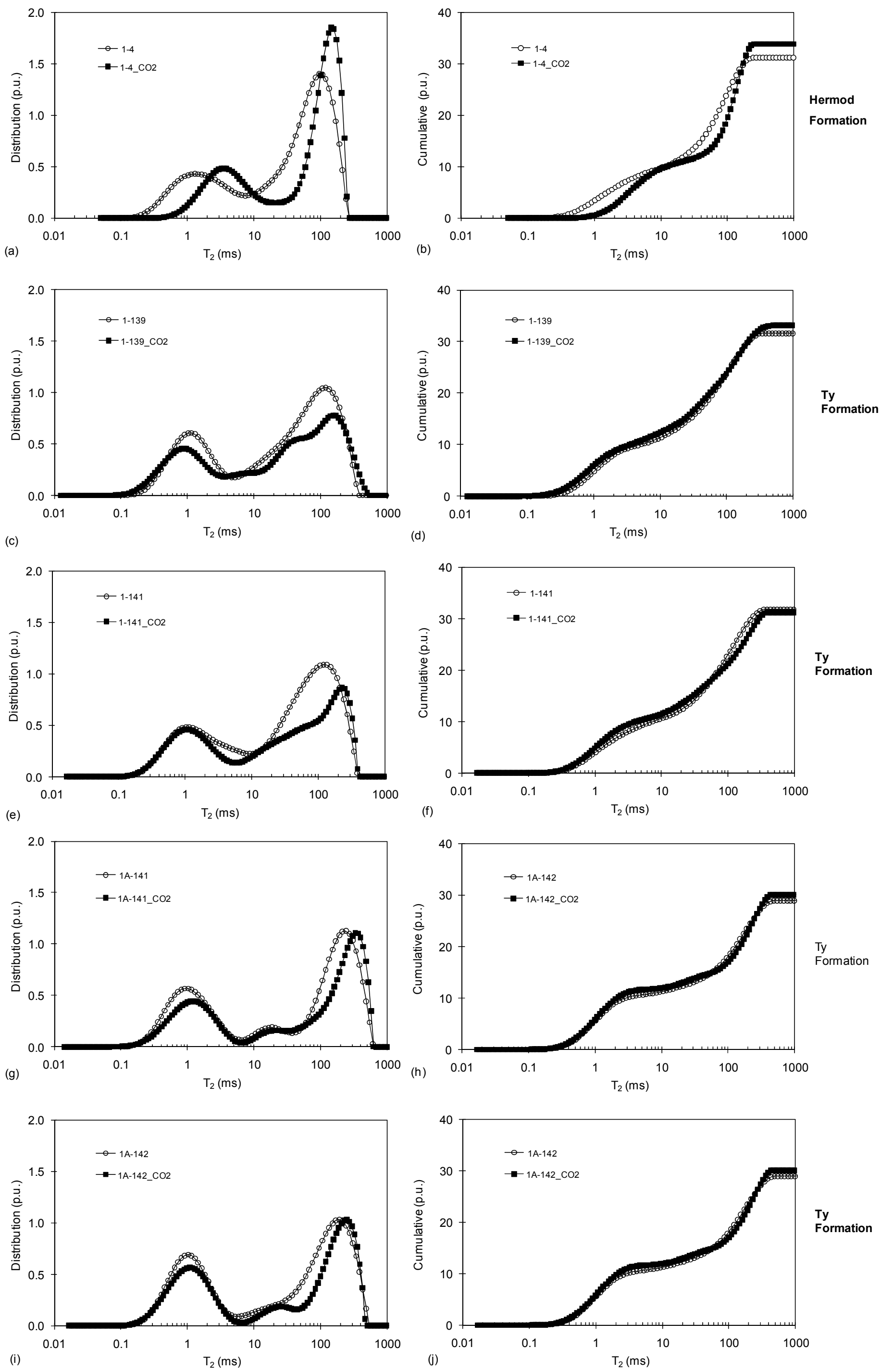

Figure 8. *NMR T_2 distribution and cumulative distribution of greensand samples in porosity units (p.u.) before and after CO_2 injection: (a)-(b) sample 1-4, (c)-(d) sample 1-139, (e)-(f) sample 1-141, (g)-(h) sample 1A-141, (i)-(j) sample 1A-142.*

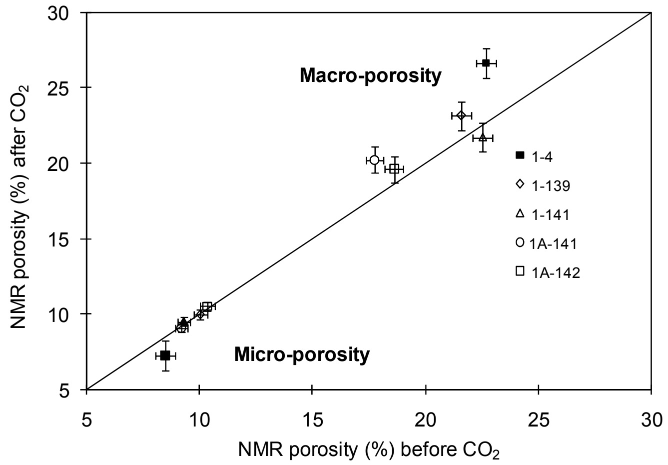

Figure 9. *Micro-porosity and macro-porosity of greensand as measured from NMR measurements before and after CO_2 injection.*

An example of predicted permeability distribution obtained by using Equation (3) is shown in Fig. 10. At low T_2, the amplitude of permeability is close to zero which means micro-porosity does not contribute significantly to fluid flow. From 5.2 ms to 100 ms, the amplitude of permeability is small but above 100 ms the contribution to permeability increases. NMR predicted permeability after CO_2 injection tends to increase (Fig. 10 and Fig. 11). From NMR permeability distribution, we observed that permeability is dominated by the size of macro-pores in the greensand. So NMR predicted permeability after CO_2 injection increases due to the increasing size of macro-pores as shown in Fig. 9. The increase of macro-pores size is probably due to migration of fine pore-filling minerals. The increase in Klinkenberg permeability can thus not be explained by fracturing (Fig. 10 and Fig. 11).

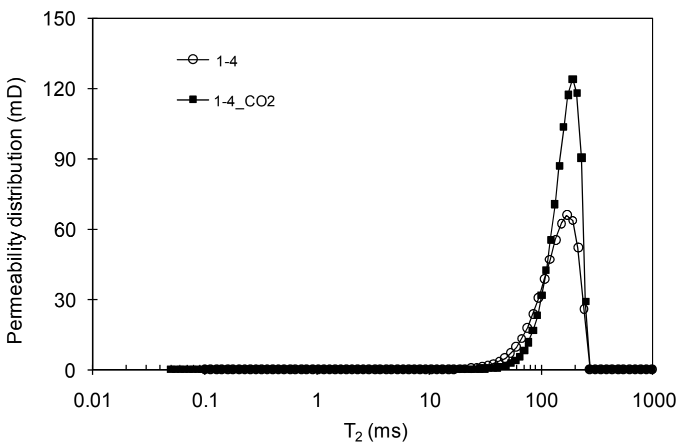

Figure 10. *Permeability distribution as calculated from the permeability modeling for sample 1-4.*

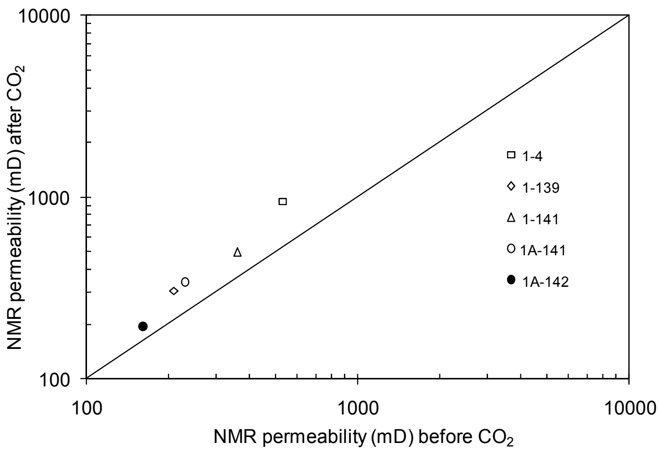

Figure 11. *NMR predicted permeability before and after CO_2 injection.*

Effect of CO_2 injection on elastic velocities

P-wave and S-wave velocity for the brine saturated condition are almost constant before and after the CO_2 flooding experiment (Fig. 12a, Fig. 12b, and Table 3). Even though P-wave and S-wave velocity for dry condition show more scatter before and after CO_2 injection, they probably remain unchanged (Fig. 12c, Fig. 12d, and Table 4).

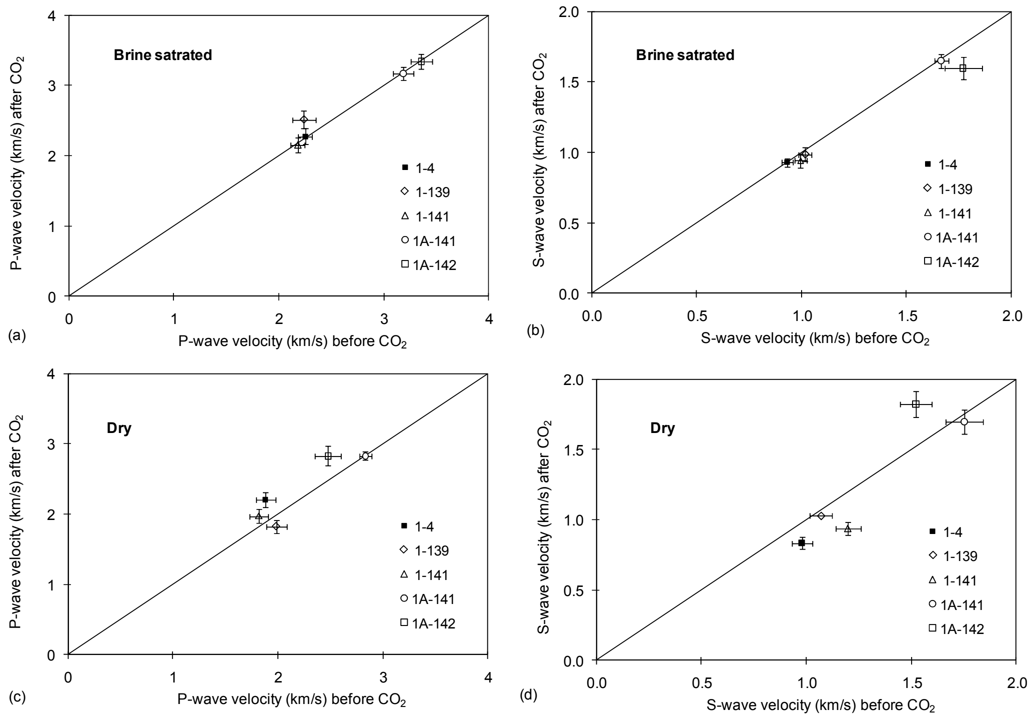

Figure 12. *Laboratory measured (a) P-wave velocity and (b) S-wave velocity of brine saturated greensand samples before and after CO_2 injection. Laboratory measured (c) P-wave velocity and (d) S-wave velocity of dry greensand samples before and after CO_2 injection.*

Table 3. *P-wave velocity and S-wave velocity of brine saturated greensand samples before CO_2 and after CO_2 injection as a function of confining stress.*

	Sample	1-4		1-139		1-141		1A-141		1A-142	
Confining stress	(MPa)	V_p (km/s)	V_s (km/s)	V_p (km/s)	V_s (km/s)	V_p (km/s)	V_s (km/s)	V_p (km/s)	V_s (km/s)	V_p (km/s)	V_s (km/s)
	1	1.98	0.75	1.94	0.80	1.90	0.71	2.90	1.43	3.01	1.47
	2	2.06	0.81	2.00	0.84	1.95	0.73	3.00	1.53	3.16	1.59
	3	2.10	0.84	2.08	0.92	2.05	0.88	3.10	1.59	3.20	1.67
	4	2.15	0.86	2.15	1.00	2.08	0.91	3.13	1.61	3.25	1.68
	5	2.19	0.88	2.16	1.00	2.11	0.98	3.14	1.64	3.32	1.73
Before CO_2 injection	6	2.21	0.92	2.20	1.01	2.14	0.99	3.16	1.66	3.34	1.75
	7	2.25	0.93	2.24	1.02	2.18	1.00	3.18	1.66	3.36	1.77
	8	2.25	0.93	2.24	1.02	2.18	1.01	3.18	1.66	3.36	1.77
	9	2.25	0.93	2.24	1.02	2.18	1.01	3.18	1.66	3.36	1.77
	10	2.25	0.93	2.24	1.02	2.18	1.01	3.18	1.66	3.36	1.77
	11	2.25	0.93	2.24	1.02	2.18	1.01	3.18	1.65	3.36	1.77
	12	2.25	0.93	2.24	1.02	2.18	1.01	3.18	1.65	3.36	1.77
	1	2.01	0.83	2.32	0.89	1.88	0.86	3.00	1.59	3.14	1.42
	2	2.05	0.85	2.37	0.93	1.93	0.88	3.04	1.62	3.20	1.47
	3	2.10	0.87	2.43	0.95	2.02	0.90	3.09	1.62	3.27	1.50
	4	2.15	0.88	2.49	0.96	2.06	0.91	3.12	1.63	3.29	1.51
	5	2.24	0.92	2.51	0.98	2.08	0.92	3.12	1.64	3.31	1.54
After CO_2 injection	6	2.26	0.93	2.51	0.98	2.12	0.94	3.14	1.64	3.33	1.57
	7	2.28	0.93	2.51	0.98	2.15	0.94	3.17	1.65	3.34	1.60
	8	2.28	0.93	2.51	0.98	2.15	0.94	3.17	1.65	3.34	1.60
	9	2.28	0.93	2.51	0.98	2.15	0.94	3.17	1.65	3.34	1.60
	10	2.28	0.93	2.51	0.98	2.15	0.94	3.17	1.65	3.34	1.60
	11	2.28	0.93	2.51	0.98	2.15	0.94	3.17	1.65	3.34	1.60
	12	2.28	0.93	2.51	0.98	2.15	0.94	3.17	1.65	3.34	1.61

Table 4. *P-wave velocity and S-wave velocity of dry greensand samples before CO_2 and after CO_2 injection as a function of confining stress.*

	Sample	1-4		1-139		1-141		1A-141		1A-142	
	Confining stress (MPa)	V_p (km/s)	V_s (km/s)	V_p (km/s)	V_s (km/s)	V_p (km/s)	V_s (km/s)	V_p (km/s)	V_s (km/s)	V_p (km/s)	V_s (km/s)
Before CO_2 injection	1	1.58	0.81	1.67	0.94	1.25	0.94	2.58	1.50	2.10	1.22
	2	1.62	0.85	1.74	0.97	1.41	1.02	2.65	1.59	2.17	1.35
	3	1.68	0.88	1.81	0.99	1.51	1.11	2.72	1.64	2.31	1.40
	4	1.76	0.90	1.88	1.09	1.60	1.15	2.78	1.69	2.35	1.42
	5	1.81	0.94	1.90	1.05	1.67	1.17	2.79	1.71	2.38	1.48
	6	1.87	0.96	1.95	1.09	1.74	1.19	2.81	1.73	2.47	1.50
	7	1.88	0.98	1.98	1.07	1.82	1.20	2.83	1.75	2.48	1.52
	8	1.90	0.99	2.00	1.10	1.87	1.22	2.85	1.81	2.56	1.54
	9	1.91	1.00	2.02	1.11	1.91	1.23	2.87	1.82	2.57	1.56
	10	1.91	1.01	2.07	1.13	1.94	1.24	2.89	1.83	2.59	1.57
	11	1.91	1.01	2.11	1.15	1.97	1.25	2.91	1.85	2.61	1.58
	12	1.91	1.01	2.13	1.16	1.99	1.26	2.92	1.86	2.66	1.59
After CO_2 injection	1	1.90	0.73	1.52	0.80	1.37	0.65	2.58	1.40	2.36	1.56
	2	1.95	0.75	1.59	0.82	1.50	0.75	2.66	1.46	2.45	1.61
	3	2.00	0.76	1.72	0.87	1.63	0.85	2.72	1.56	2.56	1.68
	4	2.06	0.77	1.76	0.93	1.75	0.87	2.78	1.62	2.68	1.73
	5	2.12	0.83	1.77	0.96	1.87	0.90	2.79	1.66	2.76	1.76
	6	2.17	0.82	1.78	1.00	1.93	0.92	2.81	1.67	2.80	1.79
	7	2.21	0.84	1.82	1.03	1.97	0.94	2.83	1.70	2.83	1.83
	8	2.26	0.85	1.84	1.06	2.01	0.96	2.85	1.70	2.85	1.84
	9	2.26	0.86	1.90	1.07	2.04	0.98	2.87	1.72	2.87	1.86
	10	2.26	0.87	1.94	1.09	2.05	1.00	2.89	1.73	2.89	1.87
	11	2.26	0.88	1.96	1.08	2.07	1.02	2.91	1.73	2.91	1.89
	12	2.26	0.88	1.98	1.12	2.08	1.03	2.94	1.74	2.94	1.89

Physical properties of brine and CO_2

Elastic properties of CO_2 saturated brine were calculated by using the method described by Garcia (2001). Due to CO_2 dissolution, the density of brine is increased by about 2% and bulk modulus is increased by 1.5% to 2.5%, whereas the velocity is increased by less than 1%. Both CO_2 saturated brine and CO_2 are influenced by temperature and pressure (Fig. 13). However, temperature and pressure effects are more pronounced on CO_2 than on brine. At room conditions the ratio of bulk modulus between CO_2 and CO_2-saturated brine is around 20500 whereas this ratio is only around 17 at reservoir conditions (Fig. 13 and Table 5). At room conditions the ratio of density between CO_2 and CO_2-saturated brine is around 533 whereas this ratio is only around 1.5 at reservoir conditions. Therefore, CO_2 at reservoir condition can be considered a highly compressible liquid, while its density is nearly equal to the density of brine.

Table 5. *CO_2 and CO_2-saturated brine properties at room and reservoir conditions. Brine density was calculated based on Batzle and Wang (1992) as cited by Mavko et al. (2009). CO_2 saturated brine density was calculated by using the method of Garcia (2000), whereas CO_2 saturated bulk modulus was calculated from density of CO_2 saturated brine as shown in equation (8).*

		Bulk modulus (GPa)	P-wave velocity (m/s)	Density (g/cm^3)	
Fluids	CO_2 saturated brine at 0.1 MPa and 22^{0}C			1.065	Measured
		2.67	1590	1.066	Calculated
	CO_2 saturated brine at 38 MPa and 115^{0}C			1.025	Measured
		2.92	1680	1.033	Calculated
	CO_2 at 0.1 MPa and 22^{0}C	0.00013	264	0.002	
	CO_2 at 38 MPa and 115^{0}C	0.167	490	0.686	

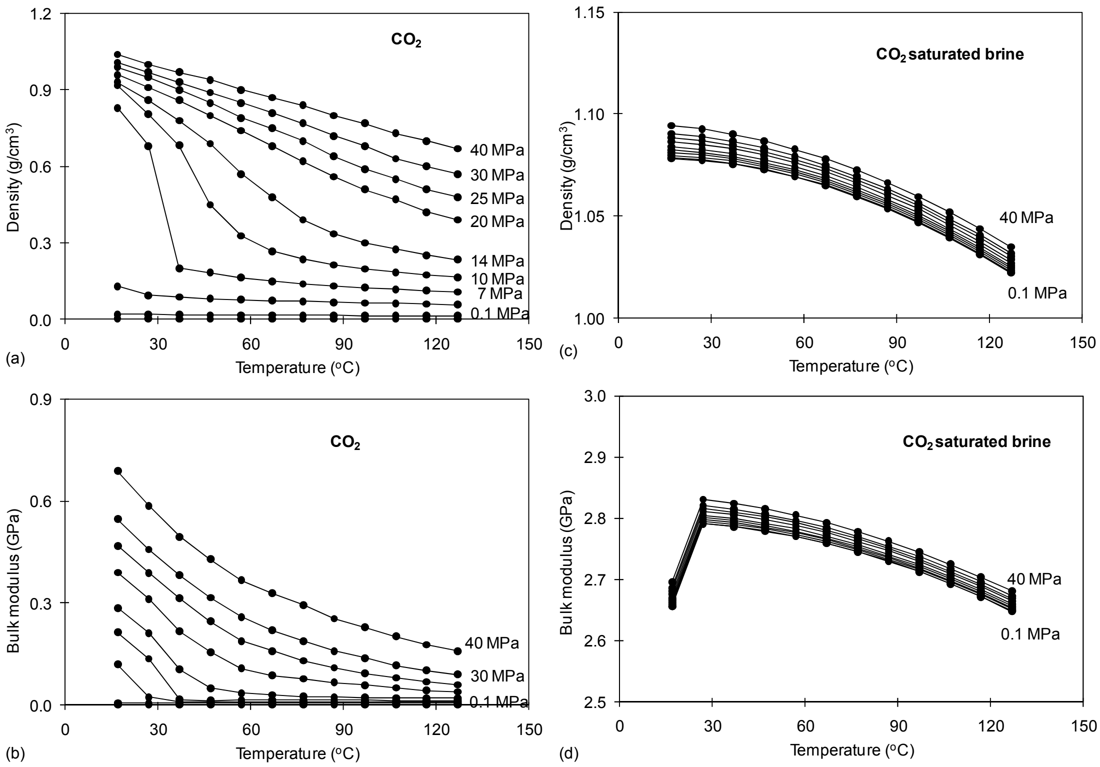

Figure 13. *Properties of CO_2 and of CO_2-saturated brine properties as function of temperature and pressure: (a) density of CO_2, (b) density of CO_2 saturated brine, (c) Bulk modulus of CO_2, (d) Bulk modulus of CO_2 saturated brine. Bulk modulus and density of CO_2 are based on Wang (2000) measurements, whereas brine density was calculated based on equations of Batzle and Wang (1992) as cited in Mavko et al., (2009). CO_2 saturated brine density was calculated based on Garcia (2001). Bulk modulus of CO_2 saturated brine was calculated from CO_2 saturated brine density as shown in equation (8).*

Rock physics modeling of CO_2 bearing greensand

For modeling purpose we converted air brine capillary pressure curves to CO_2 brine capillary pressure curves (Fig. 14). Capillary pressure curves show that the higher permeability Hermod Formation sample has low irreducible water saturation, whereas the lower permeability Ty Formation samples have high irreducible water saturation (Fig. 14a). Irreducible water saturation from capillary pressure was obtained at P_c 0.7 MPa, and varies between 25% and 37% of the total porosity. The micro-pores of glauconite thus apparently remain brine filled even at a capillary pressure of 0.7 MPa.

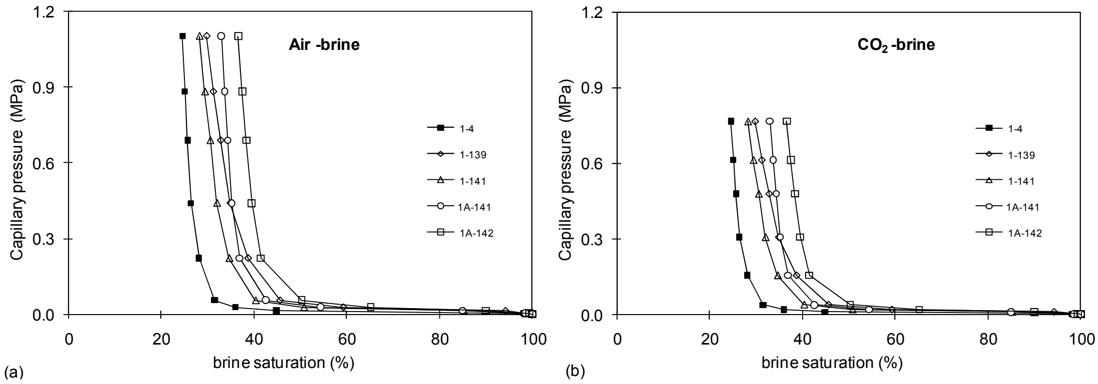

Figure 14. *(a) Air-brine capillary pressure measured in laboratory, (b) CO_2-brine capillary pressure calculated from air-brine capillary pressure.*

P-wave velocity and S-wave velocity of CO_2 bearing greensand as calculated by using Gassmann's equations are presented in Fig. 15. CO_2 saturation levels were obtained from CO_2 brine capillary pressure curves. The modeling results demonstrate that the largest changes in CO_2 saturated properties occur when the first small amounts of CO_2 are injected into brine saturated greensand. At higher CO_2 saturation levels, the change in elastic properties is relatively small. Our modeling results show that the effect of CO_2 flooding decreases V_p on average by 10%-17% and up to 41% in high-porosity greensand. CO_2 flooding also increases V_s, typically 1%-2% and decreases density on average by 3%-5% (Table 6). This result is in accordance with sensitive analysis by Sengupta and Mavko (2003) which indicates that Gassmann's equations are most sensitive to the brine saturated V_p, while the sensitivity to shear wave velocity and bulk density is much lower.

In comparison with the Reuss model or uniform saturation, the Voigt model or patchy saturation shows a more gradual decrease in P-wave velocity with CO_2 content and always leads to higher velocities (Fig. 15). Therefore, it is crucial to define whether the patchy or the uniform model should be used to calculate elastic properties of CO_2 saturated greensand.

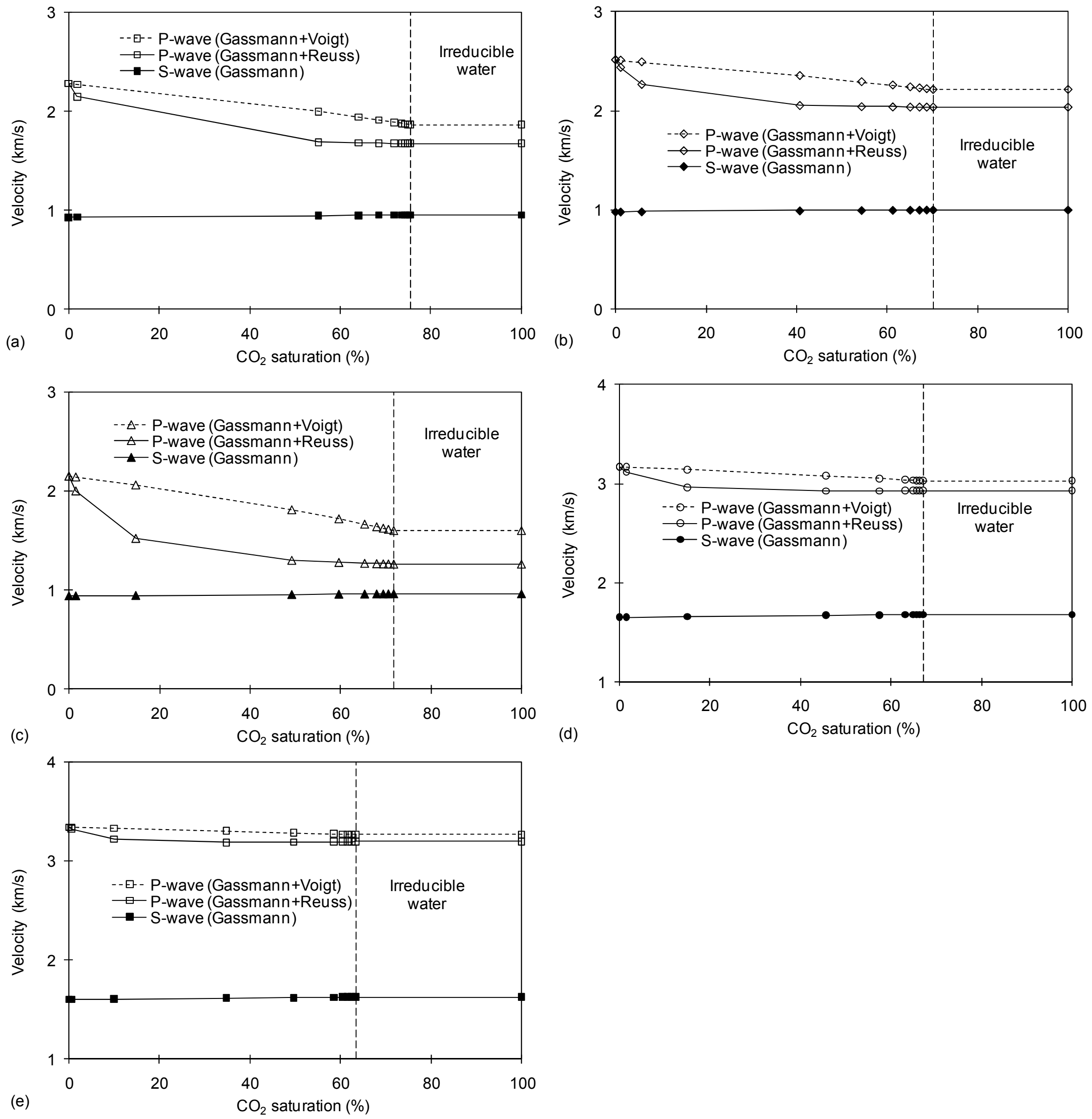

Figure 15. *P-wave velocity and S-wave velocity of CO_2 bearing greensand samples as estimated by using Gassmann's equations: (a) sample 1-4, (b) sample 1-139, (c) sample 1-141, (d) sample 1A-141, (e) sample 1A-142.*

Table 6. *Changes in elastic velocities and density of greensand at partial CO_2 saturation. CO_2 saturated greensand properties were calculated by using Gassmann's equations (Gassmann 1951).*

Sample ID	Porosity (%)	Permeability (mD)	Changes in V_p (%) Patchy		Uniform	Changes in V_s (%)	Changes in bulk density (%)
1-4	37.3	530	-18.3		-26.5	2.3	-4.6
1-139	34.2	360	-11.9		-18.8	2.1	-3.9
1-141	34.9	230	-25.6		-41.2	2.1	-4.1
1A-141	30.1	210	-4.4		-7.6	1.6	-3.2
1A-142	29.3	160	-2.2		-4.4	1.5	-2.9
Aveage	**33.2**	**298.0**	**-12.5**		**-19.7**	**1.9**	**-3.7**

AVO modeling of CO_2 saturated greensand

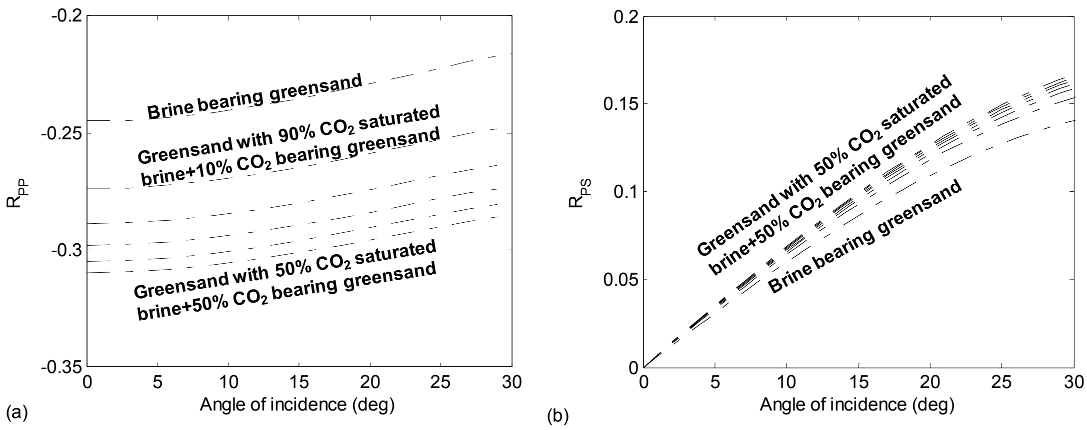

Figure 16. *Refection coefficient (R) versus incident angle for an interface of shale and greensand with varying saturation of CO_2 and CO_2 saturated brine: (a) PP refection coefficient (R_{pp}), (b) PS refection coefficient (R_{ps}).*

Fig. 16a represents the PP reflection coefficient as a function of incident angle, whereas Fig. 16b represents the PS reflection coefficient as a function of incident angle. For the PP reflectivity (Fig. 16a), the corresponding AVO response shows a negative zero-offset reflectivity and a positive AVO gradient. The AVO response of CO_2 saturated greensand is distinguishable both at zero and far offset. For the PS reflectivity coefficient, the AVO response of CO_2 saturation is distinguishable at far offset only. All curves are ambiguous at zero offsets, as the P-to-S reflection coefficient goes to zero for normal incidence (Fig. 16b). Fig. 16a demonstrates that for the PS reflection the largest change in the AVO response occurs when the first 10% CO_2 are injected into a brine saturated greensand. At higher CO_2 saturation levels, the change in AVO response is relatively small. PP refection coefficients are monotonically decreasing whereas PS reflection coefficients are monotonically increasing with CO_2 saturation increase.

Conclusion

Our laboratory results show that CO_2 injection has no major effect on porosity, as well as on electrical and elastic properties of the greensand frame.

Klinkenberg permeability of the greensand increased after CO_2 injection. An NMR T_2 distribution and NMR permeability modeling approach was used to evaluate whether the permeability increase was due to the fractures or due to an increase in matrix permeability. The NMR data indicates that permeability after CO_2 injection increased due to an increase in size of macro-pore. The increase of macro-pores size is probably due to migration of fine pore-filling minerals. The increased permeability is thus not caused by fracturing.

Rock physics modeling results show that the effect of CO_2 flooding alone would decrease V_p by 2%-41%. CO_2 flooding would also increase V_s, typically by 1.9% and decrease density by 3%-5%.

AVO modeling indicates that the largest change in the AVO response occurs when the first 10% CO_2 are injected into a brine saturated greensand.

Acknowledgements

We wish to thank Dan Olsen (GEUS) for CO_2 injection experiments. Niels Springer and Hans Jørgen Lorentzen (GEUS) are thanked for help with the permeability measured on CO_2 injected samples. Sinh Hy Nguyen (DTU) is tanked for help with porosity and BET measured on CO_2 injected sample. Hector Ampuero Diaz (DTU) prepared polished thin sections. Monzurul Alam is acknowledged for doing NMR measurement on CO_2 injected samples. DONG Energy A/S is acknowledged for financial support.

References

Batzle, M., Wang, Z., 1992. Seismic properties of pore fluids. Geophysics 57, 1396–1408.

Bennion, D. B., Bachu, S., 2006. The Impact of Interfacial Tension and Pore Size Distribution/Capillary Pressure Character on CO_2 Relative Permeability at Reservoir Conditions in CO_2-Brine Systems. Proceedings of the SPE/DOE Symposium on Improved Oil Recovery, Tulsa, OK, April 22-26, 2006; SPE Paper 99325, 9.

Brown, S., Bussod, G., Hagin, P., 2007. AVO Monitoring of sequestration: A benchtop-modeling study. The Leading Edge 26, 1576-1583.

Buckley, S.E., Leverett, M., 1942. Mechanism of fluid displacement in sand. Trans. of AIME 146, 107-116.

Carcione, J., Picotti, S., Gei, D., Rossi, G., 2006. Physics and seismic modeling for monitoring CO_2 storage. Pure and Applied Geophysics 163, 175–207.

Castagna, J. P., 1993. Comparison of AVO indicators: A modeling study. Geophysics 59, 1849-1855.
Castagna, J. P., Smith, S. W., 1994. Comparison of AVO indicators: A modeling study. Geophysics 59, 1849-1855.

Castagna, J., Swan, H. W., Foster, D. J., 1998. Framework for AVO gradient and intercept interpretation. Geophysics 63, 948-956.

Chang, Yih-Bor., Costs, B.K., Nolen, J.S., 1998. A compositional Model for CO_2 Floods Including CO_2 Solubility in Water. SPE Reservoir Evaluation & Engineering 4, 155-160.

Garcia, J. E., 2001. Density of aqueous solutions of CO_2. Technical Report LBNL-49023, Lawrence Berkeley National Laboratory, Berkeley, CA.

Gassmann, F., 1951. Elastic waves through a packing of spheres. Geophysics 16, 673-685.

Hossain, Z., Fabricius, I. L., Christensen, H. F., 2009. Elastic and nonelastic deformation of greensand. The Leading Edge 28, 260-262.

Hossain, Z., Fabricius, I.L, Grattoni A. C., Solymar, M., 2011. Petrophysical properties of greensand as predicted from NMR measurements. Petroleum Geoscience (in Press)

Hossain, Z., Mukerji, T., Dvorkin, J., Fabricius, I.L., 2010a. Rock Physics model of glauconitic greensand from the North Sea. Extended abstract, 80^{th} SEG annual conference, Denver October 17-25, Colorado, USA.

Hossain, Z., Mukerji, T., Fabricius, I.L., 2010b. Vp-Vs relationship of glauconitic greensand. Extended abstracts, 72^{nd} Annual EAGE conference, June 14-17, Barcelona, Spain.

Kazemeini, S.H., Juhlin, C., Fomel, S., 2010. Monitoring CO_2 response on surface seismic data; a rock physics and seismic modeling feasibility study at the CO_2 sequestration site, Ketzin, Germany. Journal of Applied Geophysics 71, 109–124.

Lei, X., Xueb, Z., 2009. Ultrasonic velocity and attenuation during CO_2 injection into water-saturated porous sandstone: Measurements using difference seismic tomography. Physics of the Earth and Planetary Interiors 176, 224-234.

Li, Y., Downton, J., Xu, Y., 2007. Practical aspects of AVO modeling. The Leading Edge 26, 295-311
Liu, Y., 1998. Acoustic properties of reservoir fluids. PhD thesis, Stanford University.

Ma, J., Morozov, I., 2010. AVO modeling of pressure-saturation effect in Weyburn CO_2 sequestration. The Leading Edge 29, 178-183.

Mavko, G., Mukerji, T., Dvorkin, J., 2009. The Rock Physics Handbook—Tools for Seismic Analysis in Porous Media. Second Edition, Cambridge University Press.

McKenna, J.J., Gurevich, B., Urosevic, M., Evans, B.J., 2003. Rock physics-application to geological storage of CO_2. APPEA Journal 43, 567–576.

Osif, T.L., 1988. Effect of salt, gas, temperature and pressure on the compressibility of water. SPE reservoir Engineering 2, 175-181.

Ross, G.D., Todd, A.C., Tweedie, J.A., Will A.G., 1982. The dissolution effects of CO_2-brine systems on the permeability of U.K. and North Sea calcareous sandstones. Proceeding at the DOE Symposium on Enhanced Oil Recovery, April 4-7 1982, Tulsa, TX; SPE paper 10685, 8

Sayegh, S.G., Najman, J., 1987. Phase behaviour measurements of CO_2–SO_2–brine mixtures. Canadian Journal of Chemical Engineering 65, 314–320.

Schiøler, P., Andsbjerg, J., Clausen, O. R., Dam, G., Dybkjær, K., Hamberg, L., Heilmann-Clausen, C., Johannessen, E. P., Kristensen, L. E., Prince, I., 2007. Lithostratigraphy of the Paleocene: Lower Neogene succession of the Danish North Sea. Geological Survey of Denmark and Greenland Bulletin 12, 77.

Sengupta, M., Mavko, G., 2003. Impact of flow-simulation parameters on saturation scales and seismic velocity. Geophysics 68, 1267–1280.

Siggins A. F., 2006. Velocity-effective stress of CO_2-saturated sandstone. Exploration Geophysics 37, 60-66.

Solymar, M., 2002. Influence of composition and pore geometry on immiscible fluid flow through greensand. Ph.D.Thesis, Chalmers University of Technology.

Solymar, M., Fabricus, I.L., Middleton, M.F., 2003. Flow characterization of glauconitic sandstones by interated Dynamic Neutron Radiagraphy and image analysis of backscattered electron micrographs. Petroleum Geoscience, 9, 175-183.

Stokkendal, J., Friis H., Svendsen, J. B., Poulsen, M. L. K., Hamberg, L., 2009. Predictive permeability variations in a Hermod sand reservoir, Stine Segments, Siri Field, Danish North Sea. Marine and Petroleum Geology 26, 397-415.

Wang, Z. Michael E. C. and Robert T. L., 1998. Seismic monitoring of a CO_2 flood in carbonate reservoir: A rock physics study. Geophysics 63, 1604-1617.

Wang, Z., 2000. Dynamic versus static properties of reservoir rocks, in seismic and acoustic velocities in reservoir rocks. SEG Geophysics Reprint Series 19, 531-539.

Wang, Z., and Nur, A.M., 1989. Effects of CO_2 flooding on wave velocities in rocks with hydrocarbon. SPE Reservoir Engineering 4, 429–436.

Wang, Z., Sun, M., Batzle, M., 2010.CO_2 velocity measurement and models for temperatures up to 200^o C and pressure un to 100 MPa. Geophysics 75, 123–129.

Xue, Z., Ohsumi, T., 2004. Seismic wave monitoring of CO_2 migration in water-saturated porous sandstone. Exploration Geophysics 35, 25–32.

V

Conference paper

Hossain, Z. and Mukerji T. (2011): Statistical rock physics and Monte Carlo simulation of seismic attributes for greensand from the North Sea (Accepted for EAGE annual meeting, Vienna, May 23-26, 2011).

Statistical rock physics and Monte Carlo simulation of seismic attributes for greensand

Zakir Hossain
Technical University of Denmark

Tapan Mukerji
Stanford Center for Reservoir Forecasting

Summery

The main objective of this study is to estimate uncertainly and map probabilities of occurrences of different seismic attribute of greensand to improve hydrocarbon detectivity. Greensands are sandstone composed of mixture of quartz and micro-porous glauconite grain. Glauconite grains are soft and have much lower elastic modulus than quartz grains. Therefore, lower acoustic impedance of glauconite grains in greensand may mask information between solid and fluid; between hydrocarbon and brine as well between greensand and shale. We applied statistical rock physics method which consists of the four main steps: data classification, data augmentation based on Monte Carlo simulation, attributes calculation and classification success ratio analysis. We used non-parametric Monte Carlo simulation and parametric Monte Carlo simulation method. Elastic impedance-acoustic impedance attribute may be used as seismically discriminating lithologies and identifying partial oil saturations of greensand reservoir.

Keywords: Greensand, Elastic impedance, Monte Carlo, Bayesian

Introduction

Greensands are complex type of reservoir rock. Greensands are mainly composed of mixture of quartz and glauconite grains. Glauconite grains are porous and soft and thus have much lower elastic modulus than quartz grains. Therefore, lower acoustic impedance of glauconite grains in greensand may mask information between solid and fluid; between hydrocarbon and brine as well between greensand and shale. The main objective of this study is to estimate uncertainly and map probabilities of occurrences of different seismic attribute of greensand to improve hydrocarbon detectivity. We use well log data in the Nini Field, of the North Sea to compute the different seismic attributes.

Method

We applied statistical rock physics method based on Avseth *et al.* (2005), Gonzalez *et al.* (2003) and Mukerji *et al.* (2001). The methodology consists of the four main steps: data classification, data augmentation based on Monte Carlo simulation, attributes calculation and classification success ratio analysis.

For non-parametric Monte Carlo simulation (NMC), we used sonic and density logs from Nini field. The loggings data are classified into the group of interest e.g. shale, oil bearing greensand and brine bearing greensand. For parametric Monte Carlo simulation (PMC), we used sonic and density data derived from rock physics soft-sand and stiff-sand model for greensand (Hossain et al. 2010). Glauconite bearing sandstone from the North Sea field can be modeled with the soft-sand model and stiff-sand model (Hossain et al. 2010) thus we selected this model.

Monte Carlo (MC) simulation is a powerful numerically intensive procedure. MC simulation, by taking into account whole distributions of values instead of single average values, help to avoid the flaw of averages (Avseth et al. 2005). Assuming that V_p, V_s, and ρ values were a good representation of the oil bearing greensand, brine bearing greensand and shale in the study area, the number of data points was extended by drawing correlated Monte Carlo (CMC) simulations according to (Avseth et al. 2005).

Two types of attributes were calculated: layer attributes- *lp-ls,* λ - μ, λ - ν, *le(10^o)- Ip* and interface attributes-*A-B*. *Ip* and *ls* is the acoustic impedance; λ, μ, and ν are Lame's parameters, shear modulus and Poisson's ratio; $l_e(10^{o})$ is the PS elastic impedance for 10 degrees (Mukerji *et al*. 2001), while *A* and *B* are the intercept and gradient respectively from Aki and Richards approximation as cited in the Mavko et al. (2009). All these attributes can be analytically defined from

PP seismic data and they were calculated with V_p, V_s, and ρ data. The far-offset impedance has been called the elastic impedance, as it contains information about the V_p/V_s ratio and it can be expressed in terms of the incidence angel θ and layer parameter (Mukerji et al., 2001):

$$l_e(\theta) = \left(V_P^{1+\tan^2\theta}\right)\left[\rho^{1-4\left(\frac{V_S}{V_P}\right)^2 \sin^2\theta}\right]\left[V_S^{-8\left(\frac{V_S}{V_P}\right)\sin^2\theta}\right] \tag{1}$$

The zero offset reflectivity, A, is controlled by the contrast in acoustic impedance across an interface; while the gradient, B, is controlled by the contrast in V_p/V_s ratio and as well as the contrasts in V_p and density (Mavko et al. 2009). Classification success ratio analysis was done based on Bayesian confusion matrices.

Using model based data, the statistical classification success rate was analyzed for discriminating partial water saturation by using attribute $lp\text{-}l_e(10^o)$. We applied Gassmann's (Gassmann, 1951) fluid substitution method to calculation the partial water saturated V_p, V_s, and ρ assuming the homogenous mixture of oil and brine. Effective fluid modulus and density were calculated with Reuss and arithmetic average respectively, for water saturations S_w= 1, 0.7, 0.5, 0.3, and 0:

$$\frac{1}{K_f} = \frac{S_o}{K_o} + \frac{S_w}{K_w} \tag{2}$$

$$\rho_f = \rho_o S_o + \rho_w S_w \tag{3}$$

where K_f, K_w, K_o are the bulk moduli of fluid, brine and oil and ρ_f, ρ_w, ρ_o are the corresponding densities. S_w and S_o denote the saturation of water and oil. Elastic properties of each fluid component at reservoir conditions were calculated using the equations of Batzle and Wang (1992) as cited in Mavko et al. 2009.

Results

V_p, V_s, *and* density logging data and Monte Carlo simulated results for each defined group are represented in Figure 1a and Figure 1b. Figure 1c presents the plots of attribute: acoustic impedance and elastic impedance, computed with Monte Carlo simulated V_p, V_s, *and* density whereas their 2D pdf (probability distribution function) are presented in Figure 1d. There is a clear overlap between greensand and shale in V_p-V_s and V_p-ρ planes, while in the $I_e(10^o)$-Ip plane, the groups are almost completely separated (Figure 1c).

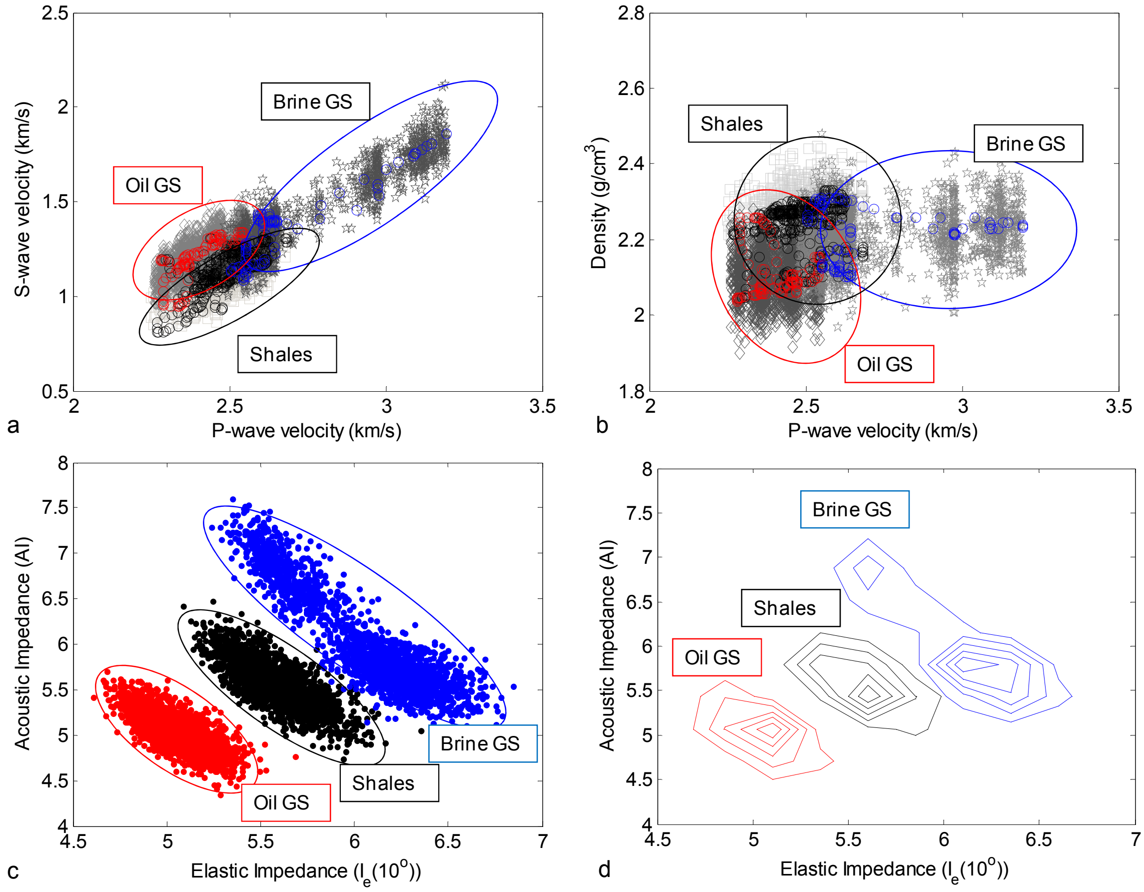

Figure 1. *(a) P-wave and S-wave velocity of brine bearing greensand (GS), oil bearing greensand and shale from well logs (colour data points) and from Monte Carlo simulation (grey data points), (b) P-wave velocity and density of brine bearing greensand, oil bearing greensand and shale from well logs (colour data points) and after Monte Carlo simulation (grey data points), (c) Elastic impedance and acoustic impedances calculated from simulated data and (d)2D pdf plot of elastic and acoustic impedance.*

Although the V_p versus V_s of greensand and shale show certain separations, the overlap of density in V_p-ρ plan is remarkable. Classification success rate of 0.98 and greater were obtained for the attributes: elastic impedance-acoustic impedance (Figure 2). PMC method does slightly better than NMC. The statistical classification success rate was analyzed for discriminating partial water saturation by using attribute: *lp-le(10°)*. Classification success rate of 0.85 and greater were obtained for all water saturation cases (Figure 3).

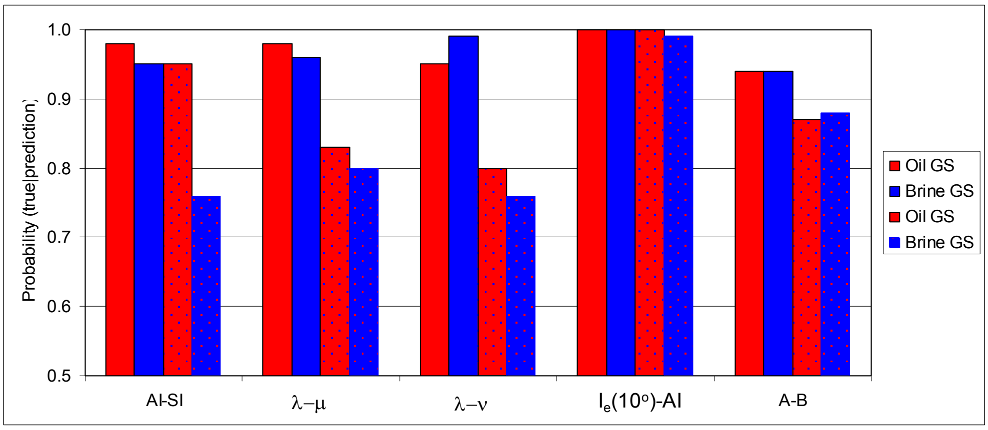

Figure 2. *Classification success rate analysis for different attributes based on Parametric Monte Carlo simulation (PMC) and non-parametric Monte Carlo simulation (NMC).*

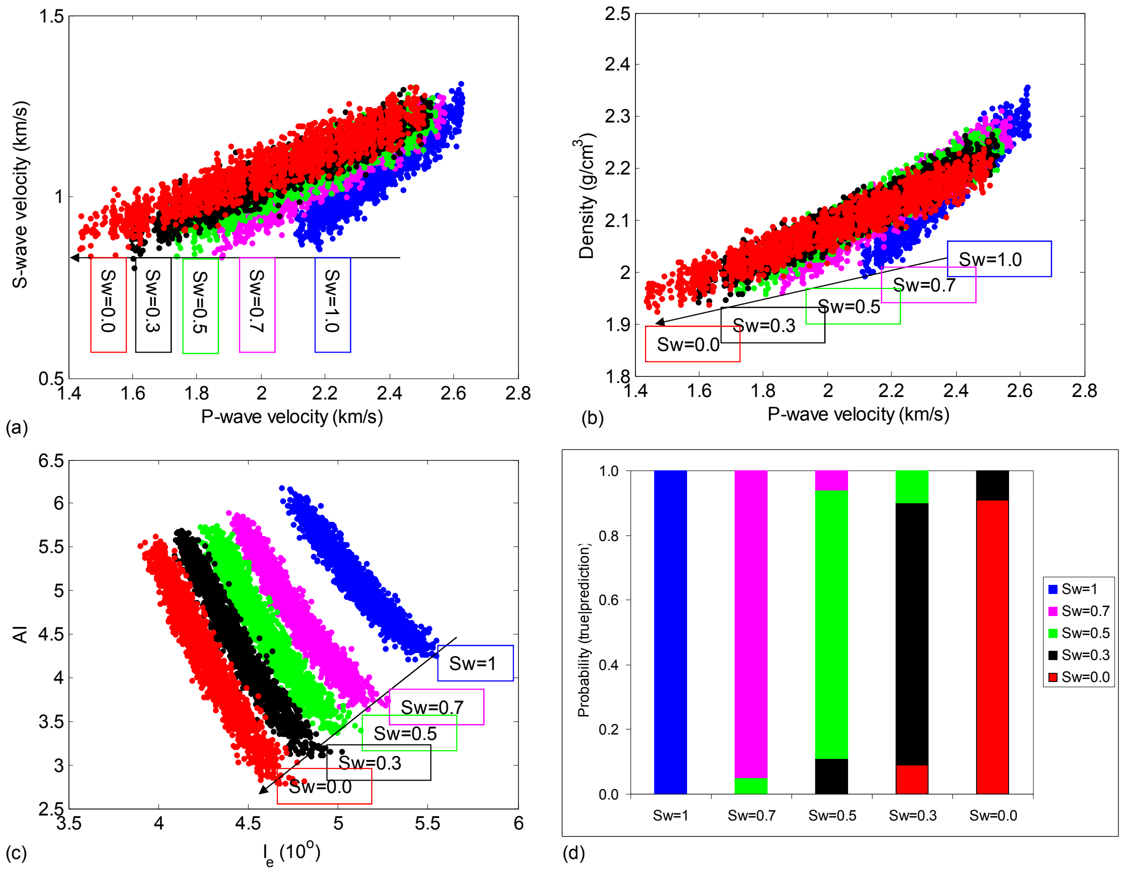

Figure 3. *(a) P-wave and S-wave velocity, (b) P-wave velocity and density, (c) Elastic impedance and acoustic impedances calculated of partial water saturated greensand after Monte Carlo simulation (d) Classification success rate analysis for partial water saturated greensand.*

Conclusions

In this study we have shown how to identify seismic attributes for greensand reservoir characterization. We combined statistical rock physics and MC simulation methods to discriminate between lithologies in greensand reservoir and to identify partial oil saturation. This study shows that Elastic impedance-acoustic impedance attribute may be used as seismically discriminating lithologies and identifying partial oil saturations of greensand reservoir.

Acknowledgements

We acknowledge Stanford Rock Physics project and department of Energy Engineering, Stanford University for their hospitality during the summer, 2009. DONG Energy A/S is acknowledged for the financial support.

References

Avseth, P., Mukerji, T. and Mavko, G. 2005. Quantitative seismic interpretation: applying rock physics tools to reduce interpretation risk: Cambridge University Press.

Avseth P., Mukerji T., Jørstad A., Mavko G. and Veggeland T. 2001a. Seismic reservoir mapping from 3D AVO in a North Sea turbidite system. Geophysics 66, 1157-1167.

Avseth P., Mukerji T., Mavko G. and Tyssekvam, J. A. 2001b. Rock physics and AVO analysis for lithofacies and pore fluid prediction in a North Sea oil field. The Leading Edge 20, 429-434.

Batzle M. and Wang Z. 1992. Seismic properties of pore fluids. Geophysics 57, 1396-1408.
Gassmann F. 1951. Elastic waves through a packing of spheres. Geophysics 16, 673-685.

Gonzalez E.F., Mukerji, T. and Mavko G. 2003. Near and far offset P-to-S elastic impedance for discriminating fizz water from commercial gas. The Leading Edge 24, 1012-1015.

Hossain, Z., Mukerji, T., Dvorkin, J. and Fabricius, I.L. 2010. Rock Physics model of glauconitic greensand from the North Sea. Extended abstract, 80th SEG annual conference, Denver October 17-25, Colorado, USA.

Mavko G., Mukerji T. and Dvorkin J. 2009. The rock physics handbook: tools for seismic analysis of porous media. Cambridge University Press. Second Edition.

Mukerji, T., Jorstad, A., Avseth, P., Mavko, G., and Granli, J. R. 2001. Mapping lithofacies and pore fluid probabilities in a North Sea reservoir: Seismic inversions and statistical rock physics. Geophysics 66, 988-1001.

VI

Journal paper

Hossain, Z., Fabricius, I.L and Christensen, H.F. (2009): Elastic and non-elastic deformation of greensand. The Leading Edge, Volume 28, Issue 1, pp. 86-88.

Elastic and nonelastic deformation of greensand

Zakir Hossain and Ida Lykke Fabricius, Technical University of Denmark, KGS.
Helle Foged Christensen, Danish Geotechnical Institute, KGS.

Analysis of greensand reservoirs all over the world has challenged geologists, engineers and petrophysicsts. One challenge is to identify from core data the degree to which deformation of the reservoir rock affects hydrocarbon production. In the central part of the North Sea, massive allochtoneous Paleocene greensands form reservoirs for oil. We study the deformation of one oil-zone sample from one of these reservoirs by sonic measurements, uniaxial compression testing, and image analysis of backscatter electron micrographs before and after testing.

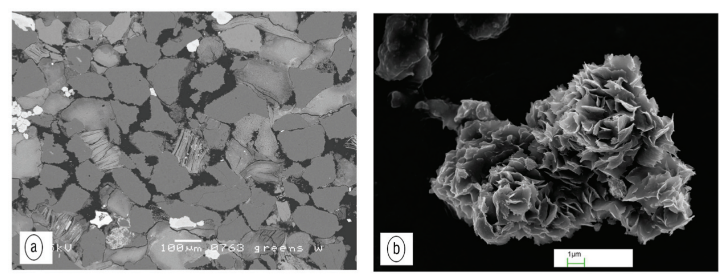

Figure 1. (a) BSE image of the North Sea greensand and (b) glauconite grain from Arnager greensand. Scale bar for greensand is 100 μm and the image represents macroporosity, quartz, and glauconite grains. Scale bar for glauconite grain is 1 μm. Micropores reside within glauconite grain.

Greensands are a mixture of stiff clastic grains, macropores, and soft microporous glauconite grains. The studied Paleocene greensand contains 22% iron-bearing illitic glauconite, 60% quartz, feldspar, and the iron-bearing 7Å clay berthierine. Macropores reside between these grains (Figure 1a), whereas the glauconite grains enclose micropores (Figure 1b). The deformation properties of these mineralogically heterogeneous sands reflect the properties of their constituents.

Deformation properties of a rock can be determined from geotechnical compression testing and from sonic measurements. The main differences between the two types of test are the frequency of deformation and the strain amplitude. When an acoustic wave propagates through a porous medium, the frequency is relatively high and the strain amplitude is low, so the deformation of the porous medium is elastic. In a static test, the frequency is low and the strain amplitude is large. So, in a porous medium, a nonelastic deformation as well as an elastic deformation can arise. Nonelastic deformation comprises closing of microcracks formed during retrieval of the core and grains sliding into a denser packing or, for greensands, a permanent deformation of glauconite grains.

Elastic deformation may be described by Young's modulus and Poisson's ratio. When during geomechanical compression, a static uniaxial stress (σ) is applied, the axial deformation (ε_z) is determined from the loading curve, and where strain gauges are applied, the radial strain $\varepsilon_x = \varepsilon_y$ may also be obtained. For a linearly elastic material, Hook's law states:

$$d\varepsilon_z = \frac{d\sigma}{E_{static}} \tag{1}$$

where the coefficient E_{static} is the static Young's modulus. The static Poisson's ratio, ν_{static}, describes the radial to axial strain and is defined as:

$$\nu_{static} = -\frac{d\varepsilon_x}{d\varepsilon_z} \tag{2}$$

The elastic deformation caused by propagation of sonic waves may be calculated from P-wave velocity (v_P), S-wave velocity (v_S), and density (ρ), of the rock, as expressed in the dynamic Young's modulus, $E_{dynamic}$:

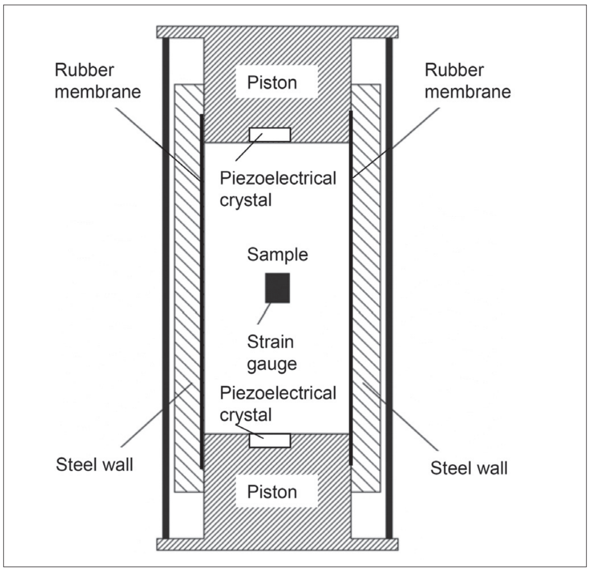

Figure 2. Triaxial cell. Strain gauges measure axial and radial strain. Confining pressure is controlled by hydraulic oil. Piezoelectrical crystals are built into the pistons for continuous measuring of P-wave and S-wave velocity during compression tests. (Modified after Olsen et al.).

$$E_{dynamic} = 2\rho v_S^2 \left(1 + \frac{(v_P^2 - 2v_S^2)}{2(v_p^2 - v_S^2)}\right) \tag{3}$$

and the dynamic Poisson's ratio becomes:

$$\nu_{dynamic} = \frac{(v_P^2 - 2v_S^2)}{2(v_p^2 - v_S^2)} \tag{4}$$

Permanent deformation of the medium may be quantified by image analysis of backscatter micrographs. Changes in

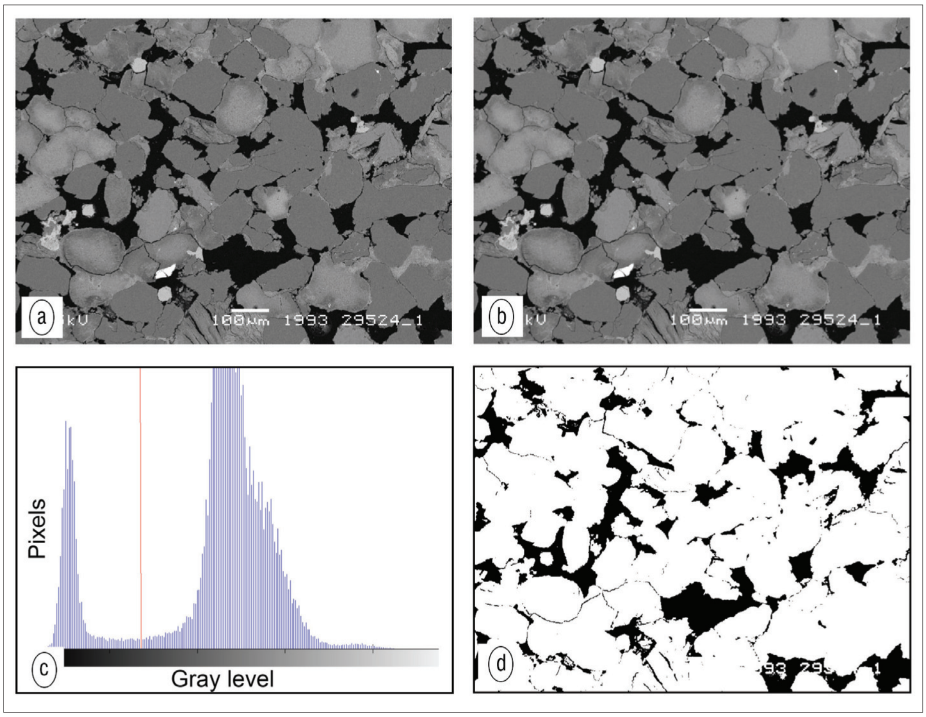

Figure 3. Measuring macroporosity by image analysis: (a) original image, (b) filtered image when noise level is reduced, (c) histogram of grey level and setting a threshold (red) to create a binary image, and (d) binary image where black pixels represent pores and white pixels represent grains. These procedures were done using MATLAB code.

macroporosity indicate sliding and rearrangement of grains, and changes in grain shape indicate permanent deformation of grains. Grain shape may be quantified as roundness and sphericity. *Roundness* is calculated from the area (A) and perimeter (P) of a grain:

$$Roundness = \frac{4\pi A}{P^2} \tag{5}$$

Sphericity is calculated from the semimajor axis (a), and semiminor axis (b), of a grain:

$$Sphericity = \frac{2\sqrt[3]{ab^2}}{a + \dfrac{b^2}{\sqrt{(a^2 - b^2)}} \ln\left(\dfrac{a + \sqrt{(a^2 - b^2)}}{b}\right)} \tag{6}$$

Testing

Compression to an axial stress of 15 MPa is done in a triaxial cell (Figure 2), while confining pressure is manually controlled to 2 MPa. The sample is drained during measurements, so the pore pressure is equal to the atmospheric pressure at the low deformation rate of 3×10^{-6} s^{-1} (1% per hour). Axial and radial strains are measured by strain gauges glued to the sample. Data are sampled with an interval of 5 s. Ultrasonic P-wave and S-wave velocity are measured with a center frequency of 132 kHz. Within the steel pistons of the triaxial cell piezoelectrical crystals are embedded so that acoustic measurements can be done continuously during the compression test.

Grain density is measured by He porosimetry, and the initial and final porosity calculated from sample dimensions of

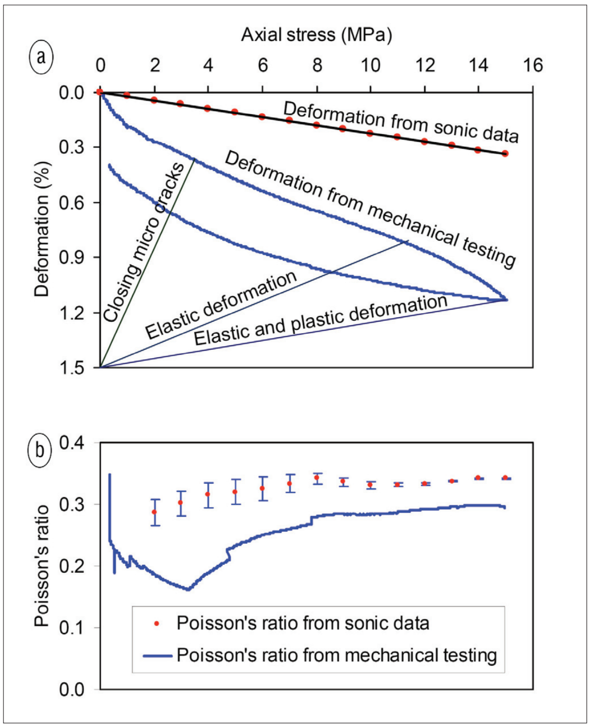

Figure 4. (a) Elastic deformation calculated from sonic data and elastic and nonelastic deformation from uniaxial compression test. Data for uniaxial compression test are obtained after the first cycle in order to minimize influence of microcracks. (b) Static and dynamic Poisson's ratios for greensand sample. Static Poisson's ratio data below 2 MPa are unreliable due to the effect of confining pressure.

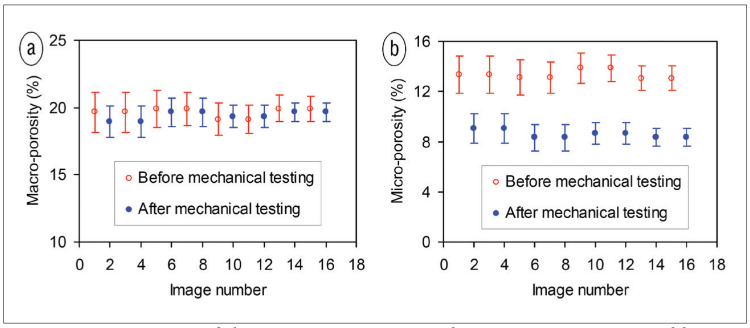

Figure 5. *Comparison of changing macroporosity and microporosity as measured by image analysis. (a) Macroporosity is practically unchanged by mechanical testing. (b) Microporosity within glauconite decreases by mechanical testing.*

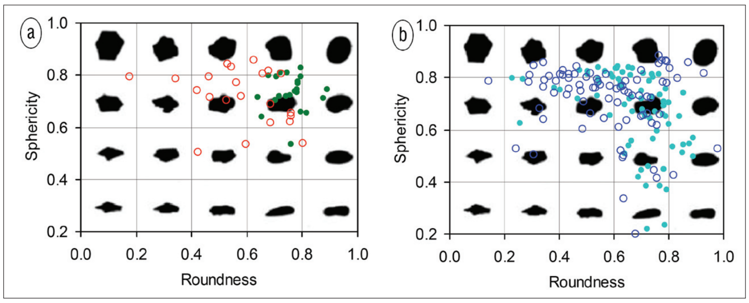

Figure 6. *Calculated roundness and sphericity of grains before and after geomechanical testing: (a) glauconite grains and (b) quartz grains. Glauconite grains are more rounded and more flattered after geomechanical testing. For quartz grains no significant change was observed. (Figure background modified after Krumbein and Sloss.)*

the plug before testing and mercury immersion of the sample after testing. Electron micrographs of polished thin sections are used for image analysis to measure macroporosity, grain roundness, and grain sphericity before and after testing (Figure 3).

As is normally the case for porous media, the deformation obtained from geomechanical testing is higher than would be expected from the dynamic $E_{dynamic}$ obtained from sonic data (Figure 4). When the resulting permanent strain ($d\varepsilon_{nonelastic}$) is taken into account, we find that the elastic strain corresponds to:

$$d\varepsilon_z = d\varepsilon_{elastic} + d\varepsilon_{nonelastic} \tag{7}$$

and that the elastic strain is higher than the strain predicted from sonic data by a factor 1.3–3. When the elastic strain is measured from the loading curve we find that:

$$d\varepsilon_{elastic} = 3\, d\varepsilon_{dynamic} \tag{8}$$

Whereas when the elastic strain is measured from the unloading curve we find:

$$d\varepsilon_{elastic} = 1.3\, d\varepsilon_{dynamic} \tag{9}$$

This confirms the common observation that Young's modulus is higher in the dynamic case than in the static case. The lower factor from the unloading curve (Equation 9) indicates that the loading is not purely elastic, but includes some degree of plastic deformation, whereas the unloading curve may be closer to truly elastic. Poisson's ratio also becomes higher in the dynamic case. From the unloading curve we find:

$$1.2\, v_{elastic} = v_{dynamic} \tag{10}$$

It should be borne in mind that deformation measured by strain gauges may underestimate the total volumetric deformation. Core analysis data indeed indicate that due to permanent nonelastic deformation the total porosity of the sample is reduced from 33% to 30%.

From image analysis we find that the permanent deformation is due to deformation of the glauconite grains and consequent reduction in microporosity rather than reduction in macroporosity (Figure 5). We find that due to the geomechanical testing, the shape of the glauconite grains has changed so that the average sphericity has decreased. By contrast quartz grains have maintained their shape (Figure 6).

Conclusions

Combining information from geomechanical testing, sonic velocity and image analysis of backscatter electron micrographs can give information on which grains in a sandstone suffers elastic deformation and which grains suffer plastic deformation.

We applied this method to an oil-zone sample from a North Sea Paleocene greensand with 20% macroporosity and 13% microporosity and found that loading to 15 MPa under uniaxial conditions resulted in 0.45% elastic deformation and from volumetric strain 1% plastic deformation. The plastic deformation is caused by permanent deformation of the glauconite grains only, so that microporosity decreases whereas macropores and quartz grains only deform elastically.

When taking the plastic deformation into account, Young's modulus determined by geomechanical testing is 1.3 to 3 times smaller than Young's modulus calculated from sonic data, and Poisson's ratio correspondingly is 1.2 times smaller when it is determined from geomechanical testing than when it is calculated from sonic data.

Suggested reading. "Paleocene" by Ahmadi et al. (in *The Millennium Atlas: Petroleum Geology of the Central and Northern North Sea*, Geological Society Publishing House, 2003). "Static and dynamic Young's moduli of chalk from the North Sea" by Olsen et al. (GEOPHYSICS, 2008). *Stratigraphy and Sedimentation* by Krumbein and Sloss (Freeman, 1963).

Corresponding author: zah@env.dtu.dk

The Department of Environmental Engineering (DTU Environment) conducts science-based engineering research within four themes:
Water Resource Engineering, Urban Water Engineering,
Residual Resource Engineering and Environmental Chemistry & Microbiology.
Each theme hosts two to four research groups.

The department dates back to 1865, when Ludvig August Colding, the founder of the department, gave the first lecture on sanitary engineering as response to the cholera epidemics in Copenhagen in the late 1800s.

DTU Environment
Department of Environmental Engineering
Technical University of Denmark

Miljoevej, building 113
DK-2800 Kgs. Lyngby
Denmark

Phone: +45 4525 1600
Fax: +45 4593 2850
e-mail: reception@env.dtu.dk
www.env.dtu.dk

ISBN 978-87-92654-35-9